On the evolution of the halocline in the upper Arctic Ocean since 2007

Cécilia Bertosio

THESE DE DOCTORAT DE SORBONNE UNIVERSITE

Spécialité: Océanographie

Ecole Doctorale 129

Réalisée au

Laboratoire d'Océanographie et du Climat:

Expérimentations et Approches Numériques

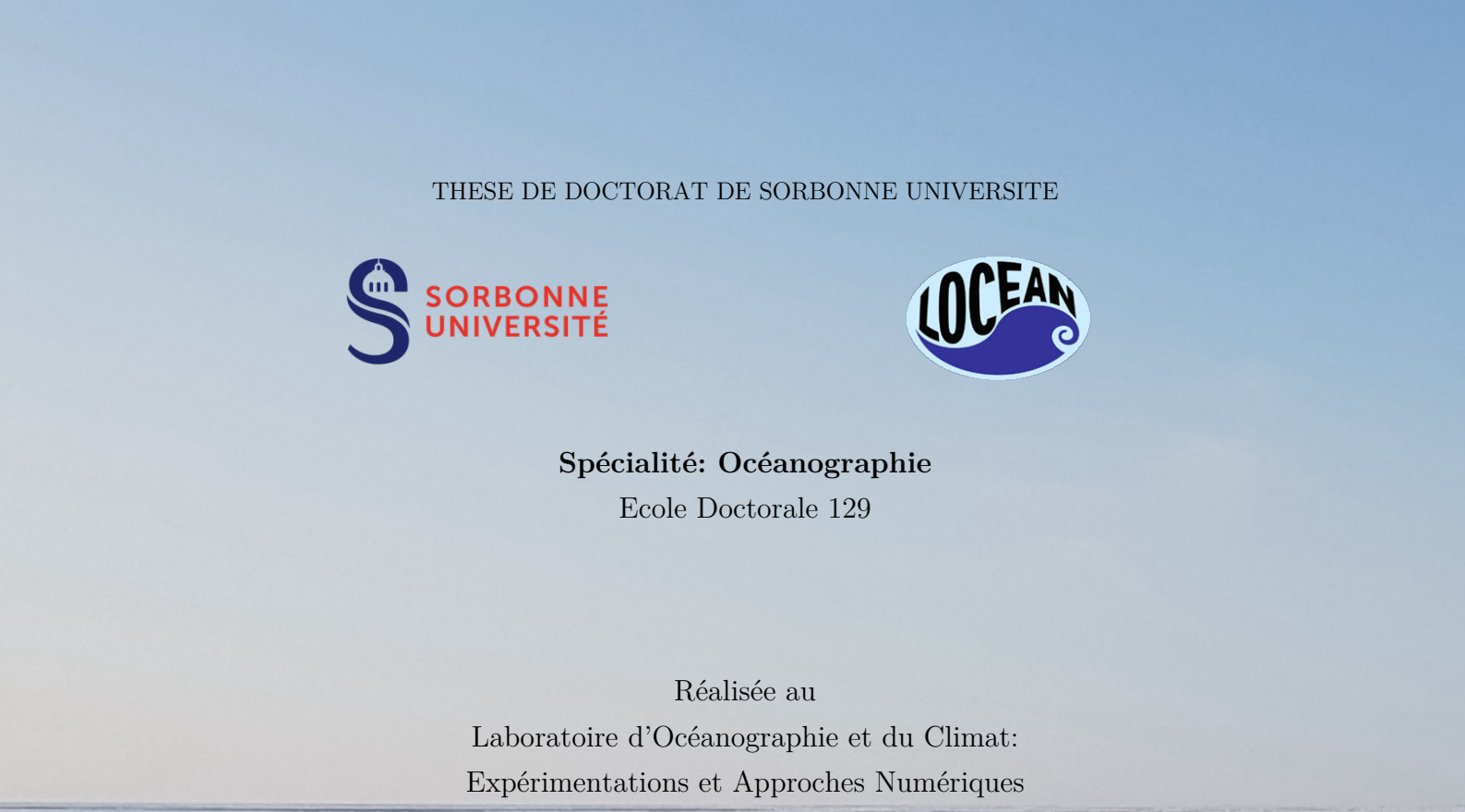

Présentée par

Cécilia Bertosio

On the evolution of the halocline in the upper Arctic Ocean since 2007

Soutenance le 10 Décembre 2021

Devant le jury composé de:

Mme Christine Provost	LOCEAN, France	*Directrice*
M. Damien Cardinal	LOCEAN, France	*Président*
M. Michael Karcher	AWI, Allemagne	*Rapporteur*
M. Jean Tournadre	IFREMER, France	*Rapporteur*
Mme Heather Regan	NERSC, Norvège	*Examinatrice*
M. Gilles Garric	Mercator-Océan, France	*Examinateur*

Cécilia Bertosio, Chukchi Borderland, *Araon, Août 2019*

Remerciements

Cette thèse n'aurait jamais pu aboutir sans l'aide et le soutien de nombreuses personnes.
Je souhaiterai remercier les membres du jury d'avoir été presents à la soutenance de thèse malgré les difficultés liées à la pandémie du Covid19. Je les remercie également pour leur temps, leurs questions et leur intérêt pour mes travaux de thèse.
Je remercie tous les co-auteurs français des articles composant cette thèse pour leur investissement et nos échanges scientifiques : Christine Provost, Marylou Athanase, Nathalie Sennechael, Gilles Garric, Jean-Michel Lellouche et Clément Bricaud. Je remercie également Joo-Hong Kim, Kyoung-Ho Cho et Taewook Park de l'équipe sud-coréenne du KOPRI pour leur contribution comme co-auteurs des article de cette thèse, mais aussi pour leur accueil à bord du brise glace Araon durant la campagne estivale de 2019.

En parlant de campagne en mer, merci à Matthieu Labaste, avec qui j'ai eu la chance partager cette mission en Arctique. Merci pour ta patience et tes conseils. Je n'oublierai jamais cette incroyable expérience !
Au-delà de l'aspect scientifique, la thèse c'est également des moments chaleureux partagés au laboratoire. Pour cela, je souhaite remercie l'équipe du couloir du 5e, tour 55-56, pour nos pauses café du matin. Merci également à celles et ceux de passage, ou qui sont arrivés vers la fin de ma thèse, et avec qui j'ai pu passer de très bons moments, boire un verre, découvrir le crochet ou le tricot, ou même partager une soirée jeux de société: Lauréline, Aude, Clément, Babette, Ruben, Louise et Margaux. Merci !

J'en arrive au noyau dur de mon entourage au laboratoire.
Camila, je te remercie pour ta gentilesse, ta bonne humeur et ton aide tout au long de ma thèse. Tes "coffee coffee coffee" du matin me manquent tellement!
Léa, merci de m'avoir fait découvrir les allentour de Jussieu, merci pour ces moments de détentes et d'échange autour d'un café ou d'un verre de vin (blanc!).
Sarah, nous avons commencé nos thèses en même temps, et c'est également ensemble que nous l'aurons terminée. Nous avons failli être la « french girl team » de la banquise et je suis certaine que nous aurions été incroyables ! A défaut de briller au pôle, je te remercie pour le tandem que nous avons formé ensemble, en particulier durant cette dernière année qui aura été fastidieuse.
Marylou, j'ai eu l'impression de t'avoir dit et écrit un million de fois merci. Et à chaque fois, j'ai eu l'impression de ne jamais le dire assez. Alors une fois de plus : merci ! Ton soutien tout particulier durant la dernière année de thèse a été sans aucun doute capital. Que ce soit le soutien moral ou le soutien scientifique. Quelque part, tu es restée ma co-bureau même après avoir terminé ta thèse.

Si j'ai eu la chance d'être bien entourée au laboratoire, j'ai également eu la chance d'avoir des ami.e.s hors laboratoire pour m'accompagner et me soutenir durant ces trois années : bibi Camille, Julie, Rémi, Florence, Nassim, Clo, QVP, Tim … et bien d'autres. Que ce soit par des sorties théâtre, ciné, jeux de sociétés ou encore des week-ends en campagne ou au bord de la mer : merci !

Merci également à ceux qui m'ont permis de m'échapper un peu durant le confinement de la COVID19 : Clotilde, Quentin, Laet, Mousse, Franz et Nassim, merci de m'avoir offert des petits espaces de télétravail hors de chez moi, me permettant ainsi de maintenir un certain équilibre.
Je souhaiterai faire un remerciement spécial à Sophie et Clément. La *Escape Game Power team* ! Au-delà de nos sorties en nombre, je voudrais vous remercier tous les deux pour votre soutien sans faille. Merci pour nos séances de télétravail avec ces pauses café du bonheur au soleil sur votre terrasse. Et merci surtout d'avoir été là dans les bons moments et dans les moments difficiles.

Merci à ma famille : Papa, Noémie et Elisa. Ces dernières années n'ont pas été faciles pour nous et je suis ravie du chemin que nous avons parcouru ensemble. Merci de m'avoir soutenue et accompagnée durant toutes mes études, depuis les classes préparatoires jusqu'à cette soutenance de thèse. Mes pensées vont également à Maman, qui me manque énormément. J'aurais tant aimé qu'elle soit avec nous. J'aime à penser que si elle avait pu nous voir, elle aurait été heureuse et fière.

Enfin, merci à toi, Guillaume. J'ai beaucoup de chance de t'avoir à mes côtés et quelques lignes dans ce manuscrit ne suffiront pas à exprimer toute ma gratitude. Tu m'as aidée à surmonter des obstacles de la vie qui étaient particulièrement difficiles. La thèse en est l'un d'eux. Merci pour ta patience, ta tolérance, ton soutien sans faille et de continuer à faire de moi une meilleure personne.

SUMMARY

The halocline of the upper Arctic Ocean is a key feature in the maintenance of the sea ice cover. This PhD thesis investigates the evolution of the halocline in the Arctic since 2007, using several tools: hydrography from autonomous drifting platforms, shipborne CTD measurements and 1/12° spatial resolution operational model simulations.

The IAOOS (Ice Atmosphere Ocean Observing System) 2017 drift in the western Eurasian Basin gathered a unique 8-months long hydrographic and biogeochemical dataset. Dissolved oxygen and nitrate data were combined to compute the NO parameter, a semi-conservative tracer, which provided valuable insights into the halocline structure (Bertosio et al., 2020). A NO minimum was found in the Nansen Basin on a σ-horizon of 27.8 $kg.m^{-3}$ corresponding to the lower halocline, while a lower NO minimum of 380 µM straddled the 27.4 $kg.m^{-3}$ isopycnal and marked the cold halocline in the Transpolar Drift.

Back trajectories of water parcels encountered along the buoy drift were computed using the Mercator physical system PSY4V3R1 (hereafter PSY4). They suggested that waters within the NO minimum at 27.4 $kg.m^{-3}$ could be traced back to the East Siberian shelf. The base of the lower halocline, at $\sigma = 27.85$ $kg.m^{-3}$, corresponded to the density attained in the deepest winter mixed layer north of Svalbard and cyclonically slowly advected from the slope into the central Nansen Basin. The 27.85 σ-horizon was associated with an absolute salinity of 34.9 $g.kg^{-1}$, a significantly more saline level than the 34.3 psu isohaline commonly used to identify the base of the lower halocline. This denser and more saline level is in accordance with the deeper winter mixed layers observed on the slopes of Nansen Basin in the last 10 years.

Datasets such as the IAOOS 2017 drift are rare in the Arctic domain. Ocean-sea ice operational analysis systems, such as PSY4, have proven to be helpful for interpreting observations in the Arctic. Following the first assessements done in the Western Nansen Basin by Athanase et al (2020), PSY4 was evaluated at a pan-Arctic scale, using nearly 20,000 independent temperature and salinity profiles over the 2007-2020 period (Bertosio et al., 2021a, *submitted to JGR*). PSY4 hydrographic properties and water mass distributions were in good agreement with observations and simulated sea surface height was consistent with altimetric data.

PSY4 simulations were used to describe changes in freshwater distribution and pathways in the Arctic ocean since 2007 (Bertosio et al., 2021a, *submitted to JGR*). PSY4 showed that the Beaufort Gyre, the largest freshwater reservoir in the Arctic, extended westward to the Mendeleev Ridge until 2011. After 2012, the freshwater content increased near the North Pole and the Beaufort Gyre shifted to the northeast. PSY4 also suggested a change in the pathways of fresher waters in the Makarov Basin after 2014, which either recirculated into the Canada Basin, or flowed out of the Arctic Basin through the western Canadian Archipelago rather than

through the Fram Strait. Coincidentally, Atlantic Waters shallowed along the East Siberian slope while the Transpolar Drift moved from the Lomonosov Ridge to align with the Mendeleev Ridge.

Changes in halocline waters were further investigated along the East Siberian Slope and in the Makarov Basin from 2007 to 2020 by combining drifting platforms observations, shipborne hydrographic data and PSY4 simulations (Bertosio et al., 2021b, *submitted in JGR*). In 2015, the upper halocline in the Makarov Basin was warmer, fresher and thicker compared to 2008 and 2017, likely resulting from the extensive westward extension of the Beaufort Gyre that year. From 2012-onwards, cold Atlantic-derived lower halocline waters, previously restricted upstream of the Lomonosov Ridge area, progressed eastward along the East Siberian slope, with a sharp shift from 155 to 170°E above the 1000 m isobath in winter 2011-2012, followed by a progressive eastward motion after winter 2015-2016 and reached the western Chukchi Sea in 2017. In parallel, an active mixing between upwelled Atlantic Water and shelf water along the slope, formed dense warm water which also supplied the Makarov Basin lower halocline.

The shoaling of the Atlantic Waters, i.e. the Atlantification of the Arctic Ocean, previously restricted to the Eurasian Basin, now reaches the Amerasian Basin where lower halocline properties are impacted.

RÉSUMÉ

La halocline de l'océan Arctique est un élément clé dans le maintien de la couverture de glace de mer. Cette thèse étudie l'évolution de la halocline de l'océan Arctique depuis 2007, en utilisant plusieurs outils : des mesures hydrographiques à partir de plateformes autonomes dérivantes, des mesures CTD et les simulations du modèle opérationnel de haute resolution spatiale (1/12^{e} de degré).

La plateforme IAOOS 2017 (Ice Atmosphere Ocean Observing System) a dérivé dans l'ouest du bassin Eurasien, effectuant des mesures hydrographiques et biogéochimiques sur 8 mois. Les concentrations d'oxygène dissous et de nitrates ont été combinées pour calculer le paramètre NO, un traceur semi-conservateur, qui a fourni des informations précieuses sur la structure de la halocline (Bertosio et al., 2020). Dans le bassin de Nansen, un minimum de NO était associé à $\sigma = 27{,}8$ kg.m^{-3} et correspondait à la halocline inférieure. Dans le bassin d'Amundsen, un minimum plus faible de NO de 380 µM chevauchait l'isopycne de 27,4 kg.m^{-3} et marquait la halocline froide advectée par la dérive transpolaire arctique.

Des rétro-trajectoires de particules d'eau rencontrées le long de la dérive de la IAOOS 2017 ont été calculées en utilisant le modèle opérationel de Mercator Océan (PSY4V3R1, ci-après PSY4). Ces rétro-trajectoires suggèrent que les eaux associées au minimum de NO à $\sigma = 27{,}4$ kg.m^{-3} dans le bassin d'Amundsen résulte de l'advection d'eau de la mer de Sibérie orientale via la derive transpolaire. Dans le bassin de Nansen, la base de la halocline inférieure située à $\sigma = 27{,}85$ kg.m^{-3}, correspond à la densité atteinte dans la couche de mélange hivernale la plus profonde au nord de Svalbard et à une lente advection cyclonique depuis le plateau vers le bassin central de Nansen. La base de la halocline était également associée à une salinité absolue de 34.9 g.kg^{-1}, ce qui est plus salé que l'isohaline 34.3 psu usuellement utilisé pour identifier la base de la halocline inférieure. Ces observations sont en accord avec les couches de mélange hivernales plus profondes observées sur les pentes du bassin de Nansen au cours des 10 dernières années.

Les jeux de données, tels que ceux de la IAOOS 2017, restent rares en Arctique. Les modèles opérationels, tels que PSY4, se sont avérés utiles pour interpréter les observations dans le domaine Arctique. Les performances de PSY4 dans l'Océan Arctique ont été évaluées en utilisant près de 20 000 profils indépendants de temperature et de salinité sur la période 2007-2020 (Bertosio et al., 2021a, *soumis*). Les propriétés hydrographiques et les distributions des masses d'eau de PSY4 sont en bon accord avec les observations in-situ, et la hauteur de la surface de la mer simulée était cohérente avec les données altimétriques satellitaires.

Les simulations PSY4 ont été utilisées pour décrire les changements dans la distribution et la circulation d'eau douce dans l'océan Arctique depuis 2007 (Bertosio et al., 2021a, *soumis dans JGR*). PSY4 a montré que la gyre de Beaufort, le plus grand réservoir d'eau douce de l'Arctique, s'est étendue vers l'ouest jusqu'à la dorsale de Mendeleev jusqu'en 2011. Après 2012, le contenu en eau douce a augmenté près du pôle Nord et la gyre de Beaufort s'est déplacée vers le nord-est. PSY4 a également suggéré un changement dans les trajectoires des eaux douces du bassin de Makarov après 2014, qui ont soit recirculé dans le bassin du Canada, soit quitté le

bassin arctique par l'ouest de l'Archipel Canadien, plutôt que par le détroit de Fram. En parallèle, les eaux Atlantiques deviennent moins profondes le long du talus de la Sibérie orientale et dans le bassin de Makarov, tandis que la dérive transpolaire s'est déplacée de la dorsale Lomonosov pour s'aligner sur la dorsale de Mendeleev.

Les changements des eaux de la halocline le long du talus de la Sibérie orientale et dans le bassin de Makarov ont donc été étudiés plus en détail de 2007 à 2020 en combinant les observations des plates-formes dérivantes, les données hydrographiques des navires et les simulations PSY4 (Bertosio et al., 2021b, *soumis dans JGR*). En 2015, la halocline supérieure du bassin de Makarov était plus chaude, moins salée et plus épaisse par rapport à 2008 et 2017, résultant probablement de l'extension vers l'ouest de la gyre de Beaufort cette année-là. À partir de 2012, les eaux relativement froides de la halocline inférieure issues des eaux Atlantique, auparavant en amont de la dorsale Lomonosov, ont progressé vers l'est le long du talus de la Sibérie orientale, avec un déplacement marqué au cours de l'hiver 2011-2012, suivi d'un mouvement progressif vers l'est après l'hiver 2015-2016. Ces eaux ont atteint l'ouest de la mer des Tchouktches en 2017. En parallèle, un mélange actif entre les eaux Atlantiques, moins profondes, et les eaux du plateau le long de la pente, a contribué à la formation d'eaux relativement chaudes et denses qui ont également alimenté la halocline inférieure du bassin de Makarov.

La remontées des eaux de l'Atlantique vers la surface, c.a.d. *l'Atlantification* de l'océan Arctique, auparavant limitée au bassin Eurasien, atteint maintenant le bassin Amérasien où les propriétés de la halocline inférieure sont impactées.

GLOSSARY

AO	Arctic Oscillation
TPD	Transpolar Drift
BG	Beaufort Gyre
FW	Freshwater
AW	Atlantic Water
FSB	Fram Strait Branch
BSB	Barents Sea Branch
PW	Pacific Water
PSW	Pacific Summer Water
PWW	Pacific Winter Water
LH	Lower Halocline
CH	Cold Halocline
UH	Upper halocline
IAOOS	Ice Atmosphere Ocean Observing System

Contents

Preamble

The Arctic region has long remained unexplored. In the 16th century, explorations motivated by the desire to find new trade routes between Europe and China contributed to map for the first time thousands of kilometers of coastline. In late 18th and early 19th century, a belief of an ice-free ocean beyond the pack ice arose, which initiated a race to the north pole.

Many expeditions trying to sail north ended by ships getting caught in the ice and abandoned. In 1893, Fridtjof Nansen and Otto Sverdrup went on expedition on Fram, a ship able to withstand the ice press. Three years later, Fram was released from the ice north of Svalbard and steamed towards Tromsø. The voyage of Fram gave the first information of the inner part of the Arctic Ocean: it was a deep ocean and it was ice covered (Nansen, 1902). After the drift of Fram, several oceanographic studies were conducted over the 20th century (e.g., Knipowisch, 1905; Helland-Hansen and Nansen, 1909; Roald Amundsen, 1903–1905).

During the 21th century, international scientific cooperations promote the increase of expeditions (e.g., the Beaufort Gyre Exploration Project, the Nansen and Amundsen Basins Observational Systems, Arctic PASSION). Recently, the MOSAiC expedition in 2019 gathered hundreds of researchers from different countries onboard the German icebreaker Polarstern which drifted for a year trapped in the ice, enabling data to be collected over a full year. Technologies have also evolved and highly developed measurement techniques were especially designed for operation in the Arctic environment (Krishfield et al., 2008; Provost et al., 2015). Nevertheless, the sea ice cover and the winter conditions during the polar night still challenge expeditions and measurements, and the Arctic domain remains poorly documented.

In recent decades, the Arctic has undergone severe changes associated with a “polar amplification” of global changes. The surface air temperature of the Arctic has increased to more than double the global average over the past two decades (Notz & Stroeve, 2016). The increase in air temperature contributes to reducing sea ice cover, allowing more energy to be absorbed at the ocean surface and melting back the ice (Vihma, 2014). This processus is called sea ice albedo feedback. The expansion of ice-free ocean surfaces increases warm input to the surface atmosphere, which contributes to decrease the differences in air temperature between high and low latitudes. Consequently, intrusions of warm and humid air in the Arctic region are enhanced along with an increase in precipitation falling as snow or rain, affecting the surface albedo (Bintanja & Andry, 2017; Bintanja & Selten, 2014; Woods & Caballero, 2016). In parallel, summer sea ice extent is in rapid decline (Kwok, 2018). Since the late 1970s, the 14 lowest sea ice extents all occurred in the last 14 years (nsidc.org). The historic minimum sea ice extent was reached in September 2012 with only 3.4 million km^2, and more recently, the second lowest extent was recorded in September 2020 (3.8 million km^2, nsidc.org). Some climate model scenarios suggest that the Arctic Ocean may be seasonally ice free by 2050 (Collins et al., 2013).

The Arctic region is a key element of the global climate system that can influence mid-latitude climate (Jung et al., 2015). The Arctic halocline is a structure in the Arctic Ocean that contributes to maintaining the sea ice cover : it insulates the ocean surface layer, under the sea ice, from underneath warm and salty waters. In a context of “polar amplification” of global changes, dedicated attention to the strengh and evolution of the Arctic halocline is necessary for a better understanding of climate changes, now perceptible on time scale of the order of a decade (Polyakov et al., 2018). This thesis is dedicated to the evolution of the halocline in the upper Arctic Ocean since 2007. Chapter 1 introduces upper Arctic water circulation with a focus on the Arctic halocline.

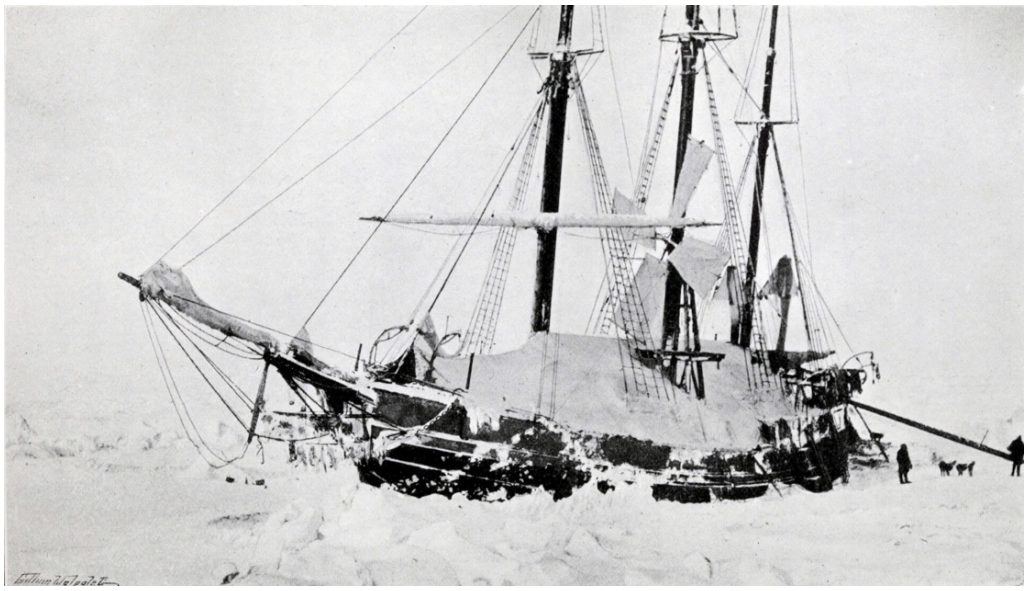

Fram, trapped in the ice (January 1895)

Chapter I

A review of the Arctic Ocean circulation and halocline

Contents

I.1. Around and above the Arctic Ocean

I.1.1. General features of the Arctic Ocean

The Arctic Ocean extends from the Bering Strait, on the Pacific side, to the Fram Strait, on the Atlantic side (**Figure 1**).

The Arctic Ocean is a small ocean: about 4 000 km long and 2 400 km wide, which is smaller than Europe. There are two main deep basins (~ 4 000 m deep) separated by the Lomonosov Ridge, the Eurasian Basin and the Amerasian Basin. The Eurasian Basin is subdivided into the Amundsen and Nansen basins (separated by the Gakkel Ridge) and the Amerasian Basin into the Makarov and Canada basins (separated by the Alpha and Mendeleyev Ridges). Several shallow seas (< 400 m deep) surround these basins: the Barents Sea, Kara Sea, Laptev Sea, East Siberian Sea, Chukchi Sea and Beaufort Sea. The ratio shelf to basin area is a unique features of the Arctic Ocean with the area of the Arctic shelves being almost half the area of the deep Arctic basins (Jakobsson, 2002). The complex bathymetry exerts a strong control on the ocean circulation (**Figure 1**).

Atlantic Water enters east of the wide (450 km) and deep (2 545 m) Fram Strait, or through the Barents Sea (~ 230 m deep) (red large arrow in **Figure 1**). Atlantic Water inflow at Fram Strait is about 7 Sv (1Sv = 10^6 m^3s^{-1}), while Barents Sea inflow is around 2 Sv (Woodgate, 2012). On the other side of the Arctic Ocean, the relatively shallow (50 m deep) and narrow (85 km wide) Bering Strait is the only gateway to Pacific Water (inflow at about 0.8 Sv) (green large arrow in **Figure 1**). Outflows exit the Arctic Ocean along the Greenland shelf, west of Fram Strait (~ 9 Sv), or north of Canada, via the Canadian Archipelago (~ 1-2 Sv) (Beszczynska-Möller et al., 2011).

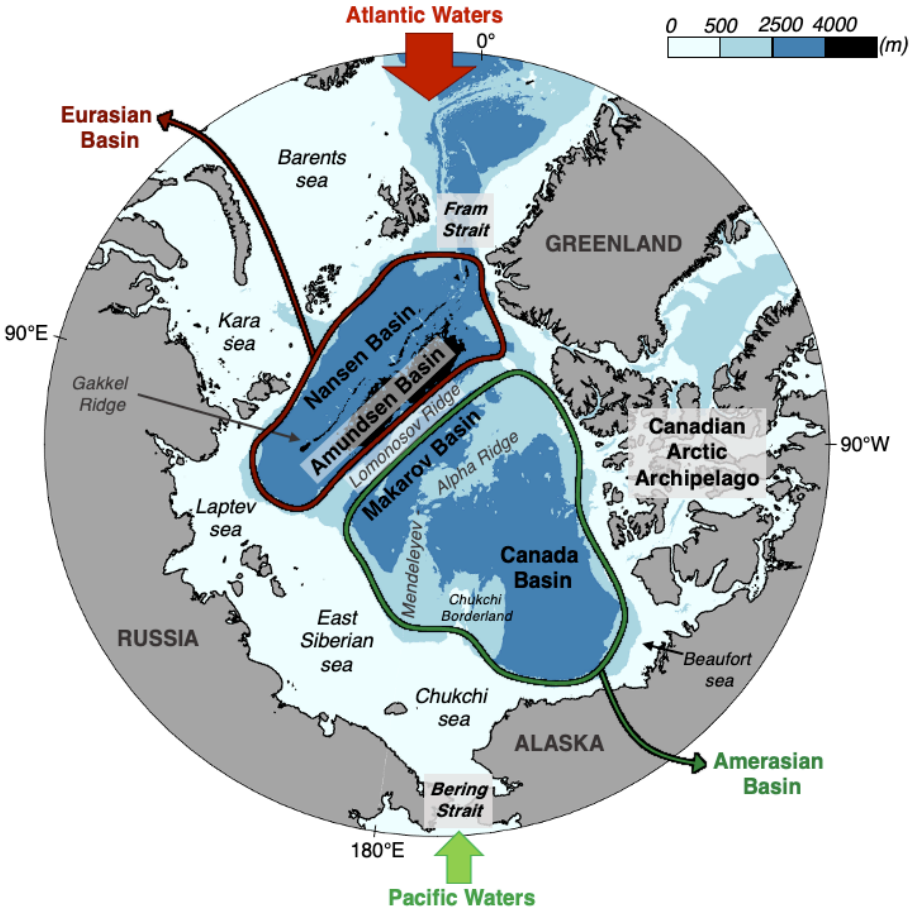

Figure 1: Major geographic features of the Arctic

I.1.2. Atmospheric circulation

The Arctic atmospheric circulation is dominated by a large-scale low-pressure system (the polar vortex) from the tropopause to the lower mesosphere (about 10 to 50 km above the sea). This vortex is associated with a large-scale cyclonic (anti-clockwise) circulation bounded by a strong west-to-east atmospheric current, and trapping cold air in the Arctic regions (**Figure 2a-b**). The strength of the vortex conditions the maintenance of cold air over the Arctic. Some years, the polar vortex can break up into several vortices, which favor the intrusion of warmer air towards the pole (Overland & Wang, 2016).

Arctic atmospheric variations are partly captured by the Arctic Oscillation (AO) index (Thompson & Wallace, 1998). The AO is obtained from the first mode of the principal

component analysis (EOF) computed with monthly mean height anomalies of 1000 h-Pa over 20°N-90°N. In other words, the AO quantifies the variation of the pressure difference between the North Pole and 20°N latitude compared to the mean (**Figure 2d**). Positive values of the AO index are characterized by lower-than-average air pressure over the Arctic along with higher-than-average pressure over the northern Pacific and Atlantic Oceans. In this case, the mid-latitude jet stream is farther north than average, keeping the air cold in the Arctic, and storms shift northward (**Figure 2a**). Conversely, negative values of AO index correspond to higher-than-average air pressure over the Arctic region and lower-than-average pressure over the northern Pacific and Atlantic Oceans. During that regime, the mid-latitude jet stream weakens, shifts toward the equator and intrusions of warm (resp. cold) air towards the high (resp. low) latitudes are favoured (**Figure 2b**).

The Arctic is also under the influence of two local atmospheric patterns: the Beaufort High centered over the Canadian Basin, and the Icelandic Low located at the gateway to the Eurasian Arctic, bringing relatively warm and humid cyclones from the North Atlantic to high latitudes (e.g., Proshutinsky & Johnson, 1997)(**Figure 2c**).

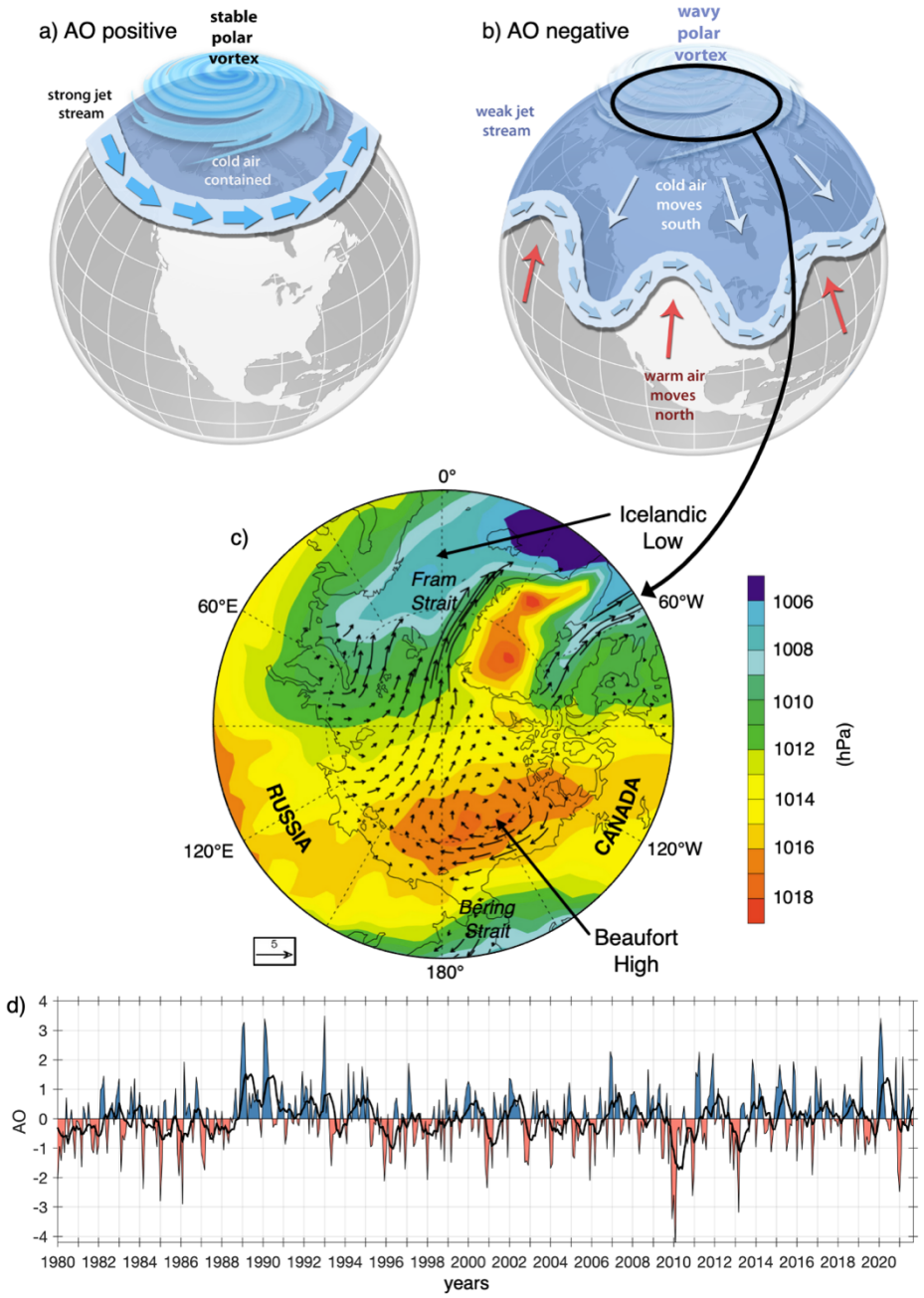

Figure 2: Atmospheric drivers during (**a**) positive and (**b**) negative AO phase (adapted from NOAA). (**c**) Annual mean sea level pressure over the period 1979–2008 from the NCEP–NCAR reanalysis with overlay of mean sea ice velocity vectors for 1979–2006 (cm.s^{-1}). Adapted from (Serreze & Barrett, 2011). (**d**) Time serie of AO index. Black line corresponds to six months-running mean. AO values from NOAA.

I.1.3. Oceanic surface circulation

Ocean surface circulation is forced by winds (Thorndike & Colony, 1982). The two main ice-ocean surface circulations in the Arctic are the Transpolar Drift and the Beaufort anticyclonic gyre (Armitage et al., 2018)(**Figure 3**).

The Transpolar Drift (TPD) current advects the ice and surface water (~ first 20 meters) from the Siberian shelf towards Greenland and the Nordic Seas. Velocities in the TPD are about 6-10 cm.s^{-1}, suggesting a transport time of water from the Siberian plateau to the Fram Strait of about 1 year (e.g., Armitage et al., 2017).

The Beaufort Gyre (BG), a large-scale surface anticyclonic oceanic circulation, about 800 km in diameter, dominates the Canada Basin surface circulation. The BG is primarily forced by the Beaufort High (Aagaard & Carmack, 1989; Serreze et al., 2011). The BG is characterized by typical velocities at the surface of about 5-6 cm.s^{-1} (Armitage et al., 2017; McPhee, 2012).

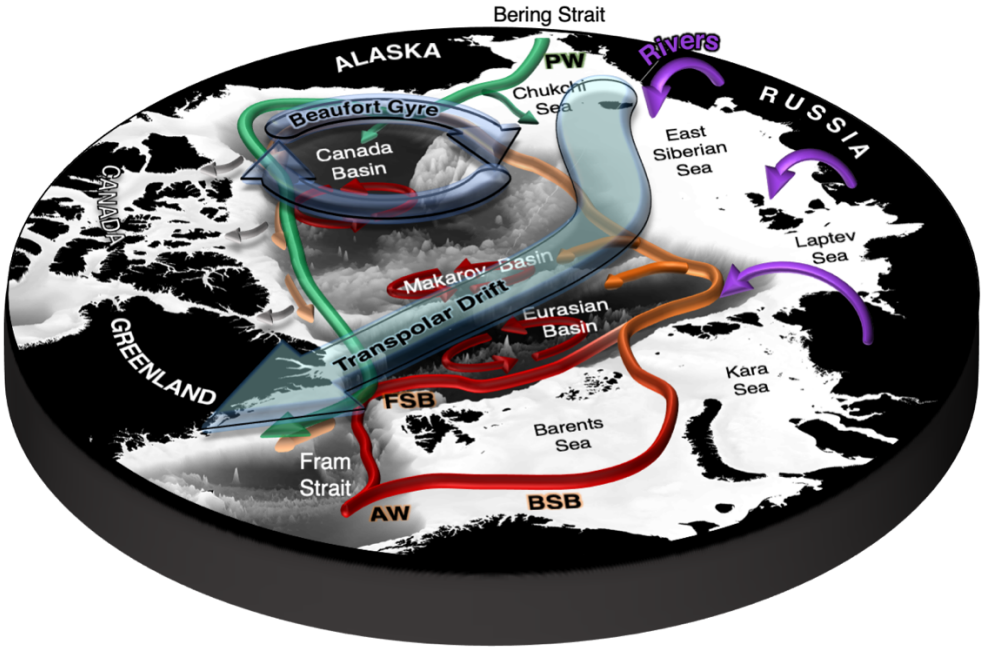

Figure 3: Circulation in the Arctic Ocean. Surface currents are represented by blue arrows, sub-surface currents of Atlantic (AW) and Pacific (PW) water are represented by red-orange and green arrows, respectively. The gray arrows indicate the outflow through the Canadian Archipelago. Purple arrows represents rivers input. Adapted from Carmack et al. (2016). *FSB: Fram Strait Branch; BSB: Barents Sea Branch.*

The strength and the position of the TPD and the BG are associated with the relative position and intensity of the Beaufort High and Icelandic Low pressure systems (Boyd et al., 2002; Morison et al., 1998; Steele & Boyd, 1998; Timmermans et al., 2011). Positive AO indices (i.e. extensive atmospheric low anomaly over the entire Arctic) lead to a strengthened cyclonic oceanic circulation regime in the Eurasian Basin, potentially extending to the Makarov Basin, and a strong anticyclonic circulation of the Beaufort Gyre, limited to the Canadian Basin (Morison et al., 2012, 2021; Q. Wang, 2021). In that case, the origin of the TPD is further east,

toward Mendeleev Ridge. Conversely, during negative AO periods, the origin of the TPD shifts west, toward Lomonosov Ridge, and there is an expansion of the Beaufort Gyre anticyclonic circulation toward the Eurasian Basin (Kwok et al., 2013; Morison et al., 2021; Proshutinsky & Johnson, 1997; Rigor et al., 2002). The time scales of ocean adjustment to changes in atmospheric forcing in the central Arctic remain uncertain. Morison et al. (2006) nevertheless estimate this time scale at about 3 to 7 years.

I.2. Hydrography and stratification of the Arctic Ocean

A key feature of the Arctic Ocean is that it is predominantly stratified by salinity (β-oceans) in contrast with mid-latitudes oceans that are stratified by temperature (α-oceans, Carmack, 2007). Indeed, density variations can be expressed as $d\rho/\rho = -\alpha d\Theta + \beta dS_A$, where S_A is absolute salinity, Θ is conservative temperature, α is the thermal expansion and β the haline contraction. At cold temperatures, the coefficient of thermal expansion α is small and temperature variations have little effect on density. Consequently, the distribution of water masses in the Arctic consists of relatively fresh and cold waters overlying saltier and warmer waters. Strong gradients in temperature, salinity and density are confined to the upper hundred meters of the water column.

I.2.1. Freshwaters

Freshwaters (FW) play a major role in the Arctic Ocean. Conventionally, in the Arctic, a water mass can be considered as fresh if the salinity is lower than the salinity of AW at their entrance of the Arctic, i.e. than the reference salinity of 34.8 psu (e.g., Proshutinsky et al., 2009). FW can be in solid phase (snow, sea ice) or in liquid phase. Over the period 2000-2010, the average annual volume of total freshwater in the Arctic Ocean (solid and liquid) was estimated at 115 300 km^3, of which 88% was liquid (Haine et al., 2015).

The main liquid freshwater sources are rivers (3% of the total liquid freshwater, **Table 1**), Pacific Water (2%, **Table 1**) and net precipitation (precipitation minus evaporation, ~ 2%, **Table 1**). Most of the liquid freshwater is found in the Canada Basin, particularly in the Beaufort Gyre where about 23 300±2 000 km^3 are stored (~20%). Since the early 2000s, liquid freshwater has been accumulating in the Beaufort Gyre (Proshutinsky et al., 2009) where a 40% increase in liquid freshwater (~ 6 400 km^3) was observed compared to 1970s climatology (Proshutinsky et al., 2019).

Table 1: Freshwater budget for the Arctic Ocean from selected published sources.*

Source	*Aagaard and Carmack* [1989]	*Serreze et al.* [2006]	*Haine et al.* [2015]	*Haine et al.* [2015]
Period	Prior to 1989	~1979–2001	1980–2000	2000–2010
		Reservoirs (km^3)		
Liquid freshwater	80,000	74,000 ± 7,400	93,000	101,000
Sea ice	17,300	10,000	17,800	14,300
Total freshwater	97,300	84,000	110,800	115,300
		Fluxes ($km^3\ yr^{-1}$)		
Runoff	3,300	3,200 ± 110	3,900 ± 390	4,200 ± 420
P-E	900	2,000 ± 200	2,000 ± 200	2,200 ± 220
Bering Strait (total)	1,670	2,500 ± 300	2,540? ± 300	2,640 ± 100
Fram Strait liquid	−980	−2,700 ± 530	−2,700 ± 530	−2,800 ± 420
Fram Strait ice	−2,790	−2,300 ± 340	−2,300 ± 340	−1,900 ± 280
Davis Strait (total)	−920	−3,380 ± 320	−3,360 ± 320?	−3,220 ± 190
Miscellaneous	−290	−90 ± 90	40 ± 90?	80 ± 90?
Total inflow	6,120	7,950 ± 400	8,800 ± 530?	9,400 ± 490
Total outflow	−5,520	−8,720 ± 700	−8,700 ± 700	−8,250 ± 550
Residual	890	−770 ± 800	100 ± 900?	1,200 ± 730

*Positive flows indicate freshwater sources to the Arctic Ocean. "Miscellaneous" includes the Barents Sea, Fury and Hecla Straits, and freshwater flow from Greenland. They are included separately in the total inflow and outflow, where possible. Aagaard & Carmack (1989) and Serreze et al. (2006) consider the Arctic Ocean to exclude the AAC and Baffin Bay, while Haine et al. (2015) include them. The Fram Strait liquid flow includes the East Greenland Current, the Deep Outflow, and the West Spitsbergen Current. Uncertainties (on the mean values) are shown when available. P represents precipitation and E represents evaporation. From Carmack et al. (2016).

The largest volumes of sea ice (solid freshwater) are found north of the Canadian Archipelago and near Greenland where the ice is still thick and old (Carmack et al., 2016). Ice growth and melt influence the characteristics of the surface ocean. Areas of ice formation are sources of salinity to the ocean through the release of brine, inducing convection and a transformation of the upper water column. Sea ice has a large seasonal cycle. About 35% of the sea ice present at the end of winter survives the summer to become multiyear ice, while the remaining 65% melts within the Arctic or is exported to the south. The winter maximum extent occurs in March, while the sea-ice minimum is in September. In 2018, average winter (fall) ice thickness was about 2 m (1.5 m) (Kwok, 2018). The seasonal freeze-melt cycle exchanges freshwater between the liquid and solid phases with an amplitude of about 13 400 km^3 (~ 12%, averaged over the 2000s, Haine et al., 2015).

Freshwater exits the Arctic to mid-latitudes through Fram Strait (~ 4% of the total freshwater) or Davis Strait (~ 3%, south Canadian Archipelago). When the exported FW reaches the northern subarctic seas, it influences the surface salinity (e.g., Dickson et al., 1988; Haak et al., 2003) and the rate of dense water formation. Changes in freshwater export from the Arctic could influence both deep water formation in the North Atlantic and the Atlantic Meridional Overturning Circulation (Haine et al., 2015; Nummelin et al., 2016; Sévellec et al., 2017; Thornalley et al., 2018).

I.2.2. Waters masses

The upper Arctic Ocean (0-1000 m) is composed of a mixed-layer, Pacific-origin water layer (PW), and Atlantic-origin water layer (AW).

The mixed-layer, an homogenized layer at the surface of the ocean, exhibits different depths for each basin along with a strong seasonal variability: from ~ 8 m (summer) to ~ 30 m (winter) the Amerasian Basin; and from ~ 20 m (summer) to more than 100 m (winter) in the Eurasian Basin (Peralta-Ferriz & Woodgate, 2015).

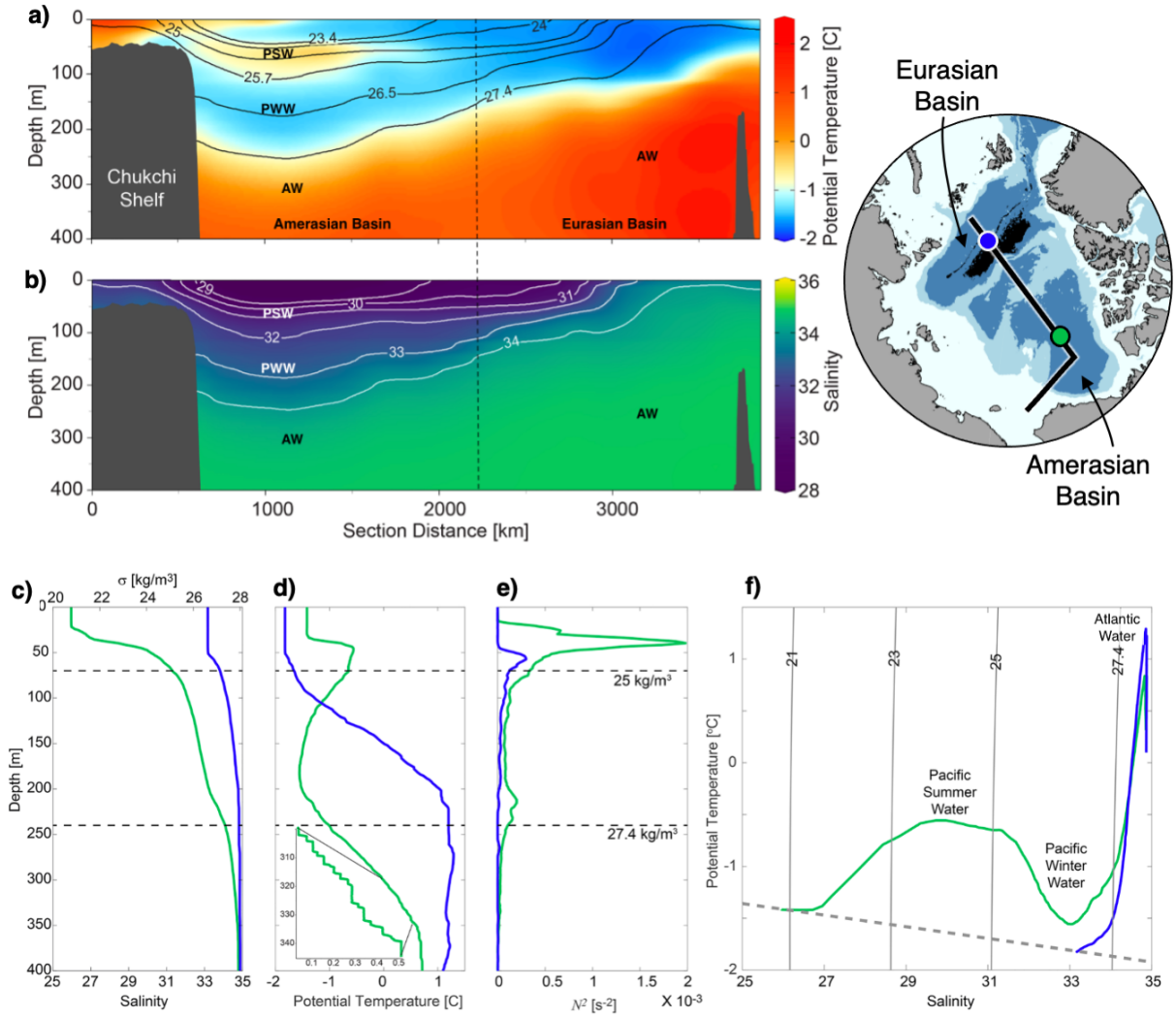

Figure 4: Cross-arctic sections of (**a**) potential temperature (◦C) and (**b**) salinity from the Chukchi Sea (0 km) to the Eurasian Basin (3000 km). The position of the section is shown on the map (thick black line). Examples of profiles of (**c**) salinity (psu), (**d**) potential temperature (°C), (**e**) buoyancy frequency (N^2, s^{-2}), and (**f**) corresponding T-S diagram in the Canada Basin (green profiles) and the Eurasian Basin (blue profiles). The upper x-axis in (**c**) shows the corresponding density, and the horizontal dashed lines mark the depths of σ = 25 kg.m^{-3} and σ = 27.4 kg.m^{-3} in the Canada Basin. The gray contours in (**f**) are isopycnals (kg.m^{-3}), and the gray dashed line is the freezing line (referenced to zero pressure). *PSW: Pacific Summer Water; PWW: Pacific Winter Water; AW: Atlantic Water.* Adapted from Timmermans & Marshall (2020)

The warm AW is found throughout the Arctic at different depths, from near the surface at the entrance of the Eurasian Basin to 300-500 m in the Amerasian Basin (red arrows in **Figure 3, Figure 4a-b,** blue profiles in **Figure 4c-f**). AW is an important source of heat (Θ ~ 0-3°C) and salt (34.8 < S < 35.2 psu) (**Figure 4**). T-S characteristics of AW are strongly modified along the AW progression in the Arctic Ocean through convection, mixing or heat loss toward the atmosphere.

The PW lies between the surface mixed-layer and AW (~ 50-150 m depth) and is mainly found in the Amerasian Basin, especially in the Canada Basin (**Figure 4**). PW provides a source of oceanic heat, nutrients and freshwater (Woodgate, 2012). The PW layer is divided into two sub-layers: the summer PW (PSW) layer overlying the winter PW (PWW) layer (**Figure 4a-b**). PSW results from the summer warming (by solar input) and freshening (by ice melt) of the PW during their progression between Bering Strait and the deep basins (e.g., Steele et al., 2004; Timmermans et al., 2014). PSW is therefore characterized by a local temperature maximum (-1 < Θ < 1°C) and salinities between 31 and 32 psu. Relatively dense PWW results from winter cooling and salinity increase (by brine release) and inserts beneath the PSW layer (green profiles in **Figure 4c-f**). PWW are characterized by a local temperature minimum, close to the freezing point, and salinities of the order of 33 psu (e.g., Pickart et al., 2005). Note that, since 2014, dramatic winter-only (January– March) freshening made PWW fresher (and lighter) than summer waters (Woodgate & Peralta-Ferriz, 2021). Consequently, PWW shoaled and no longer ventilates the base of the Arctic upper halocline at 33 psu.

I.2.3. The Arctic halocline definition

The Arctic halocline is a layer of variable thickness located in the first 300 meters of the water column where salinity increases with depth. It is a fundamental structure of the Arctic Ocean insulating the cold, low-salinity surface layer from the underneath warm, salty AW. The Arctic halocline is thus a key element in maintaining the sea ice cover.

The halocline has been defined either by a salinity constant, a salinity range (Steele et al., 1995), a depth range (Boyd et al., 2002; Steele & Boyd, 1998), or a minimum temperature (resulting from winter convection). The top of the halocline is usually associated with the base of the mixed-layer, where vertical temperature and salinity gradients become significant (Bourgain & Gascard, 2011). The base of the halocline has been defined through several criteria such as constants of density ratio ($R_\rho = (\alpha d_z\Theta)/(\beta d_z S_A) = 0.05$; Bourgain & Gascard, 2011), density ($\sigma = 27.85$ kg.m^{-3}, Bertosio et al., 2020) or salinity ($S_A = 34.46$ g.kg^{-1}; Rudels et al., 1996).

The complexity of the Arctic halocline comes from the fact that the layer comprises several water masses from different sources (**Figure 5**). In the Barents Sea and Nansen Basin, the cooling, freshening and mixing of Atlantic-origin waters form lower halocline waters (LH) (black and blue areas in **Figure 5**) (Rudels et al., 1996, 2004; Steele & Boyd, 1998). Advection of the relatively cold and low salinity shelf waters from Kara, Laptev and/or East Siberian Seas in the Eurasian Basin contributes to form an homogeneous near-freezing temperature layer in the upper part of the halocline, also referred as cold halocline water (CH) (green area in **Figure 5**) (Alkire et al., 2010, 2017; Polyakov, Rippeth, et al., 2020; Steele & Boyd, 1998).

The influence of Pacific-derived water to the halocline layer, restricted to the Amerasian Basin, forms the upper halocline waters (UH) overlying the LH (orange area in **Figure 5**) (e.g., Timmermans et al., 2017; Wang, 2021).

I.3. The lower halocline

The LH differs from one basin to another, with lower temperatures in the Eurasian Basin (Θ close to the freezing point) compared to the Amerasian Basin (Θ > -1.5°C). Generally, the lower halocline results from modified AW, formed in the Eurasian Basin, which circulates cyclonically in the Arctic Basin, reaching the Amerasian Basin. However, waters modified on the shelves can be dense enough to supply the lower part of the halocline.

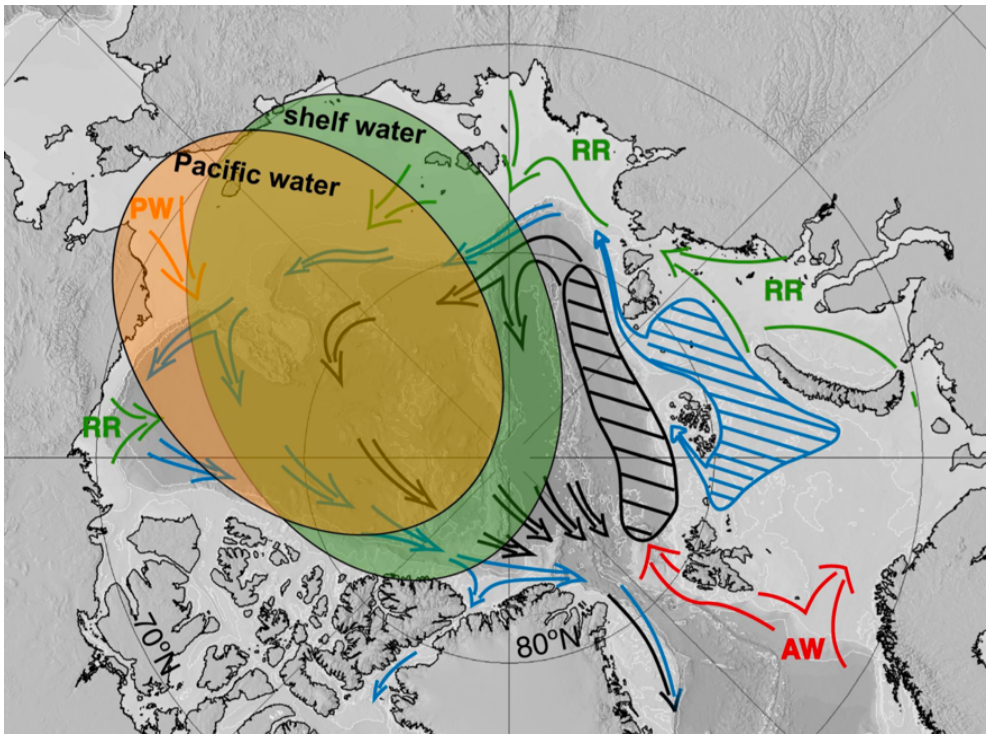

Figure 5: Diagram showing Atlantic inflow (AW, red), river runoff (RR, green), Pacific inflow (PW, orange), the formation zone (black diagonals) and circulation (black arrows) of the Fram Strait branch halocline, and the formation zone (blue diagonals) and circulation (blue arrows) of the Barents Sea branch halocline. The circles indicate areas where the lower halocline waters are overlain by less saline waters of the continental shelf and the Pacific. Based on Rudels et al. (2004)

I.3.1. Formation in the Nansen Basin and the Barents Sea

The LH in the western Eurasian Basin results from the modifications of AW. At the entrance to the Arctic Ocean, AW (Θ > 0°C, S > 35 psu) split in two branches (red arrows in **Figures 3** and **5**). One part, the Fram Strait Branch (FSB), flows through the eastern side of the deep Fram Strait (**Figure 3**; black area in **Figure 5**). The other part progresses in the Barents Sea (~ 2 Sv)

(Ingvaldsen et al., 2002; Schauer et al., 2002) and constitutes the Barents Sea Branch (BSB, **Figure 3**; blue area in **Figure 5**).

The AW of the FSB that reaches the Nansen Basin progresses cyclonically along the topographic slopes. Strong winter convections in the Nansen Basin and above deep plateaus north of Svalbard homogenize the upper part of the Atlantic layer from the surface to the thermocline, which freshen and cool the AW (S ~ 34.2-34.4 psu) (Athanase et al., 2020; Rudels et al., 1996). The following summer, the melting of the subsurface ice temporarily isolates the convective winter layer which forms a seasonal lower halocline. This lower halocline remains until it is homogenized by a sufficiently deep winter convection into a new mixed layer (Rudels et al., 2004, 2013, 2015). This scenario is repeated during the progression of waters in the Nansen Basin until reaching the Laptev Sea, where a large volume of relatively low salinity shelf water crosses the shelf break and penetrates above the LH (**Figure 5** and **Figure 6**). These low salinity surface waters isolate the pre-existing winter mixed layer which then becomes a permanent lower halocline. This mechanism is also known as an "advective-convective" mechanism (**Figure 6**).

AW from the BSB are cooled over the sea ($\Theta < 0°C$), however remaining relatively salty and dense (S ~ 34.5 psu) (Rudels et al., 2004). When these modified waters are advected to the deep basin, they can enter the LH of the FSB (**Figure 3**) (Aagaard et al., 1981; Rudels et al., 2004; Steele & Boyd, 1998). This mechanism is known as the "advective" mechanism (**Figure 6**).

These two mechanisms present distinct curves in the T-S diagram (**Figure 6**). A sharp bend below the mixing line, along an isopycnal, to the freezing point, reflects convection under growing ice. Conversely, a bend above the mixing line reflects advection and mixing to some extent of fresher water at the freezing point with the entire layer initially formed by convection (Kikuchi et al., 2004).

I.3.2. Modification in the eastern Eurasian Basin, north Laptev Sea

In the Nansen Basin, east of St. Anna Trough, AW coming from the FSB and BSB flow cyclonically along the bathymetric slope and become overrun north of the Laptev Sea by low salinity shelf water, forming a cold halocline (CH) (**Figure 3 and Figure 5**). The upper parts of the AW layer become isolated from the surface processes and cold halocline waters further insulate the sea ice cover from the heat stored in the Atlantic layer. The heat from AW is instead trapped in the lower halocline, where the temperature gradually increases (Rudels, 2012). Note that the extent of year-round CH influence varies: for example, the Eurasian Basin CH has retreated during the 1990s to cover significantly less area than in previous years (Steele & Boyd, 1998).

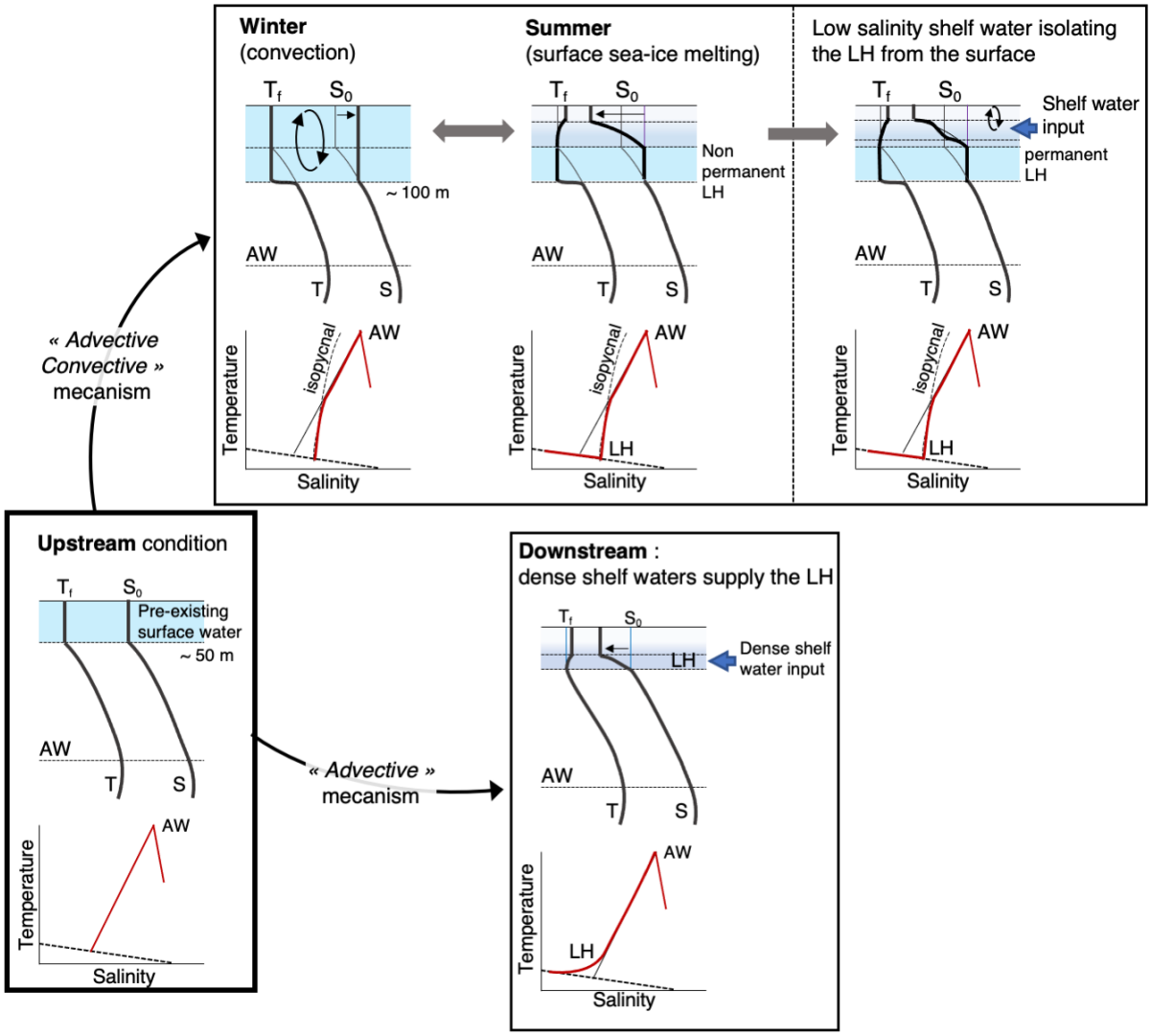

Figure 6: Schematic view of the Atlantic halocline formation process by "advection-convection" or "advection" with associated profiles and TS diagrams. The dotted lines in the TS diagrams show the freezing point. LH corresponds to the lower halocline water, and AW to the Atlantic water. Adapted from Kikuchi et al. (2004)

Consistent cross-slope differences in the lower halocline water characteristics were observed north Laptev Sea (Dmitrenko et al., 2011). Over the slope, the lower halocline water core was on average warmer and saltier relative to the off-slope lower halocline. Although on-slope and off-slope lower halocline waters have different formation histories (from the FSB or BSB), an important part of the heat and salt lost from the AW is gained by the overlying lower halocline over the continental slope area, resulting from enhanced vertical mixing over the sloping topography.

As the AW boundary current reaches the Lomonosov Ridge, a part of the AW current and LH bifurcate northward to flow along the ridge, while the remaining AW and LH enter the Makarov Basin. The colder FSB, located farther away from the slope, supplies the halocline in the Amundsen, Makarov and northern Canada basins (Rudels et al., 2015), while the BSB

remains at the slope and passes between the Chukchi Sea and the Chukchi Cap into the southern Canada Basin (e.g., McLaughlin et al., 2009; Woodgate et al., 2007). Recent changes in halocline waters along the East Siberian Slope and in the Makarov Basin are examined in Chapter 4.

I.3.3. The lower halocline in the Canada Basin

The pathway of the lower halocline water across the Lomonosov and Mendeleyev Ridges into the Canada Basin is still uncertain due to fragmental data in the Makarov Basin.

LH in the Canada Basin exhibits contrasted properties between northern and southern Canada Basin (Shimada et al., 2005). LH flowing from the west along Siberian/Chukchi slope, were associated with relatively low oxygen values (< 290 µmol.kg^{-3}), and mainly found in the southern Canada Basin. Additionnaly, AW can upwell onto the Chukchi Sea slope/shelf or Chukchi Borderland, and mix with less dense and nutrient-rich PW to form LH waters (Woodgate et al., 2005). In the northern part of the Canada Basin, the LH is influenced by waters from the Makarov Basin that directly spread in the northern Canada Basin and exhibit relatively larger oxygen values (> 315 µmol.kg^{-3}) (Shimada et al., 2005).

I.4. The upper halocline

The halocline structure in the Amerasian Basin differes from that of the Eurasian Basin, as PW supplies the upper halocline. PW enters through the relatively shallow and narrow Bering Strait and crosses the Chukchi or East Siberian Seas, before reaching the deep Canada and Makarov basins. PW properties are modified through seasonal processes and along their path. In addition to its distinct signature in temperature-salinity space, PW is characterized by low dissolved oxygen values (e.g., Falkner et al., 2005).

I.4.1. The Pacific water pathways and modifications in the Chukchi Sea

In summer, PSW may be subdivided into Alaskan Coastal Water and the summer Bering Sea Water. The Alaska's coastal waters are warm and relatively fresh (Θ > 1°C, S < 32 psu, Steele et al., 2004) progressing northward in mid to late summer via the Alaska Coastal Current until the Barrow Canyon (**Figure 7**). A portion of the branch progresses eastward along the Beaufort Sea slope (Nikolopoulos et al., 2009) and another part flows westward via the Chukchi Slope Current (Corlett & Pickart, 2017). The relatively colder and saltier summer Bering Sea water branch (0 < Θ < 3°C, 32 < S < 33 psu; Pisareva et al., 2015) splits into two parts north of the Bering Strait, one progressing northward through the Central Channel, and the other progressing toward Herald Canyon.

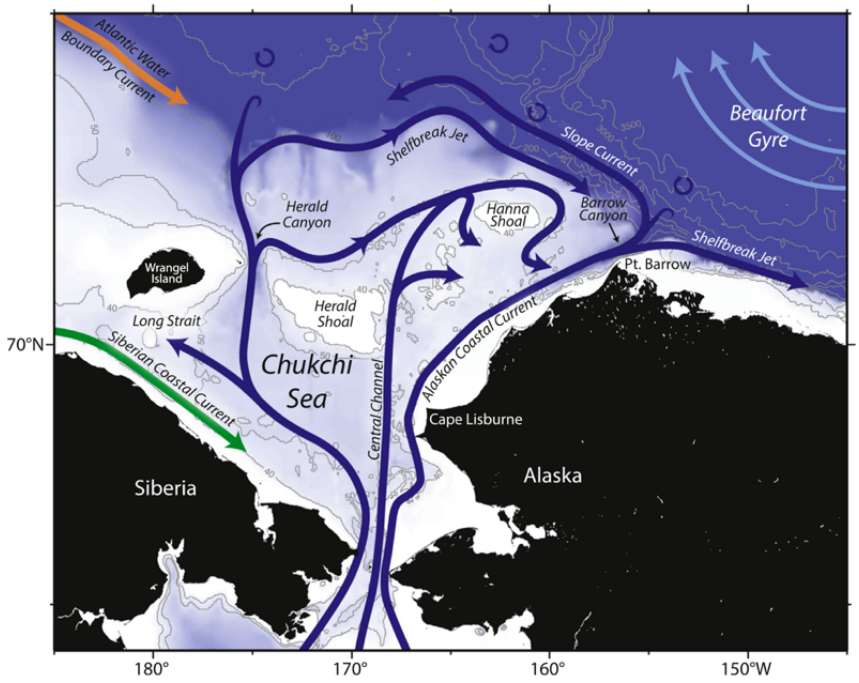

Figure 7: Schematic circulation of the Chukchi Sea and place names, from Corlett & Pickart (2017)

During winter, strong air-sea forcing, brine rejection and subsequent ice formation induce cooling and salinification of the water mass, also known as newly ventilated PWW or winter Bering Sea Waters (e.g., Muench et al., 1988; Steele et al., 2004). PWW has long been recognized as a primary component of the western Arctic halocline. The water can also be formed and/or further transformed due to leads and polynyas (Itoh et al., 2012; Weingartner et al., 1998). During spring and summer, when the pack-ice recedes and warmer waters enter the Chukchi Sea, the PWW is warmed via mixing and solar heating, and no longer near the freezing point. This modified water mass is referred to as remnant Pacific Winter Water (Linders et al., 2017; Pisareva et al., 2015). Both PWW and remnant Pacific Winter Water are rich in nutrients, resulting from interactions with the sediments, as the dense water flows on the bottom.

The mechanisms of lateral propagation of PW into the basin interior, although not fully understood, are thought to be promoted by eddy flows (Mathis et al., 2007; Pickart et al., 2005, 2009), upwelling/downwelling under the effect of the wind (Lin et al., 2019; Spall et al., 2008; Williams & Carmack, 2015) or by subduction (Timmermans et al., 2017).

I.4.2. The Canada Basin and the Beaufort Gyre

The upper halocline in the Canada Basin is constituted by PSW overlying PWW (**Figure 4**). There are distinct halocline sources between the northern and the southern Canada Basin. The northern Canada Basin more commonly contains summer Bering Sea water and less salty Pacific Winter water inputs via the western Chukchi Sea (Shimada et al., 2005; Steele et al., 2004). In constrast, the southern Canada Basin more commonly contains summer Alaskan Coastal Water and saltier Pacific Winter water produced by ice formation in the eastern Chukchi Sea.

Changes in PW spatial distribution in the Canada Basin are driven by the atmospheric Beaufort High and related to the AO index (Steele et al., 2004). During strongly positive AO years, summer Bering Sea water mainly flows via the Transpolar Drift Stream while during lower AO index both types of PSW (Bering Sea and Alaskan Coastal water) are swept into a larger and stronger Beaufort Gyre (**Figure 8**).

The Canada Basin is dominated by the anticyclonic Beaufort Gyre. Understanding the Beaufort Gyre dynamic helps in describing the halocline evolution in the Canada Basin. The Beaufort Gyre is driven by an anticyclonic wind stress leading to an Ekman convergence and freshwater accumulation toward the center of the gyre (Coachman, 1969; Proshutinsky et al., 2002, 2009, 2015). Consequently, isopycnals bend and the halocline is deeper in the center of the gyre (**Figure 9**). The resulting baroclinic instabilities produce mesoscale eddies which counterbalance the freshwater accumulation and ensure an equilibrium state of the Beaufort Gyre (e.g., Davis et al., 2014; Manucharyan et al., 2016; Manucharyan & Spall, 2016).

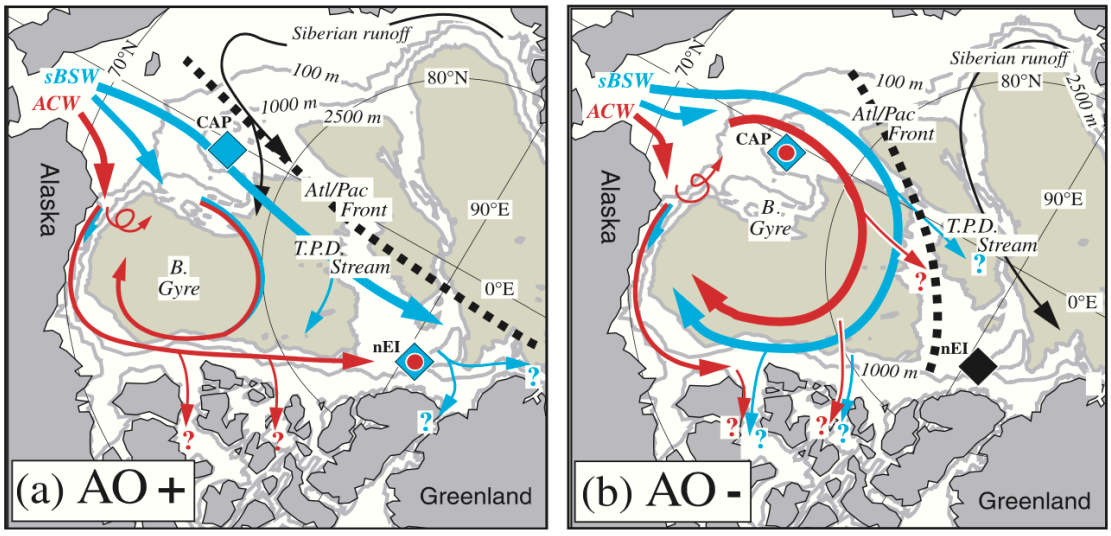

Figure 8: Schematic circulation of summer Pacific halocline water, separated into ACW (red) and sBSW (blue) components, in (a) positive Arctic Oscillation states and in (b) negative Arctic Oscillation states. Two key locations are marked by red circles (ACW) and blue diamonds (sBSW), i.e., the Chukchi Abyssal Plain (CAP) and the area north of Ellesmere Island (nEI). These are color-coded by the influence of ACW and sBSW in different regimes. The black diamond at nEI in AO- conditions indicates a lack of recent renewal of summer Pacific halocline water, at least as determined by a temperature maximum. The hypothesized outflow to the North Atlantic Ocean through the Canadian Archipelago and Fram Strait is illustrated by arrows with question marks, indicating a lack of data in our study. The Atlantic/Pacific front and the main axis of Siberian river runoff are also indicated. From Steele et al. (2004).

An alternative mechanism, called the ice-ocean governor, suggests that the surface stress at the ice-ocean interface is controlled by the relative velocity between the sea ice and the ocean (Meneghello, Marshall, Campin, et al., 2018; Meneghello, Marshall, Timmermans, et al., 2018). Similar ocean and ice velocities cancel the momentum transfer and maintain the gyre at an equilibrium state. Mesoscale eddies are commonly found in the Arctic Ocean (Hunkins, 1974; Manley & Hunkins, 1985; Meneghello et al., 2017; Timmermans et al., 2008; Zhao et al., 2014, 2016) and the ice-ocean governor theory has recently been extended by Doddridge et

al. (2019) to include the effect of eddy diffusivity. Their results suggest that predicting the gyre halocline depth in response to surface forcing and changing sea ice conditions requires accurately capturing the tripartite balance between the ice-ocean governor, wind stress, and eddy fluxes (**Figure 9**). Manucharyan & Isachsen (2019) additionally showed that continental slopes constraining the Beaufort Gyre affect key gyre characteristics leading to deeper halocline and prolonged equilibration time.

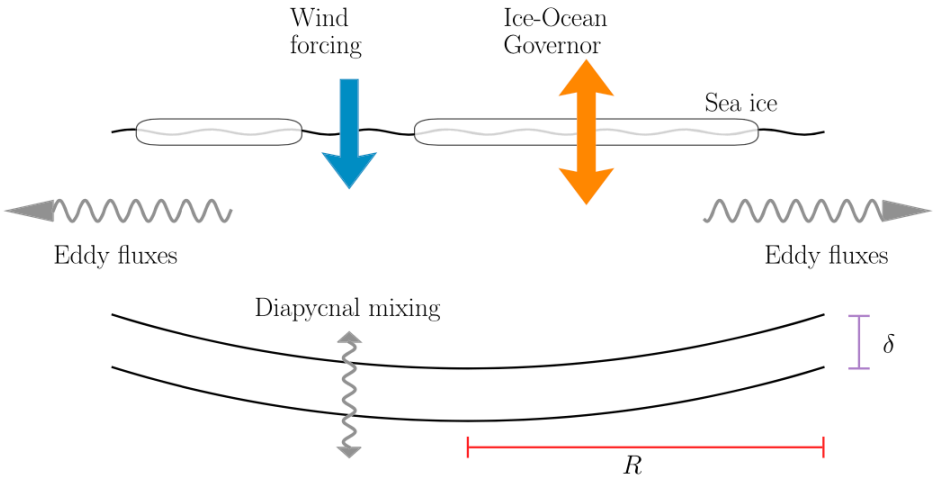

Figure 9: Schematic of the tripartite equilibrium: wind stress (blue arrow) and the ice-ocean governor (orange double-headed arrow) contribute to Ekman pumping, and the residual between these two is balanced by eddy fluxes and diapycnal mixing (horizontal and vertical wavy gray arrows, respectively). The red and purple segments indicate the radius of the gyre (R) and the thickness of the stratified halocline (δ). From Doddridge et al. (2019)

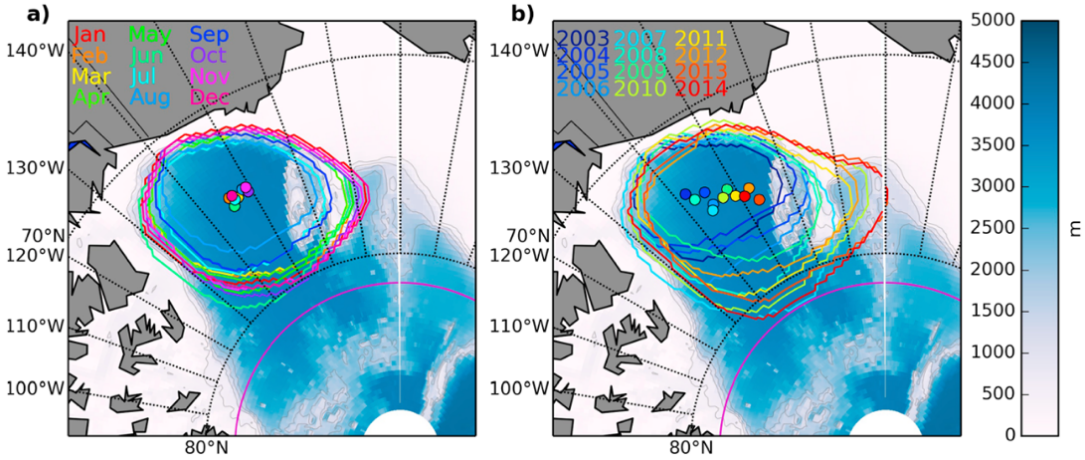

Figure 10: (a) Monthly climatological extent and (b) annual average extent of the Beaufort Gyre from 2003 to 2014, as defined by the largest closed contour of the dynamic ocean topography. The location of the maximum dynamic ocean topography for each contour is also shown. Superimposed on the bathymetry of the general Arctic Ocean bathymetric map (with 500, 1000, 1500, and 2000 m contours drawn in gray) with the 2003-2010 northern boundary of the dataset, at 81.5°, shown in magenta. From Regan et al. (2019)

The Beaufort Gyre has a maximum westward extension in winter (November-December) in response to stronger anticyclonic winds (Proshutinsky et al., 2009; Regan et al., 2019). In summer, winds are weaker and the gyre exhibits minimal extension around August-September (Regan et al., 2019; **Figure 10**). These variations are found in the seasonal evolution of the freshwater content in the gyre with a maximum in winter and a minimum in late summer (Proshutinsky et al., 2009). Freshwater content is additionally maximal in June resulting from an interplay between Ekman convergence strength and the availability of freshwater from sea ice melt and atmospheric forcing (Armitage et al., 2016; Regan et al., 2019).

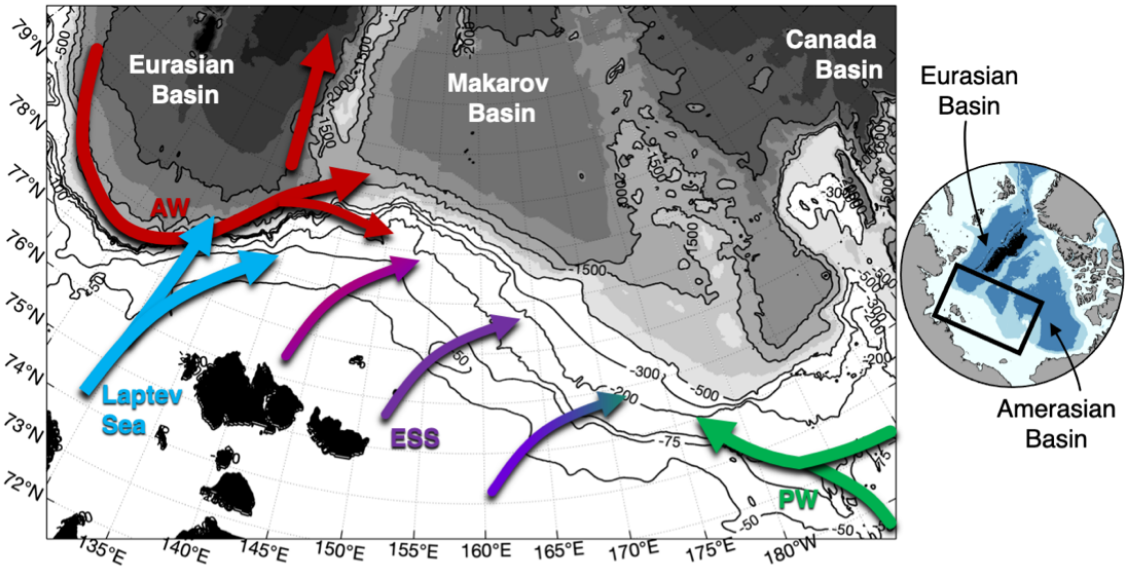

Figure 11: Summary of circulation in the Siberian Seas (black boxe on the pan-Arctic map to the right). Red arrow shows the Atlantic waters (AW) boundary current from the Eurasian Basin, which partly enter the Amerasian Basin. Purple arrows illustrate the export of nutrient-rich water from the East Siberian Sea (ESS) shelf into the deep basin at a salinity of around 33, with differences between the western and eastern part of the ESS and the green arrow the nutrient-rich Pacific water (PW). The blue arrows show the influence of Laptev Sea waters. Inspired from Anderson et al. (2017)

I.4.3. East Siberian Sea and the Makarov Basin waters

High salinity waters from the East Siberian Sea (ESS) are a source of the halocline in the Amerasian Basin. The ESS presents contrasted hydrography and biogeochemical properties with the western part, influenced by Atlantic-origin waters, and the eastern part influenced by Pacific-origin waters (**Figure 11** and **Table 2**) (Anderson et al., 2011; Semiletov et al., 2005). Several studies pointed out that the distinction between Pacific-origin waters from the western Chukchi Sea or the eastern ESS is complicated as both display similar biogeochemical and hydrographic properties, such as high nutrient concentrations, low dissolved oxygen concentrations, and low pH (Alkire et al., 2019; Nishino et al., 2008; X. Wang et al., 2021; Woodgate & Peralta-Ferriz, 2021). Chukchi and ESS shelf waters converged toward the central ESS and spread northward to ventilate the upper halocline of the deep basins via the Canadian and Siberian branches of the TPD (Alkire et al., 2019). In 2008 and 2015, Alkire et al. (2019)

used the semi-conservative chemical parameter NO (with NO = 9 NO_3^- + O_2) and found lower NO values west of 165-170°E over the ESS shelf and in Makarov Basin, which was attributed to ESS-origin water influence to the west, and western Chukchi Sea water influence to the east.

Table 2: Water and sediment characteristics of the Western and Eastern areas of the East-Siberian Sea in 2000 (from Semiletov et al., 2005)

	Western Area			Eastern Area		
Parameters	Mmin	Max	$\bar{x}$	Min	Max	$\bar{x}$
Depth, m	7	20	13	7	41	25
		Surface water				
Temperature, °C	1.41	4.70	*2.62*	−0.88	2.11	*0.58*
Salinity, ‰	10.5	29.7	*22.3*	27.5	31.7	*29.7*
PM, mg/l	4.7	79.7	*24.2*	1.2	7.3	*3.3*
pH	7.9	8.1	*7.9*	7.9	8.4	*8.2*
Nitrate, µM	0.11	5.54	*1.69*	0.05	3.52	*0.51*
Silicate, µM	8.2	73.9	*31.5*	0.5	9.1	*2.4*
Phosphate, µM	0.53	1.5	*1.05*	0.33	1.66	*0.77*
TIC, mM	0.86	1.25	*1.1*	1.47	2.06	*1.78*
		Near bottom water				
Temperature, °C	0.22	3.61	*2.23*	−1.76	0.76	*−0.17*
Salinity, ‰	17.1	31.0	*24.5*	31.2	33.4	*32.2*
PM, mg/l	5.2	106.4	*25.3*	2.4	7.9	*5.3*
pH	7.7	8.1	*7.9*	7.8	8.2	*7.9*
Nitrate, µM	0.12	5.56	*1.94*	0.21	15.61	*4.34*
Silicate, µM	7.9	48.6	*28.6*	0.5	43.5	*12.8*
Phosphate, µM	0.1	1.92	*1.21*	1.02	2.41	*1.68*
TIC, mM	0.85	1.73	*1.26*	1.75	2.26	*1.97*

* PM : Particulate material; TIC : Total Inorganic Carbon;

I.5. Motivations and scientific objectives

I.5.1. Evolution of the Arctic halocline in a changing Arctic

Recent changes in the eastern Eurasian Basin, including reduced sea ice, enhanced vertical heat fluxes, shoaling AW and weaker stratification, have been referred to as the Atlantification of the Arctic Ocean (Lind et al., 2018; Polyakov et al., 2017).

In that context, a contrasted evolution in the strength (i.e. stratification) of the Arctic halocline has been observed since 1981. The stratification of the halocline, evaluated by the frequency of Brunt Vaïsala (N^2) or by the available potential energy (APE), has increased in the Amerasian Basin and weakened in the Eurasian Basin (**Figure 12h**) (Bourgain & Gascard, 2011; Polyakov et al., 2018).

The upper Eurasian Basin salinity has increased since 2000 (Polyakov, Alkire, et al., 2020). In the eastern Eurasian Basin, a substantial weakening of the cold halocline stratification was observed from 2013 to 2018, partially associated with the shoaling of the AW (Polyakov et al., 2017; Polyakov, Rippeth, et al., 2020). The loss of stratification in the eastern Eurasian Basin cold halocline was related to upstream processes, such as salinity changes observed in the northern Barents Sea and closely linked to declines in sea ice imports to the Barents Sea (Lind et al., 2018; Polyakov, Rippeth, et al., 2020).

In contrast, the upper Amerasian Basin is freshening and the stratification is increasing (**Figure 12e and 12h).** The evolution of the freshwater stored in the Beaufort Gyre dominates freshwater evolutions of the Amerasian Basin as well as the halocline stratification (**Figure 12f and 12i**). Changes in atmospheric forcing driving the Beaufort Gyre, such as a weakening of the Beaufort High and dominance of the Icelandic Low, will favor freshwater release from the gyre, which may also be accompanied by a greater volume of Atlantic Water (Timmermans & Marshall, 2020). The excess freshwater released could potentially impact the large-scale ocean circulation by freshening the upper subpolar North Atlantic and eventually have significant implications for the strength of the Atlantic Meridional Overturning Circulation (Zhang et al., 2021)

Concomitantly, the loss of sea ice contributes to intensify solar absorption by the ocean. In the northern Chukchi Sea, the increase heat input was associated with the increase of the heat content in the Beaufort Gyre halocline, from 2 x 10^{20} J before 2000 to 3.7 x 10^{20} J after 2014 (Timmermans et al., 2018). One scenario is that as warming continues, α will increase, and temperature will have an increasingly important influence on the density, possibly compensating the salinity variations (Timmermans & Marshall, 2020).

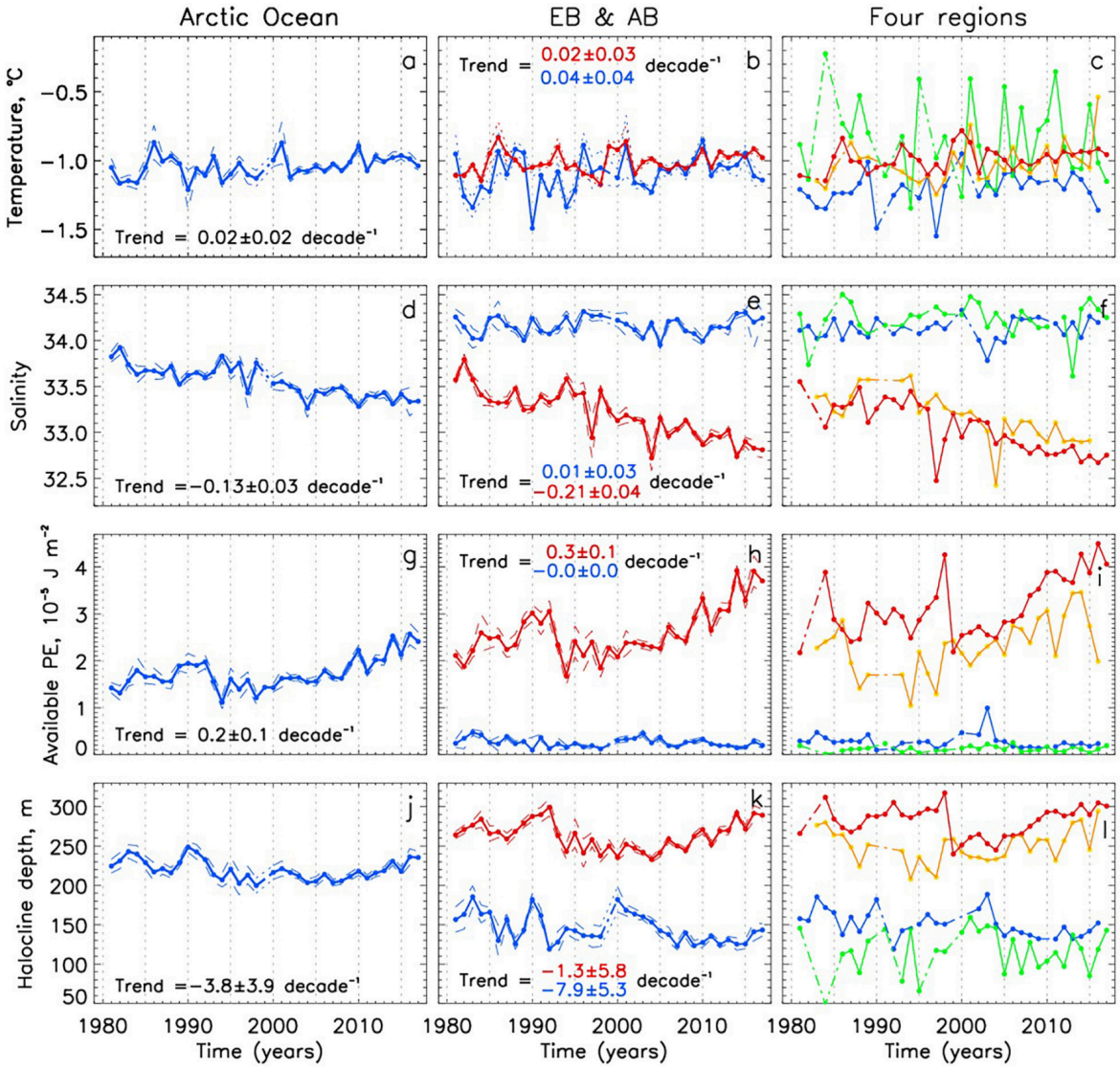

Figure 12: Annual pan-Arctic and regional halocline potential temperature θ_{halo} (**a-c**), salinity S_{halo} (**d-f**), available potential energy APE (**g-i**), and depth of halocline base H_{halo} (**j-l**). Solid lines connect dots with no gaps in between whereas dash-dotted lines are used to fill gaps. Dashed or dotted lines show standard errors at 95% confidence level. In (**b**,**e**,**h**,**k**) red lines are used for Amerasian Basin and blue lines are used for Eurasian Basin. In (**c**,**f**,**i**,**l**) blue, green, yellow, and red lines are used for Eastern Eurasian Basin, Western Eurasian Basin, Chukchi Sea, and Beaufort Gyre regions, respectively. From Polyakov, Alkire, et al., (2020)

I.5.2. PhD objectives

The recent Atlantification of the eastern Arctic Ocean, observed over the last decade, represents an important step toward a new Arctic climate state. The role of the halocline strength governing communication between the Arctic Ocean interior and ice cover has been identified as a climate indicator (Polyakov et al., 2018). Nevertheless, the Arctic halocline remains rather little documented as observations are scarse. Hence, it is important to document the structure of the halocline in the latest years, as well as the processes governing the evolution of the strength and sources of the halocline.

In-situ observations in the Canada Basin contributed to document the halocline in this region (e.g., Proshutinsky et al., 2009, 2020; Shimada et al., 2005; Timmermans et al., 2017, 2018; Woodgate et al., 2005; Zhao et al., 2014). Hence, we attempted to understand the structure, sources and strength of the halocline in recent years in the western Eurasian Basin (Chapter 2) and in the Makarov Basin (Chapter 4).

As the evolution of the halocline is closely linked to the distribution of freshwater, we attempted to describe pan-Arctic scale changes in the freshwater distribution and pathways in recent years (Chapter 3). An important issue was to determine whether a recently documented extension of the Beaufort Gyre until 2014 by Regan et al. (2019) was temporary.

Finally, we attempted to understand to which extend the halocline is impacted by the on-going Atlantification.

A dual approach, combining the analyses of observations and model outputs, was performed. In particular, data from IAOOS platforms were used (Ice Atmosphere Ocean Observing System, www.iaoos.ipev.fr) (**Figure 13a**). The IAOOS platforms were developed conjointly by the French polar institute Paul-Emile Victor (IPEV) and French laboratory LOCEAN (Laboratoire d'Océanographie et du Climat: Expérimentations et Approches Numériques). The IAOOS autonomous platforms are equipped with instruments documenting the four media (ocean, ice, snow, and atmosphere) while drifting with the ice (Provost et al., 2015) and provide valuable observations in the high Arctic Ocean. Deployments of IAOOS platforms in the Amerasian Basin were done in collaboration with the Korean Polar Research Institute (KOPRI). I had the opportunity to participate in the deployment of two IAOOS platforms in August 2019 from the Korean icebreaker *R/V Araon* during the summer cruise in 2019 over the Chukchi Sea (**Figure 13b-c**).

We complemented in-situ measurement with simulations from the last release of the real time high resolution 1/12° global system PSY4V3 developed by Mercator Ocean (Lellouche et la., 2013, 2018). The model was developed for the Copernicus Marine Environment Monitoring Service (http://marine.copernicus.eu/) and was parameterized and run at Mercator Ocean (Ramonville-Saint-Agne, France). We performed a thorough evaluation of the Mercator Ocean global operational system (PSY4V3R1, hereafter PSY4) in the Arctic domain using independent data (not used in the model assimilation) from different sources: hydrographic cruises, autonomous platforms towed by ice, mooring data, satellite data.

The thesis is organized as follows : Chapter 2 presents a characterization of the halocline in the western Eurasian Basin in 2017 combining PSY4 simulations with a semi-conservative biogeochemical parameter, computed using data from a IAOOS that carried for the first time a biogeochemical sensor. In Chapter 3, PSY4 is first assessed on a pan-Arctic scale, and used to describe changes in freshwater distribution and pathways since 2007. Chapter 4 focuses on halocline modifications in the Makarov Basin and along the East Siberian Sea slope using autonomous platforms, shipborne CTD and PSY4. Finally, Chapter 5 presents conclusions and some perspectives.

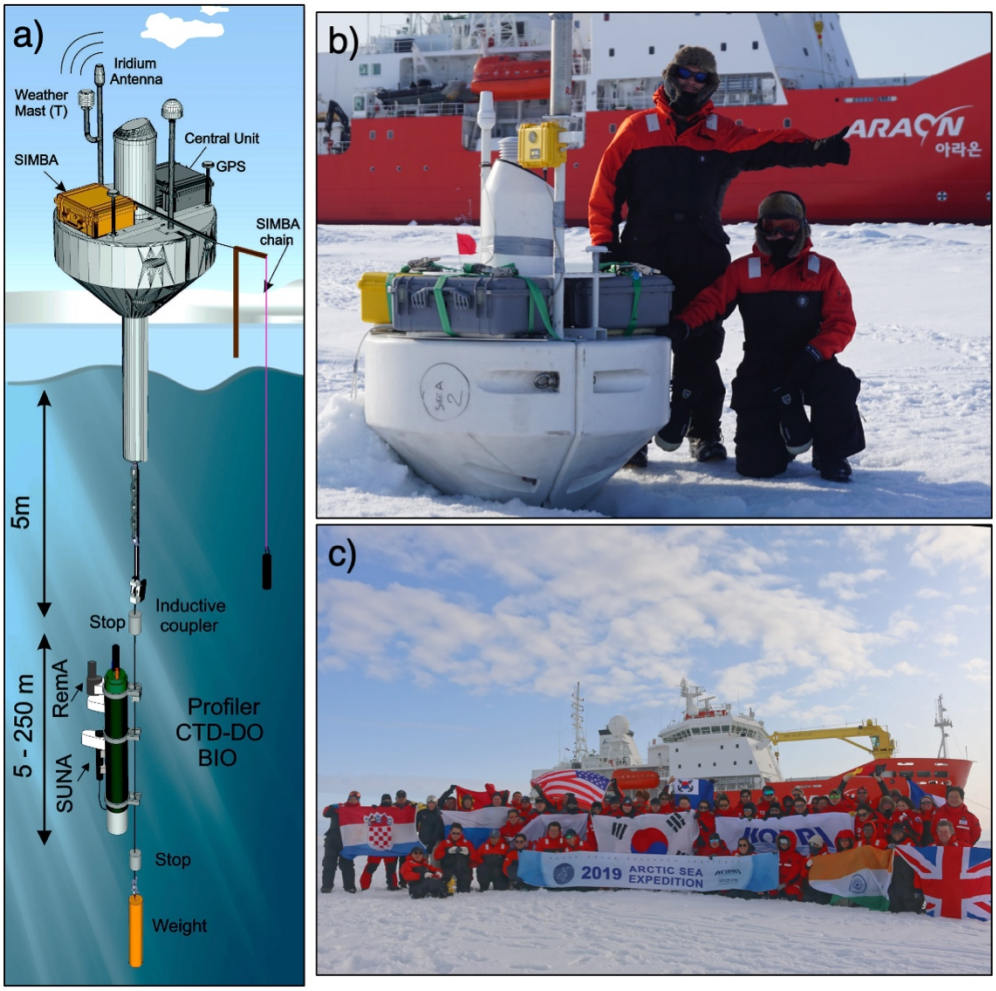

Figure 13: (**a**) Schematic of the IAOOS platform: ocean, ice and atmosphere part. (**b**) Picture of a IAOOS deployment. (**c**) Team of the Arctic Sea expedition 2019 over the Chukchi Sea onboard the Korean icebreaker *R/V Araon* (August 2019).

Chapter II

The halocline structure, sources and strength in the Western Eurasian Basin in 2017

Contents

II.1. Introduction

Recent observations are rare and valuable in the Eurasian Arctic Basin. In April 2017, two IAOOS plateforms were deployed from the Barneo ice camp, a temporary drifting station located always north of 88°N. They acquired data in the Western Eurasian Basin during 8 months, the longest most eastward spread IAOOS dataset in the Eurasian Basin. The two platforms followed an unusually meandering trajectory, circulating eastward in the Nansen Basin interior before looping back towards Fram Strait. For the first time, one of the two IAOOS profiler was equipped with biogeochemical sensors which provided the first autonomous nitrate profiles in the Arctic. This unique dataset permitted to reveal fresher mixed layer and shallower warm layer in 2017 compared to climatology (Athanase et al., 2019) and to examine under-ice phytoplankton blooms (Boles et al., 2020). Here, we combine physical and biogeochemical data to investigate the halocline structure, sources and strength in the western Eurasian Basin.

II.2. The Western Eurasian Basin Halocline in 2017: Insights from Autonomous NO Measurements and the Mercator Physical System

JGR Oceans

RESEARCH ARTICLE
10.1029/2020JC016204

The Western Eurasian Basin Halocline in 2017: Insights From Autonomous NO Measurements and the Mercator Physical System

Cécilia Bertosio[1], Christine Provost[1], Nathalie Sennéchael[1], Camila Artana[2], Marylou Athanase[1], Elisabeth Boles[1,3], Jean-Michel Lellouche[2], and Gilles Garric[2]

[1]Laboratoire LOCEAN-IPSL, Sorbonne Université (UPMC, Univ. Paris 6), CNRS, IRD MNHN, Paris, France, [2]MERCATOR OCEAN, Parc Technologique du Canal, Ramonville Saint Agne, France, [3]Now at Environmental Fluid Mechanics Laboratory, Stanford University, Stanford, CA, USA

Abstract We present the first sensor-based profiles of the quasi-conservative NO parameter obtained with an autonomous ice-tethered buoy in the Arctic Ocean. Data documented the halocline in the Transpolar Drift and Nansen Basin in 2017. A NO minimum was found in the Nansen Basin on a σ-horizon of 27.8 kg·m^{-3} corresponding to the lower halocline, while a lower NO minimum of 380 μM straddled the 27.4 σ-horizon and marked the cold halocline in the Transpolar Drift. Back trajectories of water parcels encountered along the buoy drift were computed using the Mercator physical system. They suggested that waters within the NO minimum at 27.4 kg·m^{-3} could be traced back to the East Siberian Sea continental. These trajectories conformed with the prevailing positive phase of the Arctic Oscillation. The base of the lower halocline, at the 27.85 σ-horizon, corresponded to the density attained in the deepest winter mixed layer north of Svalbard and cyclonically slowly advected from the slope into the central Nansen Basin. The 27.85 σ-horizon is associated with an absolute salinity of 34.9 g·kg^{-1}, a significantly more saline level than the 34.3 psu isohaline commonly used to identify the base of the lower halocline. This denser and more saline level is in accordance with the deeper winter mixed layers observed on the slopes of Nansen Basin in the last 10 years. A combination of simulations and NO parameter estimates provided valuable insights into the structure, source, and strength of the Arctic halocline.

Plain Language Summary Dissolved oxygen and nitrate data, measured for the first time by an autonomous ice-tethered profiler in the Arctic Ocean, were combined to compute the NO parameter, a tracer useful for differentiating oceanic water masses. Together with ocean and sea ice model simulations, the spatial distribution of this NO parameter provided valuable insights into the structure and sources of the water in the central Arctic. The halocline, a layer near the surface where salinity increases rapidly with depth, isolates sea ice from the heat stored in the salty Atlantic water below. Waters in the halocline could be traced back to two different sources: the East Siberian Sea continental slope and the slope north of Svalbard where deep winter convection is important. Additionally, our analyses show that previous definitions of the bounds of the halocline layer no longer apply, likely because of increasing influence of saltier Atlantic water near the surface.

Key Points:
- First profiles of the NO parameter from an autonomous ice-tethered buoy in the Arctic Ocean documented the halocline in 2017
- In Nansen Basin, a NO minimum on the 27.8 σ-horizon traced the deepest winter mixed layer and lower halocline waters
- In the transpolar drift, a smaller NO minimum on the 27.4 σ-horizon (cold halocline) was traced back to the East Siberian Seas

Correspondence to:
C. Bertosio,
cecilia.bertosio@locean-ipsl.upmc.fr

Citation:
Bertosio, C., Provost, C., Sennéchael, N., Artana, C., Athanase, M., Boles, E., et al. (2020). The western Eurasian Basin halocline in 2017: Insights from autonomous NO measurements and the Mercator physical system. *Journal of Geophysical Research: Oceans*, *125*, e2020JC016204. https://doi.org/10.1029/2020JC016204

Received 4 MAR 2020
Accepted 18 JUN 2020
Accepted article online 23 JUN 2020

1. Introduction

The halocline, a subsurface layer with increasing salinity with depth, is a fundamental structure of the upper Arctic Ocean. The halocline acts as an insulating barrier separating the cold and fresh surface mixed layer (SML) and sea ice from the warm and salty Atlantic water (AW) below: hence, it is a key feature in the maintenance of the sea ice cover (e.g., Steele & Boyd, 1998). The Arctic Ocean halocline is complex, consisting of several water masses and source regions. The halocline can be divided into lower, cold, and upper halocline layers. The lower halocline waters (LHW) are formed via freshening, cooling, and mixing of AW with sea ice melt water upon entry in the Arctic north of Svalbard or the Barents Sea (Rudels et al., 1996). In the LHW, temperature and salinity ($34 < S < 34.5$) increase with depth until the upper limit of the warm and salty AW. The cold halocline waters, characterized with homogeneous near-freezing temperatures and large vertical salinity gradient ($33 < S < 34$), result from additional influences from the Kara, Laptev, and/or East Siberian Sea (Alkire et al., 2017; Rudels et al., 2004; Steele & Boyd, 1998). The upper halocline waters

(UHW) are made of fresher Pacific-derived contributions overriding the denser Atlantic-origin halocline waters. UHW are mainly found in the Amerasian Basin, and their horizontal extent and incursion in the Eurasian Basin vary between years, mainly depending on the position of the Transpolar Drift (TPD; e.g., Alkire et al., 2019; Anderson et al., 2013). Observational activities in the Canada Basin have revealed that UHW had a complex structure resulting from the distinct water sources (Alkire et al., 2010; Shimada et al., 2005), the different paths traveled on the shelves (Bourgain et al., 2013; Steele et al., 2004), and from variable seasonal ventilation (Timmermans et al., 2017).

The halocline strength, that is, its stratification, shows large interannual and spatial variations (e.g., Bourgain & Gascard, 2011; Polyakov et al., 2018). Nevertheless, trends are clear, and since 1981, there is a contrasted evolution in the strength of the Arctic halocline with an increasing stratification in the Amerasian Basin and a weakening in the Eurasian Basin (Polyakov et al., 2018). These changes are concomitant with the progression of AW signature from the western Eurasian Basin to the eastern Eurasian Basin, called "Atlantification" (Polyakov et al., 2017). The major driver for these changes is a powerful combination of processes associated with declining sea ice cover and weakening of stratification in the layers over the AW leading to an increase in winter convection depth.

Tracers (isotopes and nutrients) have proven very useful in helping to identify variations in sources of the water masses composing the halocline in the Central Arctic and suggesting circulation patterns (e.g., Alkire et al., 2007, 2015). In particular, the NO parameter, a semiconservative tracer combining nitrate and dissolved oxygen (DO), has been used to trace water masses at depths and below the active layer of mixing. Defined as $NO = 9 \times [NO_3] + [O_2]$ (Broecker, 1974), it exhibits a minimum in the lower halocline (Jones & Anderson, 1986) that is consistent with a convective formation of LHW in the western Eurasian Basin (Rudels et al., 1996). Sensor-based observations yielding high-resolution vertical profiles of the NO parameter displayed another NO minimum in the upper halocline in the Makarov Basin in 2007 and 2008. This NO minimum was indicative of a ventilation source, most likely from Siberian shelves, not present in the Amundsen Basin (Alkire et al., 2010). Recently, it was shown that significant contrasts in the NO parameter help identify the front separating UHW contributions from Atlantic (lower NO) and Pacific (higher NO) waters in the Central Arctic Ocean in summer 2015 (Alkire et al., 2019).

If the NO parameter has proven to be a useful qualitative tracer of halocline waters from the Amerasian Basin and LHW from the Eurasian Basin, inferring routes and time scales from NO distribution is speculative. Sea ice back trajectories have been used for interpreting the origin and path of the mixed layer waters (e.g., Kipp et al., 2018). However, the circulation of surface and halocline waters (upper and a fortiori lower) may not necessarily be coupled (Alkire et al., 2007). Indeed, observations and numerical models show significant velocity shear in the upper layers.

We examine the NO parameter distribution in the halocline of the western Eurasian Basin in 2017 making use of the first sensor-based profiles of the NO parameter gathered with an autonomous ice-tethered platform in the Arctic Ocean. We also examine how an ocean-sea ice operational system can help interpret the observed NO distribution. The data were gathered during an 8-month drift of IAOOS23 platform from the North Pole to Fram Strait in 2017 along a meandering path across the western Eurasian Basin (Provost et al., 2017; Figure 1a). High colored dissolved organic matter (CDOM) fluorescence values and low nitrate concentrations in the upper layer (Figures 1b and 1c) were associated with water masses coming from Siberian shelves and carried with the TPD across the Central Arctic (Athanase et al., 2019). Several mesoscale structures were observed in the halocline and in the Atlantic warm layer (HE1, HE2, HE3, AW1, and AW2 in Figures 1c and 1d), and Mercator Ocean operational system helped interpret the origin of the observed mesoscale structures (Athanase et al., 2019). The data also documented two under-ice blooms: an early spring bloom in Amundsen Basin consisting of small, potentially mixotrophic phytoplankton and a summer bloom in Nansen Basin which contained a greater diversity of planktonic size classes (Boles et al., 2020).

The paper is organized as follows. Section 2 describes the in situ data focusing on the NO parameter, methods for halocline depth and strength estimates, and the Mercator Ocean operational system. Section 3 presents a NO-focused upper layer hydrography, while section 4 focuses on halocline structure, sources, and strength making use of the operational system. Section 5 discusses water mass source inferences and comparisons with previous studies. Section 6 highlights major findings and puts the work into perspective.

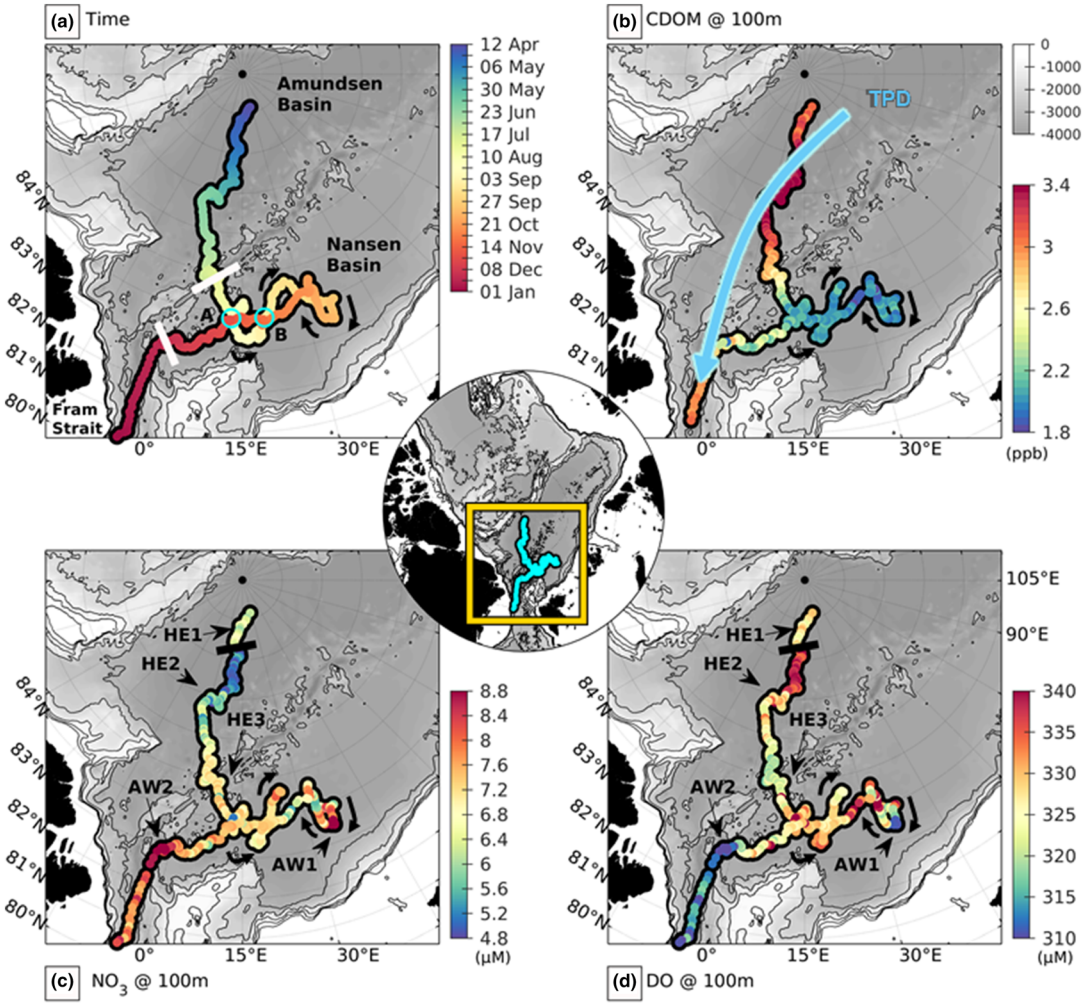

Figure 1. Along the trajectory in color: (a) date; blue circles highlight crossover points A and B; white segments delimit boundaries between basins; small black arrows mark the direction of the platform drift. (b) Colored dissolved organic matter fluorescence (CDOM, ppb) at 100 m; blue arrow sketches the transpolar drift (TPD) characterized with CDOM > 3 ppb; (c) NO_3 (μM) at 100 m and (d) dissolved oxygen (DO, μM) at 100 m. Three halocline eddies (HE) and two Atlantic water mesoscale structures (AW) are labeled. Background is bathymetry in gray scale with isolines at 500, 1,000, 2,000 and 3,200 m. The black solid line at 88.2°N indicates a frontal zone.

2. Data and Methods

2.1. Upper Ocean Data and NO Parameter

To avoid redundancy with previous works, we briefly recall the data used here and refer the reader to the description of the experimental setup and data processing in Athanase et al. (2019). The unique 8-month-long data set used here consists of a total of 431 profiles of temperature, salinity, and DO and 427 profiles of CDOM fluorescence and nitrate concentration (upper 250 m from IAOOS23 profiler; Table 1 in Athanase et al., 2019). After data processing, quality control, and interpolation, conservative temperature (CT), absolute salinity (SA), and DO data have 0.5 m vertical resolution and an accuracy of 0.005°C, 0.02 $g{\cdot}kg^{-1}$, and 2.5 μM, respectively. NO_3 data have a 1 db vertical resolution and a 2 μM accuracy (see Appendix A), and CDOM data have a 1 db vertical resolution and a manufacturer accuracy of ±0.28 ppb (Athanase et al., 2019; Boles et al., 2020) (Figure 2).

Measurements of DO and nitrates were interpolated and combined to compute the NO parameter ($NO = 9 \times [NO_3] + [O_2]$) with a 1 db vertical resolution. A conservative uncertainty on absolute values of the NO estimates is about ±10 μM. NO values range from 375 to 410 μM, a range comparable to estimates

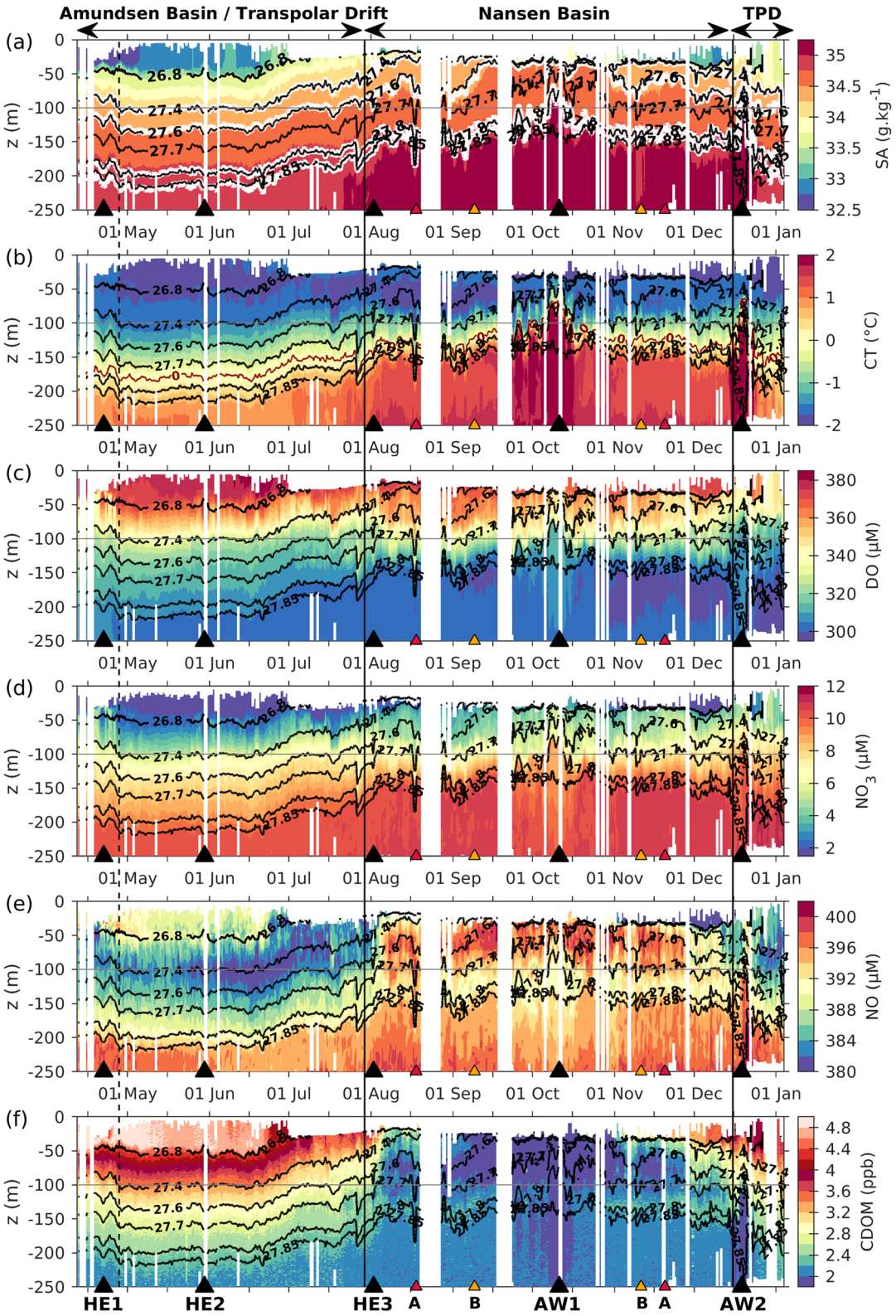

Figure 2. Hydrographic variables along the trajectory (*x* axis is time, and *y* axis is depth): (a) absolute salinity (SA, $g{\cdot}kg^{-1}$) with isohalines 34.2, 34.46, 34.8, and 34.9 $g{\cdot}kg^{-1}$ in white; (b) conservative temperature (CT, °C) with 0°C temperature isoline in purple; (c) dissolved oxygen concentration (DO, µM); (d) nitrate concentration (NO_3, µM); (e) NO parameter (µM); and (f) colored dissolved organic matter fluorescence (CDOM, ppb). Black lines depict density isolines from 26.8 to 27.9 $kg{\cdot}m^{-3}$. Vertical black lines delimit boundaries between basins. The dashed vertical line indicates the position of a frontal zone at 88.2°N. Positions of HE1, HE2, HE3, AW1, AW2, and two crossover points A and B are marked at the bottom.

from Alkire et al. (2010, 2017) in the Central Arctic (see Appendix A) and show a consistent distribution in space and time (Figure A2).

2.2. Halocline Definition and Characterization From Physical Parameters

The upper limit of the halocline, or depth of the SML (H_{SML}), coincides with a strong maximum in the Brunt-Väisälä frequency N^2 (Figure 4a in Athanase et al., 2019). Note that several profiles did not reach the near surface as a strong stratification at the base of the summer mixed layer, at about 30-m depth, probably impeded the ascent of the profiler, particularly in July–August 2017.

Several definitions for the depth of the lower halocline boundary (H_{halo}) can be found in the literature. Rudels et al. (1996) estimated H_{halo} as the depth of the 34.3 psu isohaline (i.e., SA = 34.46 g·kg^{-1}) as the 34.3 value appeared to be the maximum salinity reached by the winter mixed layer north of Svalbard. Bourgain and Gascard (2011) defined H_{halo} as the depth where the density ratio R_ρ ($R_\rho = \alpha\partial_z CT/\beta\partial_z SA$, where α is the thermal expansion coefficient and β the haline contraction) had a value of 0.05. The choice of threshold in SA or R_ρ for estimating the halocline depth is discussed in section 5 in light of the hydrographic measurements including NO.

The halocline thickness is then defined as $\Delta H_{halo} = H_{halo} - H_{SML}$. To measure the halocline strength, that is, its stratification, we used the available potential energy (APE), an indicator proposed by Polyakov et al. (2018), with APE$=\int_{z1}^{z2} g(\rho - \rho_{ref})z\mathrm{d}z$, where z_2 is the surface, z_1 the depth of the halocline base H_{halo}, g the gravity acceleration, ρ_{ref} is potential density at the base of the halocline, and z is depth.

Profiler observations are not Lagrangian as the platform drifted with the ice rather than the ocean, and we used model outputs to investigate possible water parcel paths and time scales.

2.3. Mercator Ocean Operational System and Satellite-Derived Products

The global Mercator Ocean operational system PSY4V3R1 (hereafter PSY4) was developed for the Copernicus Marine Environment Monitoring Service (http://marine.copernicus.eu) with a (1/12)° horizontal resolution and 50 vertical z levels with typically 1 m resolution at the surface decreasing to 450 m at the bottom and 22 levels within the upper 100 m. A full description of the system components is available in Lellouche et al. (2018). PSY4 only simulates physical variables and no biogeochemical variables. Skills of PSY4 in reproducing physical variables (sea ice, temperature, salinity, and ocean currents) in the western Eurasian Basin have been assessed in Koenig, Provost, Sennéchael, et al., 2017, Koenig, Provost, Villacieros-Robineau, et al., 2017, Ivanov et al. (2018), and Athanase et al. (2019). In particular, daily Mercator Ocean system temperature and salinity profiles show a general agreement with a well-positioned 27.8 isopycnal with adequate salinities (within 0.05) and temperatures (within 0.3°C) (Figure 10 in Athanase et al., 2019).

We used daily horizontal model velocities to investigate possible origins of water parcels encountered in the halocline during the drift. Lagrangian backward and forward trajectories of synthetic particles were tracked using a simple prediction-correction scheme similar to that employed by Fillipi et al. (2010).

Mean velocities over year 2017 at the surface (sea ice) and at 50 and 220m depth in the ocean show a common pattern with a swift drift from the East Siberian Sea toward the North Pole as well as a slower drift from the Laptev Sea toward the North Pole (Figures 3a–3c). Note the small scale of spatial structures in ocean mean velocities (Figures 3b and 3c).

Back trajectories of the modeled ice followed the platform trajectory, thus showing the reliability of Mercator ice drift (Figure 3d). They suggested that the ice floe originated from the Laptev Sea in October–November 2015 and was 1.5 years old when the IAOOS platform was installed. Back trajectories calculated from satellite-derived ice drift (doi: 10.5067/INAWUWO7QH7B) provided the same result (not shown). Sources and time scales of advection of halocline water parcels are examined in section 4.

3. NO-Focused Upper Layer Hydrography

Athanase et al. (2019) and Boles et al. (2020) documented general hydrography and biology, respectively, from the same data set. For the sake of completeness and clarity, we complemented new sections of DO

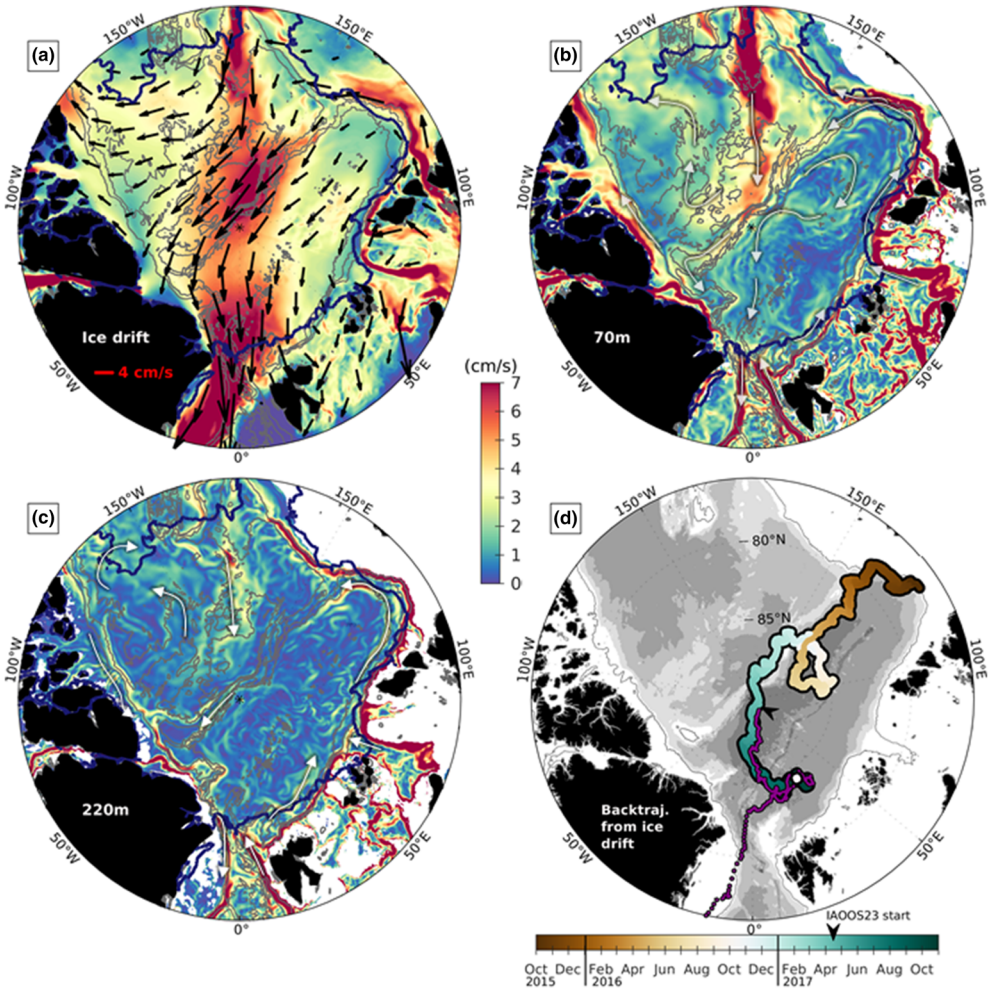

Figure 3. (a) Sea ice horizontal velocities averaged over 2017 from PSY4 outputs. Velocity amplitude in the background with a 1/12° spatial resolution, arrows subsampled every 40 grid cells for the sake of clarity. (b) Amplitude of mean ocean horizontal velocities in 2017 at 70 m (b) and 220 m (c) from PSY4 outputs. The three maps have the same color bar. The 100% ice cover limit in 2017 is shown in dark blue in (a)–(c). White arrows in (b) and (c) sketch current direction. (d) Back trajectory (color scale is time) from IAOOS23 ice floe using PSY4 sea ice velocities; the white dot is the back trajectory starting point from late October 2017; purple line is IAOOS23 trajectory.

and NO with sections of CT, SA, NO_3, and CDOM previously shown in Athanase et al. (2019) and Boles et al. (2020) (Figure 2).

Waters in the TPD (sampled in Amundsen Basin and Fram Strait) were less saline, colder, and lighter than those sampled in Nansen Basin. The mixing lines between AW and lower salinity, near-freezing surface layers, had a steeper slope in Nansen Basin than in the TPD (Figure 4a). The contrasting bends in the CT-SA curves separating near-surface and Atlantic waters illustrate the distinct stratifications in the TPD and Nansen Basin upper water columns (Figure 4a). In the TPD, the bend above the mixing line between AW and SML in the wide SA range 33.5–34.9 ($26.8 < \sigma < 27.85$ kg·m^{-3}) reflects low-salinity, river/shelf water input (Kikuchi et al., 2004). In contrast, the sharp bend below the mixing line from profiles in Nansen Basin indicates convectively formed waters with a reduced range of salinity and density ($34.3 < SA < 34.9$ g·kg^{-1} and $27.5 < \sigma < 27.85$ kg·m^{-3}).

DO concentration varied from relatively high near-surface values close to saturation level (from 390 to 345 μM varying with CT) to a minimum of 305 to 295 μM at SA of 34.9 g·kg^{-1} ($27.8 < \sigma < 27.85$ kg·m^{-3}) (Figures 2c and 4b). In contrast, nitrate concentrations were small near the surface with values below

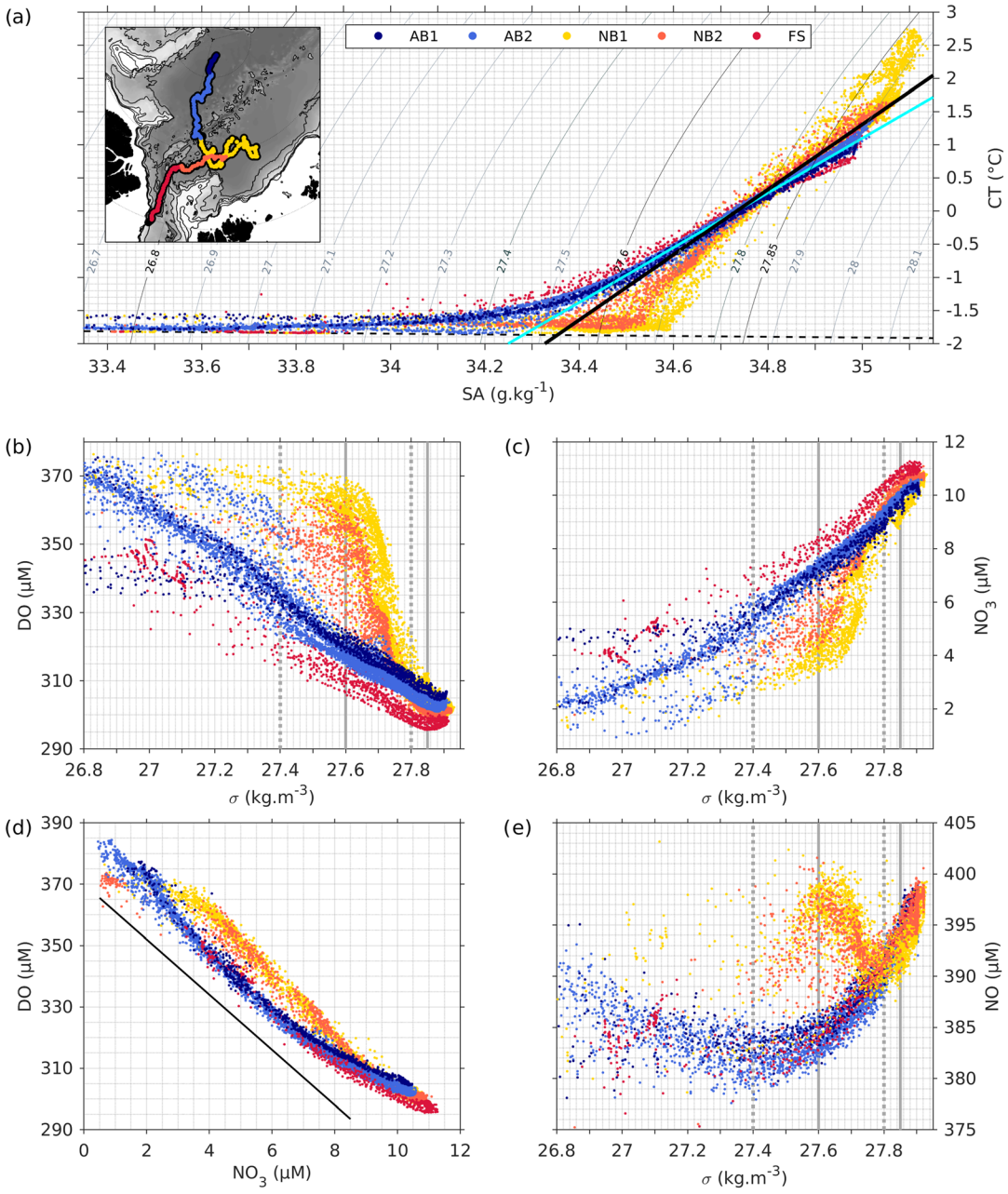

Figure 4. Colors represent regions (Amundsen Basin: AB1 and AB2; Nansen Basin: NB1 and NB2; Fram Strait: FS; and the Transpolar Drift (TPD) corresponds to AB1, AB2, and FS). Diagrams of select variables: (a) CT-SA with two mixing lines, one for TPD (solid line cyan) and the other for Nansen Basin (solid line black); mixing lines are drawn through values of CT and SA at 180- and 250-m depths (following Kikuchi et al., 2004); (b) DO-σ; (c) NO_3-σ; (d) DO-NO_3 where a black line with a slope of −9 is represented; (e) NO-σ. Vertical dotted lines mark densities associated to NO minima (27.4 and 27.8 kg·m^{-3}), and vertical plain lines correspond to bottom of cold and lower halocline densities (27.6 and 27.85 kg·m^{-3}).

2 µM and increased with depth to reach values in excess of 10 µM at σ of 27.85 kg·m^{-3} (SA of 34.9 g·kg^{-1}). The larger DO values in the Nansen Basin in the σ range 27.4–27.8 kg·m^{-3} (yellow and orange dots in Figure 4b) were consistent with recently ventilated waters (Figure 4a) that were relatively depleted in nitrate compared to waters from the TPD (Figure 4c). For a given density, waters in the TPD (blue in Amundsen Basin and red in Fram Strait; Figures 4b–4d) showed a progressive increase in nitrate and decrease in DO.

The DO-NO_3 diagram (Figure 4d) shows that the ratio of DO to nitrate concentrations is close to Redfield stoichiometry in Nansen Basin (orange and yellow dots), except in the upper layer (large DO small NO_3) because of nitrate uptake due to primary production (Boles et al., 2020). In the TPD, the ratio deviated from a straight line (Figure 4d), and this departure reflected in the NO parameter which showed a marked minimum of 380–385 μM at σ values of 27.3–27.6 kg·m^{-3} (Figure 4e). In Nansen Basin, the NO parameter showed a minimum of 390–395 μM at σ values of about 27.8 kg·m^{-3}.

Along the drift, the NO parameter shows a distinct spatial distribution from that of its parent constituents (Figures 2c–2e). Salient features in the NO distribution are the minimum centered on the 27.4 isopycnal in the TPD (Amundsen and Fram Strait) and a weaker minimum centered on the 27.8 isopycnal in Nansen Basin (Figure 2e). Throughout the drift, NO shows values of 390–395 μM on the 27.8 kg·m^{-3} isopycnal which lies at about 110-120 m depth in Nansen Basin and close to 200 m in Amundsen Basin. Abrupt changes in NO above the 27.8 kg·m^{-3} horizon occurred on the southern side of Amundsen Basin and at the exit to Fram Strait with a stark contrast between waters from the TPD (in Amundsen and in Fram Strait; Figure 1a), poorer in DO and NO (leading to NO < 380 μM) than waters below the mixed layer in the upper Nansen Basin (NO > 390 μM). Origins of the NO minima on 27.4 and 27.8 kg·m^{-3} isopycnal horizons (SA = 34.2 and 34.8 g·kg^{-1}) are discussed below.

4. Halocline Structure, Sources, and Strength Along the Drift

4.1. TPD: Halocline Structure and Origin of the NO Minimum at 27.4

Below the SML (H_{SML} is about 45 m) and above isopycnal 27.6 kg·m^{-3} (located at about 120 m depth and highlighted with a thick black line in Figure 5), vertical salinity gradients were large ($\partial_z SA > 1 \times 10^{-2}$ g·kg^{-1}·m^{-1}), and vertical temperature gradients were small ($\partial_z CT < 1 \times 10^{-2}$°C·m^{-1}) (Figures 5a and 5b). The vertical derivative of NO parameter changed sign on the 27.4 σ-isoline corresponding to the NO minimum (Figure 5c). The 70 m-thick layer between the SML and isopycnal 27.6 with SA in the range 33.4 to 34.46 g·kg^{-1}, cold temperatures below −1.5°C and including the NO minimum (Figures 2b and 2d), corresponded the cold halocline layer. Between isopycnals 27.6 and 27.85 kg·m^{-3} (thick black lines in Figure 5), the vertical salinity gradient was small ($0.5 < \partial_z SA < 1 \times 10^{-2}$ g·kg^{-1}·m^{-1}), the vertical temperature gradient was larger ($\partial_z CT > 1.5 \times 10^{-2}$°C·m^{-1}), and vertical NO gradient was positive (>0.1 μM. m^{-1}). We considered that isopycnal 27.85 kg·m^{-3} marked the upper limit of the Atlantic layer (at σ > 27.85 kg·m^{-3}, temperatures were positive above 0.5°C and salinity values above 34.9 g·kg^{-1}) and the lower limit of the lower halocline. Thus, the LHW layer in the TPD in Amundsen Basin lay within isopycnals 27.6 and 27.85 kg·m^{-3} in the salinity range 34.46 to 34.9 g·kg^{-1} and temperature range −1°C to 0.5°C. The LHW layer was about 60 m thick.

Isopycnal 27.4 kg·m^{-3}, associated to the location of the NO minimum in Amundsen Basin (Figure 2e), corresponded to a density ratio R_ρ of 0.05 (Figure 5d), isopycnal 27.6 kg·m^{-3}, the base of the cold halocline there, to an R_ρ of 0.1 and isopycnal 27.85 kg·m^{-3}, the base of the lower halocline, to R_ρ values larger than 0.3 (Figure 5d).

Profiles from 18 June (in blue in Figures 5e–5g) illustrate the vertical structure in the TPD in Amundsen Basin with a NO minimum between 60 and 110 m corresponding to an R_ρ value between 0 and 0.1 and a density between 27.05 and 27.6 kg·m^{-3}.

In an attempt to understand the origin of water parcels in the NO minimum centered on the 27.4 σ-horizon in Amundsen Basin, we performed back trajectories at different depths and starting at different times (every 5 days from 30 April to 30 June) from a box extending from 85°N to 87°N and from 12°W to 12°E (black box in Figures 6a–6c). Back trajectories from the 5 to 70 m depth range consistently suggested contributions from the East Siberian Sea and Laptev Sea continental slopes (Figures 6a and 6b). Advective time scales from the East Siberian Sea slope (~79°N, 165°E) varied with depth (~1 year at 5 m; ~1.5 to 2 years at 70 m). On the other hand, 2-year-long back trajectories at 110 (not shown) and 220 m (Figure 6c) were short and indicated old recirculating Modified AW. These deep trajectories (Figure 6c) were consistent with the low CT and SA observed in the Amundsen Basin Modified AW (Figures 2a, 2b, and 4a).

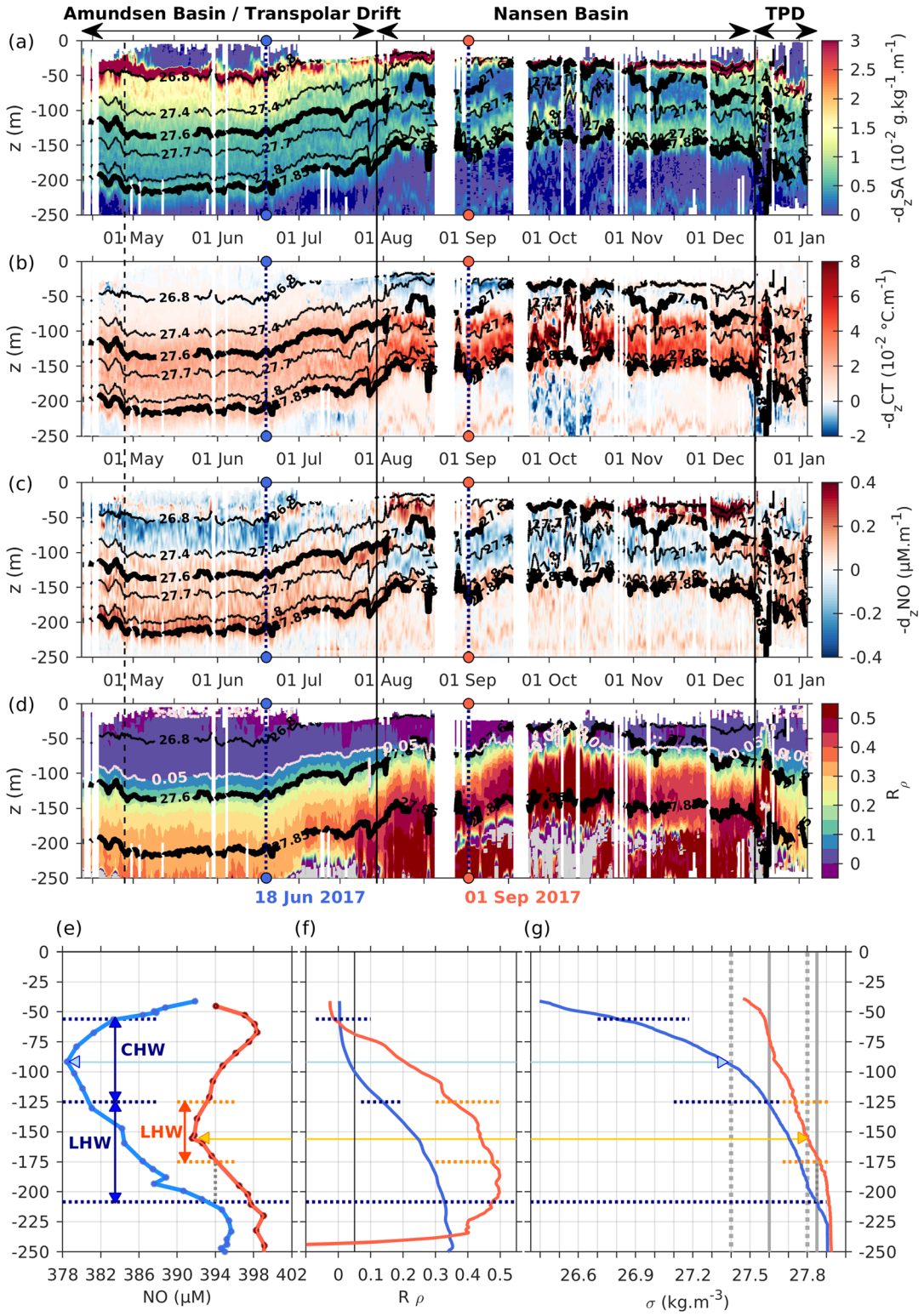

Figure 5. Vertical gradient of variables along the drift trajectory (x axis is time, and y axis is depth): (a) SA (10^{-2} g·kg^{-1}·m^{-1}); (b) CT (10^{-2}°C·m^{-1}); (c) NO (µM·m^{-1}); (d) density ratio R_ρ with isoline 0.05 in white. Isopycnals are in black. Profiles of (e) NO parameter, (f) density ratio R_ρ, and (g) potential density σ in Amundsen Basin on 18 June in blue and in Nansen Basin on 1 September in orange. Black line in (f) marks $R_\rho = 0.05$. Limits of cold halocline (CHW) and lower halocline (LHW) are represented with dotted lines.

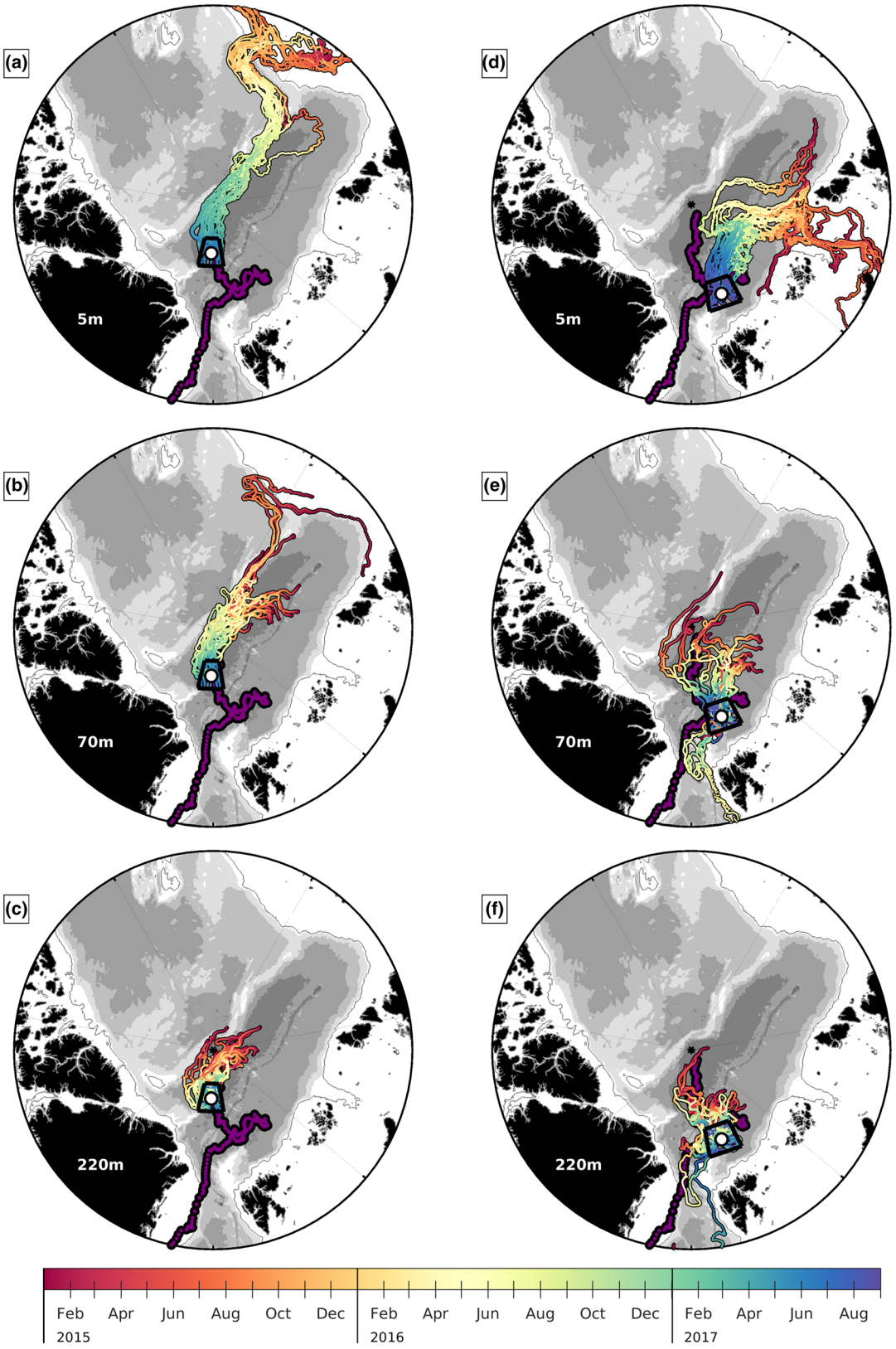

Figure 6. Back trajectories in Amundsen Basin from 18 June 2017 (a–c) at 5, 70, and 220 m depth calculated with PSY4 velocities from a box centered on the location of the NO minimum (85–87°N; 12°W–12°E). Back trajectories in Nansen Basin from 1 September 2017 (d–f) at 5, 70, and 220 m starting in the box (83–85°N; 10–30°E). Color is time.

4.2. Upper Layer Structure in the Nansen Basin

In Nansen Basin (1 August to 19 December), H_{SML} was about 40 m. In contrast with the stratification in the TPD, salinity and temperature vertical gradients below the mixed layer covaried: they were small ($\partial_z SA < 1 \times 10^{-2}$ g·kg^{-1}·m^{-1} and $\partial_z CT < 4 \times 10^{-2}$°C·m−1) down to 27.7 kg·m^{-3} isopycnal depth (Figures 5a and 5b). The vertical NO derivatives changed sign from negative to positive on the 27.8 σ-horizon (in the LHW) which corresponded to a local minimum in NO (Figures 5c and 2e). Profiles from 1 September showed a local minimum in NO (392 μM) at about 150 m on the 27.8 σ-horizon, corresponding to an R_ρ value between 0.4 and 0.5 (Figures 5e–5g, red profiles). The rather small stratification between the base of the mixed layer and the 27.8 σ-horizon suggests a former deep winter mixed layer. Note that the same NO value (about 392 μM) is also found on the same σ-horizon (27.8 kg·m^{-3}) in the TPD in the Amundsen Basin and in Fram Strait (Figure 2e).

Back trajectories were performed from a region well documented by IAOOS23 during its meandering path from the end of July to mid-December (83–85°N;10–30°E) at different depths and starting at different times (every 5 days from 1 August to 15 December) (examples in Figures 6d–6f). Model back trajectories at 5 m suggested contributions from low-salinity shelf waters (Kara and Barents Seas) moving offshore (Figure 6d). This indicated capping with relatively low salinity water. Away from the continental slope and below the near-surface waters, upper layer velocities were small in the Nansen Basin (Figure 3b), and 3-year-long back trajectories were rather short (Figure 6e). Upper layer water parcels had been in the region for several years and could be traced back to the continental slopes in general with time scales equal to or larger than 3 years (not shown).

In the AW layer of the Nansen Basin, model back trajectories indicated contributions from recirculating AW from western Nansen Basin and new AW from Fram Strait (Figure 6f). The contribution of AW from the south (from Yermak Plateau and western Fram Strait) was larger in December than in previous months (not shown). The slight differences observed in the AW characteristics before and after the end of November (yellow and orange dots in Figure 4) could be associated with the circulation change.

4.3. Halocline Strength

The halocline depth H_{halo}, taken as the depth of the 27.85 isopycnal, varied from about 200 m in Amundsen Basin to 150 m in Nansen Basin (Figure 7a). The halocline eddies HE1 and HE2 encountered in Amundsen Basin (Figure 1c) led to a shoaling of the mixed layer there and a deepening of the base of the halocline and resulted in a halocline thickness of 180 m, the largest encountered during the drift. The smallest H_{halo} was encountered above the two AW mesoscale structures AW1 and AW2 crossed in Nansen Basin (Figure 7a). The depth of the cold halocline, that is, the depth of isopycnal 27.6 kg·m^{-3}, was about 120 m in Amundsen Basin. There was no cold halocline in Nansen Basin where the 27.6 kg·m^{-3} isopycnal shoaled to the depth of the mixed layer (~30 m).

Missing density data in the mixed layer were interpolated using an iterative neighboring approach (Figure 7b), and the strength of the halocline layer was estimated with the APE (section 2.2), a measure of stratification over the whole halocline (from isopycnal 27.85 kg·m^{-3} to the surface) and over the cold halocline (from isopycnal 27.6 kg·m^{-3} to the surface) (Figure 7d). The strength of the whole halocline ranged from values above 6×10^4 J·m^{-2} in Amundsen Basin to less than 0.8×10^4 J·m^{-2} in the Nansen Basin (Figure 7e). At the exit of the TPD in Fram Strait, the APE increased to values above Nansen Basin values but still lower than Amundsen Basin values. The strength of the cold halocline was about half that of the whole halocline and zero in Nansen Basin.

For the sake of comparison, we computed APE from the colocalized model density along the drift (Figure 7c). The depths of the 27.85 and 27.6 isopycnals along the drift compared rather well to observations (Figures 7a and 7b). The model was rather good at representing the temperature and salinity fields as shown in Athanase et al. (2019). However, the frontal region between the fresher Canadian waters and saltier Eurasian waters was represented too further west by about 20° at the time of the buoy drift (April–May). This salinity bias translated into a σ difference of 2 kg·m^{-2} in the upper 50 m in the frontal region (Figure 7d). As a result, the maximum difference in APE between model and observations, reached in the frontal region, was about 3×10^4 J·m^{-2} (Figure 7e).

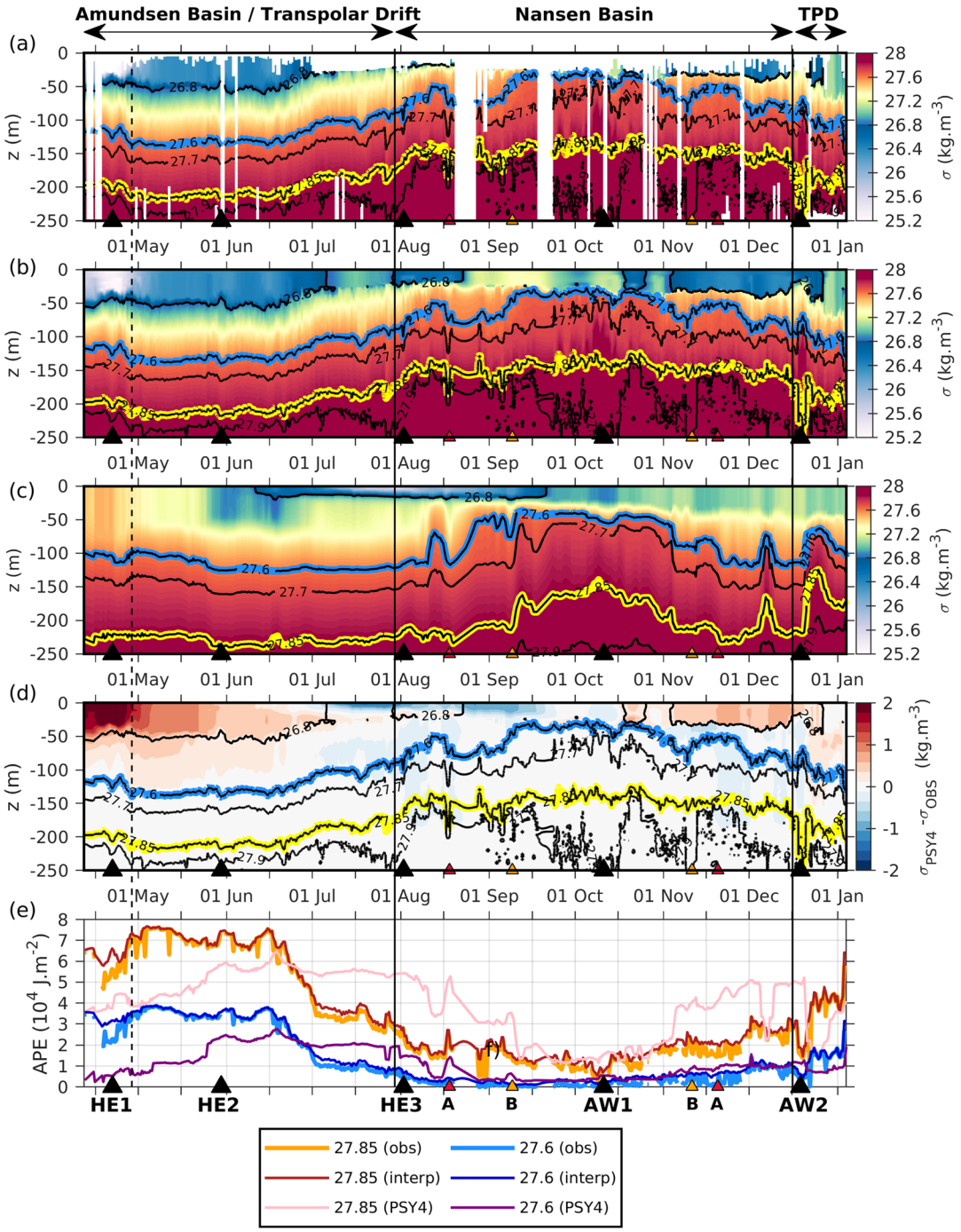

Figure 7. Potential density along the drift trajectory: (a) from observations and (b) from observations interpolated to the surface (c) from PSY4 (x axis is time, and y axis is depth, isopycnals 27.6 and 27.85 kg·m^{-3} in blue and yellow). (d) Differences between model outputs and observations of potential density. Isopycnals are from observations. (e) Available potential energy (APE, 10^4 J·m^{-2}) calculated from isopycnals 27.85 and 27.6 kg·m^{-3} from observations (orange and light blue), observations interpolated to the surface (red and dark blue) and from PSY4 (pink and purple). Triangles mark positions of halocline eddies (HE1, HE2, and HE3), Atlantic water mesoscale structures (AW1 and AW2), and two crossover points A and B.

The modeled yearly mean APE over the drift region (Figure 8a) provided the spatial distribution of APE over the drift area and showed a maximum difference of less than 2×10^4 J·m^{-2} in the frontal region in the Amundsen region. The modeled mean APE ranged from 0 in the eastern Nansen Basin to 60×10^4 J·m^{-2}

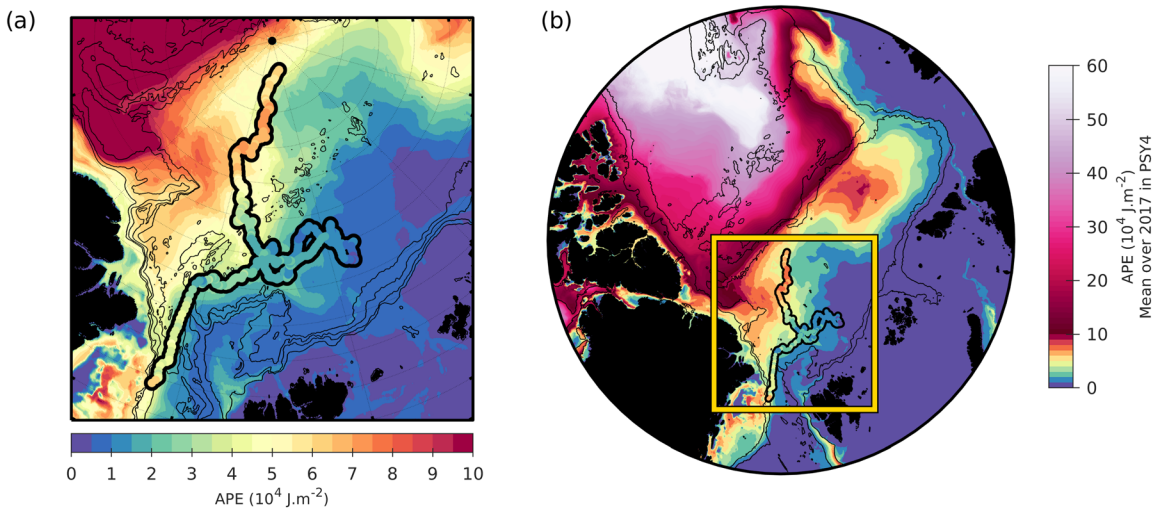

Figure 8. (a) Annual mean model halocline strength (APE from isopycnal 27.85 to the surface) in 2017 and halocline strength along the trajectory from observations. (b) Same as a on a larger Arctic domain.

in the Beaufort gyre region (Figure 8b). The panarctic values are comparable to those estimated in Polyakov et al. (2018). The APE range in the drift area is comparably small (0 to 7 × 10^4 J·m^{-2}).

5. Discussion

5.1. Limitation in NO Estimates and Inferences From Back Trajectories

NO profiles varied over a limited range from 375 to 404 μM compared to the accuracy in NO absolute values in the absence of concomitant bottle data for calibration (cf. Appendix A). However, NO values provided consistent evolution both in time and space (vertical and horizontal) suggesting a high reliability of relative values. It is remarkable that NO values from the TPD in Amundsen and in Fram Strait match each other so well (red and blue dots in Figure 4e) in spite of their differences in NO_3 and DO concentration (Figures 4b and 4c).

While back trajectories should be considered with caution and not over interpreted, they still provide valuable suggestions. Model skills were illustrated through comparisons to IAOOS23 observations (Athanase et al., 2019) with in particular AW1 and AW2 quite well reproduced in characteristics including location and time. However, as no ocean data besides sea ice concentration are assimilated in the ice-covered ocean, we cannot expect mesoscale features to closely match observations in time and space. We performed 2-D back trajectories until January 2014 and obtained consistent results with different starting boxes and different starting times.

5.2. NO Minimum on the 27.8 σ-Horizon

The NO minimum in the LHW (on the 27.8 σ-horizon) in the Nansen Basin (SA of 34.8 g·kg^{-1}, CT about 0°C) is arguably formed with the mechanism initially proposed by Rudels et al. (1996), that is, successive winter deep mixed layers and summer phytoplankton blooms. The upper part of the water column undergoes convective mixing through cooling and brine release during sea ice winter formation creating a winter mixed layer. Later, phytoplankton blooms remove NO_3, and summer temperatures degas the excess DO to the atmosphere. Subsequent winter mixed layer convection homogenizes and replenishes with some (although less and less) nitrate. NO diminishes in the upper layer. Starting with NO_3 concentrations of 6.7 mmol·kg^{-1} and NO value of 408 mmol·kg^{-1} (DO = 350 mmol·kg^{-1}), Rudels et al. (1996) estimated that 3 years were necessary to reach NO values of 385 mmol·kg^{-1} (comparable to the values observed here). Here in Nansen Basin, the stratification is small between the summer mixed layer and the 27.85 σ-horizon. The NO minimum probably lies at the base of a previous deep winter mixed layer.

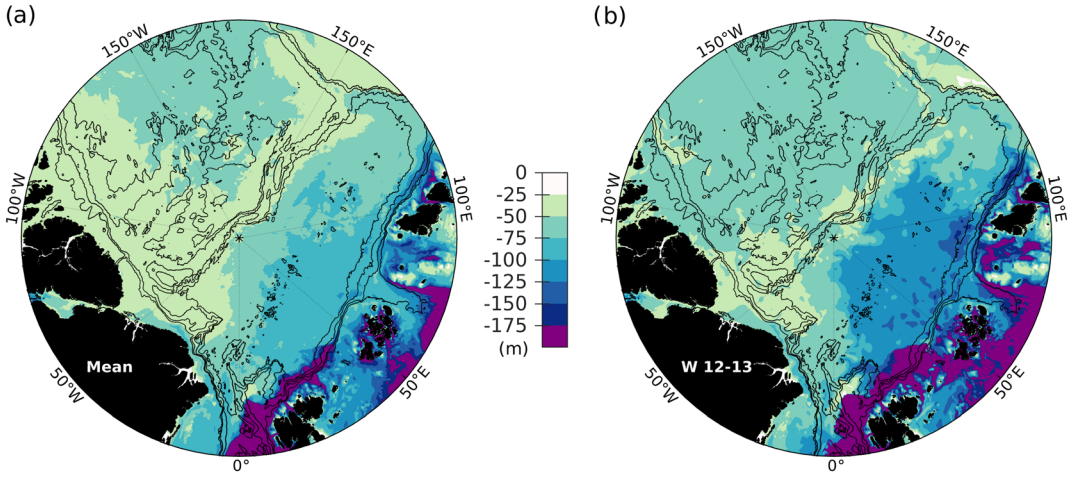

Figure 9. (a) Maxima of winter mixed layer depths from PSY4 averaged over 2007–2017 (in m). (b) Maxima of mixed layer depths during winter 2012–2013.

Over 2007–2017, the modeled winter mixed layers reached depths in excess of 100 m in western Nansen Basin with particularly large values north of Svalbard where winter ventilation often reached deeper than 200 m (Figure 9a). In particular, the model showed wide spread deep mixed layers along the continental slope in winter 2012–2013, with depths similar to those documented at 30°E that winter (e.g., Pérez-Hernández et al., 2019) (Figure 9b). According to the model, these were the deepest winter mixed layers found in that region over the last 10 years. Model results suggested advective pathways from the slope to the inner Nansen Basin in the layer 30–140 m with time scales larger than 3 years (section 4.2). Model mixed layer depths, advective pathways, and time scales were consistent with the observed NO minimum and the NO minimum formation process described by Rudels et al. (1996).

Note that the minimum in NO on the 27.8 σ-horizon corresponds to a local maximum in CDOM (2.4 ppb) below the very low CDOM values in the Nansen Basin halocline (Figure 2f). Nansen Basin halocline is not fed with CDOM-loaded waters from Siberian shelves, and the autochthonous CDOM resulting from primary production is subject to removal processes. There are four major CDOM removal processes: fractionation during sea ice formation, flocculation, microbial degradation, and photochemical degradation (Stedmon et al., 2011). While they are all likely to contribute to the very low CDOM values in the Nansen Basin halocline, their relative importance is uncertain.

5.3. NO Minimum Centered on the 27.4 σ-Horizon

The NO minimum ranging from 375 to 385 μM centered on the 27.4 σ-horizon (around 100-m depth) (Figure 4e) was found at the base of fresh (SA < 33 g·kg^{-1}) waters at close to freezing temperatures with a high CDOM content (CDOM > 3.60 ppb) (Figure 2). The NO minimum was traced back to the slope of the East Siberian Sea with an advective time scale of about 1.5 to 2 years at 70-m depth (Figure 6a). The ocean pathways of Eurasian runoff are modulated by the Arctic Oscillation (Morison et al., 2012). In a period of cyclonic wind regime (positive phase of the Arctic Oscillation), the Siberian runoff is diverted by eastward winds toward the Makarov Basin, and the ocean TPD originates from the East Siberian Seas. Since 2015, a positive Arctic Oscillation index has prevailed (e.g., https://www.cpc.ncep.noaa.gov/products/precip/CWlink/daily_ao_index/month_ao_index.shtml), and the upper ocean mean flow in Mercator Ocean system has shown large velocities from the East Siberian Seas toward the North Pole (e.g., Figures 3a–3c). East Siberian shelf waters have been advected to Amundsen Basin and have been ventilating the Eurasian Arctic Halocline. These waters typically exhibit low NO values because of reduced DO concentrations (Figure 4b) due to remineralization of allochthonous organic matter in both dissolved and particulate forms (Alkire et al., 2010; Alkire et al., 2019; Anderson et al., 2017).

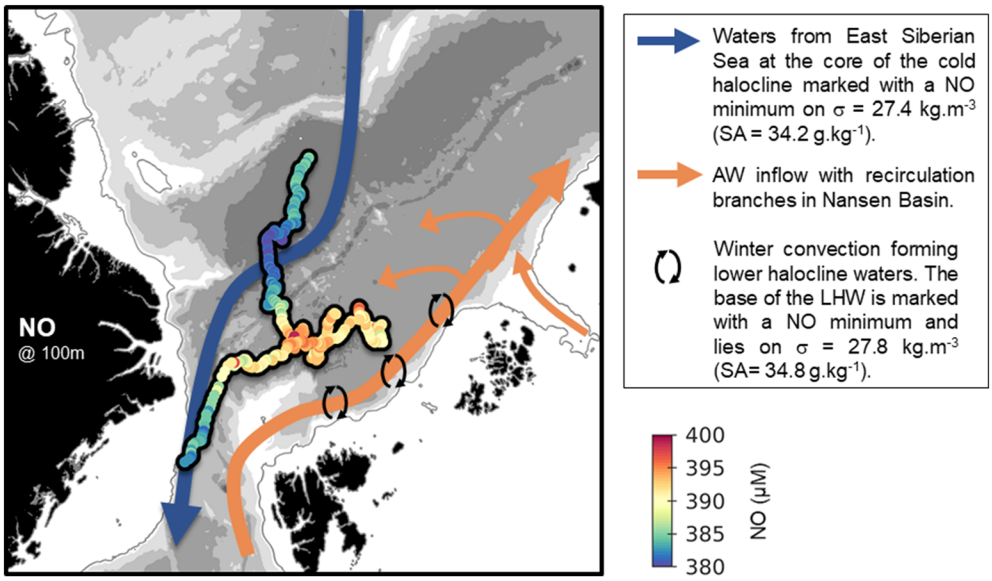

Figure 10. NO concentration at 100 m along the drift and schematics of processes associated with NO distribution. The 100-m depth is close to the core of the cold halocline in Amundsen Basin and to the base of the lower halocline in Nansen Basin (Figure 2e). The NO minimum (380 μM) in the TPD results from advection of low NO waters (depleted in DO) from the East Siberian Seas contributing to the cold halocline on σ-horizon 27.4 (SA = 34.2 g·kg^{-1}). The relatively low NO values (390 μM) in Nansen Basin mark the base of the lower halocline. The lower halocline waters, which are formed through deep convection along the path of the Atlantic water inflow, now reach σ-horizon 27.85 (SA = 34.9 g·kg^{-1}).

5.4. Definition of the Base of the Halocline of LHW in a Period of Atlantification

In section 2.2, we recalled the two criteria that are commonly used for defining the base of the lower halocline: the depth of the 34.3 psu (SA = 34.46 g·kg^{-1}) isohaline (Rudels et al., 1996) and the depth where the density ratio R_ρ reaches 0.05 (Bourgain & Gascard, 2011). Those two criteria are not appropriate anymore to define the base of the lower halocline in a period of strong Atlantification (Polyakov et al., 2017). Winter mixed layers in parts of Nansen Basin now regularly reach 150 m depth (Figures 8a and 8b) and homogenize the water column down to a density of 27.85 kg·m^{-3} and a salinity of 34.9 g·kg^{-1}. Winter mixed layers of 150 m depth or more have been observed along the continental slope at different longitudes (e.g., Pérez-Hernández et al., 2019; Polyakov et al., 2017). Atlantification resulted in a salinification of the mixed layer in Nansen Basin. A more appropriate criterion for H_{halo} would be the depth of the SA = 34.9 g·kg^{-1} isohaline.

The behavior of the density ratio changed from Amundsen Basin to Nansen Basin due to increasing vertical temperature gradients combined with lower vertical salinity gradients in Nansen Basin (Figures 5a, 5b, and 5d). In Nansen Basin, a large range of R_ρ was observed between isopycnals 27.6 and 27.7 kg·m^{-3} ($0 < R_\rho < 0.5$). R_ρ was not an appropriate criterion in Nansen Basin. In the TPD, in Amundsen Basin and Fram Strait, an R_ρ of 0.05 corresponded to the NO minimum and isopycnal 27.4 kg·m^{-3} (Figures 5e–5g).

Our APE estimates were similar to those of Polyakov et al. (2018) in spite of their smaller H_{halo} estimate from using the $R_\rho = 0.05$ criterion. Indeed, if H_{halo} is sensitive to the used criterion, stratification is not, as the most important contributions to APE come from the upper and cold halocline (stratification is weak in LHW). Preliminary accuracy estimates suggest that the model may be a good tool to monitor changes in APE. This needs to be further investigated.

6. Summary and Conclusions

We examined the halocline in the western Eurasian Basin using the first autonomous NO measurements and outputs from an operational physical model. Both approaches were complementary and insightful despite their respective limitations (section 5.1). Figure 10 summarizes our findings.

The IAOOS23 platform was deployed on a floe near the North Pole within the TPD on 12 April 2017. In the TPD, halocline waters comprised waters from the East Siberian Seas and were characterized with a NO minimum of 380 μM on the σ-horizon 27.4 kg·m^{-3} (SA = 34.2 g·kg^{-1}) and high CDOM values (range 3 to 4 ppb). The NO minimum was likely caused by reduced DO concentrations because of remineralization on the shelves, while the large CDOM concentrations resulted from Siberian runoff. The runoff and upper layer ocean pathways were expected from the prevailing positive phase of the Arctic Oscillation (Morison et al., 2012).

The platform left the TPD in August 2017 when winds from the south and from the west pushed the ice toward the east. It then sampled the upper layer from the inner Nansen Basin. Stratification at the base of the summer mixed layer in Nansen Basin was strong due to surface warming and sea ice melt (impeding the profiler to ascend into the mixed layer), and velocities below the summer mixed layer were decoupled from ice drift velocities. The change in stratification, CDOM, and NO at the exit of the TPD was stark: the weak stratification below the summer mixed layer until σ-horizon 27.85 was associated with convective winter mixed layer depths. The LHW convective formation mechanism, called "basin-derived" in Alkire et al. (2017), occurred down to isopycnal 27.85 which was marked with a consistent light NO minimum. The NO minimum at the base of the lower halocline is likely formed according to the coupled biogeochemical process described in Rudels et al. (1996). The depths of the winter mixed layers in Nansen Basin have increased, and the convective layers now reach salinity of 34.9 which marks the limit of the weak lower halocline. The 34.3 psu (SA = 34.46 g·kg^{-1}) isohaline which formerly indicated the base of the lower halocline (Rudels et al., 1996) is now located at the base of the cold halocline (27.6 kg·m^{-3}) in Amundsen Basin.

Autonomous NO measurements were shown to be factible, and conservation of NO parameter at depth was a useful constraint in controlling potential sensor drift (see Appendix A). NO proved to be a useful indicator of halocline structure despite our fragmentary documentation of ocean biogeochemistry in the Arctic. However, a better understanding of Arctic Ocean sources and sinks of nitrate (e.g., Alkire et al., 2019; Chang & Devol, 2009; Gihring et al., 2010) is needed for a quantitative assessment of the halocline water mass composition.

We followed Polyakov et al. (2018) and computed APE as a measure of the strength of the halocline along the drift. The halocline strength was extremely weak in Nansen Basin as a result of Atlantification. Mercator physical system provided reasonable APE estimates. It is important to further assess model skills in monitoring APE in these regions where data gathering requires substantial resources and efforts.

Appendix A: NO_3 and DO Validation and NO Estimates

The ocean profiler on IAOOS23 equipped with a Submersible Ultraviolet Nitrate Analyzer (SUNA) and a DO Aandera 4340 optode was set to perform two profiles a day with measurements on the way up starting from the bottom (250 m).

There was no bottle data and no postdrift calibration as the profiler was lost over shallow topography in Fram Strait. Instrumental drift was evaluated by examining values at 240 m depth and differences at the crossover points visited at different times (e.g., Points A and B in Figure 1a) (see supporting information in Boles et al., 2020). Remarkably little instrumental drift occurred over the 8-month period, except possibly for nitrate concentrations which exhibit a sudden jump of +1.53 ± 0.15 μM on 5 November and return to values prior to the jump by 25 December (Boles et al., 2020). In the absence of contemporaneous bottle data, we used chemistry data from North Pole Earth Observatory (NPEO) from previous years (Falkner et al., 2009) available online (https://arcticdata.io/catalog/view/doi:10.18739/A27H1DK9T).

The SUNA provided both computed nitrate concentrations and absorbance spectra. Nitrate concentrations were recalculated from the spectra using small adjustments in the optical wavelength offset parameter, typically in the range from 206 to 212 nm following the ARGO DAC protocol (Johnson et al., 2018) and compared to the sensor-provided nitrate profiles (SUNA) and to several NPEO profiles (ISUS instrument calibrated with bottle measurements) made in the same area (Figure A1, left panel). The change of the optical wavelength offset parameter led to a shift of nitrate concentrations (Figure A1, left panel). Nitrate concentrations computed with λ = 210 nm were close to those obtained directly from the SUNA sensor. We

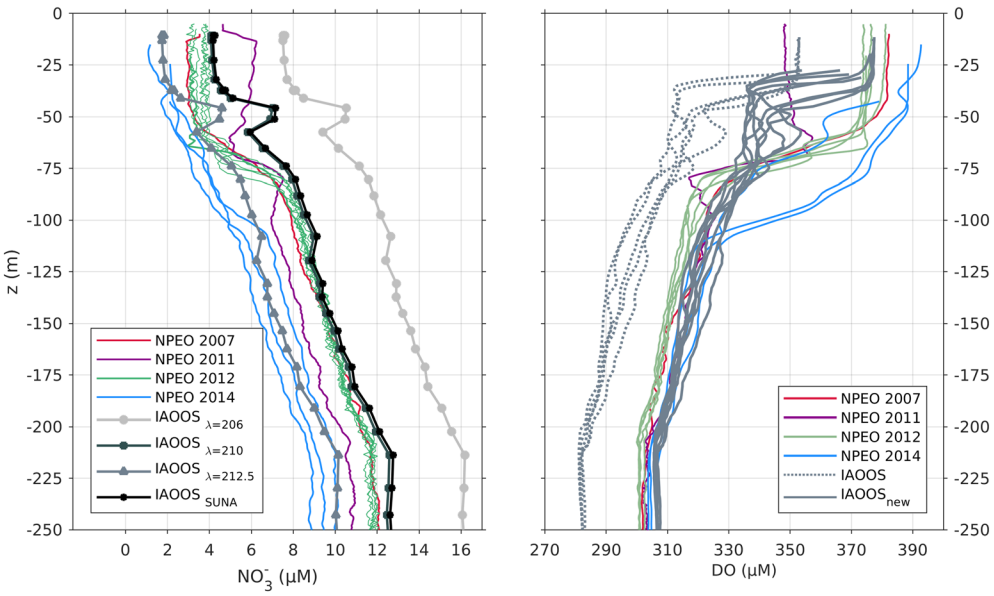

Figure A1. (left) Nitrate concentrations computed from spectrum with three wavelength offsets (206, 210, and 212.5 nm) and directly obtained from SUNA (thick gray and black lines) and from NPEO (ISUS calibrated with bottle measurements) at Barneo site near the North Pole (different years in color) (http://psc.apl.washington.edu/northpole/). (right) Dissolved oxygen concentrations from IAOOS23 in gray (dotted line: raw, solid line: adjusted) and DO from NPEO measurements near the North Pole (different years in color).

chose to use nitrate concentrations computed from spectrum with $\lambda = 212.5$ nm which provided values comparable to NPEO data (Figure A1, left panel).

DO concentrations were retrieved following Thierry et al. (2016). Apparent oxygen utilization (AOU) was computed and compared to AOU derived from DO bottle measurements from NPEO. Comparisons suggested a systematic offset of 25 µM, which was corrected (Athanase et al., 2019). DO concentrations were then recalculated from the corrected AOU (Figure A1, right).

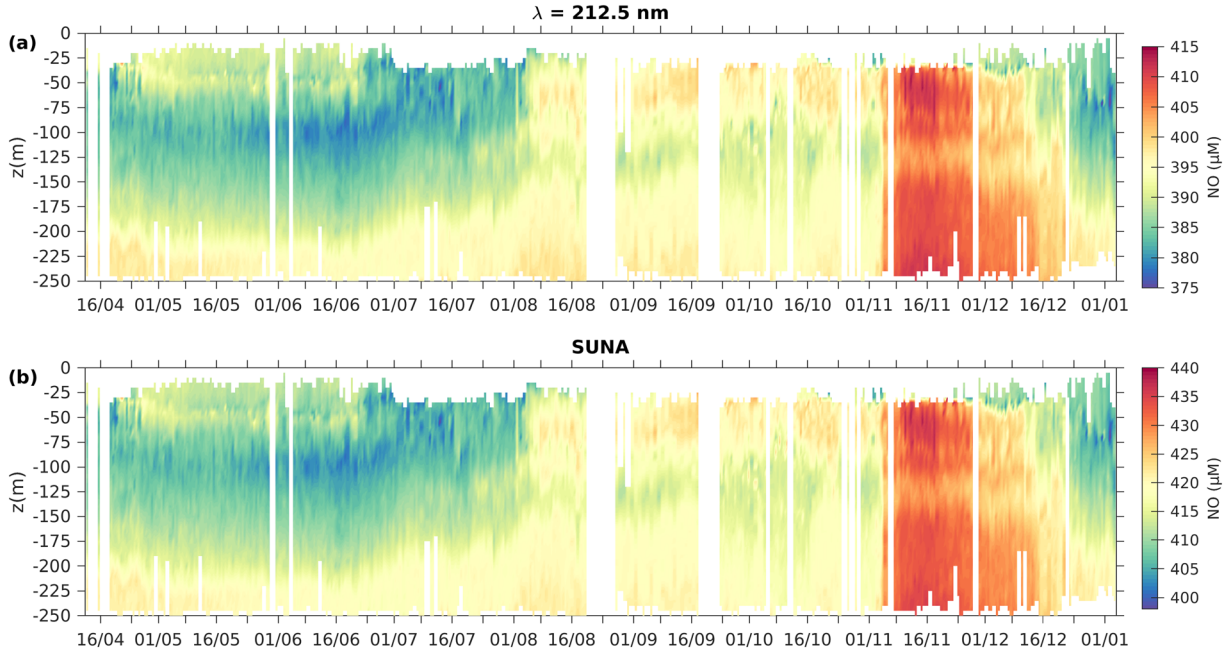

Figure A2. NO parameter along the drift using nitrate concentrations: (a) calculated from spectrum (with a 212.5-nm offset) and (b) from SUNA data. Vertical structure and time evolution do not change. Values are globally shifted by 22 to 25 µM.

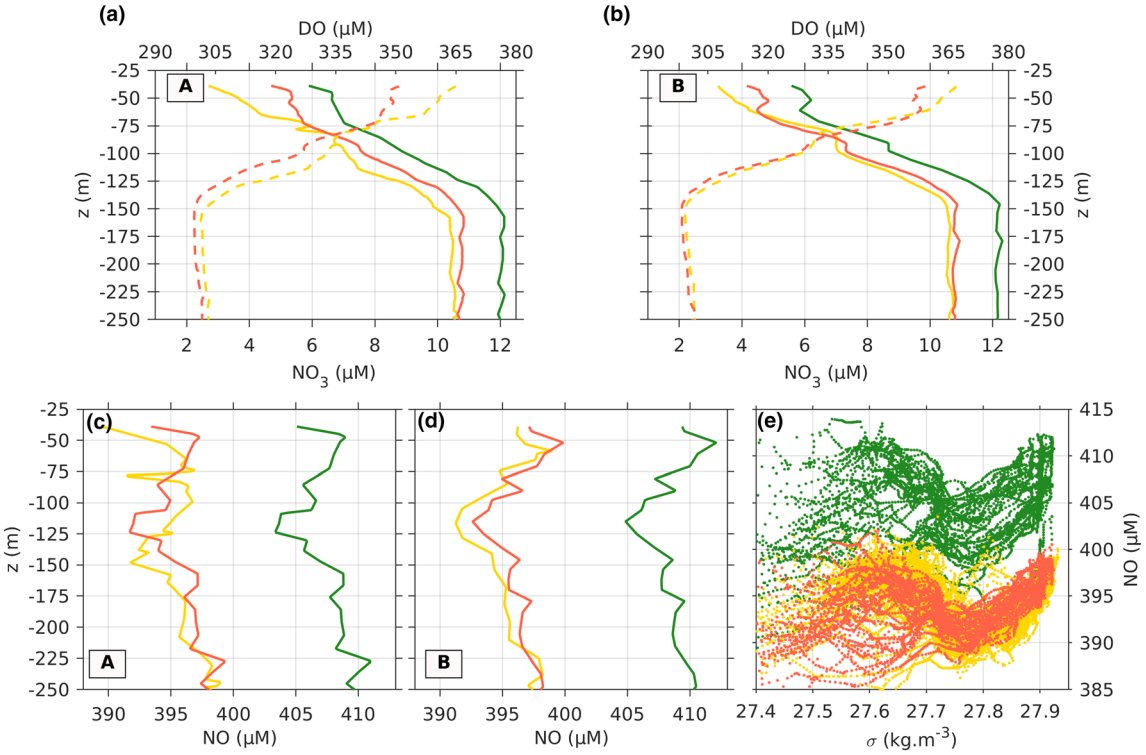

Figure A3. (a) DO (dashed lines) and NO_3 (solid lines) profiles at crossover point A (18 August in yellow and 20 November in green before correction and orange after correction). (b) Same as (a) for the Crossing Point B (9 September and 11 November). (c) NO profiles at Location A on 18 August (yellow) and on 20 November (green before correction and orange after correction). (d) Same as (c) at Location B. (e) NO-σ diagram for all profiles in Nansen Basin between 1 August to 20 December (same color code as Figure 4e) (yellow profiles unchanged and green profiles corrected to orange).

DO and nitrate concentrations were used to compute the NO parameter $NO = 9 \times [NO_3] + [O_2]$. The adjustment for calibration of nitrate and DO concentrations resulted in shifts between 21 and 24 µM in NO which did not change either NO time evolution or NO vertical structure. In particular, the depths of NO minima were conserved (Figure A2).

Boles et al. (2020) suggested that nitrate concentration values after 5 November should be used with caution as they exhibited a sudden jump of $+1.53 \pm 0.15$ µM on 5 November throughout the sampled water column. Nitrate concentration values returned to values prior to the jump after 25 December, after the profiler crossed a swift current associated with a recirculating branch of the West Svalbard Current labeled as AW2 in Figure 1a (Athanase et al., 2019). The nitrate concentration jump from 5 November to 25 December translated into suspiciously large NO values (Figure A2). As large spikes were observed in the backscatter starting in October (Boles et al., 2020), the vertically constant jump (caused by lower absorption values in the SUNA spectra) could be due to an aggregate of sinking algal matter dimming the SUNA window until it was washed away by the strong currents associated with AW2.

We tentatively corrected the NO_3 values during the jump, considering that NO was conserved at depth. The correction is detailed for Points A and B that were sampled two times, before and after the "nitrate jump": A on 18 August and 20 November and B on 9 September and 11 November (Figures 1a, A2, and A3). The corrected NO_3 values (orange solid lines in Figures A3a and A3b) were slightly larger than the nitrate concentration measured during the first crossing (yellow solid lines in Figures A3a and A3b) in agreement with slightly diminished DO concentration (dashed lines in Figures A3a and A3b).

NO parameter conservation at depth was an interesting constraint.

Data Availability Statement

IAOOS23 data and NPEO chemistry data can be found online (10.17882/59183 and https://arcticdata.io/catalog/view/doi:10.18739/A27H1DK9T, respectively).

Acknowledgments

We are deeply grateful to the many people who participated in the development and tests of the biogeochemical profiler at Ifremer facilities in Brest (France) and during the N-ICE 2015 ice camp from RV *Lance* north of Svalbard: Magali Garracio, Antoine Guillot, Christine Drezen, Michel Calzas, Nicolas Villacieros Robineau, Jean-Philippe Savy, and Victoire Rérolle. We thank Zoé Koenig, Matthieu Labaste, Victoire Rérolle, and Sergey Pisarev for their contribution to the preparation and deployment of the IAOOS platforms from the North Pole in April 2017. Magali Garracio was essential to the data recovery and decoding processes. Discussions with Catherine Schmechtig and Paul Dodd on the data processing and Véronique Garçon on the manuscript are gratefully acknowledged. The development and field work were funded through the ANR EQUIPEX IAOOS project through ANR-10-EQX-611 32-01 grant and the ICE-ARC program from the European Union 7th framework programme, Grant 603887. Elisabeth Boles and Marylou Athanase were supported through the Pan Arctic Options Belmont Forum project (ANR-14-AORS-003-01). Cecilia Bertosio was supported through IAOOS Grant S18JROI002 at Sorbonne University.

References

Alkire, M. B., Falkner, K. K., Morison, J., Collier, R. W., Guay, C. K., Desiderio, R. A., et al. (2010). Sensor-based profiles of the NO parameter in the central Arctic and southern Canada Basin: New insights regarding the cold halocline. *Deep Sea Research, Part I*, *57*(11), 1432–1443. https://doi.org/10.1016/j.dsr.2010.07.011

Alkire, M. B., Falkner, K. K., Rigor, I., Steele, M., & Morison, J. (2007). The return of Pacific waters to the upper layers of the central Arctic Ocean. *Deep Sea Research, Part I*, *54*(9), 1509–1529. https://doi.org/10.1016/j.dsr.2007.06.004

Alkire, M. B., Morison, J., & Andersen, R. (2015). Variability and trends in the meteoric water, sea-ice melt, and Pacific water contributions to the central Arctic Ocean, 2000–2013. *Journal of Geophysical Research: Oceans*, *120*, 1573–1598. https://doi.org/10.1002/2014JC010023

Alkire, M. B., Polyakov, I., Rember, R., Ashik, I. M., Ivanov, V., & Pnyushkov, A. V. (2017). Lower halocline water formation and modification, a comparison of physical and geochemical methods. *Ocean Science*, *13*(6), 983–995. https://doi.org/10.5194/os-13-983-2017

Alkire, M. B., Rember, R., & Polyakov, I. (2019). Discrepancy in the identification of the Atlantic/Pacific front in the central Arctic Ocean: NO versus nutrient relationships. *Geophysical Research Letters*, *46*, 3843–3852. https://doi.org/10.1029/2018GL081837

Anderson, L. G., Andersson, P. S., Björk, G., Jones, E. P., Jutterström, S., & Wåhlström, I. (2013). Source and formation of the upper halocline of the Arctic Ocean. *Journal of Geophysical Research: Oceans*, *118*, 410–421. https://doi.org/10.1029/2012JC008291

Anderson, L. G., Björk, G., Holby, O., Jutterström, S., O'Regan, C. M., & Pearce, I. (2017). Shelf-basin interaction along the Laptev-East Siberian Sea. *Ocean Science*, *13*(2), 349–363. https://doi.org/10.5194/os-13-349-2017

Athanase, M., Sennéchael, N., Garric, G., Koenig, Z., Boles, E., & Provost, C. (2019). New hydrographic measurements of the upper Arctic western Eurasian Basin in 2017 reveal fresher mixed layer and shallower warm layer than 2005–2012 climatology. *Journal of Geophysical Research: Oceans*, *124*, 1091–1114. https://doi.org/10.1029/2018JC014701

Boles, E., Provost, C., Garçon, V., Koenig, Z., Bertosio, C., Athanase, M., & Sennéchael, N. (2020). Under-ice phytoplankton blooms in the central Arctic Ocean: Insights from the first biogeochemical IAOOS platform drift in 2017. *Journal of Geophysical Research: Oceans*, *125*, e2019JC015608. https://doi.org/10.1029/2019JC015608

Bourgain, P., & Gascard, J. C. (2011). The Arctic Ocean halocline and its interannual variability from 1997 to 2008. *Deep Sea Research, Part I*, *58*(7), 745–756. https://doi.org/10.1016/j.dsr.2011.05.001

Bourgain, P., Gascard, J. C., Shi, J., & Zhao, J. (2013). Large-scale temperature and salinity changes in the Canadian Basin of the Arctic Ocean at a time of a drastic Arctic Oscillation inversion. *Ocean Science*, *9*(2), 447–460. https://doi.org/10.5194/os-9-447-2013

Broecker, W. S. (1974). "NO": A conservative water mass tracer. *Earth and Planetary Science Letters*, *23*(1), 100–107. https://doi.org/10.1016/0012-821X(74)900036-3

Chang, B., & Devol, A. (2009). Seasonal and spatial patterns of sedimentary denitrification rates in the Chukchi Sea. *Deep Sea Research, Part II*, *56*(17), 1339–1350. https://doi.org/10.1016/j.dsr2.2008.10.024

Falkner, K. K., Collier, R., & Alkire, M. (2009). North Pole Environmental Observatory ISUS nitrate data. Arctic data Center. https://doi.org/10.18739/A27H1DK9T

Fillipi, J.-B., Komatsu, T., & Tanaka, K. (2010). Simulation of drifting seaweeds in East China Sea. *Ecological Informatics*, *5*(1), 67–72. https://doi.org/10.1016/j.ecoinf.2009.08.011

Gihring, T. M., Lavik, G., Kuypers, M. M., & Kostka, J. E. (2010). Direct determination of nitrogen cycling rates and pathways in Arctic fjord sediments (Svalbard, Norway). *Limnology and Oceanography*, *55*(2), 740–752. https://doi.org/10.4319/lo.2010.55.2.0740

Ivanov, V., Smirnov, A., Alexeev, V., Koldunov, N. V., Repina, I., & Semenov, V. (2018). Contribution of convection-induced heat flux to winter ice decay in the western Nansen Basin. *Journal of Geophysical Research: Oceans*, *123*, 6581–6597. https://doi.org/10.1029/2018JC013995

Johnson, K., Pasqueron de Fommervault, O., Serra, R., D'Ortenzio, F., Schmechtig, C., Claustre, H., & Poteau, A. (2018). Processing Bio-Argo nitrate concentration at the DAC Level. Argo data management. https://doi.org/10.13155/46121

Jones, E. P., & Anderson, L. G. (1986). On the origin of the chemical properties of the Arctic Ocean halocline. *Journal of Geophysical Research*, *91*(C9), 10,759–10,767. https://doi.org/10.1029/JC091iC09p10759

Kikuchi, T., Hatakeyama, K., & Morison, J. H. (2004). Distribution of convective lower halocline water in the eastern Arctic Ocean. *Journal of Geophysical Research*, *109*, C12030. https://doi.org/10.1029/2003JC002223

Kipp, L. E., Charette, M. A., Moore, W. S., Henderson, P. B., & Rigor, I. G. (2018). Increased fluxes of shelf-derived materials to the central Arctic Ocean. *Science Advances*, *4*(1), eaaO1302. https://doi.org/10.1126/sciadv.aao1302

Koenig, Z., Provost, C., Sennéchael, N., Garric, G., & Gascard, J. C. (2017). The Yermak Pass Branch: A major pathway for the Atlantic water north of Svalbard? *Journal of Geophysical Research: Oceans*, *122*, 9332–9349. https://doi.org/10.1002/2017JC013271

Koenig, Z., Provost, C., Villacieros-Robineau, N., Sennéchael, N., Meyer, A., Lellouche, J.-M., & Garric, G. (2017). Atlantic waters inflow north of Svalbard: Insights from IAOOS observations and Mercator Ocean global operational system duringN-ICE2015. *Journal of Geophysical Research: Oceans*, *122*, 1254–1273. https://doi.org/10.1002/2016JC012424

Lellouche, J. M., Greiner, E., Le Galloudec, O., Garric, G., Regnier, C., Drévillon, M., et al. (2018). Recent updates on the Copernicus Marine Service global ocean monitoring and forecasting real-time 1/12° high resolution system. *Ocean Science*, *14*(5), 1093–1126. https://doi.org/10.5194/os-14-1093-2018

Morison, J., Kwok, R., Peralta-Ferriz, C., Alkire, M., Rigor, I., Andersen, R., & Steele, M. (2012). Changing Arctic Ocean freshwater pathways. *Nature*, *481*(7379), 66–70. https://doi.org/10.1038/nature10705

Pérez-Hernández, M. D., Pickart, R. S., Torres, D. J., Bahr, F., Sundfjord, A., Ingvaldsen, R., et al. (2019). Structure, transport, and seasonality of the Atlantic water boundary current north of Svalbard: Results from a yearlong mooring array. *Journal of Geophysical Research: Oceans*, *124*, 1679–1698. https://doi.org/10.1029/2018JC014759

Polyakov, I. V., Pnyushkov, A. V., & Carmack, E. C. (2018). Stability of the Arctic halocline: A new indicator of arctic climate change. *Environmental Research Letters*, *13*(12), 125,008. https://doi.org/10.1088/1748-9326/aaecle

Polyakov, I. V., Pnyuskov, A. V., Alkire, M. B., Ashik, I. M., Baumann, T. M., Carmack, E. C., et al. (2017). Greater role for Atlantic inflows on sea ice loss in the Eurasian Basin of the Arctic Ocean. *Science*, *356*(6335), 285–291. https://doi.org/10.1126/science.aai8204

Provost, C., Sennéchael, N., Garçon, V., Boles, E., Athanase, M., Koenig, Z., & Labaste, M. (2017). Arctic western Eurasian Basin: IAOOS 23 physical and biogeochemical profiles in 2017. *SEANOE*. https://doi.org/10.17882/59183

Rudels, B., Anderson, L. G., & Jones, E. P. (1996). Formation and evolution of the surface mixed layer and halocline of the Arctic Ocean. *Journal of Geophysical Research*, *101*(C4), 8807–8821. https://doi.org/10.1029/96JC00143

Rudels, B., Jones, E. P., Schauer, U., & Eriksson, P. (2004). Arctic sources of the Arctic Ocean surface and halocline waters. *Polar Research*, *23*(2), 181–208. https://doi.org/10.1111/j.1751-8369.2004.tb00007.x

Shimada, K., Itoh, M., Nishino, S., McLaughlin, F., Carmack, E., & Proshutinsky, A. (2005). Halocline structure in the Canada Basin of the Arctic Ocean. *Geophysical Research Letters*, *32*, L03605. https://doi.org/10.1029/2004GL021358

Stedmon, C. A., Amon, R. M. W., Rinehart, A. J., & Walker, S. A. (2011). The supply and characteristic of Colored dissolved organic matter (CDOM) in the Arctic Ocean: Pan Arctic trends and differences. *Marine Chemistry*, *124*(1-4), 108–118. https://doi.org/10.1016/j.marchem.2010.12.007

Steele, M., & Boyd, T. (1998). Retreat of the cold halocline layer in the Arctic Ocean. *Journal of Geophysical Research*, *103*(C5), 10,419–10,435. https://doi.org/10.1029/98JC00580

Steele, M., Morison, J., Ermold, W., Rigor, I., Ortmeyer, M., & Shimada, K. (2004). Circulation of summer Pacific halocline water in the Arctic Ocean. *Journal of Geophysical Research: Oceans*, *109*, C02027. https://doi.org/10.1029/2003JC002009

Thierry, V., Bittig, H., Gilbert, D., Kobayashi, T., Sato, K., & Schmid, C. (2016). Processing Argo OXYGEN data at the DAC level, v2.2. https://doi.org/10.13155/39795

Timmermans, M.-L., Marshall, J., Proshutinsky, A., & Scott, J. (2017). Seasonally derived components of the Canadian Basin halocline. *Geophysical Research Letters*, *44*, 5008–5015. https://doi.org/10.1002/2017GL073042

Chapter III

Freshwater distribution and pathways in the Arctic Ocean since 2007

Contents

III.1. Introduction

We suggested in the previous chapter that the halocline layer in Amundsen Basin 2017 comprised water advected from the Siberian Seas through the surface circulation Transpolar Drift. Understand the changes in freshwater distribution and pathways is needed to help understand sources of the halocline.

Two highly resoluted (1/12°) global systems were available at Mercator Océan: the reanalysis GLORYS12 and the real time system PSY4V3R1 (PSY4). The former provides fields since 1993 while the latter starts in 2007. A preliminary validation of the two systems on a pan-Arctic scale was performed by using drifting plateforms measurements (ITPs and IAOOS) and moorings data. Model-observation differences in temperature and salinity were similar for both systems, in the Canada Basin (**Figure 3.1b** and **3.1d**). However, in the Eurasian Basin, GLORYS12 exhibited warmer (~ +1°C at 100 m) and fresher (~ -1.5 $g.kg^{-1}$ at surface) waters when compared to observations and PSY4 (**Figure 3.1a** and **3.1c**). We therefore chose to use PSY4 for our study.

The next section is composed of a paper under review at *Journal of Geophysical Research: Ocean*. We further evaluated PSY4 performances on a pan-Arctic scale and analysed simulated sea surface height and freshwater changes from 2007 to 2020.

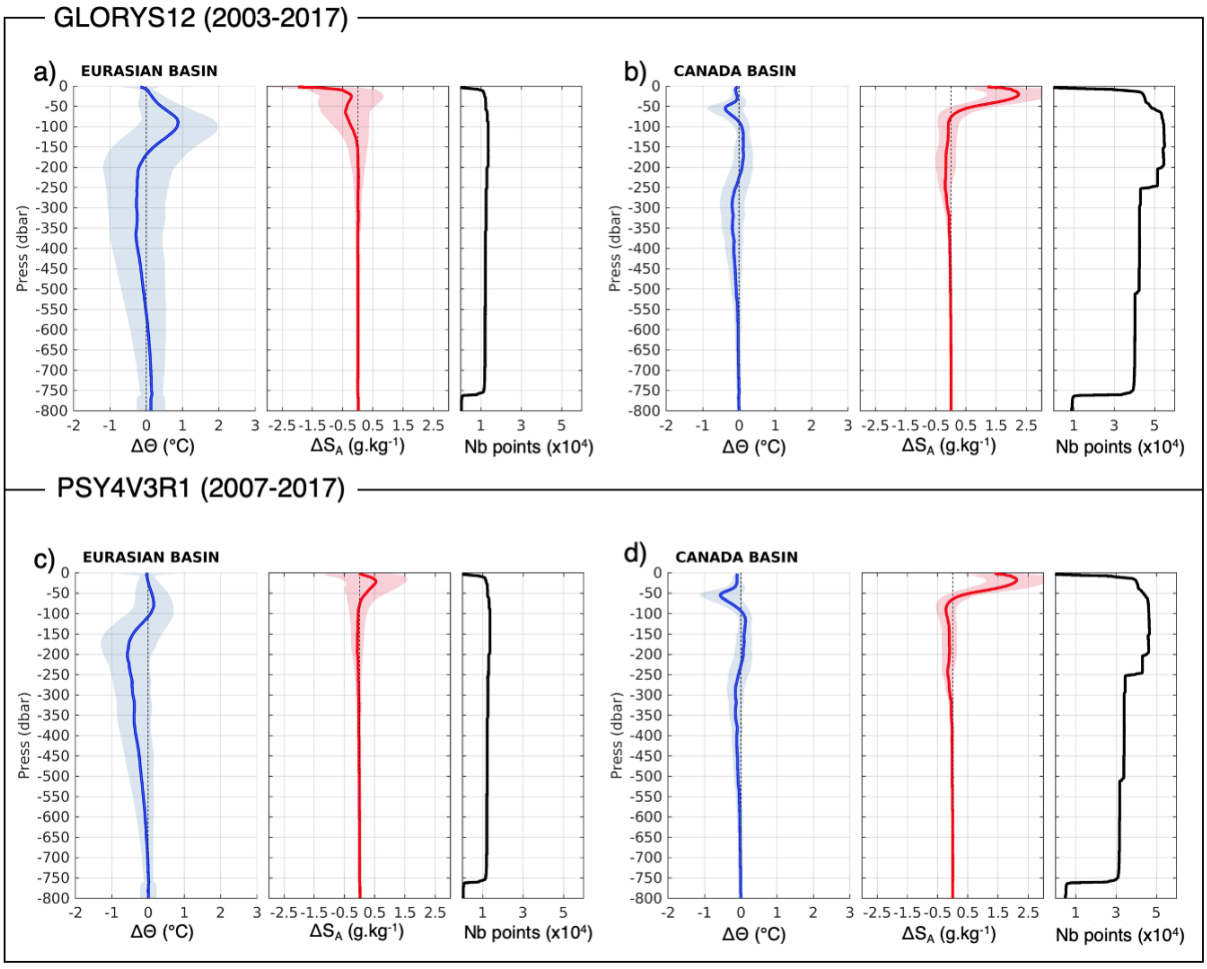

Figure 3.1: Model-observation differences of conservative temperature (blue) and absolute salinity (red) for GLORYS12 (top) and PSY4 (bottom) in the (**a**,**c**) Eurasian Basin and (**b**,**d**) the Canada Basin

III.2. Changes in freshwater distribution and pathways in the Arctic Ocean since 2007 in the Mercator Ocean global operational system

Changes in Freshwater Distribution and Pathways in the Arctic Ocean since 2007 in the Mercator Ocean Global Operational System

Cécilia Bertosio[1], Christine Provost[1], Marylou Athanase[2], Nathalie Sennéchael[1], Gilles Garric[3], Jean-Michel Lellouche[3], Clément Bricaud[3], Joo-Hong Kim[4], Kyoung-Ho Cho[4], Taewook Park[4]

[1]: Laboratoire LOCEAN-IPSL, Sorbonne Université (UPMC, Univ. Paris 6), CNRS, IRD, MNHN, Paris, France
[2]: Alfred-Wegener-Institut, Bremerhaven, Germany
[3]: MERCATOR-OCEAN, Toulouse, France
[4]: Division of Polar Ocean Sciences, Korea Polar Research Institute, Incheon 21990, Republic of Korea

Key points:

- The Mercator Ocean model was capable of reproducing observed spatial patterns of Arctic freshwater content and sea surface height
- After 2012, waters in the Makarov Basin near the North Pole freshened and Atlantic-origin waters shoaled along the East Siberian slope
- After 2015, liquid freshwater outflow increased through the western Canadian Archipelago and decreased through Fram Strait

Abstract

Arctic low-salinity waters, referred to as "freshwaters", are cold and play a major role in preserving the sea ice cover. We examined changes in Arctic freshwater distribution and circulation since 2007 using the 1/12° global Mercator Ocean operational model. We first evaluated model simulations over the upper water column in the Arctic Ocean, using nearly 20,000 independent in-situ temperature-salinity profiles over the 2007-2020 period. Simulated hydrographic properties and water mass distributions were in good agreement with observations. Comparison with long-term mooring data in the Bering Strait and Beaufort Gyre highlighted the model's capabilities for reproducing the interannual evolution of Pacific Water properties. Taking advantage of the good performance of the model, we examined the interannual evolution of the freshwater distribution and circulation over 2007-2020. The Beaufort Gyre is the major freshwater reservoir across the full Arctic Ocean. After 2012 the gyre extended northward and increased the freshwater content in the Makarov Basin, near the North Pole. Coincidentally, the freshwater content decreased along the East Siberian slope, along with the Atlantic Waters shoaling, and the Transpolar Drift moved from the Lomonosov Ridge to align with the Mendeleev Ridge. We found that these changes in freshwater distribution were followed in 2015 by a marked change in the export of freshwater from the Arctic Ocean with a reduction in Fram Strait (-30%) and an increase in the western Canadian Archipelago (+16%). One year later, the freshwater export increased downstream at the Davis Strait, the gateway to the North Atlantic Ocean.

Plain language summary

We evaluated 14 years of simulations from a high-resolution ocean model to identify changes in the upper water column of the Arctic Ocean since 2007. Comparisons of simulations with observations highlighted model's capabilities for reproducing the properties of the Arctic Ocean. After 2012, the model showed that the Beaufort Gyre, known to be the largest reservoir of freshwater in the Arctic Ocean, retreated to the northeast, and the freshwater content increased near the North Pole. Coincidentally, the surface ice and ocean circulation (Transpolar Drift) shifted to the east from 140°E to 180°W. We documented changes in the freshwater pathway exiting the Arctic with more freshwater outflow through the western Canadian Archipelago after 2015 compared to the previous years.

1. Introduction

In contrast with the midlatitudes and tropics, the stratification of the Arctic Ocean is essentially salinity-driven (Carmack, 2007; Timmermans & Jayne, 2016). Low-salinity waters of the upper water column are cold and play a major role in isolating sea ice at the surface from the heat carried by the underlying Atlantic Waters (AW, defined as $S_A > 34.9$ g kg^{-1}, $\Theta > 0$°C; Rudels et al., 1996). The low-salinity waters (with a wide range of salinities $0 < S_A < 34.9$ g kg^{-1}) make up the halocline and the surface mixed layer and are commonly called freshwaters (e.g., Rabe et al., 2014; Wang et al. 2017; Proshutinsky et al., 2019; Karpouzoglou et al., 2022). Freshwater inputs to the Arctic Ocean comprise three sources: continental runoff, Pacific-derived water, and net precipitation (e.g., Aagaard and Woodgate, 2001; Serreze et al., 2006; McClelland et al., 2012). During the 2000-2010 period, the continental runoff was estimated at ~133 mSv, the Pacific-derived freshwater input at ~82 mSv, and precipitation at ~70 mSv (Rabe et al., 2014; Haine et al., 2015; 1 mSv = 1 milliSverdrup = 10^3 m^3 s^{-1}).

The distribution of freshwater content (FWC) in the Arctic Ocean is governed by wind-driven and density-driven oceanic circulation. The combined effects result in a non-uniform distribution over the Arctic domain with a maximum FWC in the Canada Basin and a minimum in the Nansen Basin (**Figure 1a**). The wind-driven ocean circulation features the Transpolar Drift (TPD), a stream transporting sea ice and relatively fresh waters from the Siberian shelves across the Arctic towards the Fram Strait (e.g., Morison et al., 1998; 2012), and the Beaufort Gyre (BG), a large-scale gyre dominating the Canada Basin circulation (**Figure 1a**). Studies showed that upper ocean circulation regime changes are linked to the variations of the Arctic Oscillation index (e.g., Armitage, 2018; Karcher et al., 2012; Morison et al., 2012; Wang, 2021). The Arctic Oscillation index is derived from patterns of sea level pressure anomalies and reflects a back-and-forth shift of atmospheric pressure between the Arctic and the mid-latitudes of the North Pacific and North Atlantic (Thompson & Wallace, 1998). Positive values of the Arctic Oscillation index denote a strengthened cyclonic (anticlockwise) ocean circulation regime in the Eurasian Basin, a TPD toward Mendeleev Ridge and a strong anticyclonic (clockwise) BG restricted to the Canada Basin (**Figure 1**)

(e.g., Swift et al., 1997; Morison et al., 1998, 2012, 2021; Wang, 2021). Negative Arctic Oscillation index values correspond to a TPD toward the Lomonosov Ridge (Morison et al., 2021) and an extended anticyclonic BG in the Amerasian Basin. Wang (2021) additionally showed that during negative Arctic Oscillation index periods, FWC increases in the central Arctic.

The BG is governed by wind stress, dynamic feedback between ice motion and upper ocean current, and lateral eddy fluxes (Doddridge et al., 2019). The resulting surface stress leads to an Ekman convergence and freshwater accumulation toward the center of the gyre (Proshutinsky et al., 2002, 2009, 2015). The FWC variability is associated with sea surface height (SSH) variations through the halosteric effect (i.e., saline contraction or expansion of a water parcel), thus SSH patterns are good indicators of changes in the FWC distribution (Armitage et al., 2016, Wang 2021). Recent satellite observations of SSH indicated a northwestward expansion of the Beaufort Gyre from 2003 to 2014, resulting from an intensification and pattern change in the wind stress field (Regan et al., 2019). The center of the BG is characterized by a maximum SSH and a thick and strong halocline (Regan et al., 2019; Polyakov et al., 2018). The BG halocline comprises Pacific Waters that enter the Arctic via the Bering Strait (**Figure 1**) (Shimada et al., 2005; Proshutinsky et al., 2019). Seasonal processes modify Pacific Waters before they reach the BG halocline. In summer, solar input and ice melt warm and freshen the Pacific Summer Waters (PSW; $31 < S_A < 32$ g kg^{-1}; $-1 < \Theta < 1$°C). In winter, ice formation and brine release cool and increase the salinity of Pacific Winter Waters (PWW; $32.2 < S_A < 33.2$ g kg^{-1}; $\Theta \sim -1.8$°C) (Timmermans & Marshall, 2020; Woodgate & Peralta-Ferriz, 2021).

The BG constitutes the largest freshwater reservoir of the Arctic Ocean, it stores approximately 23,000 ± 2,000 km^3 of freshwater and accumulated an additional 6,400 km^3 of freshwater over the last decade (Carmack et al., 2016; Proshutinsky et al., 2019). Proshutinsky et al. (2019) showed that the freshwater increase in the gyre largely resulted from a redirection of nearby river discharge and Pacific Water contribution. This increase in freshwater storage in the BG was concomitant with a steady increase in pan-Arctic freshwater content from the early 1990s until 2007 (Rabe et al., 2014; Proshutinsky et al., 2019; Solomon et al., 2020;

Wang, 2021). After 2007, the Arctic freshwater reached a plateau due to compensation between a FWC increase in the BG and a FWC decrease in the other basins (Solomon et al., 2020).

Under dominant cyclonic winds, the freshwater accumulated in the gyre can be released into the larger Arctic Ocean (Proshutinsky et al., 2002; Proshutinsky & Johnson, 1997; Zhong et al., 2019; Zhang et al., 2021) and eventually discharged to the North Atlantic through Fram Strait (~ 89 mSv over 2000–2010; Haine et al., 2015) and the Canadian Archipelago (~ 68 mSv before 2006; Beszczynska-Möller et al., 2011). The Arctic freshwater outflow is a key feature impacting the large-scale circulation in the North Atlantic Ocean, such as the Atlantic Meridional Overturning Circulation which is driven by vertical density gradients. Hence, an excessive freshwater release could reduce surface ocean density and weaken the Atlantic Meridional Overturning Circulation (Rahmstorf et al., 2015; Zhang et al., 2021). Monitoring the recent evolution of the FWC distribution in the Arctic is thus crucial to increasing our understanding of the ongoing Arctic changes and their potential impact at lower latitudes.

Despite significant international efforts in the last decade (e.g., Toole et al., 2011; Koenig et al., 2017b), hydrographic data remain sparse in the Arctic (Behrendt et al., 2018). Coupled ocean-sea ice operational analysis systems helped interpret observations in this region (e.g., Zhang et al., 2016). The Mercator Ocean operational 1/12° physical system PSY4 (Lellouche et al., 2018) has proven capable of reproducing the hydrography, mesoscale structures, and seasonal signals in the western Nansen Basin (Athanase et al., 2019; Koenig et al., 2017a). PSY4 provided insights on the development of new pathways of AW, the intensification of the circulation north of Svalbard, the progressive warming and thickening of the AW layer (Athanase et al., 2021) and documented interannual variations of winter mixed layers and processes modifying AW (Athanase et al., 2020).

This paper aims to further assess PSY4 capabilities over the Arctic deep basins and to use the 14-year simulation to investigate changes in freshwater distribution and pathways in the Arctic Ocean since 2007. In particular, we examine whether the northwestward extension of the BG

beyond the Chukchi Plateau (**Figure 1**) documented until 2014 (Regan et al., 2019) is a temporary shift or a new geographical position for the gyre.

In this paper, we explore changes in freshwater circulation and outflows of the Arctic Ocean with PSY4. Section 2 introduces the Mercator Ocean operational system and describes the independent in-situ data used to evaluate the model. The performance of the model is assessed over the Arctic Ocean halocline in section 3. In section 4, we investigate the interannual evolution of the upper water column from 2007 onwards. Results are discussed in section 5 and a conclusion is provided in section 6.

2. Operational system and non-assimilated data

2.1. Mercator Ocean operational system

The global operational system PSY4 was developed at Mercator Ocean for the Copernicus Marine Environment Monitoring Service (CMEMS; http://marine.copernicus.eu/) and simulates physical ocean variables (e.g., temperature, salinity, sea surface height, and velocity) and sea ice variables from 2007 onwards (Lellouche et al., 2018). The physical configuration is based on a 1/12° tripolar grid (Madec and Imbard, 1996) (grid spacing of 3-5 km in the Arctic), with 50 vertical levels of decreasing resolution from 1 m at the surface to 450 m at the bottom, including 22 levels within the upper 100 m. The system PSY4 uses version 3.1 of the Nucleus for European Modelling of the Ocean model (NEMO; Madec et al., 2008) and the Louvain-La-Neuve thermodynamic-dynamic sea Ice Model (LIM2, Fichefet and Maqueda, 1997). At the surface, the model is driven by atmospheric analyses and forecasts obtained from the European Centre for Medium-Range Weather Forecasts-Integrated Forecast System (ECMWF-IFS) at 3-hr resolution. Apart from sea ice concentrations (from Ocean Sea Ice - Satellite Application Facilities products, https://doi.org/10.48670/moi-00134), no assimilation is performed in the ice-covered ocean in the Arctic. The PSY4 system was initialized in October 2006 using quality-controlled ocean temperature and salinity profiles from the dataset EN4.2.1 (Good et al., 2013). Details about initialization and bathymetry used in PSY4 are given in Supporting Information. So far, PSY4 evaluations in the Arctic have focused on the upper

600 m of the western Eurasian Basin. The model performed adequately in simulating sea ice cover, temperature, salinity, and ocean currents, as well as reproducing observed mesoscale structures (e.g., Athanase et al., 2019, 2020; Koenig et al., 2017a, 2017b).

2.2. Particle tracking method

We used daily horizontal model velocities to investigate the possible origin and fate of water parcels. Lagrangian backward and forward trajectories of synthetic particles were tracked using a simple prediction correction scheme similar to that employed by Fillipi et al. (2010) and previously used in Bertosio et al. (2020). We released 160 particles in a box spanning the BG region 72-79°N, 170°W-130°W, and 160 particles in another box in the central Makarov Basin spanning the region 86.5–88°N, 150°W–175°W. Particles were released at depths of 5, 80, and 150 m. In this study, we only show results at 80 m depth. We performed two launches every year from 2007 to 2020: one at the end of the winter and one at the end of the summer. We tracked the particles for six years. For clarity, we only showed the first three years. We displayed the trajectories on maps using a grid of 25 × 10 km and counting when each trajectory crosses the grid cell. Trajectories of water parcels and time scales of advection are examined in section 4.

2.3. Non assimilated data for model evaluation

A total of 19,642 temperature and salinity profiles were gathered from several datasets: the UDASH database spanning 1980 to 2015 (Behrendt et al., 2018; see Supporting Information **Figure S1**); recent ice tethered platforms not included in UDASH (ITPs: Krishfield et al., 2008; IAOOS: Boles et al., 2020); and moorings (summary in **Table 1** and data distribution in **Figure 1**). Quality checks were performed to remove erroneous profiles. Mooring D (**Figure 1a**) from the Beaufort Gyre Exploration Project (BGEP) deployed in the Canada Basin provided continuous time series of temperature, salinity, and ice draft data over the 2007-2018 period (http://www.whoi.edu/beaufortgyre, see Proshutinsky et al. (2009) for further details). In the Bering Strait, the A3 mooring (**Figure 1c**) recorded near-bottom (48 m) temperature and salinity data, and velocity profiles over the 2007-2019 period (Woodgate et al., 2012, 2015;

Woodgate, 2018). Daily PSY4 fields were collocated in time and space (closest grid cell) with the in-situ profiles. We linearly interpolated profiles from both in-situ measurements and PSY4 simulated data (with a variable vertical resolution, cf. section 2.1) to the same 2-m vertical resolution to ease model-observations comparisons.

SSH fields from PSY4 were compared to the altimetry products from Armitage et al. (2016, 2017) (called CPOM hereafter) spanning the 2007-2014 period. PSY4 SSH fields were interpolated to the coarser CPOM grid (0.75° × 0.25° longitude/latitude grid).

PSY4 sea ice concentration and thickness were compared to those from the Pan-arctic Ice-Ocean Modeling and Assimilation System (PIOMAS - version 2.1). PIOMAS assimilates daily sea ice concentration (from NSIDC) and sea surface temperature (from the NCEP/NCAR reanalysis) and has been extensively validated (e.g., Schweiger et al., 2011; X. Wang et al., 2016). The PIOMAS grid is ~22 km resolution, which is coarser than the PSY4 grid (3-5 km in the Arctic). PSY4 fields were spatially downsampled to the PIOMAS grid to enable the comparison. A comparison of PSY4 with the PIOMAS sea ice data is listed in the Supporting Information.

2.4. Freshwater content and Available Potential Energy computations

In this study, we used density anomalies σ (kg m^{-3}), referred to as density hereafter. Absolute salinity S_A (g kg^{-1}) and conservative temperature Θ (°C) are used following the TEOS-10 (Thermodynamic Equations of Seawater) international standard (McDougall and Barker, 2011). However, practical salinity S was used (and not absolute salinity) for freshwater content (FWC) calculations to facilitate comparison with literature values. The FWC was computed relative to salinity 34.8 psu (~34.97 g kg^{-1} in Absolute Salinity) following Proshutinsky et al., (2009):

$$FWC = \int_{z_{34.8}}^{z_1} \frac{34.8 - S(z)}{34.8} dz \quad (1)$$

where z_1 = surface. The total freshwater volume over the Arctic basins in the model was obtained by summing the FWC multiplied by the model grid cell area when the seafloor was

deeper than 500 m. We additionally computed freshwater volume outflow at several gateways of the Arctic such as:

$$Freshwater\ volume\ outflow\ = \int_{z_{34.8}}^{z_1} \frac{34.8-S(z)}{34.8} \times v(z) \times A(z)\ dz \qquad (2)$$

where v is the velocity and A is the surface associated with the model grid cell at depth z.

As explained in the introduction, the stronger (i.e., the more stratified) the upper water column, the more the sea ice cover is isolated from the underneath warm Atlantic Waters. To quantify the strength of the complex upper water column of the Arctic Ocean, halocline water masses, and surface mixed layer, we used the bulk metric of the available potential energy (APE), initially proposed by Polyakov et al. (2018). The APE corresponds to the potential energy that can exchange reversibly with the kinetic energy. Hence, the APE gives an informative integral indicator of stratification of the Arctic Ocean and the higher the APE, the stronger the upper water column (Winters et al., 1995; Zemskova et al., 2015). At each location, it is calculated as: :

$$APE\ =\ \int_{z_{27.85}}^{surface} g\ (\sigma(z)\ -\ 27.85)\ z\ dz \qquad (3)$$

where g is the gravitational constant and σ is the density anomaly. The depth of the isopycnal 27.85 kg m^{-3} ($z_{27.85}$) was considered as the base of the halocline layer (Bertosio et al., 2020).

3. Comparison of the model with observations

3.1. Model temperature and salinity in the upper layer over Arctic deep basins

Athanase et al. (2020) carried out an extensive evaluation of PSY4 performance in the western Nansen Basin and Fram Strait. Here, we extended the evaluation to the Arctic deep basins. We investigated the horizontal distribution of the model-observation temperature and salinity differences by computing the root mean square error (RMSE) over the upper 400 m water column (**Figures 2a-b**). There was a contrasted distribution of the RMSE, with the largest temperature biases found in the Eurasian Basin (RMSE > 1°C) and large salinity biases located

in the Makarov and Canada Basins (RMSE > 0.8 g kg^{-1}). Nevertheless, PSY4 reproduced well the observed salinity and temperature horizontal patterns. For illustration, model and observation fields at the near-surface (0-20 m), in the halocline (80-100 m), and in the AW layer (180-200 m) are shown in **Figure S2.** Additionally, we investigated the vertical distribution of the differences along a transect crossing the Arctic basins by using the spatially closest profiles (**Figures 2c-h**). Note that sections along this transect are composites, comprising profiles from different years and different months. In the following analyses, we first consider the Eurasian Basin and then focus on the Canada and Makarov Basins separately.

3.1.1. The Eurasian Basin

In the Eurasian Basin, temperature differences were large along the continental slope, especially in the eastern Nansen Basin (**Figure 2a**). Vertical profiles featured a cold bias at 80-150 m where AW lies (-1 < $\Delta\Theta$ < -0.5 °C, **Table 2**), particularly pronounced in the core of the boundary current (**Figures 2c-e**). A portion of the cold bias is likely explained by an erroneously cold upstream AW core in Fram Strait (where $\Delta\Theta$ ~ -0.2°C, c.f. Athanase et al., 2020). However, negative temperature biases in the eastern Nansen Basin exceeded those in the Fram Strait, possibly resulting from overestimated convective processes in the Eurasian Arctic which amplified the cold bias in the AW layer.

In contrast, salinity biases in the Eurasian Basin were small (RMSE < 0.4 g kg^{-1}, **Figure 2b**). Below 80 m in the AW core, modeled salinities were close to the observations ($|\Delta S_A|$ < 0.04 g kg^{-1}, **Table 2**, **Figures 2f-h**). The largest salinity biases were restricted to the upper 60 m, where modeled polar surface waters were saltier than in observations (0 < ΔS_A < 0.5 g kg^{-1}, **Table 2**). Many climate models have similar surface salinity biases as processes near the surface are complex and the variability is large (Lique et al., 2016). However, data points available over the 2007-2020 period in the Eurasian Basin were insufficient to further investigate the surface salinity bias; most of the observations were from the summer period and the spacing was poor **(Figure S1)**.

3.1.2. The Makarov and Canada Basins

In the Makarov Basin, temperature biases were small compared to that in the Eurasian Basin (RMSE < 0.4°C, **Figure 2a**). The modeled halocline was slightly too warm ($\Delta\Theta \sim +0.25$°C), while the modeled AW (found below the 27.8 isopycnal) remained deeper and colder than in the observations ($\Delta z \sim 50$m, $\Delta\Theta \sim -0.2$°C) (**Figures 2c-e**). The modeled salinity in the upper 50 m was larger than observations by ~1-2 g kg^{-1} (**Figure 2h, Table 2**). Several sources can contribute to this surface salinity bias, such as too little (or too much) simulated brine rejection from sea ice growth or biases in the redistribution of modeled river discharge. In the Makarov Basin, modeled sea ice thickness and concentration were similar to the extensively-evaluated reanalysis PIOMAS (see Supporting Information). Therefore, sea ice is unlikely the primary contributor to the bias. The Makarov Basin surface waters are influenced by shelf waters from the Siberian Sea (**Figure 1**). One possibility would be that the surface salinity bias originated from the shelf area and was advected toward the basin. Modeled river discharge inputs and model performances over the shelves still need to be further investigated to determine the cause of the surface salinity bias in PSY4.

The Canada Basin benefits from a more extensive spatial and temporal measurement coverage compared to the Eurasian Basin, as numerous drifting platforms were deployed in the BG area providing year-round data **(Figure S1**). The Canada Basin upper water column comprises the surface mixed layer (in the upper 50 m), the PSW (50-100 m), PWW (100-200 m), and AW (below 300-350 m) (**Figure 3a**). The PSW, characterized by a local temperature maximum in the upper 100 m, were on average colder, saltier, and therefore denser and deeper in the model compared to observations ($\Delta\Theta \sim -1 \pm 0.4$°C, $\Delta S_A \sim 0.3$ g kg^{-1}, $\Delta\sigma \sim 0.3$ kg m^{-3}, $\Delta z \sim 30$ m; **Figures 2c-e, Figures 3a-f**). In contrast, the underlying PWW, characterized by a temperature minimum at ~ 180 m, were at the right depth, temperature, and salinity ($|\Delta\Theta| < 0.1$ °C and $|\Delta S_A| < 0.1$ g kg^{-1} in the 180-200 m layer, **Figures 2c-e, Figures 3a-f** and **Table 2**). The modeled temperature and salinity of the Canada Basin AW layer exhibited small differences when compared to observations ($|\Delta\Theta| < 0.1$ °C and $|\Delta S_A| < 0.1$ g kg^{-1} below isopycnal 27.8 kg m^{-3} in **Figures 2c-h**). Salinity biases in the Canada Basin were predominantly due to an overestimation of modeled salinities in the upper 50 m by 2 g kg^{-1} (**Figures 2b** and **2f-h**).

Such surface bias is a common feature of the state-of-the-art ocean and sea-ice models (e.g., Lique et al., 2016; Q. Wang et al., 2016; Regan et al., 2020). The PSY4 sea ice thickness in the area was overestimated compared to PIOMAS, which likely contributed to an overestimation of the modeled surface salinity (see Supporting Information). The nearby river inputs in PSY4 are also an interesting possible source of the surface salinity to investigate and should be considered in future work.

To provide an overview of the evolution of biases over time, we used year-round temperature and salinity mooring data over the 2007-2018 period in the BG area (namely BGEP mooring D; Proshutinsky et al., 2019). The model performance in representing water masses described in the previous paragraphs - which are (i) colder and deeper modeled PSW and (ii) a close accordance of the modeled PWW and AW properties with observations - remained unchanged over the 2007-2018 period (**Figure 3**). This suggested little model drift over time and it is plausible that temperature and salinity discrepancies mainly resulted from biases in the initial conditions **(Figure S3)**.

The depression of modeled isopycnals induced by the BG dynamic in the Amerasian Basin matched the observations well, with isopycnal 27.8 kg m^{-3} reaching 350 m depth in the Canada Basin (versus 200 m depth at the North Pole, **Figures 2c-g**). In 2008 and 2017, PSY4 reproduced an observed downwelling of isopycnals, however, modeled isopycnal downwelling in 2016 and 2018 was too smooth (**Figures 3g-j**). Consequently, the temperature and salinity at 255 m were overestimated during these two years, as the modeled base of the PWW layer was not deep enough (**Figure 3l**). Vertical salinity gradients at the base of PSW and PWW, i.e. in the halocline, are large and a precise simulation of the ocean at the right depth and time is demanding.

3.2. Pacific Waters inflow through Bering Strait

We devoted a focused analysis to the capability of the model to simulate the Pacific Water inflow to the Arctic Ocean through the Bering Strait, which is the second main source of freshwater to the Arctic after the continental runoff (Haine et al., 2015). We compare PSY4 to observational mooring data in the Bering Strait. The Bering Strait data come from a centrally-

located mooring labeled A3 (**Figure 4**), which has been shown to accurately represent the mean transport and hydrography of Pacific Water inflow to the Arctic through the strait (Woodgate et al., 2018; Woodgate & Peralta-Ferriz, 2021).

Modeled temperature, salinity, and northward velocities were on average larger than observations with mean yearly biases of +0.38°C, +0.26 g kg^{-1}, and +12.6 cm s^{-1} respectively (**Figures 4a-c**). Although PSY4 yearly velocity bias was large throughout the whole time series, it changed little over time (variations of ±1.7 cm s^{-1}, **Figure 4c**) and could be considered nearly constant. Interannual variations of modeled temperature, salinity, and northward velocities closely followed that from the observations as quantified by the large correlation coefficients obtained from yearly means ($r^2 = 0.76$, $r^2 = 0.86$, and $r^2 = 0.85$ for temperature, salinity, and northward velocities respectively). The modeled warming in 2012-2019 was in close accordance with the observations (trends of +0.24°C yr^{-1} and +0.31°C yr^{-1} respectively) (**Figure 4a**). From 2012 onwards, the model reproduced the observed freshening (~ -0.02 g kg^{-1} yr^{-1} in PSY4 and ~ -0.05 g kg^{-1} yr^{-1} in observations). Particular fresh events recorded in winter (impacting PWW), such as in 2013, 2016 and 2019 (Woodgate, 2018; Woodgate & Peralta-Ferriz, 2021), were replicated in the model with a model-observation salinity correlation at $r^2 = 0.87$ in winter (versus $r^2 = 0.57$ in summer, **Figure 4b**). PSY4 additionally showed reduced velocities in the winters of 2012, 2016, and 2019 in agreement with observations (**Figure 4c**).

Seasonal cycles were reproduced well with an overlap of standard deviation envelopes from the model and observations (**Figures 4a-f**). During summer (August-September), modeled PSW were too warm ($0.5 < \Delta\Theta < 2$°C, **Figure 4d),** and too salty ($0.5 < \Delta S_A < 1.3$ g kg^{-1}, **Figure 4e**). Such a warm and salty summer bias probably resulted from upstream bias in the North Pacific. In contrast, in winter modeled PWW exhibited realistic temperatures (Θ ~ -1.8°C) and salinities ($\Delta S_A < 0.2$ g kg^{-1}, **Figures 4d-e**). Modeled velocities displayed a realistic seasonal signal with larger values in summer than in winter, a maximum in May-June, and a minimum in November, as in the observations (**Figure 4f**).

The modeled circulation patterns north of the Strait, which shape the distribution of Pacific Waters in the Canada Basin and Makarov Basin, were consistent with observation-based

descriptions in the literature (**Figure 4h**). Indeed, the Pacific inflow split into two branches north of mooring A3 (Spall et al., 2008). One branch circulated northeastward and separated into two parts: one following the Alaska coast and entering the Canada Basin via Barrow Canyon, and another going north in the central Chukchi Sea (Pisareva et al., 2015). The second branch flowed west and exited the Chukchi Sea through Herald Canyon while feeding the central branch of the Chukchi Sea (Corlett & Pickart, 2017; Stabeno et al., 2018).

The modeled net volume flux through the strait averaged over 2008-2019 (~ 1.3 Sv; 1 Sv = 1 Sverdrup = 10^6 $m^3.s^{-1}$; green curve in **Figure 4g**) was a little larger than that found by Woodgate (2018) (Δ ~ 0.2 Sv), likely resulting from the shift of ~13 cm s^{-1} found in modeled velocities. Nevertheless, the mean freshwater content net transport (~ 90 mSv, purple curve in **Figure 4g**) was consistent with that computed by Woodgate (2018) (~ 95 mSv). Particular observed events, such as smaller transports in 2012 (Woodgate, 2018), were reproduced in PSY4.

3.3. Freshwater content and Sea Surface Height

Modeled FWC over the Arctic basins showed a spatial distribution in accordance with the observations, with values lower than 10 m in the Eurasian Basin and 15-30 m in the Makarov and Canada Basins (**Figures 5a-b**). In particular, the modeled and observed FWC were the largest in the BG area, where it is known to have accumulated since the early 2000s compared to pre-1990 climatologies (e.g., Proshutinsky et al., 2009 and 2019). Due to the surface salinity bias, PSY4 generally underestimated the FWC (ΔFWC ~ 0-3 m, **Figure 5c**). Yet, model-observation differences remained smaller than 10 % of the mean observed value. This is relatively low, as simulated Arctic FWC can largely vary from one model to the other, in particular in the Canada Basin where values range from 6 to 20 m (c.f. Figure 2 in Jahn et al., 2012; Salomon et al., 2020). We additionally computed the modeled FWC at the mooring location in the BG from the depth of the salinity reference up to 70 m, as the mooring data were only available below 70 m (**Figure 3m**). In that case, modeled salinity near the surface was not taken into account and the model-observation differences remained on average less than 2 m

(15% of the mean observed values) over the entire 2007-2018 period. Improving the surface salinity in the model thus would benefit the modeled FWC.

In the Arctic, spatial patterns of SSH closely follow that of the FWC, with low SSH values in the Eurasian Basin (SSH < 10 cm) and large values in the BG (SSH > 50 cm, Wang 2021; **Figure 6a**). We found that model SSH was in close accordance with the altimetry data **(Figure S4)**. Model-altimetry SSH differences were on average lower than 12 cm and localized over bathymetric slopes. Significant SSH differences between the model and observations were confined to shelves and the eastern Eurasian Basin while values in the Amerasian Basin (area of interest) remained smaller than 25% (**Figure S4**). The large differences in percentage have to be considered with the coarse resolution of the altimetry product in mind. Indeed, the CPOM grid (0.75° x 0.25°) likely does not capture sharp SSH gradients close to the continental shelves.

In summary, PSY4 generally reproduced the observed temperature and salinity in the upper Arctic Ocean. Quantitative comparisons showed that modeled PSW were warmer than observations in the Bering Strait and colder in the Canada Basin, while differences in PWW were small. Pacific Water inflow at Bering Strait was consistent with observations and was associated with a realistic freshwater flux and a slightly overestimated volume flux (**Figure 4g**). AW in the Eurasian Basin was colder than observations. Overall, the spatial structures of the modeled FWC and SSH were in accordance with the observations. In the next section, we examine the interannual evolution of SSH and FWC in the Arctic Ocean.

4. Interannual evolution of the Arctic upper water column from 2007 to 2020

4.1. Modeled sea surface height trends and variations

The SSH is closely related to FWC distribution as illustrated in **Figure 6a.** However, SSH does not depend on the choice of a reference value, in contrast to FWC. For our analysis, we removed regions over the shelves where SSH variability is much larger than in the basin (e.g., Armitage et al., 2018). We additionally removed the seasonal cycle to only consider interannual variations.

Over the 2007-2020 period, the SSH trends were the largest in the Amerasian Basin with ~ +1.5 cm yr^{-1} near the North Pole and ~ -1.5 cm yr^{-1} along the slope north of the East Siberian Sea (**Figure 6b**). In both cases, the 14-years trends were larger than the interannual standard deviation. Furthermore, the monthly variability of SSH was the highest in the southern Mendeleev Ridge (180°E) where the standard deviation exceeded 7 cm (**Figure 6c**).

Considering these SSH trends and variations, we chose four locations where time series illustrated the dominant interannual variations in SSH (**Figure 6d**). Two points were taken along the East Siberian Sea where the SSH trend was negative, including one where the standard deviation was large (purple triangle and green square in **Figure 6a**). The SSH time series along the East Siberian Sea slope showed two local maxima in 2011 and 2014 despite the overall decrease (purple line, **Figure 6d**). South of the Mendeleev Ridge (green square in **Figure 6a**), SSH increased until reaching a plateau from 2011 to 2016 (SSH ~ 38 cm, green line, **Figure 6d**). Hence, the negative linear trend at this location resulted from the sharp step in 2016-2017 (ΔSSH ~ 35 cm).

In the Beaufort Sea, SSH diminished during the 2011-2014 period (blue diamond and blue line in **Figures 6a-d**). This was consistent with the shift of the BG toward the Mendeleev Ridge described by Regan et al. (2019). Interestingly, the SSH over the Beaufort Sea gradually increased after 2014, suggesting a return of the gyre extension to the east (blue line in **Figure 6d**). In contrast, SSH gradually increased near the North Pole after 2012, from 10 cm to nearly 30 cm in 2020, (yellow line in **Figure 6d**), in accordance with the strong positive trend of +1.5 cm yr^{-1}.

Interannual variations of SSH were further examined using an Empirical Orthogonal Function "(EOF) analysis, after detrending and removing the seasonal cycle from the data. The leading mode (EOF1, **Figure 6e**), explaining 45.6% of the variance, featured opposite sign patterns with positive SSH anomalies on the western part of the Amerasian Basin (~ 4 cm) and negative SSH anomalies on the eastern part of the basin (~ -4 cm). The associated time series exhibited low-frequency variations **(Figure 6f)**. During 2011-2017, the EOF analysis suggested an increase of SSH in the west that can be interpreted as a western extension of the BG towards the Chukchi Plateau (Regan et al., 2019, 2020). Before 2010 and after 2018, as the Principal Component was negative, there was a decrease in SSH over the Mendeleev Ridge combined

with an increase on the Beaufort Sea and north of the Canadian Archipelago. This simultaneous eastward and a northward shift of large SSH values suggested substantial variations of the BG, which we further examine in the following.

4.2. Focus on the Amerasian Basin

4.2.1. Evolution of the Beaufort Gyre from model sea surface height.

Following Regan et al. (2019, 2020), the center of the gyre was defined as the maximum SSH (hereafter SSH_{max}) located in a box 190-230°E, 70.5-80.5°N. The limit of the gyre was taken as the largest closed SSH isocontour (hereafter SSH_{min}) surrounding the center. We considered that the selected SSH isocontour should not cover any plateaus shallower than 250 m, to discard closed isocontours entering the Amundsen Gulf. The gyre center and limit derived from PSY4 (**Figures 7a** and **7c**) were similar to those derived from altimetry data over 2007-2014, the period used in Regan et al. (2019). The SSH_{max} exhibited a minimum in 2014. The SSH_{min} notably increased in 2016 from persistent values of around 35 cm between 2007 and 2015 to around 40 cm from 2017 to 2020. The increase of SSH_{min} in 2016 was accompanied by a large decrease of the gyre area from a maximum of 1.3×10^{12} km^2 at the end of 2015 to 0.75×10^{12} km^2 at the beginning of 2017.

From 2016 onwards, large SSH values on the shelves off Alaska (SSH ≥ 35 cm, c.f. positive trend over the shelves in **Figure 6b**) led to isocontour breakup in this area. We tentatively considered the 35 cm SSH isocontour (hereafter SSH_{35}) as the limit of the gyre (purple line in **Figure 7c**) and closed it along the 500 m isobath. The interannual variations of the SSH_{35} differed from those in Regan et al. (2019) method after 2016. In particular, the BG area using SSH_{35} remained large, with 1.3×10^{12} km^2 (**Figures 7a-d**).

Using both methods, the northern limit of the BG shifted discernibly from 81°N to 86°N in 2016 (**Figure 7e**), with an associated SSH increase near the North Pole (section 4.1 and **Figure 6d**, yellow line). After 2016, the SSH_{35}-derived northern limit continued its progression until 87°N, while the limit derived from SSH_{min} returned southward, leading to the difference in BG areas (**Figures 7d-e**).

The western limit of the BG (i.e., boundary location with the smallest longitude and latitude) was similar following both methods. The BG western limit was located between the western Chukchi Plateau and Mendeleev Ridge (~ 170°W-180°E) from 2007 to 2009 **(Figure 7f)**. From 2010 to 2016, the limit extended over the Mendeleev Ridge (~ 170°E-180°E). This is consistent with the westward extension of the gyre described by Regan et al. (2019) and explains the SSH plateau found in the area (*section 4.1.* and green line, **Figure 6d**). Eventually, the gyre moved back eastward after 2016, inducing the increase of SSH near the Beaufort Sea described in *section 4.1.* (blue line in **Figure 6d**).

4.2.2. Freshwater content increase in the central Makarov Basin

The progressive increase in SSH near the North Pole associated with BG migration suggests a related change in FWC in the Makarov Basin. From 2010 to 2011 the BG was skewed to the southwest and its north limit was south of 83°N. During this time, FWC north of the gyre in the Makarov Basin decreased from 16 m close to the Mendeleev-Alpha Ridge to 6 m near the Lomonosov Ridge (**Figure 8a**). The Hovmöller diagram along a section crossing the Makarov Basin showed that the FWC increased near the North Pole (horizontal plain line in **Figure 8d**) from ~ 11 m in 2012 to ~ 17 m in 2018. Indeed, from 2014-2015 the BG boundaries penetrated the Makarov Basin via the Mendeleev-Alpha Ridge junction (**Figure 8b**). Coincidently, the halocline deepened by about 50 m between the 2007-2011 and 2016-2020 periods, inducing a negative salinity difference centered at 100 m depth of -1.3 g kg^{-1} (**Figure 9**). In 2019-2020, the contours of the gyre extended northward, and a new secondary reservoir of FWC emerged along the southern flank of the Mendeleev-Alpha Ridge (FWC ~ 21 m, **Figure 8c**). The emergence of this new reservoir of FWC contributed to extending the BG limit northward (when defined by SSH_{35}).

This spatial redistribution of FWC was accompanied by an Arctic-wide increase in FWC **(Figure 8e)**. The annual average of the modeled freshwater volume calculated over the deep basins (bathymetry > 500 m) increased from a minimum of 53,000 km^3 in 2013 to a maximum of 60,000 km^3 in 2020. Note that values of annual freshwater volume from PSY4 and before 2013 are comparable to the annual freshwater volume of about 50,000 km^3 computed in Rabe

et al. (2014) over the 2007-2012 period. PSY4 values suggested that this Arctic-wide modeled freshwater volume increase resulted essentially from the accumulation of freshwater in the Amerasian Basin (green and black curves in **Figure 8e**).

4.2.3. Progressive Atlantic Water shoaling along the East Siberian Sea slope

Another striking feature was the reduction of the SSH along the northern edge of the East Siberian Sea described in *section 4.1.* The SSH fields averaged over 2011 and 2016 are shown in the background of the maps in **Figures 7a** and **7b**, respectively. In 2016, the 10 cm iso-contour delineated a region with low SSH encroaching the Makarov Basin along the East Siberian Sea slope. Such low SSH (< 10 cm), comparable to values encountered in the Eurasian Basin, likely delineated denser waters of Eurasian origin. The longitude of the 10 cm iso-contour easternmost position in the area of the slope (white arrow in **Figure 7a**) has increased from 160°E in 2011 to a maximum of 180°E in 2017, exceeding 150°E after 2014 permanently (**Figure 7g**). Accordingly, the FWC decreased along the northern border of the East Siberian Sea after 2012 to less than 8 m (position ~200 km of the section in **Figure 8d**). This reduction in FWC resulted from a shoaling of isohalines by about 50 m near the continental slope (**Figures 9a-b**), inducing a large positive salinity difference in the upper 150 m (+ 1.7 g kg^{-1}, **Figure 9**) between the 2007-2011 and 2016-2020 periods. This is consistent with a shoaling of the warm, salty AW as a result of Atlantification (e.g., Polyakov et al., 2017, 2020b).

In summary, the modeled SSH evolution (driven by FWC variations via the halosteric effect) documented three major changes in the central Arctic since 2007. The BG extended westward from 2011 to 2016 and then retreated eastward. Near the North Pole, the SSH (and thus FWC) began to increase from 2012 as the BG extended northward. In parallel, the FWC decreased after 2012 along the East Siberian Sea slope, due to the progressive shoaling of AW. Modeled ocean circulation, freshwater pathways, and outflows from the Arctic are examined in the following section.

4.3. Recent changes in the upper layer ocean circulation and freshwater pathways

4.3.1. Large-scale changes in ocean circulation

To illustrate large-scale changes in upper ocean circulation, we averaged horizontal velocity fields over different periods: 2007-2020, 2010-2011, 2014-2015, and 2019-2020 (**Figure 10**). The 2007-2020 mean modeled ocean circulation in the upper water column was consistent with the descriptions found in the literature (**Figure 10a)**. The westward current larger than 9 cm s^{-1} south of the BG corresponded to the Chukchi slope current described by Corlett and Pickart (2017). The modeled TPD was on average confined over the Makarov Basin (**Figure 10a**, see e.g., Karcher et al., 2012; Kwok et al., 2013; Timmermans & Marshall, 2020). The mean anticyclonic surface circulation in the Canada Basin, corresponding to the BG, was associated with surface velocities smaller than 3 cm s^{-1} as in Armitage et al. (2017).

The Chukchi Slope Current, which reached the western part of Mendeleev Ridge in 2010-2011 (**Figure 10b**), retreated to the eastern part of the Chukchi plateau in 2019-2020 (**Figure 10d**). In parallel, the boundary current north of the Laptev Sea, previously not extending beyond the Lomonosov Ridge, reached the Mendeleev Ridge in 2019-2020 (**Figure 10)**. The circulation branch over the Makarov Basin in 2010-2011 and 2014-2015 was likely fed either by the BG, via the Chukchi Slope Current, or by waters from the Laptev Sea and the Eurasian Basin (**Figures 10b-c)**. The upper water column velocities suggested that the TPD intensified from 2010-2011 ($v_{80m} \sim 2.5$ cm s^{-1}) to 2014-2015 ($v_{80m} > 5$ cm s^{-1}) and shifted from the Lomonosov Ridge in 2014-2015 to the Mendeleev Ridge in 2019-2020. Velocities in the southern part of the Canada Basin also intensified in 2019-2020 compared to 2014-2015 (around 140°W near Barrow Canyon, **Figures 10b-c**).

4.3.2. Freshwater routes in the Canada and Makarov Basins

We further illustrated BG changes by following particles initially located in the gyre center with the particle tracking method described in section 2.2. We released particles in a box spanning the region 72-79°N, 170°W-130°W at various depths and different seasons (one launch at the end of the winter and the other at the end of the summer) and tracked their

trajectories for six years (the first three years at 80 m shown in **Figures 11a-b**). Particles released in the BG box upper layer first circulated anti-cyclonically in the Canada Basin, before exiting the gyre and ending their course in the central Makarov Basin (**Figures 11a-b**). From 2008 onwards, the main exit gate was to the west of the gyre, which is consistent with Hu et al. (2019). However, there was a change in the particle paths. Before 2015, particles that exited the BG flowed westward along the East Siberian Sea slope, and then entered the deep Makarov between 155°E-175°E (e.g., 2011 shown in **Figure 11a)**. There was an increase in westbound exits until 2014 (~ 10% in 2008 to more than 30% in 2014, green bars in **Figure 11c**), while the percentage of particles remaining inside the BG box decreased from ~ 60% in 2008 to ~35% in 2014 (yellow bars in **Figure 11c**). After 2015, more particles exited the gyre from the north (less than 5% in 2014 and ~ 10% in 2017, red bars in **Figure 11c**) and less from the west (~ 15% in 2017, **Figures 11b-c**), while about 40-60% of the particles remained inside the BG box. This is consistent with the northward shift of the BG and the eastward shift of the TPD: the particles leaving the gyre to the west progressed directly northward, along the Mendeleev Ridge at 180°W into the TPD (**Figure 11b**). Such changes in freshwater routes in the Amerasian Basin are in accordance with the increase of FWC near the North Pole after 2014 (**Figure 8d**).

Additionally, changes in freshwater routes in the Amerasian Basin were investigated using back-trajectories from the central Makarov Basin (86.5–88°N; 150°W–175°W) where the FWC increase was maximum. Particles were released at various depths and starting times (level 80 m shown in **Figures 11d-e** for sake of illustration). Back-trajectories over the 2010-2012 period showed larger contributions from the Eurasian Basin (>15%, **Figures 11d** and **11f**) than the Canada Basin (< 10%), with an additional contribution from the Laptev Sea near the surface (not shown). Sources and pathways changed after 2012 over the entire upper 150 m, with major contributions coming from the BG (< 10 % in the Eurasian Basin and> 20% in the Canada Basin, except in 2014 and 2018, **Figure 11f**). In 2018, the distribution of water parcels coming from the Canada and Eurasian Basins has a very similar ratio to 2010 and 2012, and further work would be needed to examine the involved processes.

The advection of particles from the BG to the Makarov Basin interior has accelerated between 2008 and 2019, as a result of the increasing upper-ocean velocities (**Figure 10**). The advection time between the two basins was about 2.5 years in 2011, against 1.5 years in 2017 **(Figures 11a-b** and **11d-e**). This could imply that low-salinity waters from the gyre would be less subject to modifications along their course to the Makarov Basin, and further supports our hypothesis of an increased water supply from the BG toward the central Makarov Basin, raising the FWC there.

4.3.3. Freshwater outflow from the Arctic Ocean

We further illustrated changes in the freshwater pathways out of the Amerasian Basin by performing forward trajectories from the center of the Makarov Basin (level 80 m in 2011 and 2017 shown in **Figures 12a-b**). We quantified exits of the particles within the three years after the launch, through the following four gateways: the Fram Strait, the Nares Strait, and the eastern and western part of the Canadian Archipelago (hereafter CA1 and CA2).

Before 2012, the BG had not yet extended toward the North Pole and particles released in the center of the Makarov Basin exited the Arctic via the Nares Strait (~ 20% at 80 m, yellow gate in **Figures 12a** and **12c**) and CA1 (~ 30%, green gate) instead of Fram Strait (~ 3%) or CA2 (~ 4%). Exit pathways changed after 2012, with particles increasingly leaving the Arctic through CA2 (~ 40-80%, blue gate) instead of Fram Strait, Nares Strait, or CA1 **(Figures 12b-c**). This is in accordance with the extended anticyclonic circulation over the Amerasian Basin resulting from BG changes and contributing to transport particles near CA2 **(Figure 12b**). Trajectories also showed that particles reached gateways faster over the years: about 2-3 years were needed in 2017 instead of ~ 3-4 years in 2011 (**Figures 12a-b**, the color of the trajectories is time).

To quantify freshwater exits from the whole Arctic toward the North Atlantic, we computed volume and freshwater outflows (i.e., southward only) at the four gateways, as described in section 2.2. We considered anomalies relative to the 2008-2014 period to document the interannual changes (**Figures 12d-e**). Mean outflow values over the early period (2008-2014), indicated in **Figures 12d-e**, were comparable to those found in the literature (see Wang et al.,

2017, their *Table A1*). Unsurprisingly, PSY4 freshwater outflows over 2008-2014 at Fram and Nares Straits (55 mSv and 36 mSv respectively) were on average smaller than values from Wang et al. (2017), likely resulting from the surface salinity bias described in section 3. Volume and freshwater mean outflows over 2008-2014 at Davis Strait (4.4 Sv and 161 mSv respectively) were larger when compared to 2004-2005 observations from Curry et al. (2011) ($\Delta \sim 2$ Sv and 50 mSv, respectively).

Both volume and freshwater outflow anomalies over 2016-2019 were large through CA2 relative to 2008-2014 (~ +0.8 Sv and +65 mSv, respectively) and downstream through Davis Strait (~ +0.5 Sv and +30 mSv). In contrast, volume and freshwater outflow anomalies at Fram Strait were smaller over the 2016-2019 period (~ -0.5 Sv and -20 mSv, respectively). The interannual evolution of the volume outflow at CA2 was similar to that of the freshwater outflow, implying that part of the freshwater outflow increase resulted from larger volume transport through the gates (blue curve in **Figures 12d-e**). The ratio between the freshwater and volume outflows supported that the 2016 anomaly was also associated with fresher waters exiting through CA2. Peaks of volume outflow anomalies through CA2 and the Davis Strait in 2016 were concomitant, while freshwater outflow anomalies at the Davis Strait lagged CA2 by 1 year (blue and black curves in **Figures 12d-e**).

In summary, trajectories illustrated that freshwater leaking from the BG fed the Makarov Basin following a more direct route from 2012 onwards, which is consistent with the FWC increase in the Makarov and North Pole region. Furthermore, outflows at the exit gateways supported a larger freshwater export through the western Canadian Archipelago rather than through Fram Strait after 2015. The total volume outflow slightly increased by 7% between 2008-2014 (mean of 5.5 Sv) and 2015-2020 (mean of 5.9 Sv), resulting from a decrease of 11% (from 1.9 to 1.7 Sv) at Fram Strait and an increase of 15% (from 3.6 to 4.2 Sv) at the Canadian Archipelago (Nares Strait, CA1 and CA2). Although the change in the total freshwater outflow from the Arctic toward the North Atlantic was rather small (+7.5%, from 230 to 248 mSv), the freshwater outflow at Fram Strait decreased by 30% (from 54 to 40 mSv) while the freshwater outflow at the Canadian Archipelago increased by 16% (from 176 to 207 mSv).

5. Discussion

We evaluated the Mercator Ocean operational physical high-resolution system PSY4 over the entire Arctic Ocean, following the satisfactory assessments performed in the western Arctic Eurasian Basin (e.g., Athanase et al., 2019, 2020, 2021). Salinity biases were generally low, except in the upper 100 m in the Amerasian Basin, as it is often the case in numerical models (e.g., Lique et al., 2016; Regan et al., 2020; Q. Wang et al., 2016). A comparison between the initialization fields in October 2006 and in-situ measurements during the same period showed that the initial condition near the surface layer was already too salty (**Figure S3**). Improving the initial state might contribute to reducing such biases. Moreover, wind-forced redirection of river discharge played a key role in the freshwater accumulation in the BG area (Proshutinsky et al., 2019) and further studies on PSY4 river inputs to the Arctic Basin may help in understanding their possible contribution to surface salinity biases.

At the Fram Strait gateway, AW entering the Arctic was found in good agreement with observations (Athanase et al., 2020). We additionally showed that PSY4 represents realistic Pacific Water hydrographic properties in the Bering Strait when compared to sustained mooring data (Woodgate & Peralta-Ferriz, 2021). Modeled volume and freshwater fluxes at the strait were close to the observation. The cold PWW was in good agreement with observations. We found that modeled AW in the Eurasian Basin and PSW in the Canada Basin were both colder than observations. PSY4 evaluation over the continental shelf such as Barents, Laptev, East Siberian, Chukchi, or Beaufort Seas, was beyond the scope of this study, and these areas would need particular attention in future studies as local shelf processes, such as winter convection, atmosphere-ocean heat exchanges or sea ice melting, are important (e.g., Rudels et al., 2015; Lind et al., 2018; Athanase et al., 2020). The large-scale distribution of SSH was consistent with the Armitage et al. (2017) remotely-sensed altimetry observations, and FWC in PSY4 was congruent to the rather scarce in situ observations in the Arctic Ocean or the mooring data in the Canada Basin (Proshutinsky et al., 2009).

The Arctic FWC is known to have increased since the 1990s and reached a plateau in 2007. We used the 14-year PSY4 simulation to document spatial redistribution of the freshwater and

SSH in the Arctic since 2007 resulting from basin-wide changes. Major findings are shown schematically in **Figure 13** with annual mean model halocline strength quantified by the Available Potential Energy (APE).

As stated in Regan et al. (2019), the BG extended westward over Mendeleev Ridge in 2011 along the East Siberian Sea slope, inducing a FWC increase along the way (orange arrows in **Figure 13a**). In 2012, PSY4 showed that large FWC values started to shift toward the center of the Makarov Basin while the BG extended northward (**Figure 13b**). This coincides with the weakening of the BG under cyclonic winds in 2012 (Zhong et al., 2019). PSY4 showed that freshwater mostly escaped the BG from the west and flowed faster toward the central Makarov Basin. The fresher waters of the gyre are largely composed of Pacific-origin waters (e.g., Hu & Mayers, 2013; Proshutinsky et al., 2019) and a northward extension of the BG contributes to a pacification of the Arctic interior as suggested by Polyakov et al. (2020a). The concomitant deepening of the isohalines near the North Pole led to the reinforcement of the halocline stratification in the center of the Arctic as quantified by the APE (**Figure 13b**). From 2017 onwards, the BG retreated from Mendeleev Ridge to the east, likely favored then by the anomalous cyclonic winds in early 2017 (Moore et al., 2018).

After 2012, the model showed that dense AW progressively shoaled along the East Siberian Sea slope (**Figure 9**) until reaching the Mendeleev Ridge by the end of 2017 (**Figure 7g**). This is in agreement with a previous model-based study that described the thickening and warming of the AW layer as far as the Mendeleev Ridge in 2010-2017, although no change had been found in the AW layer upper boundary (Grabon et al., 2021). Here, the PSY4 simulations showed that the AW shoaling was accompanied by a weakening of the halocline. This weaker halocline was previously restricted to the continental slope in the Nansen Basin (Polyakov et al., 2018) and reached the East Siberian Sea slope in 2020 (blue arrow in **Figure 13b**). Such halocline weakening is associated with the ongoing Atlantification (Polyakov et al., 2017). Observations in the Laptev Sea from 2013 to 2018 (Polyakov et al., 2020b) and near Mendeleev Ridge from 2015 to 2017 (Jung et al., 2021) supported such evolution. In parallel, PSY4 showed that the TPD shifted eastward as the Atlantic-origin waters progressed along the Siberian side of the Makarov Basin after 2012, reaching the Mendeleev Ridge (gray arrow in

Figure 13). The observed increased contribution of Siberian Sea waters to the TPD is congruent with this eastward shift (Alkire et al., 2019; Bertosio et al., 2020; Shen et al., 2016).

We illustrated changes in the freshwater pathways out of the Amerasian Basin by tracking particles released in the Makarov Basin, near the North Pole, where the freshwater content increased from 2014 to 2020. During the 2008-2011 period, the upper layer waters from the Makarov Basin exited through Fram Strait. Following the northward extension of the BG in 2011, more waters recirculated within the Canada Basin, contributing to freshwater recharge of the BG from the east, which is in agreement with Hu et al. (2019) and Wilson et al., (2021).

Over the 2014-2016 period, freshwater outflows increased through the western Canadian Archipelago (CA2; +16% compared to 2008-2014) and decreased through Fram Strait (-30%; same period). Recent observation-based studies documented such a reduction both in liquid and solid freshwater outflow at Fram Strait (Karpouzoglou et al., 2022; Sumata et al., 2022). Wang et al. (2017) suggested that the out-of-phase relationship between the freshwater transports through the Canadian Arctic Archipelago and Fram Strait can be explained by anomalous winds at the Arctic Canadian coastline and to the east of Greenland respectively. Zhang et al. (2021) showed that, during the previous historic BG freshwater release period (1983-1995), the BG freshwater exited the Arctic mostly through the Canadian Archipelago rather than Fram Strait. A similar freshwater release may have significant implications for the Labrador Sea hydrographic properties and eventually for the strength of the Atlantic Meridional Overturning Circulation (Proshutinsky et al., 2019). Changes in circulation identified in PSY4 suggested that an analogous scenario might be at play, with a BG freshwater storage two times larger than the previous historical maximum (Proshutinsky et al., 2019).

We further investigated the response of FWC distribution to the changes in atmospheric circulation patterns using the Arctic Oscillation index (from the NOAA NCEP) (**Figure S5**). Positive peaks in the Arctic Oscillation index (i.e., weak sea level pressure over the Arctic Basin) were followed by an eastward shift of the front, which would be consistent with a cyclonic mode of oceanic circulation characterized by a shifted transpolar front toward the Mendeleev Ridge (Morison et al., 2012, 2021; Wang, 2021; Armitage et al., 2018). Negative

Arctic Oscillation index peaks were followed by the return of the front toward the Lomonosov Ridge, consistent with an intensified anticyclonic circulation in the Canada Basin extending toward the Eurasian basin as described by (Morison et al., 2021; Wang, 2021). However, these qualitative covariations should be considered with caution as PSY4 only spanned the relatively short 2007-2020 period.

6. Conclusion

We evaluated the Mercator Ocean simulations over the upper water column in the Arctic Ocean. The model showed capabilities to reproduce observed hydrographic properties and water mass distributions, as well as spatial patterns of FWC and SSH. The model thus provided insights into the interannual evolution of the Arctic upper water column since 2007.

We found that the BG, the major reservoir of Arctic freshwater, extended northward from 2012-onward and consequently increased the freshwater content in the Makarov Basin, near the North Pole. This freshening of waters in the Makarov Basin resulted in a thickening and strengthening of the halocline layer. In parallel, Atlantic-origin waters shoaled along the East Siberian slope and were associated with a weakened halocline layer.

After 2015, the export of freshwater decreased at Fram Strait (-30% compared to 2008-2014) and increased at the Canadian Archipelago (+16%), followed by an increased export downstream at the Davis Strait a year later. Large freshwater releases could have significant implications for the Labrador Sea hydrographic properties and eventually for the strength of the Atlantic Meridional Overturning Circulation.

Model-derived trajectories in the Amerasian Basin showed the importance of having a sufficient spatial resolution in numerical models to resolve the circulation in the Canadian Archipelago. This study also shows the complementarity of numerical simulations and observations and the great potential of using numerical simulations to broaden the context of Arctic observations. This is especially true with operational systems that, thanks to data assimilation, can minimize biases in the Nordic Seas, the frontier inflow zones of the Arctic Ocean.

FIGURES AND TABLE

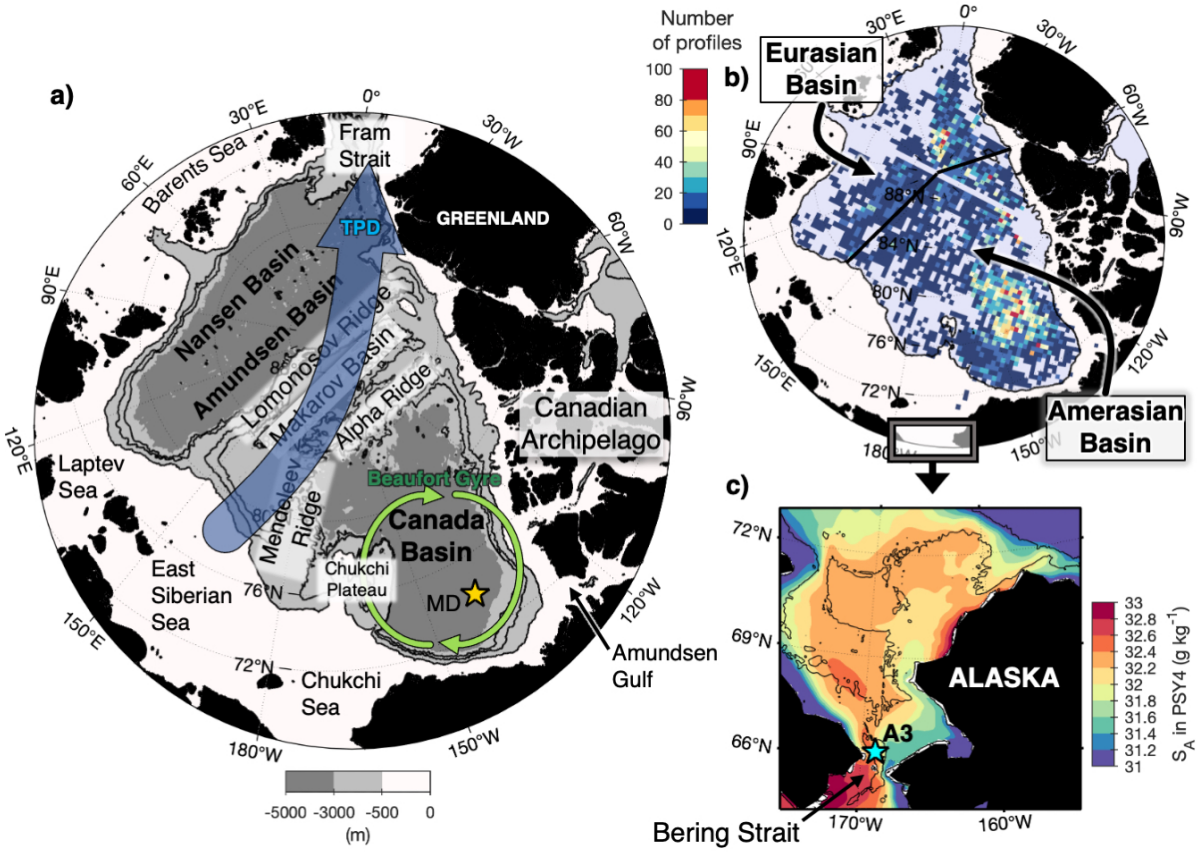

Figure 1: (**a**) Main geographic/bathymetric features. Transpolar Drift (TPD) and Beaufort Gyre are indicated with blue and green arrows respectively. Bathymetry contours correspond to 2 500, 2 000, and 50 m from IBCAO. (**b**) Number of profiles used in this study over the 2007-2014 period. Isobath 500 m is shown in black. The thin black line, corresponding to the Lomonosov Ridge, separates the Eurasian from the Amerasian Basin. (**c**) Close-up of the Bering Strait and the Chukchi Sea. Background colors correspond to PSY4 absolute salinity values over 2007-2020 (at 5 m-depth). The yellow star in (**a**) marks the location of BGEP mooring D (MD). The blue star in (**c**) indicates the location of mooring A3. Bathymetry contours are for depths 50 and 500 m.

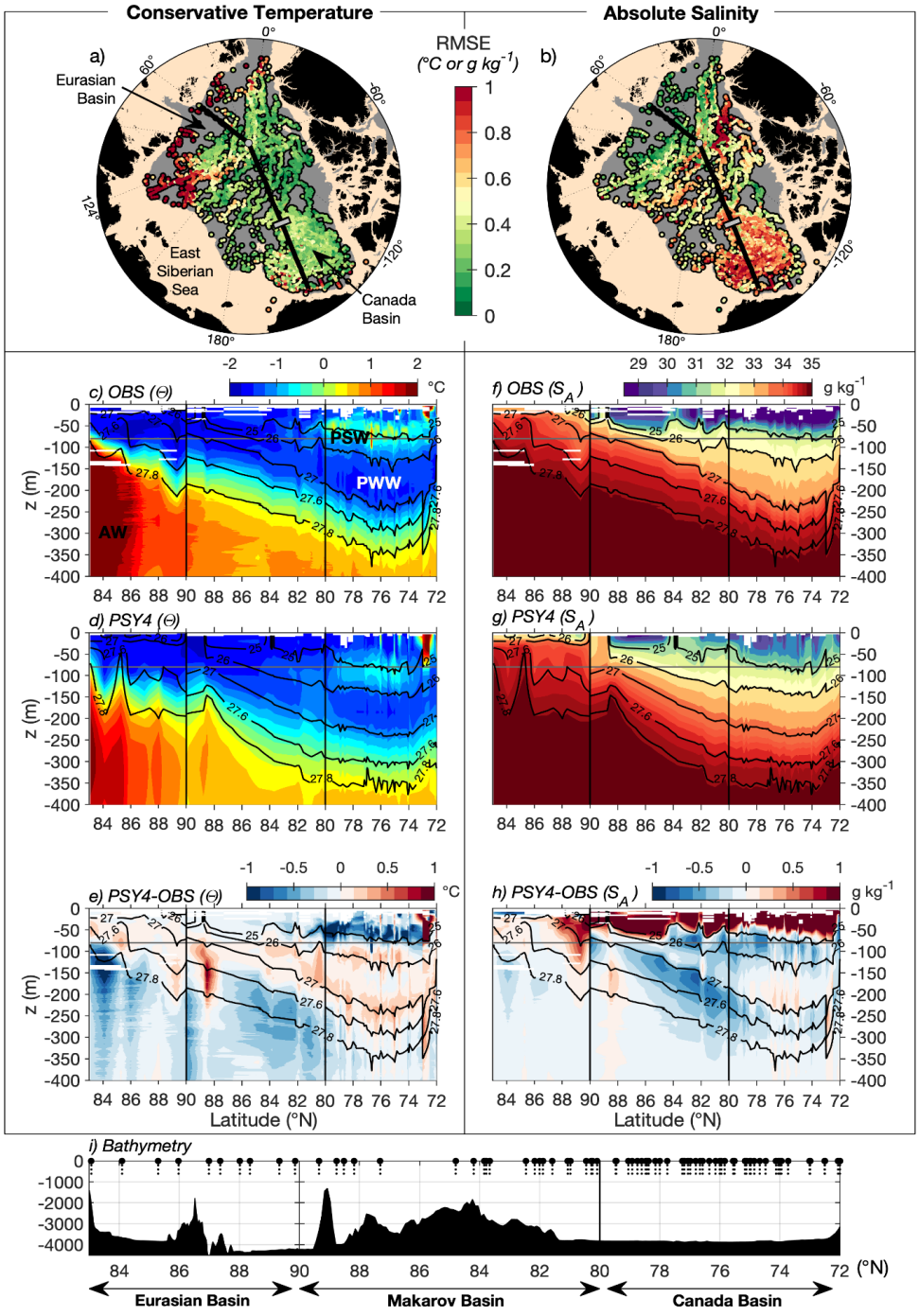

Figure 2: Comparison of the Conservative Temperature Θ (°C) and Absolute Salinity S_A (g kg^{-1}) between PSY4 and in-situ data from UDASH and ITPs. (**a**) Horizontal distribution of the root-mean-square error (RMSE) of Θ over the upper 400 m. (**b**) same as (a) for S_A. Background in grey corresponds to bathymetry deeper than 400 m. The line indicates the location of the section shown below, with a grey tick at 80°N and a grey dot at 90°N for sake of readability. (**c**) Vertical sections of temperature obtained from in-situ profiles closest to the section. Isopycnals are shown in black. The x-axis is latitude (°N). Horizontal gray lines correspond to the depth 80 m. (**d**) Same as (c) with collocated PSY4 profiles. (**e**) Temperature differences PSY4-OBS. (**f**, **g**, **h**) Same as (**c**, **d**, **e**) for S_A. (**h**) Bathymetry below the section that crosses the Eurasian Basin, Makarov Basin, and Canada Basin. Positions of profiles used for the composite sections are indicated. *PWW: Pacific Winter Waters; PSW: Pacific Summer Waters; AW: Atlantic Water*

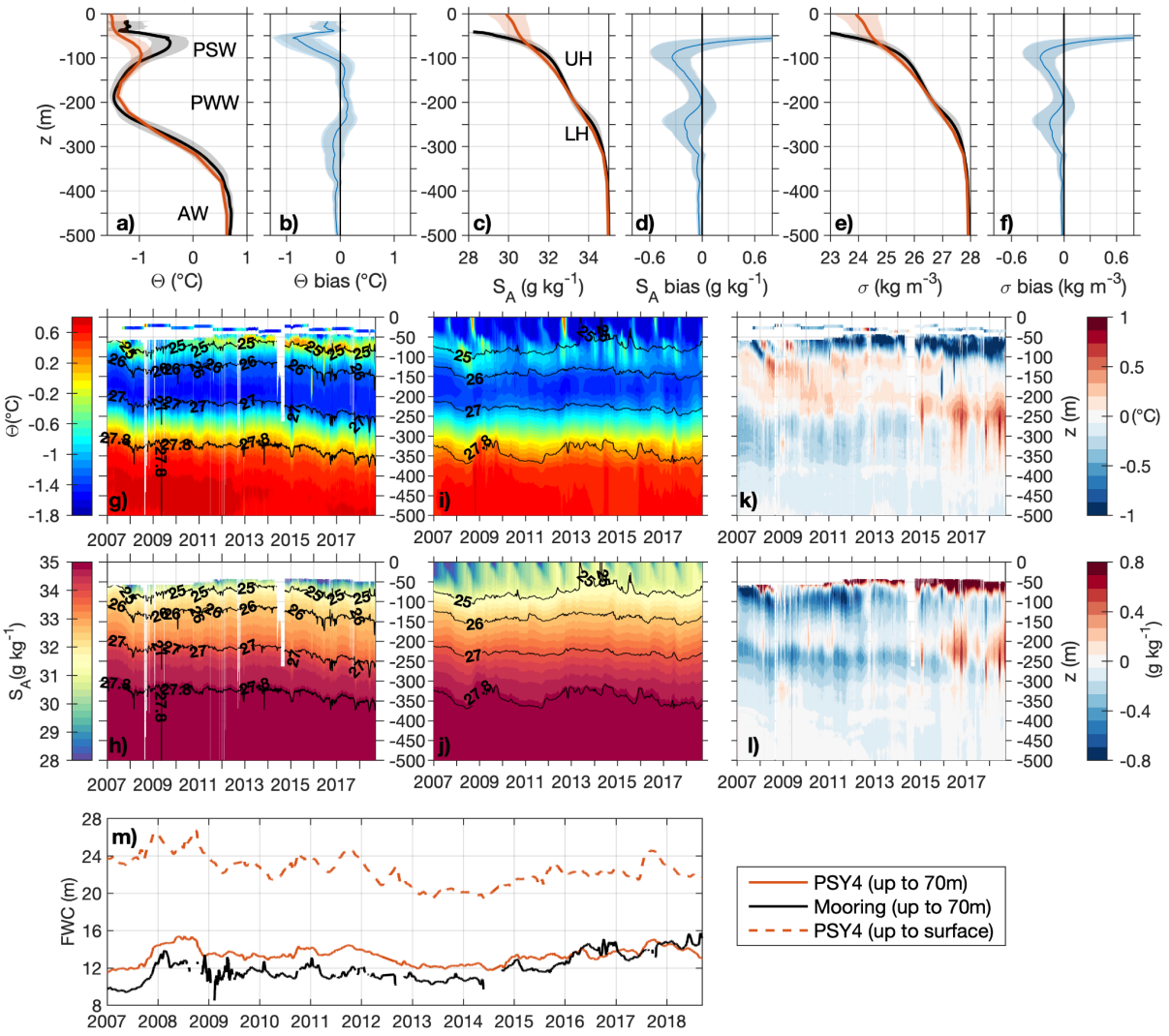

Figure 3: Mean profiles of (**a**) Θ, (**c**) S_A, and (**e**) density σ. Shaded envelopes in grey and light red are standard deviation (STD) around the mean for respectively observations and model. Mean bias profiles of (**b**) Θ, (**d**) S_A, and (**f**) σ. Shaded envelopes are for bias STD (blue) and the sum of model and observations STDs (grey) at each level. Sections of Θ and S_A from mooring D (**g-h**) and in PSY4 (**i-j**). Black lines correspond to isopycnals. Differences in Θ and S_A are respectively shown in (**k**) and (**l**). The x-axis is time and the y-axis is depth. (**m**) Time series of FWC relative to salinity 34.8 and up to 70 m (plain lines) or the surface (dotted line). *PWW: Pacific Winter Waters; PSW: Pacific Summer Waters; AW: Atlantic Water; UH: Upper Halocline; LH: Lower Halocline.*

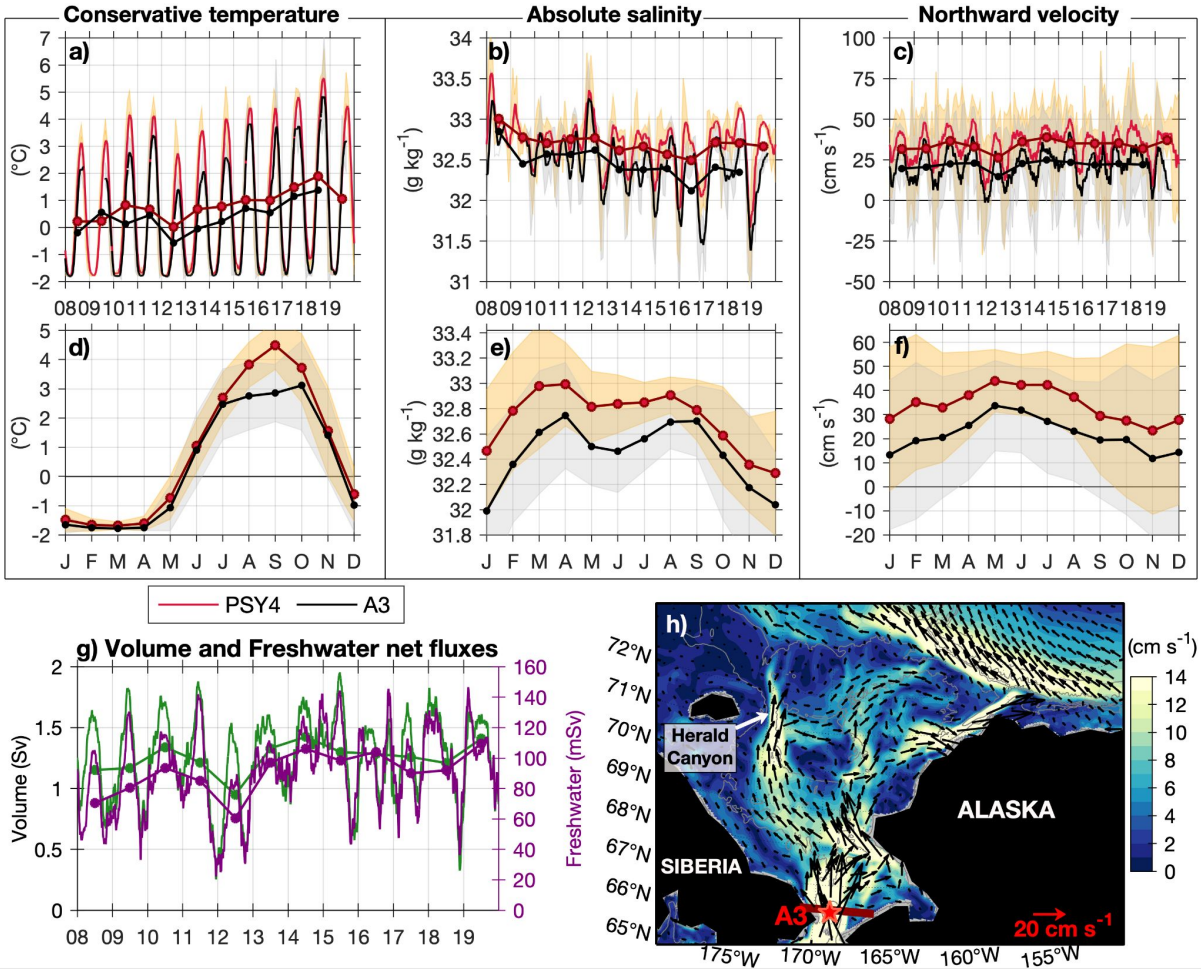

Figure 4: Properties at Bering Strait from mooring A3 data (black) and collocated profile in PSY4 (red). (**a**, **d**) Conservative temperature (Θ; °C) and (**b, e)** absolute salinity (S_A; g kg^{-1}) at 48 m. (**c, f**) Mean northward velocity at 15-40 m (cm s^{-1}). Shaded envelopes are standard deviations (monthly) for observations (grey) and model outputs (orange). (**g**) Net fluxes of volume (green, left y-axis; in Sv) and freshwater (purple, right y-axis; in mSv), positive values being northward fluxes. From (**a**) to (**g**), plain lines and circles correspond to monthly and yearly means respectively. The x-axis gives years (2007-2019) or months (first letter of each month). (**h**) Mean velocities over 2007-2020 in PSY4 at 5 m depth. The mooring A3 position is indicated with a red star.

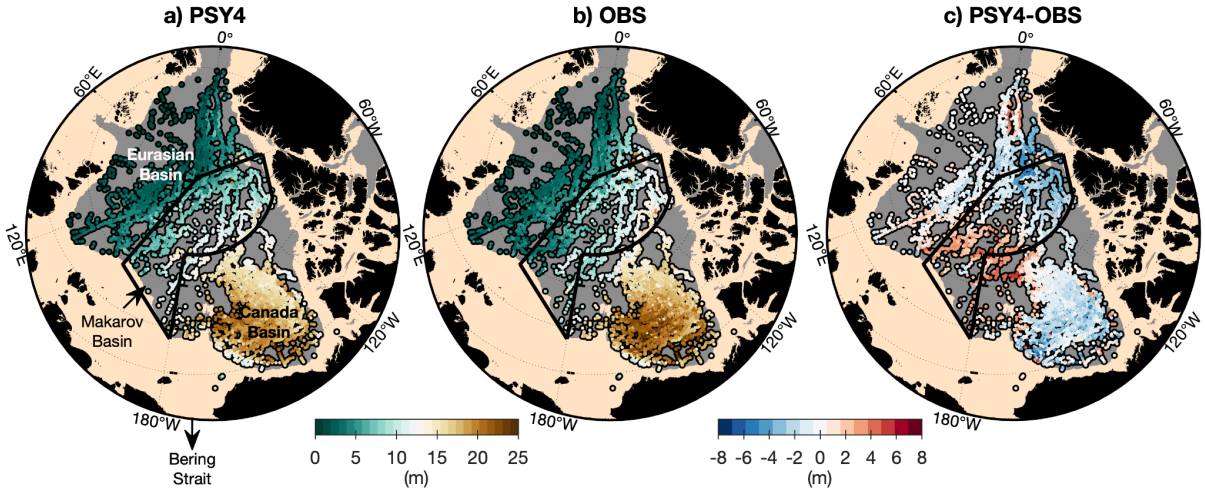

Figure 5: FWC relative to salinity 34.8 psu and computed up to the surface. (**a**) PSY4 profiles collocated both in space and time with observations. (**b**) In-situ profiles. (**c**) Model-observation difference. The black box corresponds to the Makarov Basin.

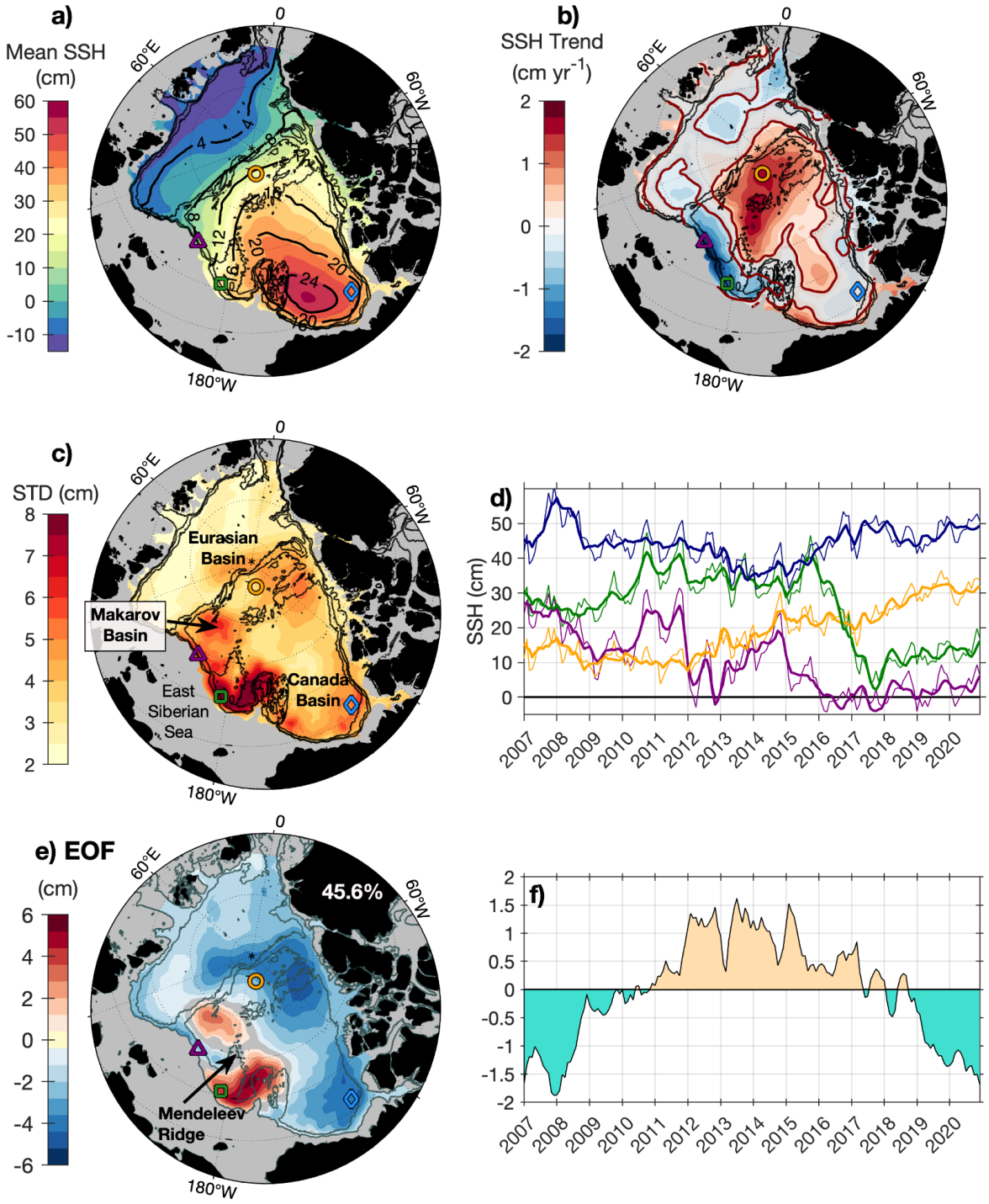

Figure 6: (**a**) Mean PSY4 SSH (cm) over the 2007-2020 period. Isocontours of mean PSY4 FWC are shown in black. (**b**) Yearly trends (cm yr^{-1}). Red isocontours delimit areas where trends are significantly larger than the standard deviation. (**c**) standard deviation from monthly SSH (cm, seasonal cycle removed, detrended field). Time series of (**d**) SSH (thin lines for monthly means and thick lines with seasonal cycle removed) at four locations indicated with colored circles in (**a-c**) (*yellow circle: close to the North Pole; purple triangle: along the East Siberian Sea slope; green square: over the Mendeleev Ridge; blue diamond: close to the Beaufort Sea*). (**e**) SSH EOF1 spatial structure and (**f**) associated Principal Component

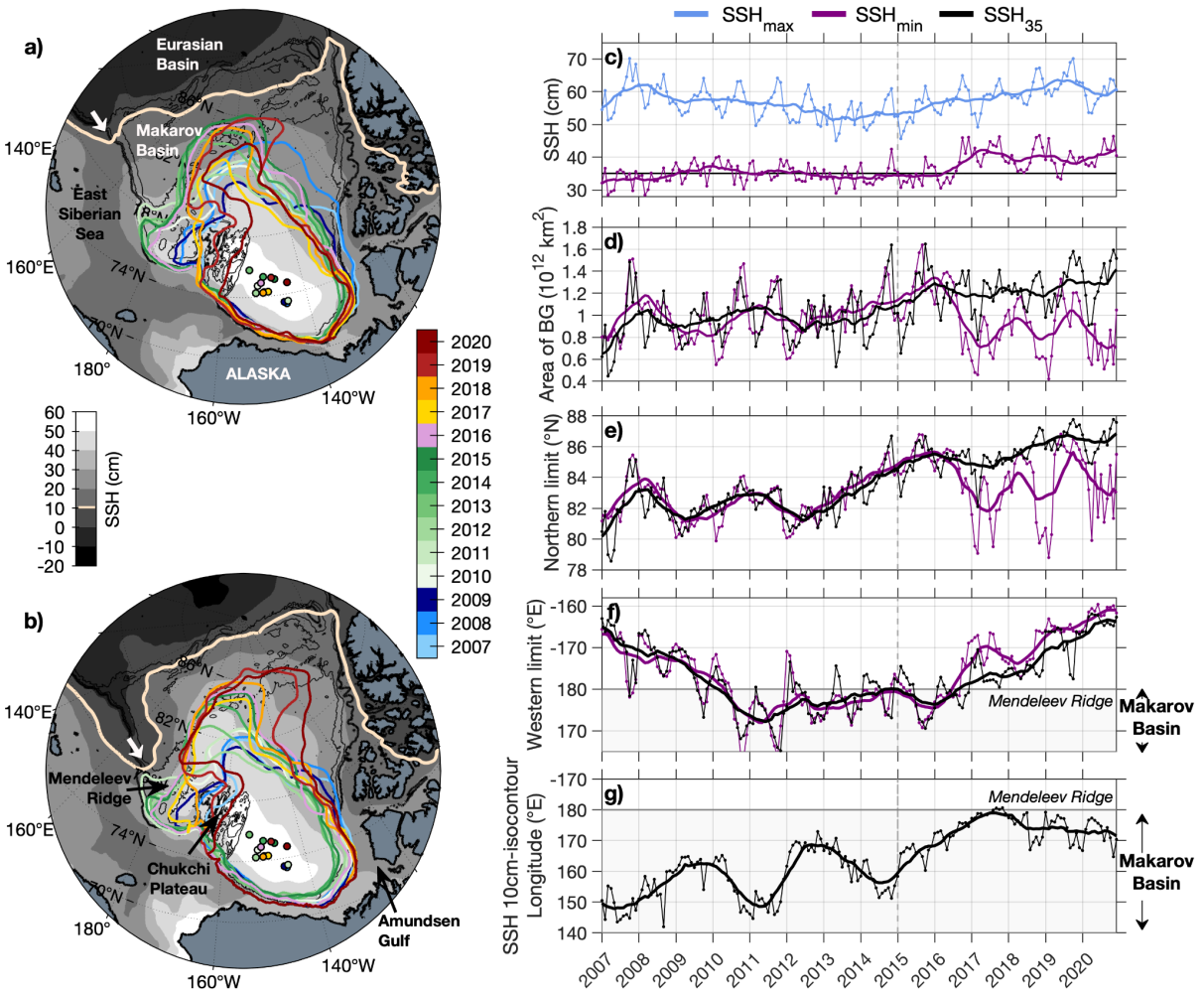

Figure 7: (a) Yearly mean SSH isocontours of the Beaufort Gyre limit from 2007 to 2020 following Regan et al (2019). Centers of the Beaufort Gyre determined from the location of SSH_{max} are indicated for each year. The background color is the SSH field in 2011 and the isocontour SSH = 10 cm is shown in beige. Black isocontours in the background indicate IBCAO bathymetry 2000, 1000, and 500 m (thick black line). **(b)** Same as (a) with Beaufort Gyre limit obtained from SSH isocontour 35 cm. Background color is the SSH field in 2016. **(c)** SSH_{max} corresponding to the Beaufort Gyre center (blue) and SSH_{min} corresponding to the BG limit in (a) (purple). The black line is for SSH = 35 cm. **(d)** Area of the Beaufort Gyre computed in **Figure 11a** (purple) or **11b** (black). **(e)** Northern limit (°N) of the Beaufort Gyre using SSH_{min} (purple) or 35 cm SSH isocontour (black). **(f)** Western limit (°E) of the Beaufort Gyre using SSH_{min} (purple) or 35 cm SSH isocontour (black). **(g)** Longitude of the easternmost point of SSH 10cm-isocontour indicated by the white arrow on (**a-b**). From **(c)** to **(g)**, thin lines are monthly means and thick lines are for 12-months running mean.

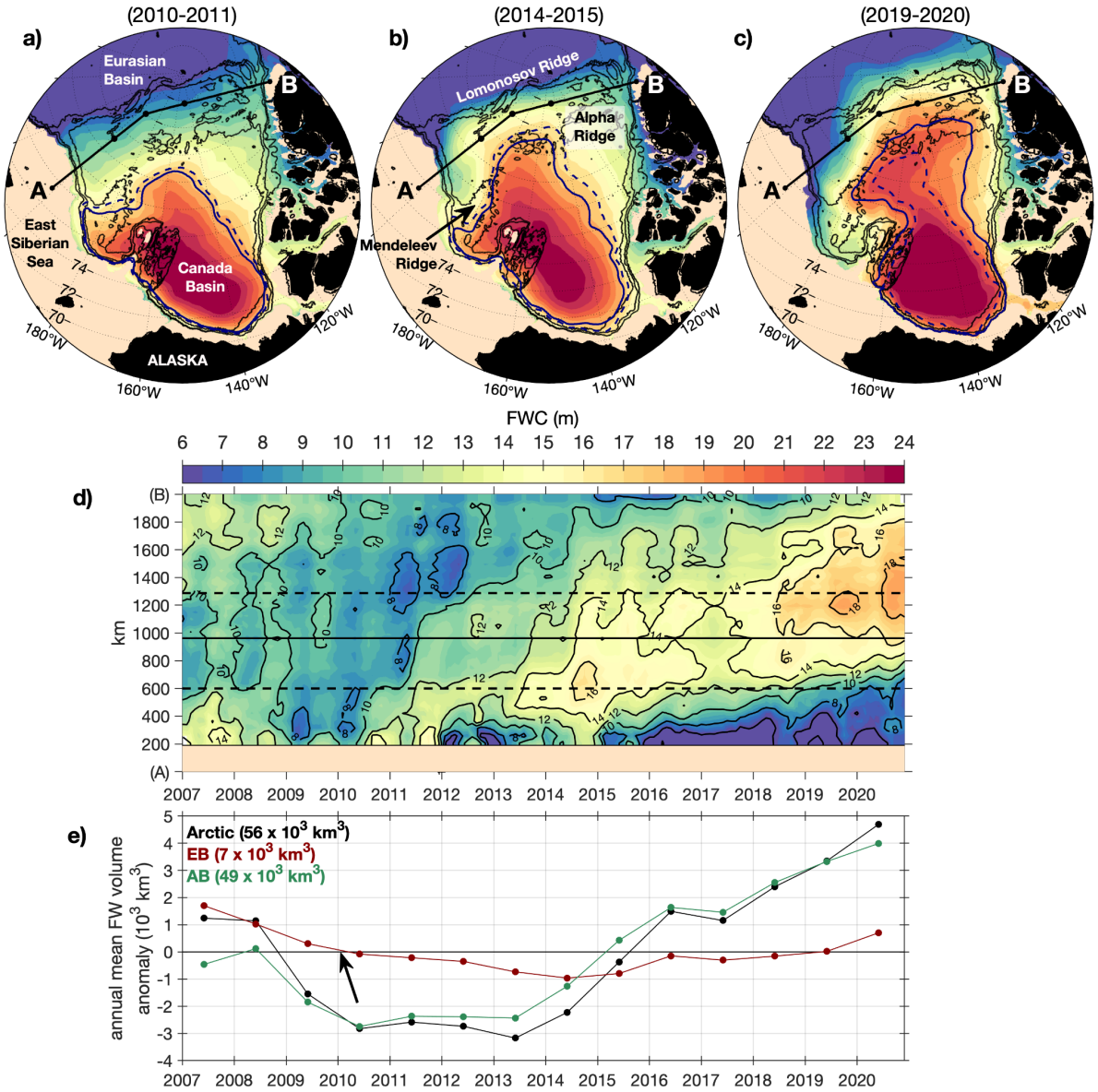

Figure 8: FWC relative to S_{ref} = 34.8 psu in the deep basin (bathymetry > 300 m) averaged over 2-year period (**a**) 2010-2011, (**b**) 2014-2015 and (**c**) 2019-2020. Plain and dashed contours are for BG limits using SSH_{35} or SSH_{min} respectively in 2011, 2015, and 2020. Colorbar is the same as panel (**d**). (**d**) Hovmoller of the monthly FWC along a section across Makarov Basin. The thin black line separates the Siberian side from the eastern side of the basin and corresponds to the black dot in the middle of the section on maps. Dashed lines correspond to the two other black dots of the section. (**e**) Yearly freshwater (FW) volume anomalies over deep basins ("Arctic" in black; bathymetry > 500 m), Eurasian Basin (EB; red), and Amerasian Basin (AB; green). The mean freshwater volume over the 2007-2020 period is given above the panel.

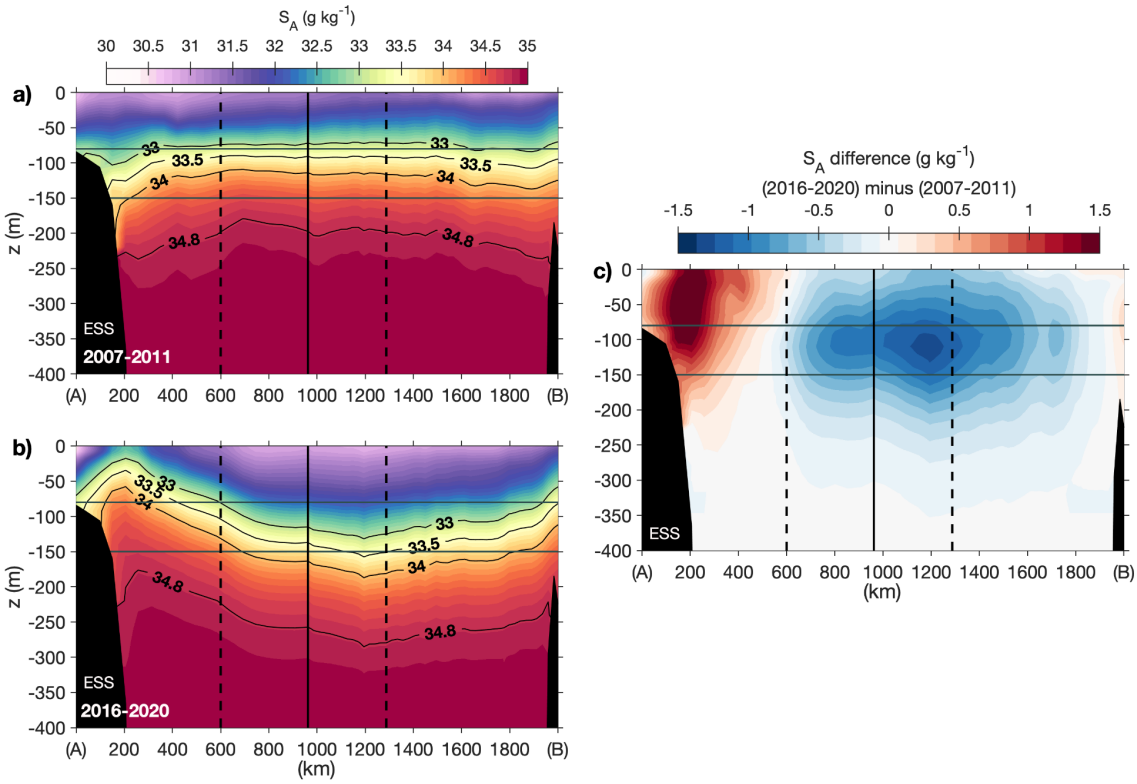

Figure 9: Absolute salinity S_A (g kg^{-1}) averaged over the (**a**) 2007-2011 and (**b**) 2016-2020 periods along the same section in the Makarov Basin already shown in **Figure 8**. The x-axis is the distance (km) starting from ESS. Horizontal black lines indicate 80 m and 150 m depth to ease the reading. The vertical black line separates the Siberian part from the central part of the basin. (**c**) S_A difference between the two periods along the section (g kg^{-1}).

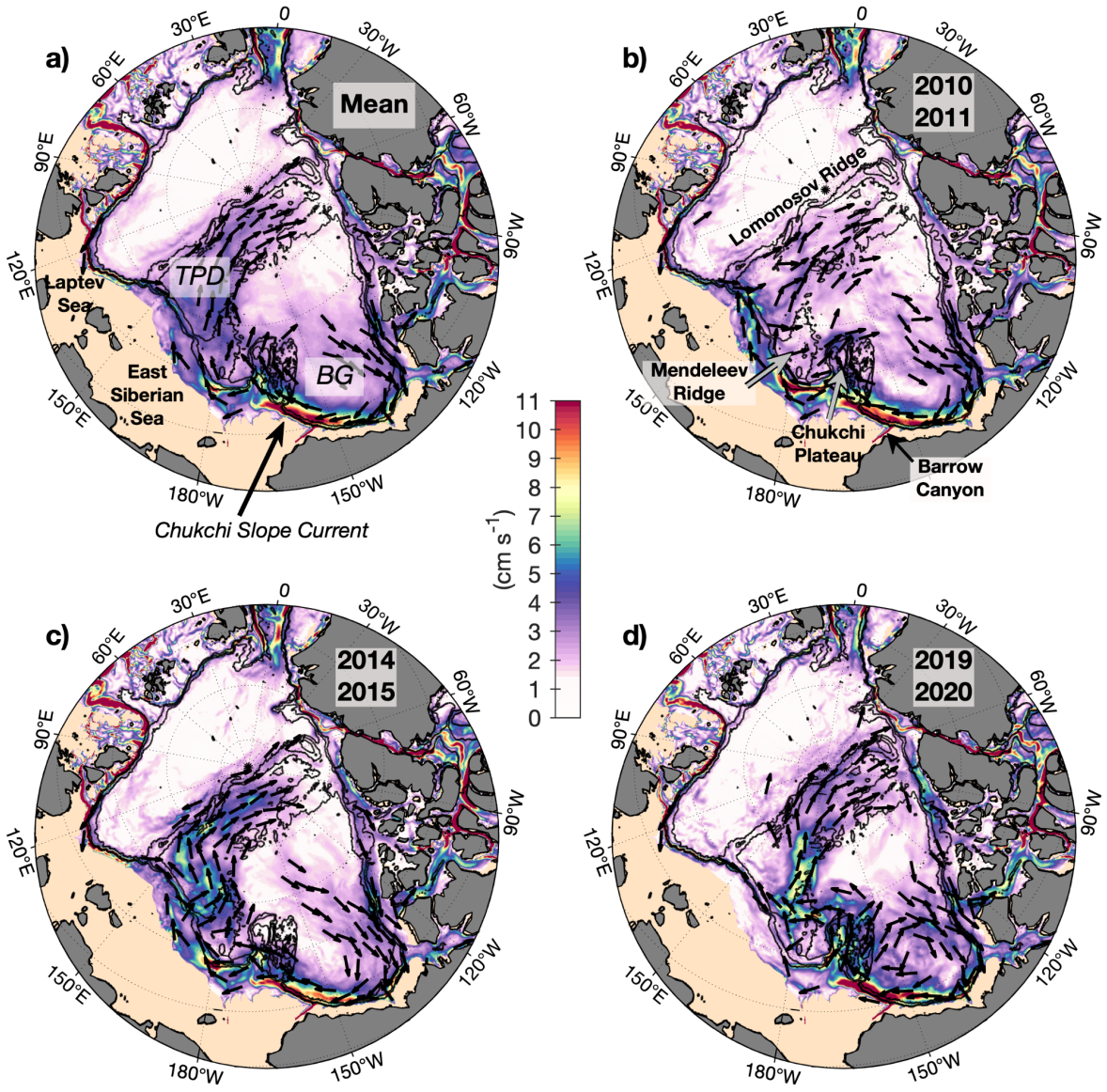

Figure 10: Ocean velocities at 80 m averaged over (**a**) the 2007-2020 period and the 2-year periods (**b**) 2010-2011, (**c**) 2014-2015, and (**d**) 2019-2020. For clarity, normalized velocity vectors are shown only in the Amerasian Basin and if velocity intensity is larger than 2 cm s^{-1} and velocity vectors over the Barents Sea were removed. *TPD: Transpolar Drift; BG: Beaufort Gyre*

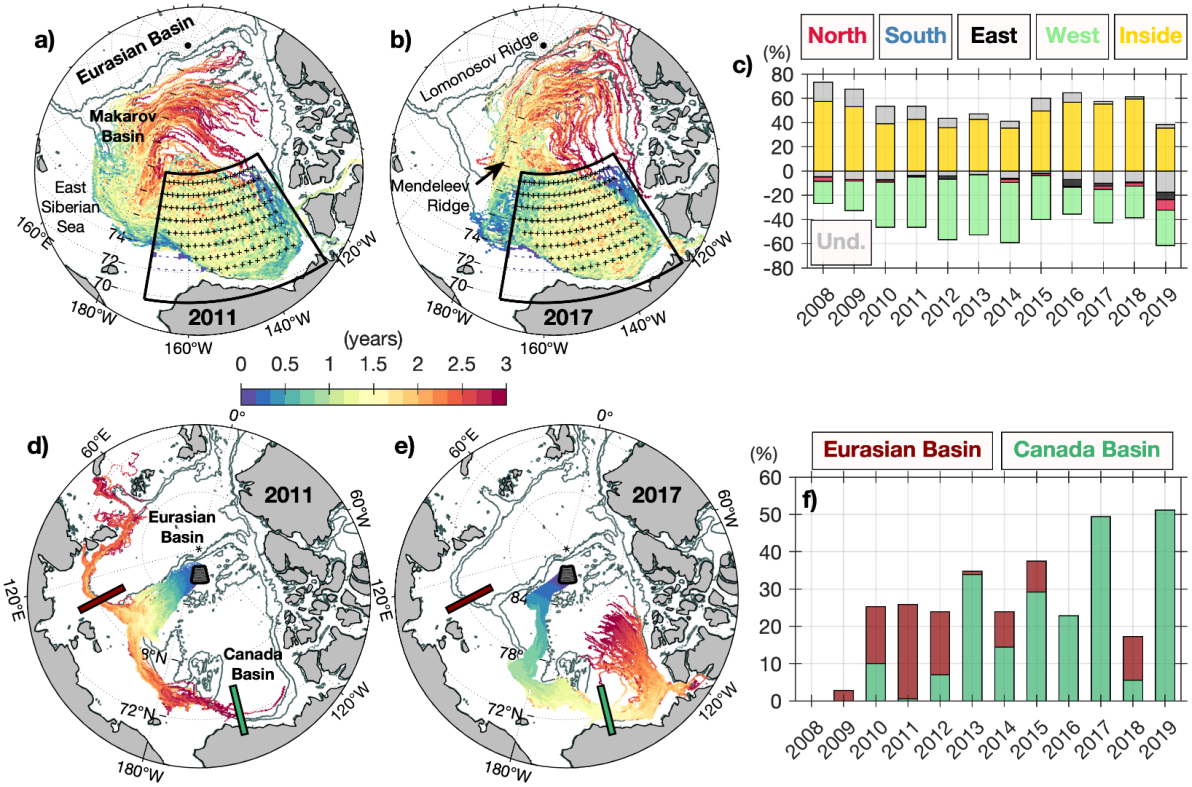

Figure 11: Trajectories calculated with PSY4 daily horizontal velocities fields at 80 m (Color is the time from launch). See section 2.2. for the method. (**a-b**) Forward trajectories of particles launched in the Beaufort Gyre in (**a**) 2011 and (**b**) 2017. (**c**) Percentage of particles entering and leaving for each side of the Beaufort Gyre box (shown in a-b) as a function of launching year, negative values corresponding to the outputs (*South: blue; West: green; North: red; East: black*). *Inside (yellow)* corresponds to particles that never leave the box. *Und (gray)* corresponds to particles that exit and enter several times during their trajectory. (**d-e**) Backward trajectories of particles from the central Makarov Basin launched in (**d**) 2011 and (**e**) 2017. (**f**) Percentage of particles from the central Makarov Basin passing through the Eurasian Basin (red) or Canada Basin (green) gateways during the three years preceding the launch (launch year on the x-axis).

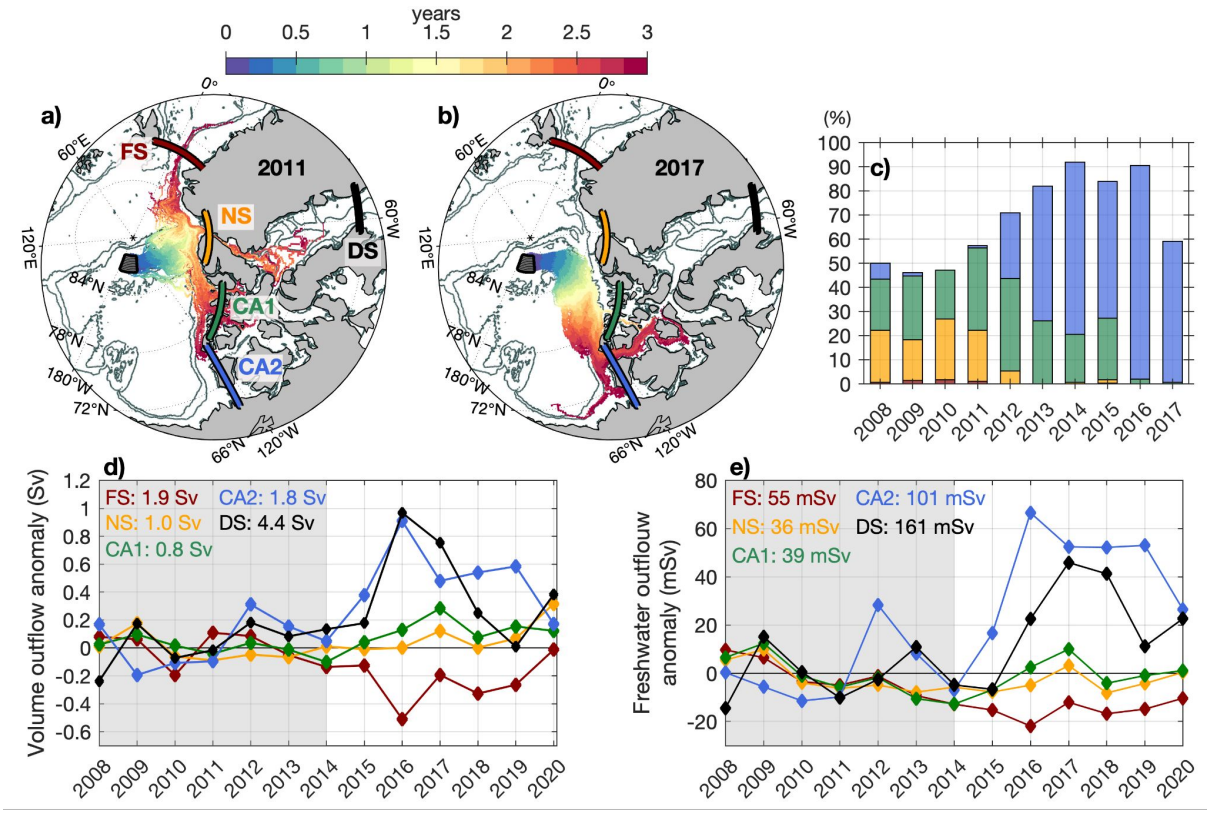

Figure 12: Forward trajectories in central Makarov Basin launched at 80 m in (**a**) 2011 and (**b**) 2017. Gates are shown in color: Fram Strait (FS, red line), Nares Strait (NS, yellow), CA1 (green), CA2 (blue), and Davis Strait (DS, black). (**c**) Percentage of particles leaving the Arctic during the three years following the launch (x-axis). Color corresponds to the gates (FS, NS, CA1, and CA2 only) shown in (**a**). Yearly anomalies relative to the 2008-2014 period (shaded in gray) of (**d**) volume outflow (Sv) and (**e**) freshwater outflow (mSv; reference 34.8 psu) through the gates (mean values over 2008-2014 indicated in color). See section 2.2. for the method.

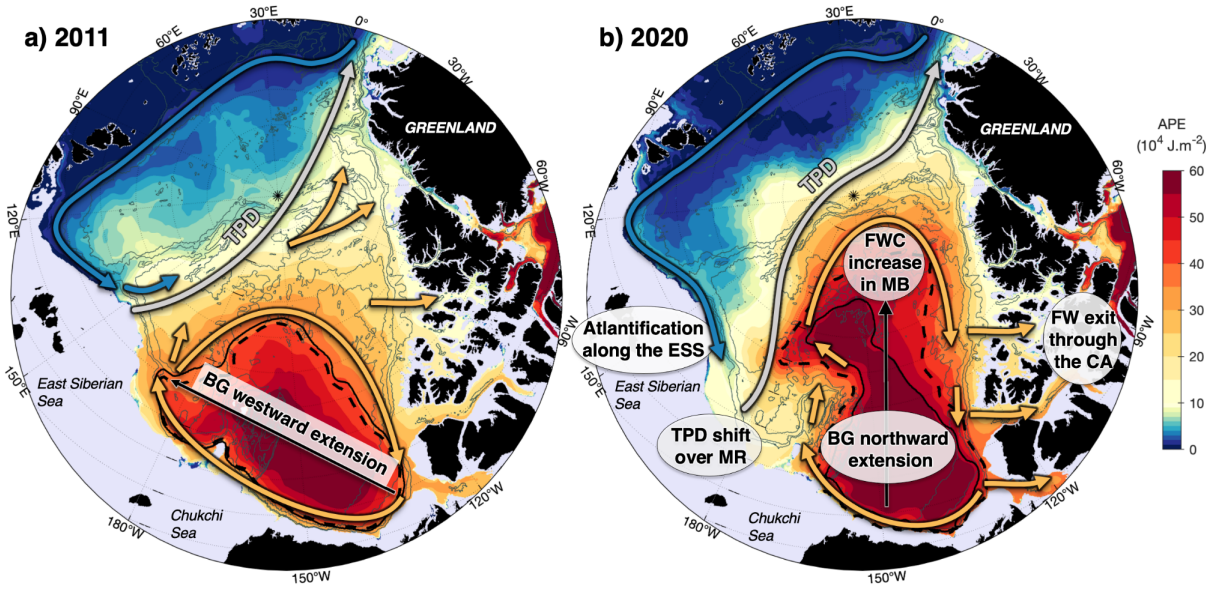

Figure 13: Annual mean model halocline strength in (a) 2011 and (b) 2020 measured with the Available Potential Energy (APE). Schematics arrows highlight major circulation changes (AW in blue and freshwater in orange). Plain and dashed black lines respectively indicate Beaufort Gyre (BG) limits from Regan et al. (2019) criterion and SSH isocontour 35 cm. Before 2012, the BG extended to the west, over Mendeleev Ridge. After 2012, the BG extended northward (yellow arrows) and dense AW shoaled along the East Siberian Sea (ESS) slope (blue arrows). Hence, the freshwater content (FWC) increased in the central Makarov Basin (MB) while it decreased in the Siberian part of the basin. The Transpolar Drift (TPD, in gray arrows) shifted toward Mendeleev Ridge (MR).

Table 1: Data used for model evaluation.

Dataset	Parameters	Dates	Reference	Web site
UDASH database CTD	T, S 19,642 profiles	2007-2015	Behrendt et al. (2018)	*PANGEA*: https://doi.pangaea.de/10.1594 / PANGAEA.872931
Drifting platforms ITPs and IAOOS		2014-2019	Krishfield et al. (2008) Athanase et al. (2019)	*WHOI*:https://www2.whoi.edu /site/beaufortgyre/data/ *SEANOE*: https://doi.org/10.17882/57288
BERING Strait *A3* moorings	T, S, U, V	mid-2007 to mid-2019	Woodgate (2018) Woodgate & Peralta-Ferriz (2021)	http://psc.apl.washington.edu/ HLD/Bstrait/Data/BeringStrait MooringDataArchive.html
BGEP D-moorings	T, S 2,200 profiles	2007-2018	Proshutinsky et al. (2009)	*WHOI*: https://www2.whoi.edu/site/be aufortgyre/data/
CPOM	SSH	2007-2014	Armitage et al. (2016, 2017)	http://www.cpom.ucl.ac.uk/dy namic_topography/
PIOMAS	Ice thickness	2007-2019	Zhang et al. (2003) Schweiger et al. (2011)	http://psc.apl.uw.edu/research/ projects/arctic-sea-ice-volume-anomaly/data/model_grid

Table 2: Statistics of Θ and SA model-observation differences at several layers in the Eurasian and Amerasian Basin*.

Layer (m)		Eurasian Basin				Amerasian Basin			
		Mean	CI (95%)	STD	RMSE	Mean	CI (95%)	STD	RMSE
ΔΘ (°C)	0-20	-0.03	[-0.03;-0.02]	0.2	0.2	-0.11	[-0.12;-0.11]	0.2	0.2
	40-60	+0.05	[+0.05;+0.06]	0.2	0.6	-0.38	[-0.39;-0.37]	0.5	0.6
	80-100	+0.15	[+0.14;+0.16]	0.4	0.3	-0.039	[-0.043;-0.035]	0.2	0.3
	140-160	-0.12	[-0.13;-0.10]	0.6	0.3	+0.11	[+0.11;+0.12]	0.2	0.3
	180-200	-0.30	[-0.30;-0.27]	0.6	0.4	+0.086	[+0.082;+0.09]	0.2	0.4
	240-260	-0.34	[-0.35;-0.32]	0.4	0.3	-0.07	[-0.07;-0.07]	0.3	0.3
	320-340	-0.26	[-0.27;-0.25]	0.3	0.3	-0.14	[-0.14;-0.14]	0.2	0.3
	400-420	-0.22	[-0.23;-0.21]	0.3	0.2	-0.11	[-0.11;-0.11]	0.1	0.2
ΔS_A ($g.kg^{-1}$)	0-20	+0.51	[+0.46;+0.53]	1.2	2.2	+2.0	[+1.98;+2.01]	1.2	2.2
	40-60	+0.36	[+0.34;+0.39]	0.8	0.9	+0.57	[+0.56;+0.58]	0.7	0.9
	80-100	0.00	[-0.01;+0.01]	0.3	0.4	-0.19	[-0.19;-0.18]	0.4	0.4
	140-160	-0.03	[-0.04; -0.03]	0.1	0.2	-0.08	[-0.09;-0.08]	0.2	0.2
	180-200	-0.04	[-0.04;-0.04]	0.1	0.2	-0.10	[-0.10;-0.09]	0.2	0.2
	240-260	-0.04	[-0.04;-0.04]	0.0	0.2	-0.14	[-0.15;-0.14]	0.2	0.2
	320-340	-0.01	[-0.01;-0.01]	0.0	0.1	-0.04	[-0.04;-0.04]	0.1	0.1
	400-420	-0.01	[-0.01;-0.01]	0.0	0.0	-0.02	[-0.02;-0.02]	0.0	0.0

Acknowledgments:

Cecilia Bertosio acknowledges support from the IAOOS grant S18JROI002 at Sorbonne University and Marylou Athanase from a postdoc funded by the BMBF research group Seamless Sea Ice Prediction. This research was a part of the project titled 'Korea-Arctic Ocean Warming and Response of Ecosystem (K-AWARE, KOPRI, 1525011760)', funded by the Ministry of Oceans and Fisheries, Korea. Discussions with H. Regan and P. Prandi are gratefully acknowledged. We thank the two anonymous reviewers for their comments which helped improve the manuscript.

Data Availability Statement:

Hydrographic data from the UDASH database are available on *PANGEA* (https://doi.pangaea.de/10.1594/PANGAEA.872931) (Behrendt et al., 2018). Temperature and salinity from drifting platform profilers ITPs and mooring data (McLane Moored Profiler) in the Canada Basin are available on the *Beaufort Gyre Exploration Project* website (https://www2.whoi.edu/site/beaufortgyre/data/) (Krishfield et al., 2008; Proshutinsky et al., 2009). IAOOS data are available on *SEANOE* (https://doi.org/10.17882/57288). Acoustic Doppler current profiler (ADCP) and temperature and salinity from mooring data in the Bering Strait are available on the *Polar Science Center* website (http://psc.apl.washington.edu/HLD/Bstrait/Data/BeringStraitMooringDataArchive.html) (Woodgate et al. 2015). Dynamic ocean topography data are available on the *Center for Polar Observation and Modelling (CPOM)* website (http://www.cpom.ucl.ac.uk/dynamic_topography/) (Armitage et al., 2016). PIOMAS model grid data are available on the *Polar Science Center* website (http://psc.apl.uw.edu/research/projects/arctic-sea-ice-volume-anomaly/data/model_grid) (Zhang et al., 2003). The Arctic oscillation index is available on the NOAA NCEP website (https://www.cpc.ncep.noaa.gov/products/precip/CWlink/daily_ao_index/ao_index.html).
The model outputs are available at Copernicus Marine Environment Monitoring Service (CMEMS; http://marine.copernicus.eu/).

REFERENCES

Aagaard, K. and R. A. Woodgate, R. A.: Some thoughts on the freezing and melting of sea ice and their effects on the ocean, Ocean Modell., 3, 127–135, 2001. https://doi.org/10.1016/S1463-5003(01)00005-1

Alkire, M. B., Rember, R., & Polyakov, I. (2019). Discrepancy in the Identification of the Atlantic/Pacific Front in the Central Arctic Ocean: NO Versus Nutrient Relationships. Geophysical Research Letters, 46(7), 3843–3852. https://doi.org/10.1029/2018GL081837

Armitage, T. W. K., Bacon, S., & Kwok, R. (2018). Arctic Sea Level and Surface Circulation Response to the Arctic Oscillation. Geophysical Research Letters, 45(13), 6576–6584. https://doi.org/10.1029/2018GL078386

Armitage, T. W. K., Bacon, S., Ridout, A. L., Thomas, S. F., Aksenov, Y., & Wingham, D. J. (2016). Arctic sea surface height variability and change from satellite radar altimetry and GRACE, 2003–2014. Journal of Geophysical Research: Oceans, 121(6), 4303–4322. https://doi.org/10.1002/2015JC011579

Armitage, T. W. K., Bacon, S., Ridout, A. L., Petty, A. A., Wolbach, S., & Tsamados, M. (2017). Arctic Ocean surface geostrophic circulation 2003–2014. The Cryosphere, 11(4), 1767–1780. https://doi.org/10.5194/tc-11-1767-2017

Athanase, M., Provost, C., Artana, C., Pérez-Hernández, M. D., Sennéchael, N., Bertosio, C., et al. (2021). Changes in Atlantic Water circulation patterns and volume transports North of Svalbard over the last 12 years (2008–2020). Journal of Geophysical Research: Oceans, 126, e2020JC016825. https:// doi.org/10.1029/2020JC016825

Athanase, M., Provost, C., Pérez Hernández, M. D., Sennéchael, N., Bertosio, C., Artana, C., et al. (2020). Atlantic Water Modification North of Svalbard in the Mercator Physical System From 2007 to 2020. Journal of Geophysical Research: Oceans, 125(10), e2020JC016463. https://doi.org/10.1029/2020JC016463

Athanase, M., Sennéchael, N., Garric, G., Koenig, Z., Boles, E., & Provost, C. (2019). New Hydrographic Measurements of the Upper Arctic Western Eurasian Basin in 2017 Reveal Fresher Mixed Layer and Shallower Warm Layer Than 2005–2012 Climatology. Journal of Geophysical Research: Oceans, 124(2), 1091–1114. https://doi.org/10.1029/2018JC014701

Behrendt, A., Sumata, H., Rabe, B., & Schauer, U. (2018). UDASH – Unified Database for Arctic and Subarctic Hydrography. Earth System Science Data, 10(2), 1119–1138. https://doi.org/10.5194/essd-10-1119-2018

Bertosio, C., Provost, C., Sennéchael, N., Artana, C., Athanase, M., Boles, E., et al. (2020). The Western Eurasian Basin Halocline in 2017: Insights From Autonomous NO Measurements and the Mercator Physical System. Journal of Geophysical Research: Oceans, 125(7), e2020JC016204. https://doi.org/10.1029/2020JC016204

Beszczynska-Möller, A., R.A. Woodgate, C. Lee, H. Melling, and M. Karcher (2011). A synthesis of exchanges through the main oceanic gateways to the Arctic Ocean. Oceanography 24(3):82–99, https://doi.org/10.5670/oceanog.2011.59.

Boles, E., Provost, C., Garçon, V., Bertosio, C., Athanase, M., Koenig, Z., & Sennéchael, N. (2020). Under-Ice Phytoplankton Blooms in the Central Arctic Ocean: Insights From the First Biogeochemical IAOOS Platform Drift in 2017. Journal of Geophysical Research: Oceans, 125(3), e2019JC015608. https://doi.org/10.1029/2019JC015608

Carmack, E. C. (2007). The alpha/beta ocean distinction: A perspective on freshwater fluxes, convection, nutrients and productivity in high-latitude seas. Deep Sea Research Part II: Topical Studies in Oceanography, 54(23), 2578–2598. https://doi.org/10.1016/j.dsr2.2007.08.018

Carmack, E. C., Yamamoto-Kawai, M., Haine, T. W. N., Bacon, S., Bluhm, B. A., Lique, C., et al. (2016). Freshwater and its role in the Arctic Marine System: Sources, disposition, storage, export, and physical and biogeochemical consequences in the Arctic and global oceans. Journal of Geophysical Research: Biogeosciences, 121(3), 675–717. https://doi.org/10.1002/2015JG003140

Corlett, W. B., & Pickart, R. S. (2017). The Chukchi slope current. Progress in Oceanography, 153, 50–65. https://doi.org/10.1016/j.pocean.2017.04.005

Curry, B., Lee, C. M., & Petrie, B. (2011). Volume, Freshwater, and Heat Fluxes through Davis Strait, 2004–05. Journal of Physical Oceanography, 41(3), 429–436. https://doi.org/10.1175/2010JPO4536.1

Doddridge, E. W., Meneghello, G., Marshall, J., Scott, J., & Lique, C. (2019). A Three-Way Balance in the Beaufort Gyre: The Ice-Ocean Governor, Wind Stress, and Eddy Diffusivity. Journal of Geophysical Research: Oceans, 124(5), 3107–3124. https://doi.org/10.1029/2018JC014897

Fichefet, T. and Maqueda, M. A. (1997). Sensitivity of a global sea ice model to the treatment of ice thermodynamics and dynamics, Journal of Geophysical Research, 102, 12609-12646. https://doi.org/10.1029/97JC00480

Fillipi, J.-B., Komatsu, T., & Tanaka, K. (2010). Simulation of drifting seaweeds in East China Sea. Ecological Informatics, 5(1), 67–72. https://doi.org/10.1016/j.ecoinf.2009.08.011

Good, S. A., Martin, M. J., & Rayner, N. A. (2013). EN4: Quality controlled ocean temperature and salinity profiles and monthly objective analyses with uncertainty estimates. Journal of Geophysical Research: Oceans, 118, 6704–6716. https://doi.org/10.1002/2013JC009067

Grabon, J. S., Toole, J. M., Nguyen, A. T., & Krishfield, R. A. (2021). An analysis of Atlantic water in the Arctic Ocean using the Arctic subpolar gyre state estimate and observations. Progress in Oceanography, 198, 102685. https://doi.org/10.1016/j.pocean.2021.102685

Haine, T. W. N., Curry, B., Gerdes, R., Hansen, E., Karcher, M., Lee, C., et al. (2015). Arctic freshwater export: Status, mechanisms, and prospects. Global and Planetary Change, 125, 13–35. https://doi.org/10.1016/j.gloplacha.2014.11.013

Hu, X., & Myers, P. G. (2013). A Lagrangian view of Pacific water inflow pathways in the Arctic Ocean during model spin-up. OceanModelling, 71, 66–80. https://doi.org/10.1016/j.ocemod.2013.06.007

Hu, X., Myers, P. G., & Lu, Y. (2019). Pacific Water Pathway in the Arctic Ocean and Beaufort Gyre in Two Simulations With Different Horizontal Resolutions. Journal of Geophysical Research: Oceans, 124(8), 6414–6432. https://doi.org/10.1029/2019JC015111

Jahn, A., Aksenov, Y., Cuevas, B. A. de, Steur, L. de, Häkkinen, S., Hansen, E., et al. (2012). Arctic Ocean freshwater: How robust are model simulations? Journal of Geophysical Research: Oceans, 117(C8). https://doi.org/10.1029/2012JC007907

Jung, J., Cho, K.-H., Park, T., Yoshizawa, E., Lee, Y., Yang, E. J., et al. (2021). Atlantic-Origin Cold Saline Water Intrusion and Shoaling of the Nutricline in the Pacific Arctic. Geophysical Research Letters, 48(6), e2020GL090907. https://doi.org/10.1029/2020GL090907

Karcher, M., Smith, J. N., Kauker, F., Gerdes, R., & Smethie, W. M. (2012). Recent changes in Arctic Ocean circulation revealed by iodine-129 observations and modeling. Journal of Geophysical Research: Oceans, 117(C8). https://doi.org/10.1029/2011JC007513

Karpouzoglou, T., de Steur, L., Smedsrud, L. H., & Sumata, H. (2022). Observed changes in the Arctic freshwater outflow in Fram Strait. *Journal of Geophysical Research: Oceans*, *127*, e2021JC018122. https://doi.org/10.1029/2021JC018122

Koenig, Z., Provost, C., Sennéchael, N., Garric, G., & Gascard, J.-C. (2017a). The Yermak Pass Branch: A Major Pathway for the Atlantic Water North of Svalbard? Journal of Geophysical Research: Oceans, 122(12), 9332–9349. https://doi.org/10.1002/2017JC013271

Koenig, Z., Provost, C., Villacieros-Robineau, N., Sennéchael, N., Meyer, A., Lellouche, J.-M., & Garric, G. (2017b). Atlantic waters inflow north of Svalbard: Insights from IAOOS observations and Mercator Ocean global operational system during N-ICE2015. Journal of Geophysical Research: Oceans, 122(2), 1254–1273. https://doi.org/10.1002/2016JC012424

Krishfield, R., Toole, J., Proshutinsky, A., & Timmermans, M.-L. (2008). Automated Ice-Tethered Profilers for Seawater Observations under Pack Ice in All Seasons. Journal of Atmospheric and Oceanic Technology, 25(11), 2091–2105. https://doi.org/10.1175/2008JTECHO587.1

Kwok, R., Spreen, G., & Pang, S. (2013). Arctic sea ice circulation and drift speed: Decadal trends and ocean currents. Journal of Geophysical Research: Oceans, 118(5), 2408–2425. https://doi.org/10.1002/jgrc.20191

Lellouche, J. M., Greiner, E., Galloudec, O. L., Garric, G., Regnier, C., Drevillon, M., et al. (2018). Recent updates to the Copernicus Marine Service global ocean monitoring and forecasting real-time 1/12° high-resolution system. Ocean Science, 14(5), 1093-1126. https://doi.org/10.5194/os-14-1093-2018

Lind, S., Ingvaldsen, R. B., & Furevik, T. (2018). Arctic warming hotspot in the northern Barents Sea linked to declining sea-ice import. Nature Climate Change, 8(7), 634. https://doi.org/10.1038/s41558-018-0205-y

Lique, C., Holland, M. M., Dibike, Y. B., Lawrence, D. M., & Screen, J. A. (2016). Modeling the Arctic freshwater system and its integration in the global system: Lessons learned and

future challenges. Journal of Geophysical Research: Biogeosciences, 121(3), 540–566. https://doi.org/10.1002/2015JG003120

Madec, G., and M. Imbard, 1996: A global ocean mesh to overcome the north pole singularity. Clim. Dyn., 12, 381-388.

Madec, G. and the NEMO team: NEMO ocean engine (2008). Note du Pôle de modélisation, Institut Pierre-Simon Laplace (IPSL), France, No. 27 ISSN, 1288-1619

McDougall, T.J. and Barker, P.M. (2011). Getting started with TEOS-10 and the Gibbs Seawater (GSW) Oceanographic Toolbox, 28pp., SCOR/IAPSO WG127, ISBN 978-0- 646-55621-5.

Moore, G. W. K., Schweiger, A., Zhang, J., & Steele, M. (2018). Collapse of the 2017 Winter Beaufort High: A Response to Thinning Sea Ice? Geophysical Research Letters, 45(6), 2860–2869. https://doi.org/10.1002/2017GL076446

Morison, J., Steele, M., & Andersen, R. (1998). Hydrography of the upper Arctic Ocean measured from the nuclear submarine U.S.S. Pargo. Deep Sea Research Part I: Oceanographic Research Papers, 45(1), 15–38. https://doi.org/10.1016/S0967-0637(97)00025-3

Morison, J., Kwok, R., Peralta-Ferriz, C., Alkire, M., Rigor, I., Andersen, R., & Steele, M. (2012). Changing Arctic Ocean freshwater pathways. Nature, 481(7379), 66–70. https://doi.org/10.1038/nature10705

Morison, J., Kwok, R., Dickinson, S., Andersen, R., Peralta-Ferriz, C., Morison, D., et al. (2021). The Cyclonic Mode of Arctic Ocean Circulation. Journal of Physical Oceanography, 51(4), 1053–1075. https://doi.org/10.1175/JPO-D-20-0190.1

Pisareva, M. N., Pickart, R. S., Spall, M. A., Nobre, C., Torres, D. J., Moore, G. W. K., & Whitledge, T. E. (2015). Flow of pacific water in the western Chukchi Sea: Results from the 2009 RUSALCA expedition. Deep Sea Research Part I: Oceanographic Research Papers, 105, 53–73. https://doi.org/10.1016/j.dsr.2015.08.011

Polyakov, I. V., Alkire, M. B., Bluhm, B. A., Brown, K. A., Carmack, E. C., Chierici, M., et al. (2020a). Borealization of the Arctic Ocean in Response to Anomalous Advection From Sub-Arctic Seas. Frontiers in Marine Science, 7. https://doi.org/10.3389/fmars.2020.00491

Polyakov, I. V., Pnyushkov, A. V., Alkire, M. B., Ashik, I. M., Baumann, T. M., Carmack, E. C., et al. (2017). Greater role for Atlantic inflows on sea-ice loss in the Eurasian Basin of the Arctic Ocean. Science, 356(6335), 285–291. https://doi.org/10.1126/science.aai8204

Polyakov, I. V., Pnyushkov, A. V., & Carmack, E. C. (2018). Stability of the Arctic halocline: A new indicator of arctic climate change. Environmental Research Letters, 13(12), 125,008. https://doi.org/10.1088/1748-9326/aaecle

Polyakov, I. V., Rippeth, T. P., Fer, I., Alkire, M. B., Baumann, T. M., Carmack, E. C., et al. (2020b). Weakening of Cold Halocline Layer Exposes Sea Ice to Oceanic Heat in the Eastern Arctic Ocean. Journal of Climate, 33(18), 8107–8123. https://doi.org/10.1175/JCLI-D-19-0976.1

Proshutinsky, A., Bourke, R. H., & McLaughlin, F. A. (2002). The role of the Beaufort Gyre in Arctic climate variability: Seasonal to decadal climate scales. Geophysical Research Letters, 29(23), 15-1-15–4. https://doi.org/10.1029/2002GL015847

Proshutinsky, A., Dukhovskoy, D., Timmermans, M.-L., Krishfield, R., & Bamber Jonathan, L. (2015). Arctic circulation regimes. Philosophical Transactions of the Royal Society A: Mathematical, Physical and Engineering Sciences, 373(2052), 20140160. https://doi.org/10.1098/rsta.2014.0160

Proshutinsky, A., Krishfield, R., Timmermans, M.-L., Toole, J., Carmack, E., McLaughlin, F., et al. (2009). Beaufort Gyre freshwater reservoir: State and variability from observations. Journal of Geophysical Research: Oceans, 114(C1). https://doi.org/10.1029/2008JC005104

Proshutinsky, A., Krishfield, R., Toole, J. M., Timmermans, M.-L., Williams, W., Zimmermann, S., et al. (2019). Analysis of the Beaufort Gyre Freshwater Content in 2003–2018. Journal of Geophysical Research: Oceans, 124(12), 9658–9689. https://doi.org/10.1029/2019JC015281

Proshutinsky, A., & Johnson, M. A. (1997). Two circulation regimes of the wind-driven Arctic Ocean. Journal of Geophysical Research: Oceans, 102(C6), 12493–12514. https://doi.org/10.1029/97JC00738

Rabe, B., Karcher, M., Kauker, F., Schauer, U., Toole, J. M., Krishfield, R. A., et al. (2014). Arctic Ocean basin liquid freshwater storage trend 1992–2012. Geophysical Research Letters, 41(3), 961-968. https://doi.org/10.1002/2013GL058121

Rahmstorf, S., Box, J. E., Feulner, G., Mann, M. E., Robinson, A., Rutherford, S., & Schaffernicht, E. J. (2015). Exceptional twentieth-century slowdown in Atlantic Ocean overturning circulation. Nature Climate Change, 5(5), 475–480. https://doi.org/10.1038/nclimate2554

Regan, H., Lique, C., & Armitage, T. W. K. (2019). The Beaufort Gyre Extent, Shape, and Location Between 2003 and 2014 From Satellite Observations. Journal of Geophysical Research: Oceans, 124(2), 844–862. https://doi.org/10.1029/2018JC014379

Regan, H., Lique, C., Talandier, C., & Meneghello, G. (2020). Response of Total and Eddy Kinetic Energy to the recent spin up of the Beaufort Gyre. Journal Of Physical Oceanography, 50(3), 575–594. https://doi.org/10.1175/JPO-D-19-0234.1

Rudels, B., Anderson, L. G., & Jones, E. P. (1996). Formation and evolution of the surface mixed layer and halocline of the Arctic Ocean. Journal of Geophysical Research: Oceans, 101(C4), 8807–8821. https://doi.org/10.1029/96JC00143

Rudels, B., Korhonen, M., Schauer, U., Pisarev, S., Rabe, B., & Wisotzki, A. (2015). Circulation and transformation of Atlantic water in the Eurasian Basin and the contribution of the Fram Strait inflow branch to the Arctic Ocean heat budget. Progress in Oceanography, 132, 128–152. https://doi.org/10.1016/j.pocean.2014.04.003

Schweiger, A., Lindsay, R., Zhang, J., Steele, M., Stern, H., & Kwok, R. (2011). Uncertainty in modeled Arctic sea ice volume. Journal of Geophysical Research: Oceans, 116(C8). https://doi.org/10.1029/2011JC007084

Serreze, M. C., Barrett, A. P., Slater, A. G., Woodgate, R. A., Aagaard, K., Lammers, R. B., Steele, M., Moritz, R., Meredith, M., and Lee, C. M. (2006). The large-scale freshwater cycle of the Arctic, J. Geophys. Res., 111, C11010. https://doi.org/10.1029/2005JC003424

Shen, Y., Benner, R., Robbins, L., & Wynn, J. (2016). Sources, Distributions, and Dynamics of Dissolved Organic Matter in the Canada and Makarov Basins. Frontiers in Marine Science, 3. https://doi.org/10.3389/fmars.2016.00198

Shimada, K., Itoh, M., Nishino, S., McLaughlin, F., Carmack, E. C., & Proshutinsky, A. (2005). Halocline structure in the Canada Basin of the Arctic Ocean. Geophysical Research Letters, 32(3). https://doi.org/10.1029/2004GL021358

Solomon, A., Heuzé, C., Rabe, B., Bacon, S., Bertino, L., Heimbach, P., et al. (2020). Freshwater in the Arctic Ocean 2010-2019. Ocean Science Discussions, 1–28. https://doi.org/10.5194/os-2020-113

Spall, M. A., Pickart, R. S., Fratantoni, P. S., & Plueddemann, A. J. (2008). Western Arctic Shelfbreak Eddies: Formation and Transport. Journal of Physical Oceanography, 38(8), 1644–1668. https://doi.org/10.1175/2007JPO3829.1

Stabeno, P., Kachel, N., Ladd, C., & Woodgate, R. (2018). Flow Patterns in the Eastern Chukchi Sea: 2010–2015. Journal of Geophysical Research: Oceans, 123(2), 1177–1195. https://doi.org/10.1002/2017JC013135

Sumata, H., de Steur, L., Gerland, S., Divine, D. V., and Pavlova, O. (2022). Unprecedented decline of Arctic sea ice outflow in 2018. Nat Commun 13, 1747. https://doi.org/10.1038/s41467-022-29470-7

Swift, J. H., Jones, E. P., Aagaard, K., Carmack, E. C., Hingston, M., MacDonald, R. W., et al. (1997). Waters of the Makarov and Canada basins. Deep Sea Research Part II: Topical Studies in Oceanography, 44(8), 1503–1529. https://doi.org/10.1016/S0967-0645(97)00055-6

Thompson, D. W. J., & Wallace, J. M. (1998). The Arctic oscillation signature in the wintertime geopotential height and temperature fields. Geophysical Research Letters, 25(9), 1297–1300. https://doi.org/10.1029/98GL00950

Timmermans, M.-L., & Jayne, S. R. (2016). The Arctic Ocean Spices Up. Journal of Physical Oceanography, 46(4), 1277–1284. https://doi.org/10.1175/JPO-D-16-0027.1

Timmermans, M.-L., & Marshall, J. (2020). Understanding Arctic Ocean circulation: A review of ocean dynamics in a changing climate. Journal of Geophysical Research: Oceans, 125, e2018JC014378. https:// doi.org/10.1029/2018JC014378

Toole, J.M., Krishfield, R.A., Timmermans, M.-L., & Proshutinsky A. (2011). The Ice-Tethered Profiler: Argo of the Arctic. Oceanography 24(3):126–135, http://dx.doi.org/10.5670/ oceanog.2011.64.

Wang, Q. (2021). Stronger Variability in the Arctic Ocean Induced by Sea Ice Decline in a Warming Climate: Freshwater Storage, Dynamic Sea Level and Surface Circulation. Journal of Geophysical Research: Oceans, 126(3), e2020JC016886. https://doi.org/10.1029/2020JC016886

Wang, Q., Ilicak, M., Gerdes, R., Drange, H., Aksenov, Y., Bailey, D. A., et al. (2016). An assessment of the Arctic Ocean in a suite of interannual CORE-II simulations. Part I: Sea ice and solid freshwater. Ocean Modelling, 99, 110–132. https://doi.org/10.1016/j.ocemod.2015.12.008

Wang, X., Key, J., Kwok, R., & Zhang, J. (2016). Comparison of Arctic Sea Ice Thickness from Satellites, Aircraft, and PIOMAS Data. Remote Sensing, 8(9), 713. https://doi.org/10.3390/rs8090713

Wang, Z., Hamilton, J., & Su, J. (2017). Variations in freshwater pathways from the Arctic Ocean into the North Atlantic Ocean. Progress in Oceanography, 155, 54–73. https://doi.org/10.1016/j.pocean.2017.05.012

Wilson, C., Aksenov, Y., Rynders, S., Kelly, S. J., Krumpen, T., & Coward, A. C. (2021). Significant variability of structure and predictability of Arctic Ocean surface pathways affects basin-wide connectivity. Communications Earth & Environment, 2(1), 1–10. https://doi.org/10.1038/s43247-021-00237-0

Winters, K. B., Lombard, P. N., Riley, J. J., & D'Asaro, E. A. (1995). Available potential energy and mixing in density-stratified fluids. Journal of Fluid Mechanics, 289, 115–128. https://doi.org/10.1017/S002211209500125X

Woodgate, R. A. (2018). Increases in the Pacific inflow to the Arctic from 1990 to 2015, and insights into seasonal trends and driving mechanisms from year-round Bering Strait mooring data. Progress in Oceanography, 160, 124–154. https://doi.org/10.1016/j.pocean.2017.12.007

Woodgate, R. A., & Peralta-Ferriz, C. (2021). Warming and freshening of the Pacific inflow to the Arctic from 1990-2019 implying dramatic shoaling in Pacific Winter Water ventilation of the Arctic water column. Geophysical Research Letters, 48, e2021GL092528. https://doi.org/10.1029/2021GL092528

Woodgate, R. A., Stafford, K., & Prahl, F. (2015). A Synthesis of Year-Round Interdisciplinary Mooring Measurements in the Bering Strait (1990–2014) and the RUSALCA Years (2004–2011). Oceanography, 28. Retrieved from https://doi.org/10.5670/oceanog.2015.57

Woodgate, R. A., Weingartner, T. J., & Lindsay, R. (2012). Observed increases in Bering Strait oceanic fluxes from the Pacific to the Arctic from 2001 to 2011 and their impacts on the Arctic Ocean water column. Geophysical Research Letters, 39(24). https://doi.org/10.1029/2012GL054092

Zemskova, V. E., White, B. L., & Scotti, A. (2015). Available Potential Energy and the General Circulation: Partitioning Wind, Buoyancy Forcing, and Diapycnal Mixing. Journal of Physical Oceanography, 45(6), 1510–1531. https://doi.org/10.1175/JPO-D-14-0043.1

Zhang, Jiaxu, Weijer, W., Steele, M., Cheng, W., Verma, T., & Veneziani, M. (2021). Labrador Sea freshening linked to Beaufort Gyre freshwater release. Nature Communications, 12(1), 1229. https://doi.org/10.1038/s41467-021-21470-3

Zhang, Jinlun & Rothrock, D. A. (2003). Modeling global sea ice with a thickness and enthalpy distribution model in generalized curvilinear coordinates, Mon. Wea. Rev. 131(5), 681-697. https://doi.org/10.1175/1520-0493(2003)131<0845:MGSIWA>2.0.CO;2

Zhang, Jinlun, Steele, M., Runciman, K., Dewey, S., Morison, J., Lee, C., et al. (2016). The Beaufort Gyre intensification and stabilization: A model-observation synthesis. Journal of Geophysical Research: Oceans, 121(11), 7933–7952. https://doi.org/10.1002/2016JC012196

Zhong, W., Zhang, J., Steele, M., Zhao, J., & Wang, T. (2019). Episodic Extrema of Surface Stress Energy Input to the Western Arctic Ocean Contributed to Step Changes of Freshwater Content in the Beaufort Gyre. Geophysical Research Letters, 46(21), 12173–12182. https://doi.org/10.1029/2019GL084652

Journal of Geophysical Research Ocean

Supporting Information for

Changes in freshwater distribution and pathways in the Arctic Ocean since 2007 in the Mercator Ocean global operational system

Cécilia Bertosio[1], Christine Provost[1], Marylou Athanase[2], Nathalie Sennéchael[1], Gilles Garric[3], Jean-Michel Lellouche[3], Clément Bricaud[3], Joo-Hong Kim[4], Kyoung-Ho Cho[4], Taewook Park[4]

[1]: Laboratoire LOCEAN-IPSL, Sorbonne Université (UPMC, Univ. Paris 6), CNRS, IRD, MNHN, Paris, France
[2]: Alfred-Wegener-Institut, Bremerhaven, Germany
[3]: MERCATOR-OCEAN, Toulouse, France
[4]: Division of Polar Ocean Sciences, Korea Polar Research Institute, Incheon 21990, Republic of Korea

Contents of this file

Text S1, S3, S6, S7
Figures S1 to S7

UDASH database information

The UDASH database provided a unique access to temperature and salinity data in the Arctic Ocean. We only considered profiles from the UDASH database. Most profiles cover the 2007-2019 period and are from the Canada Basin (**Figure S1**). Summer profiles spanned the entire Arctic (**Figure S1d**) whereas winter profiles were predominantly available in the Amundsen and Canada Basins (**Figure S1c**). Nevertheless, the final archive provided a unique access to temperature and salinity data in the Arctic Ocean.

Initial conditions, spin-up and bathymetry in PSY4

Initial conditions and spin-up: The PSY4 system was initialized in October 2006 using temperature and salinity from EN4.2.1 fields (Good et al., 2013). The October 2006 salinity field exhibited unexpected patterns in particular in the Nansen Basin with local minima or

maxima radiating from the slope towards the pole along the 50°E, 90°E and 130°E longitudes (**Figure S3**), likely created by an undesirable interpolation issue in data-sparse areas. No such patterns are visible in the Canada Basin. Radiating patterns in Eurasian Basin faded away, more rapidly in top layers than in deep layers, and were entirely dissipated in April 2008 (not shown). We considered 15 months as a reasonable time for the spin-up in the Eurasian Basin (see annex in Athanase et al., 2020) and temperatures and salinities should be considered from April 2008-onwards. In the Canada Basin evolution of temperatures and salinities are smooth starting from January 2007. PSY4 fields were considered trustworthy for the evaluation of modeled temperature and salinity.

Bathymetry: PSY4 bathymetry is a combination of interpolated ETOPO1 (Amante & Eakins, 2009) and GEBCO8 (Becker et al., 2009) databases. ETOPO1 datasets are used in regions deeper than 300 m, GEBCO8 in regions shallower than 200 m and a linear interpolation is performed in the 200–300 m layer. We examined the difference between PSY4 bathymetry (**Figure S6a**) and IBCAO (International Bathymetric Chart of the Arctic Ocean version 3.0, Jakobsson et al., 2012) (**Figure S6b**). IBCAO was interpolated to the PSY4 grid for comparison. A large-scale pattern shows up in the deep Amerasian Basin (depth > 3500 m) where PSY4 seafloor is shallower by 50 to 150 m (**Figure S6c**), resulting in a small relative error (< 5%). Other differences are small scale patterns and include the slope region near Kvitøya trough in the western Nansen Basin (discussed in Athanase et al. (2020), their figure A1).

Sea-ice in PSY4 compared to PIOMAS

Ice concentration from the two systems PSY4 and PIOMAS were in very good agreement (**Figures S7a-c**). Ice thickness distribution was consistent in the two systems (**Figures S7d-f**), despite the presence of thicker ice near the Beaufort Sea (more than 1 m) and thinner north of Greenland (~ 0.5 m, **Figure S7f**) in the PSY4 system.

Comparisons with ice draft time series from mooring D near the Beaufort Sea showed that PIOMAS ice thicknesses were closer to the mooring measurements (mean difference ~ 0.16 m) than PSY4 (~ 0.85 m, **Figure S7h**). Sea-ice growth and/or accumulation during winter was overestimated in PSY4 (from December to April, **Figure S7g**), leading to ice thickness excess up to 1 m from April to June. PSY4 ice

thickness was closer to observations by the end of the ice-melting season (in September) (**Figure S7g**). Interannual variations of Arctic sea-ice volume in PIOMAS and PSY4 were consistent with an overall decrease over 2007-2019, and a short-lived rebound over 2013-2015 (**Figure S7f**). Indeed, the two monthly time series of the volume anomaly (seasonal cycle removed) were well correlated after 2010 ($r^2 = 0.72$ over 2010-2019 and $r^2 = 0.56$ over 2007-2019), suggesting that PSY4 sea-ice volume might be in a spin-up phase during these first three years.

REFERENCES

Amante, C. & Eakins, B. W. (2009): ETOPO1 1 arc-minute global relief model: Procedures, data sources and analysis, NOAA Technical Memorandum NESDIS NGDC-24, 25 pp.

Athanase, M., Provost, C., Pérez-Hernández, M. D., Sennéchael, N., Bertosio, C., Artana, C., et al. (2020). Atlantic Water Modification North of Svalbard in the Mercator Physical System From 2007 to 2020. Journal of Geophysical Research: Oceans, 125(10), e2020JC016463. https://doi.org/10.1029/2020JC016463

Becker, J. J., Sandwell, D. T., Smith, W. H. F., Braud, J., Binder, B., & Depner, J. (2009). Global bathymetry and elevation data at 30 arc seconds resolution: SRTM30PLUS. Marine Geodesy, 32(4), 355–371. https://doi.org/10.1080/01490410903297766

Good, S. A., Martin, M. J., & Rayner, N. A. (2013). EN4: Quality controlled ocean temperature and salinity profiles and monthly objective analyses with uncertainty estimates. Journal of Geophysical Research: Oceans, 118, 6704–6716. https://doi.org/10.1002/2013JC009067

Jakobsson, M., Mayer, L., Coakley, B., Dowdeswell, J. A., Forbes, S., Fridman, B., et al. (2012). The international bathymetric chart of the Arctic Ocean (IBCAO) version 3.0. Geophysical Research Letters, 39, L12609. https://doi.org/10.1029/2012GL052219

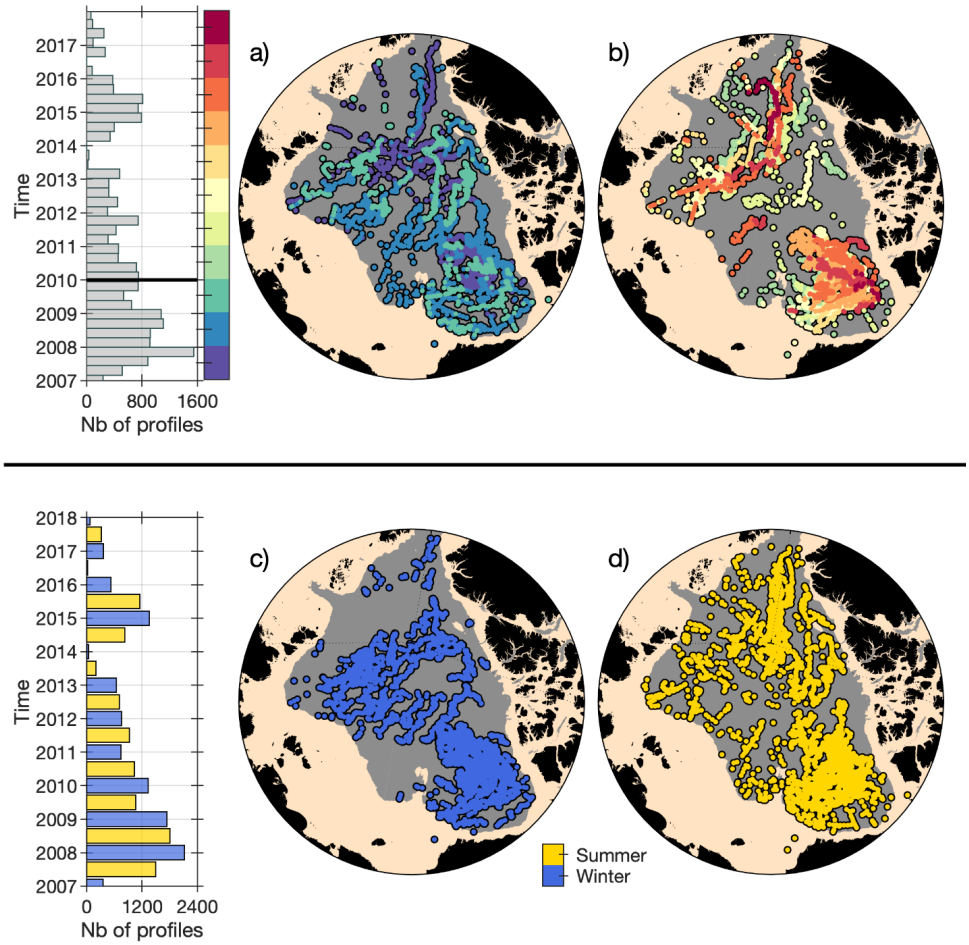

Figure S1: Spatial (maps) and temporal (histograms) distribution of in-situ data from UDASH database and drifting platforms. Color is year (**a** and **b**) or season (**c** and **d**). Note that summer is from April to September and winter from October to March of the next year.

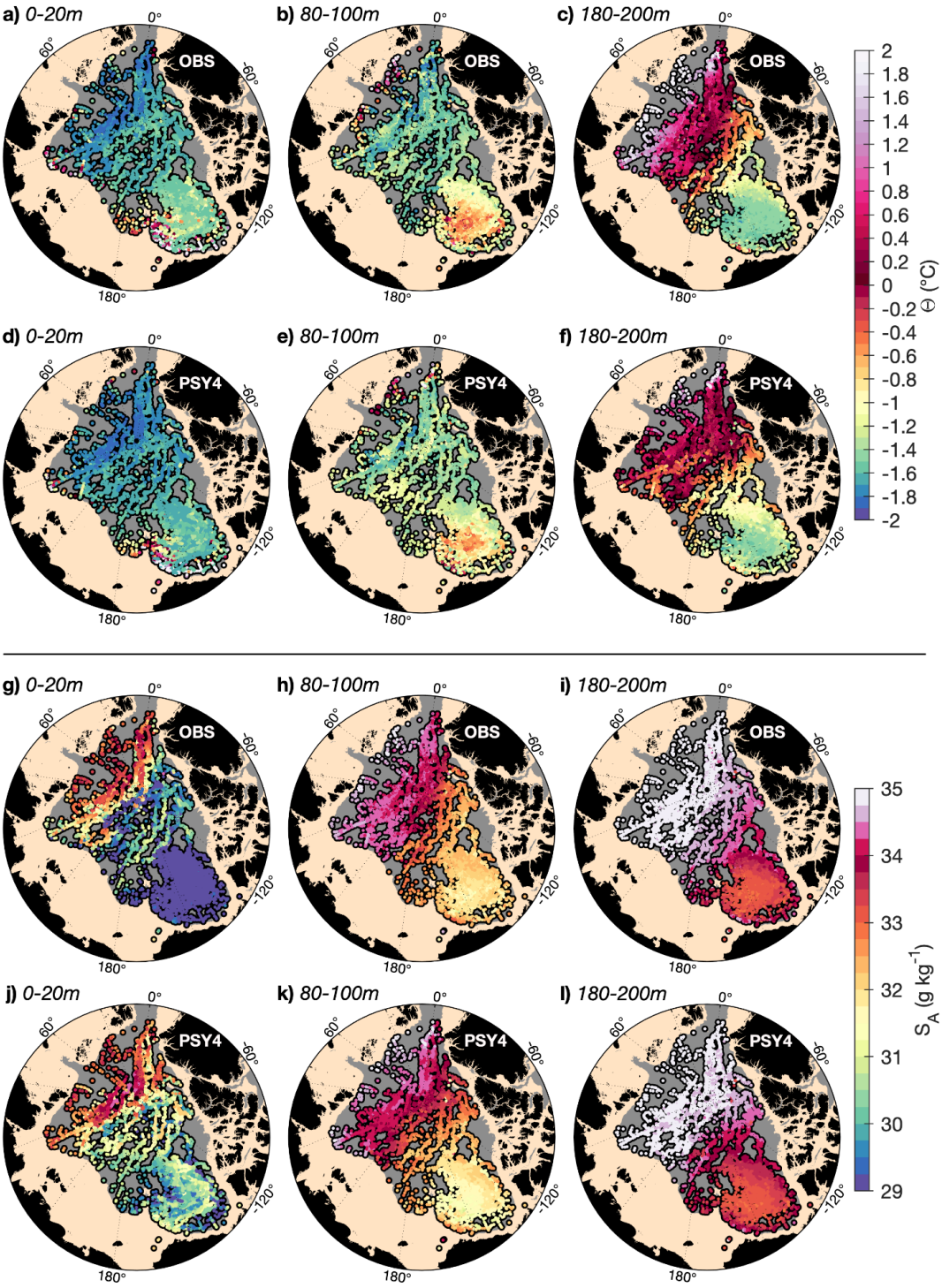

Figure S2: (Top) Conservative temperature Θ (°C) and (**bottom**) Absolute salinity S_A (g kg^{-1}) in (**a-c** and **g-i)** UDASH and (**d-f** and **j-l**) PSY4 profiles at several layers: (**a, d, g, j**) 0-20 m, (**b, e, h, k)** 80-100 m and (**c, f, i, l**) 180-200 m. Background in grey corresponds to bathymetry deeper than 500 m. Black line indicates the location of the section used in this paper with a grey bar at 80°N and grey dot at 90°N to help the reader.

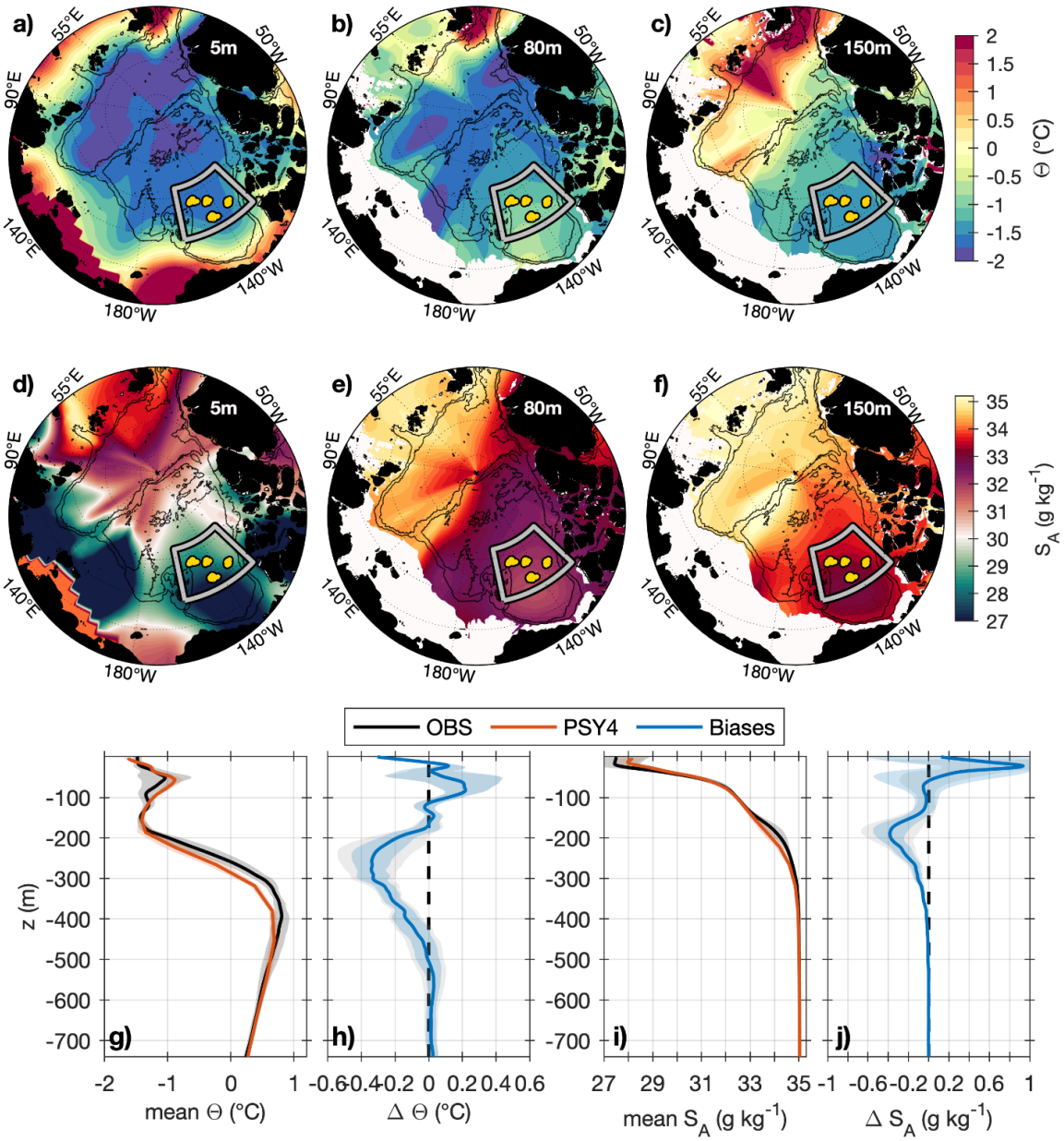

Figure S3: PSY4 initial conditions of (**a-c**) Conservative temperature (°C) and (**d-f**) Absolute Salinity (S_A, g kg^{-1}) in October 2006 and at (**a, d**) 5, (**b, e**) 80 and (**c, f**) 150 m-depth. Mean profiles from UDASH (black) and PSY4 (orange) in October 2006 of (**g**) temperature and (**i**) salinity. Location of the profiles are indicated by yellow dots in the gray box on maps. Profile differences are shown in (**h**) and (**j**). Shaded envelopes are for bias STD (blue) and sum of model and observations STDs (grey).

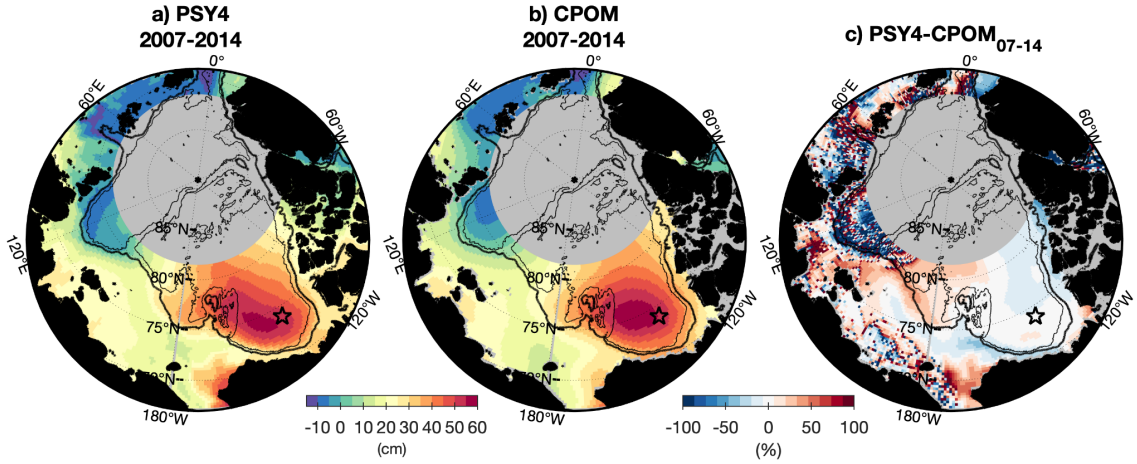

Figure S4: (**a**) PSY4 and (**b**) CPOM mean SSH over the 2007-2014 period and (**c**) the difference (in percentage relative to CPOM values).

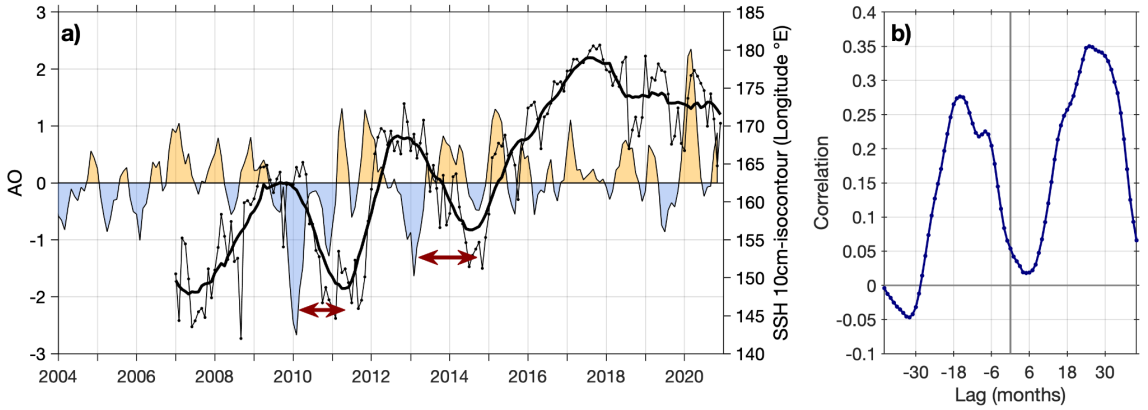

Figure S5: (**a**) Four month running mean of the monthly Arctic Oscillation index (blue-orange shades) and longitude of SSH 10 cm-isocontour along the Siberian slope (in black) as in Figure 10. Red arrows indicate noteworthy negative AO peaks followed by the decrease of the longitude which corresponds to the return of the front toward the Lomonosov Ridge. (**b**) Correlations between the AO and the longitude of the 10 cm-isocontour along the Siberian slope for several time lags (in months). Correlation is maximal with a 25-months time lag.

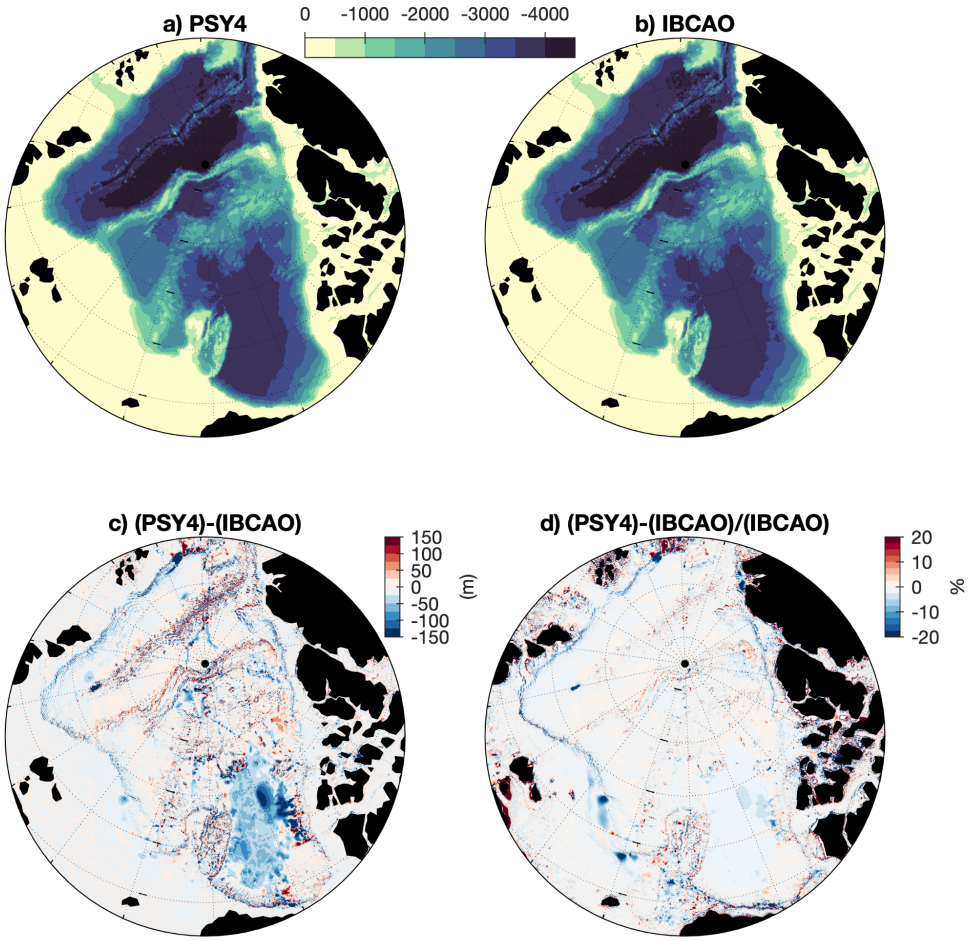

Figure S6: Bathymetry from PSY4 (**a**) and IBCAO (**b**). Difference in meters (**c**) and percentages (**d**) between PSY4 and IBCAO.

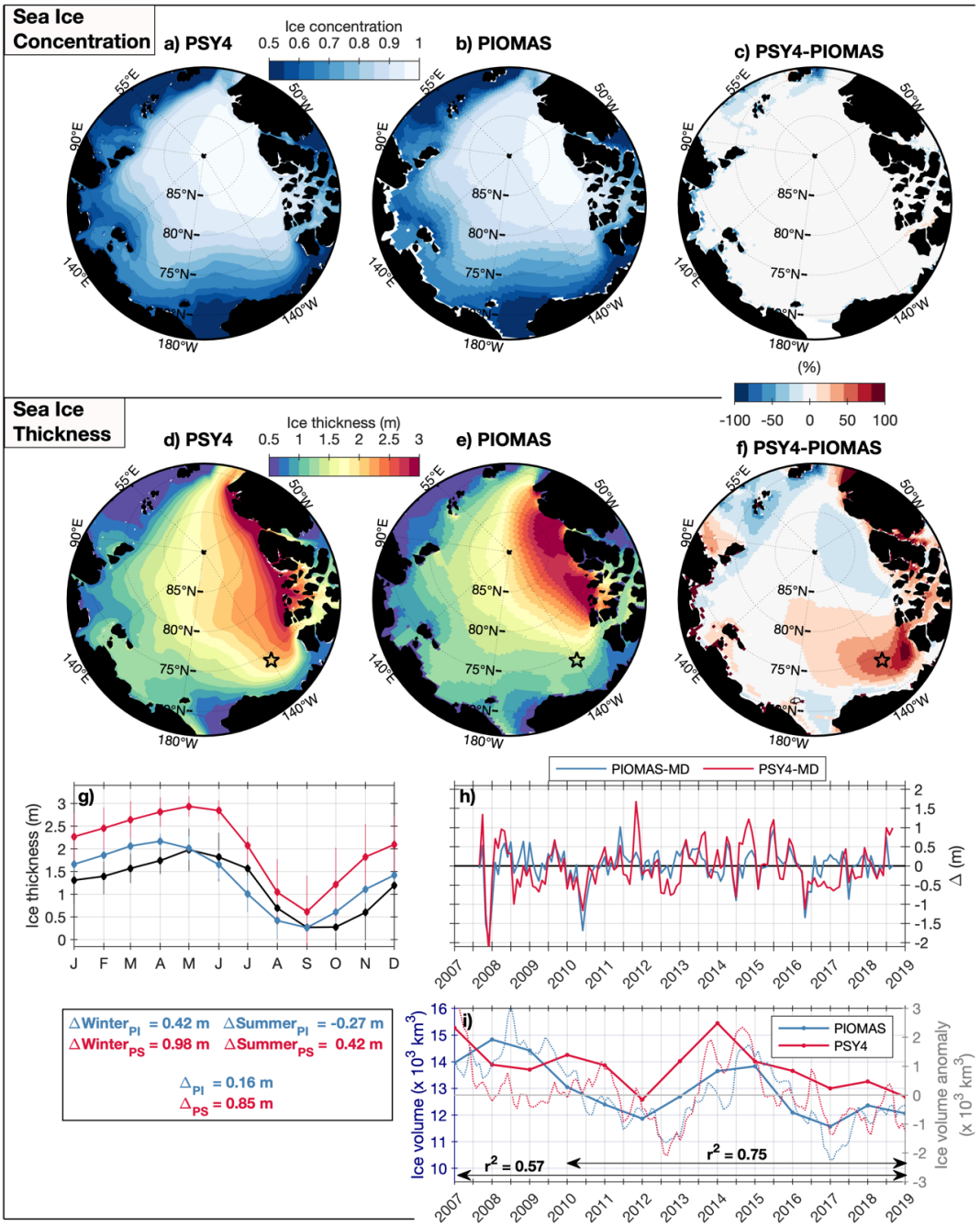

Figure S7: Sea-ice over 2007-2019 period. Mean ice concentration (resp. thickness) of (**a, d**) PSY4 and (**b, e**) PIOMAS. (**c, f**) Mean ice concentration and thickness differences in percentage relative to PIOMAS. (**g**) Monthly means of ice thickness from PSY4 (red), PIOMAS (blue) and mooring MD measurements (black) (mooring position indicated by a star on **d-f**). Vertical bars mark standard deviations. (**h**) Time series of ice thickness differences PIOMAS-MD (blue) and PSY4-MD (red), seasonal cycle removed. (**i**) Annual averages of ice volume beyond latitude 70°N (plain lines, left y-axis) and monthly ice volume anomaly (dashed lines, right y-axis) from PSY4 (red) and PIOMAS (blue).

Chapter IV

Halocline waters along the East Siberian slope and in the Makarov Basin

Contents

IV.1. Introduction

Drastic changes of sea surface height and AW depth were described in the previous chapter along the East Siberian Sea slope, likely related to the on-going Atlantification of the the Arctic. The area of the Siberian Seas and the Makarov Basin remain poorly documented as the region is difficult to reach to performed in-situ measurement. Three autonomous platforms IAOOS were deployed from the Korean icebreaker *R/V Araon* in the Makarov Basin, two in summer 2015 and one in summer 2017. They documented the upper stratification several years after the WHOI Ice Tethered Profiler (ITP29) also deployed in this area. These datasets provided an opportunity to investigate interranual changes in the halocline structure, nearby the East Siberian Sea slope. Combined with PSY4 and other shipborn CTD measurements, we attempted to determine sources of the Makarov Basin halocline.

The next section is composed of a paper that is currently under review at *Journal of Geophysical Research: Ocean*.

IV.2. Changes in Arctic Halocline Waters along the East Siberian Slope and in the Makarov Basin from 2007 to 2020

Changes in Arctic Halocline Waters along the East Siberian Slope and in the Makarov Basin from 2007 to 2020

Cécilia Bertosio[1], Christine Provost[1], Marylou Athanase[2], Nathalie Sennéchael[1], Gilles Garric[3], Jean-Michel Lellouche[3], Joo-Hong Kim[4], Kyoung-Ho Cho[4], Taewook Park[4]

[1] : LOCEAN-IPSL, Sorbonne Université (UPMC, Univ. Paris 6), CNRS, IRD, MNHN, Paris, France.

[2] : Alfred-Wegener-Institut, Bremerhaven, Germany.

[3] : MERCATOR-OCEAN, Toulouse, France.

[4] : Korea Polar Research Institute, Incheon, Republic of Korea

Key points

- Ice-tethered measurements in 2008, 2015 and 2017 in the Makarov Basin highlight changes in the upper and lower halocline properties
- The cold Atlantic-derived lower halocline progressed eastward along the East Siberian slope reaching the Chukchi Borderland.
- The Makarov Basin lower halocline was increasingly supplied with warmer waters resulting from mixing of Atlantic waters with shelf waters

Abstract

The evolution of halocline waters in the Makarov Basin and along the East Siberian continental slope is examined combining drifting platform observations, shipborne hydrographic data and simulations from a global operational physical model from 2007 to 2020. From 2012 onwards, relatively shallow and cold Atlantic-derived lower halocline waters, previously restricted to the Lomonosov Ridge area, progressed eastward along the East Siberian continental slope. Their eastward extent abruptly shifted from 155°E to 170°E in early 2012, stabilised at 170°E until the end of 2015, then gradually advanced to reach the western Chukchi Sea in 2017. Such eastward progression led to a strengthening of the associated boundary current and to the shedding of mesoscale eddies of cold Atlantic-derived waters into the lower halocline of the Makarov Basin in September 2015 and near the East Siberian continental slope in November 2017. Additionally, active mixing between upwelled Atlantic Water and shelf water formed dense warm water supplying the Makarov Basin lower halocline. The increasing contribution from Atlantic-derived waters into the lower halocline along the East Siberian continental slope and in the Makarov Basin led to a weakening of the halocline, which is characteristic of a new Arctic Ocean regime that started in the early 2000s in the Eurasian Basin. Our results suggest that this new Arctic regime may now extend towards the Amerasian Basin.

Plain language summary

In the Arctic Ocean, the "halocline" is a cold near-surface layer where salinity increases rapidly with depth. The halocline isolates the sea-ice at the surface from the heat stored in the underlying warm and salty Atlantic Waters. Hence, the strength of the halocline is a key feature in the maintenance of the sea-ice cover. In this study, various ocean measurements were combined with model simulations to document the recent evolution of the halocline in the East-Amerasian sector of the Arctic: the Makarov Basin and the East Siberian continental slope. From 2012 onwards, Atlantic Waters were found progressively closer to the surface along the slope of the East Siberian shelf. We show that these shoaled Atlantic Waters contributed to modify the temperature of the lower part of the halocline in the adjacent Makarov Basin. In the meantime, the strength of the halocline in the area decreased. Our results suggest that the progressive weakening of the halocline, emblematic of a new Arctic regime previously observed in the Eurasian Basin, now extends toward the Amerasian Basin.

1. Introduction

In the cold Arctic Ocean, stratification is driven by salinity in contrast with mid-latitudes oceans where stratification is driven by temperature (Carmack, 2007; Timmermans & Jayne, 2016). Consequently, the Arctic upper water column is composed of salty and warm Atlantic Water overlaid by relatively fresh and cold waters corresponding to the halocline layer. The Arctic Ocean halocline is about 100-200m thick with large vertical salinity gradients and insulates the sea-ice at surface from the heat carried by the underlying salty Atlantic Water layer (Carmack et al., 2016). Hence, the halocline is a key feature in the maintenance of the sea-ice cover.

The strength of the halocline has been identified as an indicator of the ongoing Arctic changes. Since 1981, the halocline has strengthened in the Canada Basin and weakened in the Eurasian Basin (Bourgain & Gascard, 2011; Polyakov et al., 2018). In recent years, sea-ice reduction, weaker stratification and shoaling of the Atlantic Water layer in the Eurasian Basin led to deeper winter convection, which contributed to a weakening of the halocline (Polyakov et al., 2017*;* Athanase et al., 2020). These changes observed in the Eurasian Basin have been referred to as the "Atlantification" of the Arctic Ocean and have accelerated over the past decade (Polyakov et al., 2017; 2020).

The structure and properties of the Arctic halocline layer differ from region to region, depending on the water mass composition and seasonal/local processes (Bourgain et al., 2011; 2012). Freshened and cooled Atlantic Water found on-top of the Atlantic layer generally constitutes the lower halocline (LH) (e.g., blue layer in **Figure 1c-d**). This LH is relatively cold and shallow in the Eurasian Basin compared to that in the Canada Basin (~ -1.7 °C versus ~ -1 °C) (McLaughlin et al., 2004; Timmermans et al., 2014). The transition zone between a cold and warm LH is believed to be located near the slope of the East Siberian shelf, although still little documented (Jung et al., 2021; Wang et al., 2021). Warmer LH water can result from diapycnal mixing between upwelled AW and bottom shelf waters, as well as enhanced vertical mixing of the LH with AW over sloped topography (Bauch et al., 2016; Fer et al., 2020; Schulz, Büttner, et al., 2021; Wang et al., 2021; Woodgate et al., 2005). The upper halocline (UH; green layer in **Figure 1d**) receives relatively fresh and cold shelf waters – comprising river runoff and Pacific-origin waters – and exhibits different hydrographic/biogeochemical

characteristics in the Eurasian, Makarov or Canada Basins (e.g., Swift et al., 1997; Rudels et al., 2015).

The halocline of the Makarov Basin remains little documented, as the region is difficult to access for the deployment of drifting platforms or hydrographic surveys (Alkire et al., 2019; Morison et al., 1998). The UH of the Makarov Basin comprises advected shelf waters from the nearby Siberian or Chukchi seas where the large-scale surface Transpolar Drift (TPD, **Figure 1a**) current starts (e.g., Steele & Boyd, 1998; Alkire et al., 2019). The TPD transports water and sea-ice across the Arctic towards the Fram Strait and marks the front between Eurasian and Canadian water column structures (Morison et al., 1998, 2012). Before the 1990s, the TPD was located west of the Makarov Basin, above the Lomonosov Ridge (Morison et al., 1998), while trans-Arctic hydrographic sections post-1994 suggested that the TPD was located east of the Makarov Basin, over the Mendeleev Ridge (e.g., Carmack et al., 2016; Rainville & Winsor, 2008; Swift et al., 1997). The shifts in the TPD position respond to changes in atmospheric forcing and can influence the location where fresh shelf waters supply the UH of the Arctic Basins (Steele & Boyd, 1998; Steele et al., 2004; Alkire et al., 2019).

The halocline of the Makarov Basin can also be impacted by the Beaufort Gyre (BG), a large-scale surface circulation that dominates the nearby Canada Basin (**Figure 1a**). The BG constitutes the largest reservoir of freshwater in the Arctic (Proshutinsky et al., 2019; Haine et al., 2015). The halocline in the gyre is thick (~250-300 m) and mainly comprises Pacific-derived waters from the Chukchi Sea (Shimada et al., 2005; Proshutinsky et al., 2019). After 2012, the BG extended westward over Mendeleev Ridge and reached the Makarov Basin (Bertosio, Provost, Athanase, et al., in *revision in JGR*; Regan et al., 2019). The impact of the extended BG on the water column in the Makarov Basin has been poorly documented so far.

In this study, we use in-situ measurements and data from the 1/12° Mercator Ocean operational physical system PSY4 to investigate the evolution of the halocline in the Makarov Basin and along the East Siberian continental slope since 2007. We narrow down the location of the transition zone between the cold and warm LH along the East Siberian continental slope over the years and examine how the LH in the Makarov Basin is impacted. The paper is structured as follows. Data and methods are described in section 2. Section 3 documents the progression of Atlantic-derived lower halocline waters along the slope over 2007-2020 from observation and model data. In section 4, we describe interannual variations of the upper and lower

halocline in the western Makarov Basin. Section 5 summarises our results and presents our conclusions.

2. Data and methods

2.1. In-situ measurements

We used datasets from autonomous ice-tethered platforms (ITP29, IAOOS15 and IAOOS25). Ice Tethered Profilers (ITPs) and Ice Atmosphere Ocean Observing System (IAOOS) consist of a surface system sitting atop an ice floe and an underwater profiler moving along a wire-rope suspended from the surface element. Ocean profilers of the three platforms were equipped with a Seabird SBE41 Conductivity-Temperature-Depth (CTD) sensor measuring temperature and salinity beneath the sea-ice as the platforms drift with the ice floe (Bertosio, Provost, Sennéchael, et al., 2021; Krishfield et al., 2008; Timmermans et al., 2010). Dissolved oxygen (DO) concentration was measured with a Seabird SBE43 sensor for the ITP29 and a Aandera 4330 optode for the two IAOOS (Bertosio, Provost, Sennéchael, et al., 2021; Timmermans et al., 2010). We focused on the data obtained from the Makarov Basin to the Mendeleev Ridge (**Figure 1b**).

ITP29 was deployed on 31 August 2008 on the western flank of the Mendeleev Ridge (~79.5°N;177°E, purple thick line in **Figure 1b**) and performed measurements in the ocean twice a day from 800 m up to 5 m (Krishfield et al., 2008; Timmermans et al., 2010). The platform crossed the Mendeleev-Alpha Ridge, the Makarov and Amundsen Basins and exited the Arctic through Fram Strait on 15 September 2010. We used the first 91 profiles which were located in the Makarov Basin (until 15 October 2008). IAOOS15 and IAOOS25 were deployed from the Korean Icebreaker R/V *Araon* during cruises in the northern Chukchi Sea (Bertosio, Provost, Sennéchael, et al., 2021). IAOOS15 was installed on 12 August 2015 in the Makarov Basin (80.8°N,173°E), about seven years after the ITP29 deployment. The IAOOS15 drifted across Mendeleev Ridge and the northern Canada Basin (blue thick line in **Figure 1b**). The platform provided temperature, salinity and DO profiles until 30 October 2016. We focused on the first 80 profiles (i.e., until 15 October 2015), as they were located in the Makarov Basin and over Mendeleev Ridge. IAOOS25 was deployed on 15 August 2017 near south-west Mendeleev Ridge (77.7°N,180°E) and drifted westward to the continental slope of the East Siberian Sea (ESS; red thick line in **Figure 1b**). IAOOS25 acquired temperature and salinity

data until 19 November 2017 and lost the profiler over the East Siberian slope. IAOOS profilers were set to perform two upward profiles per day from 5 m down to 300 m (IAOOS15) and 430 m (IAOOS25). IAOOS platforms first profiles were compared to the ship CTD profiles closest to the deployment site. After quality control, conservative temperature (Θ) and absolute salinity (S_A) have an accuracy of $\pm$0.005 °C and $\pm$0.02 g.kg^{-1}, respectively. The data were interpolated to 0.5 m vertical resolution bins. Further description of the IAOOS experimental setup and data processing is given in Athanase et al. (2019) and Bertosio, Provost, Sennéchael, et al. (2021).

We used additional shipborne CTD measurements from expeditions including SWERUS (Swedish-Russian-US Arctic Ocean Investigation of Climate-Cryosphere-Carbon Interactions) in July-September 2014 (Anderson et al., 2017), the Nansen and Amundsen Basin Observation System (NABOS and NABOS-II; Lenn et al., 2009) program in September 2007, October 2008, September 2015 and September 2018, ARA06B expedition in August 2015 with the Korean Icebreaker R/V *Araon* (Jung et al., 2021), and the Russian campaign *La-77* in September 2016 (Wang et al., 2021) (**Figure 1**).

2.2. Mercator Ocean Operational System

The global operational system PSY4 was developed at Mercator Ocean for the Copernicus Marine Environment Monitoring Service (CMEMS; http://marine.copernicus.eu/) and simulates physical ocean variables (e.g. temperature, salinity, sea surface height and velocity) and sea-ice variables from 2007 onwards (Lellouche et al., 2018). The physical configuration is based on a 1/12° tripolar grid (spacing of 3–5 km in the Arctic; Madec & Imbard, 1996), with 50 vertical levels of decreasing resolution (~1 m at the surface; ~100 m at 300 m depth), including 22 levels within the upper 100 m. The system PSY4 uses version 3.1 of the Nucleus for European Modelling of the Ocean model (NEMO; Madec et al., 2008) and the Louvain-La-Neuve thermodynamic-dynamic sea Ice Model (LIM2, Fichefet and Maqueda, 1997). At the surface, the model is driven by atmospheric analysis and forecasts obtained from the European Centre for Medium-Range Weather Forecasts-Integrated Forecast System (ECMWF-IFS; https://www.ecmwf.int/) at 3-hr resolution. Apart from sea-ice concentrations obtained from OSI-SAF products (https://doi.org/10.48670/moi-00134), no assimilation is performed in ice-covered ocean in the Arctic. Bertosio, Provost, Athanase, et al. (in *revision in JGR*) found satisfactory skills in simulating sea-ice cover, temperature, salinity, sea surface height and

ocean currents in the Arctic basin (see also Athanase et al., 2019, 2020; Koenig, Provost, Sennéchael, et al., 2017; Koenig, Provost, Villacieros-Robineau, et al., 2017). Further evaluation showed that PSY4 fields were very consistent with observations in the ESS and Makarov Basin (Supplementary **Figures S1** and **S2**).

2.3. Definition of halocline boundaries

In this study, we used density anomalies σ (kg m^{-3}), referred to as density hereafter. Absolute salinity S_A (g kg^{-1}) and conservative temperature Θ (°C) are used following the TEOS-10 (Thermodynamic Equations of Seawater) international standard (McDougall and Barker, 2011; Feistel, 2018).

The top of the halocline, i.e. the base of the mixed layer, was identified through visual inspection as the depth of the shallowest vertical salinity gradient maximum (e.g., Rudels et al., 2000; Bourgain et al., 2012; Timmermans et al., 2012). These maxima corresponded on average to the 25 kg m^{-3} isopycnal (**Figure 2a**).

The UH of the Makarov Basin is composed of advected shelf waters from the East Siberian Sea (ESS) or Chukchi Sea, that both comprise Pacific-origin waters (Anderson et al., 2011, 2017; Wang et al., 2021). We defined the UH as lying between isopycnals 25 and 26.4 kg m^{-3}, in agreement with densities of waters encountered in the ESS and Chukchi Sea (e.g., Pisareva et al., 2015; Wang et al., 2021). The base of the UH was marked by a temperature minimum around 33-33.1 g kg^{-1}, which is consistent with the definition suggested by Steele & Boyd (1998). The UH was separated from the LH by a 50m-thick layer associated with a secondary peak in the salinity vertical gradients (**Figure 2a**). The base of the LH was detected as a bend in the temperature-salinity curve, found on average between isopycnals 27.4 and 27.7 kg m^{-3} ($34.2 < S_A < 34.6$ g kg^{-1}; $-1.4 < \Theta < -0.6$ °C, **Figure 2b**). Atlantic Waters (AW, $S_A > 34.9$ g kg^{-1} and $\Theta > 0$ °C) were found below a large temperature gradient (the thermocline) and characterised by a local maximum in the temperature-salinity curve at denser values than 27.7 kg m^{-3} (**Figure 2b**).

Halocline vertical boundaries obtained from these density criteria were compared to those obtained from other criteria found in the literature. Bourgain & Gascard, (2011) identified the base of the halocline using the constant density ratio value $R_\rho = \alpha\Delta\Theta/\beta\Delta S_A = 0.05$ with α,

the thermal expansion coefficient and β, the haline contraction coefficient. In our study, densities associated with $R_\rho = 0.05$ were comprised between 27.3 and 27.75 kg m^{-3} which corresponded to the density interval we used for the LH. Alternatively, the base of the halocline defined as the depth of the value S_A = 34.46 g kg^{-1} (S = 34.3 psu) (Rudels et al., 1996) was on average 40 m shallower than isopycnal 27.7 kg m^{-3}. In Rudels et al. (1996), this salinity-based definition was applied to hydrographic profiles collected in 1980 and 1991. Recent observations in 2017 in the Western Eurasian Basin showed that water column properties changed and the base of the halocline was found closer to the 34.9 g kg^{-1} isohaline (Bertosio et al., 2020). In the rapidly changing Arctic Ocean, comparisons of isohaline- and isopycnal-based criteria should thus be interpreted with caution.

2.4. Available Potential Energy

We used the Available Potential Energy (APE) to quantify the strength of the halocline. The APE was computed as (e.g., Colin de Verdière et al., 2018, Polyakov et al., 2018; Bertosio et al., 2020):

$$APE = \int_{z_{27.85}}^{z=0} g(\sigma(z) - 27.85) z dz \quad (1)$$

where g is the gravitational constant and σ is the density anomaly. The depth $z_{27.85}$ is the depth of the isopycnal 27.85 kg m^{-3} and corresponds to the base of the halocline layer.

3. Progression of Atlantic-derived lower halocline waters along the East Siberian continental slope over 2007-2020

3.1. Lower halocline changes along the East Siberian continental slope from shipborne CTD

We documented the spatial and temporal changes of the LH using sections of shipborne CTD stations across the East Siberian continental slope (**Figure 3**). The isopycnal of 27.6 kg m^{-3} marked the location of the LH and divided the area into four sub-regions: the Lomonosov Ridge, the west ESS (wESS), the central ESS (cESS) and the east ESS (eESS). Three distinct periods were considered: 2007-2008, with data at Lomonosov Ridge and wESS; 2014-2015, with data all along the continental slope; and 2016, with data at central and eESS. Major hydrographic properties are summarised in **Table 1**.

At the Lomonosov Ridge, the LH temperature was, on average, colder than -1.5°C for all years, while salinity increased from S_A ~ 34.2-34.3 g kg^{-1} in 2007-2008 to S_A ~ 34.4-34.5 g kg^{-1} in 2014-2015 (**Figures 3a-d**). This salinity increase, associated with sustained cold temperatures, likely resulted from changes upstream of the Lomonosov Ridge or from coastal polynya water influence (Anderson et al., 2017; Bauch & Cherniavskaia, 2018; Bertosio et al., 2020; Polyakov et al., 2020). At the Lomonosov Ridge, the LH was warmer over the continental slope than off-shore ($\Delta\Theta < 0.3$ °C), potentially resulting from enhanced vertical mixing with AW over sloping topography (Dmitrenko et al., 2011; Lenn et al., 2009; Schulz, Janout et al., 2021) (green and dark red dots in **Figures 3a-d**).

From wESS to cESS, the LH salinity varied little in time, while temperatures were always higher than those at the Lomonosov Ridge ($-1.5 < \Theta < -0.5$ °C, **Figures 3e-j**). Note that, in contrast, AW was colder along the East Siberian continental slope than at Lomonosov Ridge (Θ ~ 1 °C versus $\Theta > 1$ °C). At cESS, the LH exhibited striking spatial temperature differences in 2014-2015 with waters over the continental slope warmer than offshore ($\Delta\Theta$ ~ 1 °C, black and dark red dots on **Figures 3h-i**), suggesting two different types of LH. In 2016, over the eESS continental shelf and slope, near the Chukchi Sea, a bend in the associated Θ-S_A curves suggested presence of Atlantic-derived LH that was absent in 2014 and 2015 **(Figures 3k-m)**.

3.2. Insights of the evolving contributions of the Atlantic-derived lower halocline along the East Siberian continental slope from the model data.

We used the model output to investigate the contributions of Atlantic-derived lower halocline waters to the lower halocline along the East Siberian continental slope. We considered the evolution of the temperature on the 27.6 kg m^{-3} isopycnal (in the LH) and APE from both in-situ measurements and monthly mean PSY4 fields **(Figures 4 and 5**). Interannual changes were examined along the 300 m isobath (on the continental shelf) and the 1000 m isobath (on the continental slope).

From 2007 though 2011 there was a marked temperature and APE front located between 155°E (on the shelf) and 160°E (on the slope) (**Figures 4a-b and 5**). West of this front, the LH was colder than -0.6°C and likely corresponded to cold Atlantic-derived LH from the Eurasian Basin. Low values of APE indicated a weak stratification (APE < 10×10^4 J m^{-2}, **Figures 4b and 5d**). In contrast, East of 160°E temperatures were higher than -0.4 °C with

APE > 20 × 10^4 J m^{-2} (**Figures 4a-b and 5**). The position of the front over the 2007-2011 period exhibited large seasonal variations, reaching its westernmost limits in fall/winter (**Figure 5**). The 27.6 kg m^{-3} isopycnal above the 1000 m isobath was deeper in the East than in the West: this is consistent with a thicker UH resulting from shelf water influence in the East, and inducing a deeper LH **(Figure 5c**). The front shifted eastwards in winter 2011-2012, reaching 171°E above the 1000 m isobath, and decreasing stratification over the continental slope (**Figures 4d and 5d**). Such sharp eastward shift of Atlantic-derived LH along the continental slope in winter 2011-2012 occurred at a time of large easterly winds over the ESS (**Figure S3b**), and relatively weak inflow through Bering Strait (Peralta-Ferriz & Woodgate, 2017; Serreze et al., 2019; Woodgate, 2018). From 2012 onwards, seasonal variations of the front were less pronounced. East of ~172°E, the APE increased in 2010-2011 (**Figure 5d**), which likely resulted from the BG influence that period as suggested by Bertosio, Provost, Athanase, et al. (in *revision in JGR*) and Regan et al. (2019). After winter 2015-2016, the front progressively moved east until winter 2017. From then, warm LH water (> -0.4 °C) was no longer found along the slope and the stratification was lower than 20 × 10^4 J m^{-2} (**Figures 4e-f and 5**). Indeed, cold Atlantic-derived LH from the Lomonosov Ridge likely reached the western Chukchi Sea in winter 2017.

The along-slope eastward progression of cold Atlantic-derived LH was observed from shipborne CTD measurements (**Figure 4**). Drifting platform data also suggested an evolving contribution from the cold Atlantic-derived LH to the Makarov Basin LH, which is further investigated in the following section (**Figure 4**).

4. Interannual variations in the western Makarov Basin halocline

For this section, we used measurements from the three drifting platforms in late summer of 2008, 2015 and 2017 (**Figures 6, 7** and **8**), and monthly modelled fields of temperature, salinity, and horizontal velocity (**Figures 9** and **10**) to document the evolution of the upper and lower halocline in the Makarov Basin. In particular, we aimed to investigate the evolving contribution of Atlantic-derived waters from the continental slope to the open basin.

4.1. Upper halocline: varying influence of Pacific Water

The UH ($25 < \sigma < 26.4$ kg m^{-3}) showed distinct thicknesses in 2008, 2015 and 2017 (**Figure 6 and Table 2**). The UH was thicker in 2015 (~ 110 m) compared to 2008 (~ 70 m) and 2017 (~ 40 m; **Table 2**). UH temperatures in 2008 and 2015 exhibited a local maximum (Θ_{max}) below the mixed layer at $S_A \sim 31.5$ g kg^{-1} overlying a minimum Θ_{min} at $S_A \sim 32.6$-33 g kg^{-1}, with larger values in 2015 than in 2008 ($\Delta\Theta \sim 0.4$ °C, **Table 2, Figures 7a-b**). In 2015, the salinities associated with the Θ_{max} were consistent with the influence of Pacific summer waters (Shimada et al., 2001; Steele et al., 2004; Timmermans et al, 2014; 2017). Indeed, the BG, inside which the UH is thick and largely influenced by Pacific waters, extended toward Mendeleev Ridge in 2012-2016 (Bertosio, Provost, Athanase, et al., in *revision in JGR*; Regan et al., 2019). The BG likely contributed to thicken, freshen and warm the UH in the Makarov Basin in 2015.

In 2017, temperatures in the UH were low ($\Theta < -1.4$ °C). Profiles at the beginning of the 2017 trajectory (south Mendeleev Ridge) exhibited a local $\Theta_{max} \sim -1.2$ °C on isopycnal 26 kg m^{-3} ($S_A \sim 32.5$ g kg^{-1}), interleaved between two local Θ_{min} at $S_A \sim 31.6$ and 33 g kg^{-1} (**Figures 6l** and **7c**). This local Θ_{max} was ~1 g kg^{-1} saltier and ~0.8 °C colder compared to the Θ_{max} in 2015, which suggested less influence of Pacific summer waters, as the Beaufort Gyre retreated east of the Mendeleev Ridge after 2016 (Bertosio, Provost, Athanase, et al., in *revision in JGR*). A similar local Θ_{max} at $S_A \sim 32.5$ g kg^{-1}, documented in 2004 over the nearby Chukchi Abyssal Plain (east of Mendeleev Ridge), was attributed to a boundary resulting from the existence of two temperature minima: (i) one on-top of the local Θ_{max} and resulting from advected shelf waters formed by winter convection with sea-ice formation; (ii) one below the local Θ_{max} and attributed to Pacific winter waters influenced by Chukchi Plateau waters and upwelled LH waters (Nishino et al., 2008). This local Θ_{max} in the UH in 2017 on isopycnal 26 kg m^{-3}, along with high salinity vertical gradients, supports a splitting in two sub-layers similar to that documented by Nishino et al. (2008) (at $25 < \sigma < 26$ kg m^{-3} and $26 < \sigma < 26.4$ kg m^{-3}, **Figures 6c** and **6f**).

The base of the UH was cold and associated with low dissolved oxygen values in 2008 and 2015 relative to layers above and below (DO < 270 µmol.kg^{-1}, **Figures 7a-b**), which is a characteristic feature of both Pacific winter waters (Shimada et al., 2005; Timmermans et al., 2010; Woodgate et al., 2005) and ESS waters (Alkire et al., 2019; Anderson et al., 2013). In 2008 and 2015, Alkire et al. (2019) found that the influence of ESS-origin water over the shelf

and in Makarov Basin was restricted west of 165-170°E, while the influence of western Chukchi Sea waters was restricted to the east. The drifting platforms ITP29 and IAOOS15 were both located east of 165-170°E, suggesting that low-oxygen waters at $S_A \sim 33$ g kg^{-1} were mainly influenced by Pacific winter waters from the western Chukchi Sea.

4.2. Lower halocline: evolving contribution from Atlantic-origin waters

In 2008, the LH ($27.4 < \sigma < 27.7$ kg m^{-3}) exhibited a sharp bend in the temperature-salinity curve at $S_A \sim 34.4$ g kg^{-1} and $\Theta \sim -1.2$ °C, suggesting a contribution from Atlantic-derived LH resulting from winter convection (Kikuchi et al., 2004) (**Figure 7a**). DO values in the LH, similar to those sampled in the underlying AW layer (DO ~ 290 µmol.kg^{-1}, **Figure 7a** and **Table 2**) supported an Atlantic-origin. Monthly mean in September 2008 of modelled salinity at 150 m displayed values higher than 34 g kg^{-1} west of 170°E, where the ITP29 was located, likely corresponding to the salty LH layer (**Figure 8a**). West of the Lomonosov Ridge, i.e. longitudes less than 140°E, high salinities and relatively low temperatures ($S_A > 34.5$ g kg^{-1}, $\Theta \sim -0.7$ °C) along the continental slope were associated with an eastward current (~ 7 cm s^{-1}, **Figures 8a-b**). This salty eastward current broke away from the slope east of the Lomonosov Ridge (~145°E; 80°N) and entered the Makarov Basin, developing mesoscale structures along 2000 m isobath (**Figure 8a**). This supported that the LH layer of the western part of the Makarov Basin was supplied by salty, Atlantic-derived LH directly from the Eurasian Basin. On the continental East Siberian shelf, a westward current followed the 300-500 m isobaths and carried water with relatively high temperature ($\Theta > -0.5$ °C, **Figure 8b**). The salinity values east of 180°W, i.e. east of the Mendeleev Ridge, were lower than 33.2 g kg^{-1}, suggesting that in this area the depth 150 m corresponded to the UH layer (blue area in **Figure 8a**).

In 2015 and 2017, the Θ-S_A curve obtained from the IAOOS15 and IAOOS25 data exhibited a bend in the LH associated with salinities at ~ 34.5-34.6 g kg^{-1}, which were higher than that in 2008 (S_A~ 34.4 g kg^{-1}, **Figures 7b-c**). A saltier LH base is a feature also documented in 2017 in the western Eurasian Basin (Bertosio et al., 2020). Temperatures in the LH were comprised between -1.5 and -0.7 °C in 2015 and 2017, which corresponded to a larger range of values compared to 2008 (**Figures 6k-l** and **7b-c, Table 2**). Warm LH were associated with a mixing line in the Θ-S_A curve between the base of the UH and AW in 2015 and 2017 (**Figure 7b** and **Table 2**), which suggested diapycnal mixing between AW and the overlying Pacific winter water (Wang et al., 2021; Woodgate et al., 2005). In 2015, these warm LH exhibited DO values

of ~ 240 µmol.kg^{-1} supporting the influence of the overlying UH of which DO values were similar (**Figures 6m-n** and **7b**). In spite of this warming in 2015 and 2017, profiles exhibited cold temperatures in the LH (Θ ~ -1.2 °C), similar to those sampled in 2008, suggesting that some cold Atlantic-derived LH persisted (**Figures 7b** and **7c**).

Simulated data in September 2015 suggested that the IAOOS15 location corresponded to a strong horizontal salinity front at 150 m (**Figures 8**). Modelled fields displayed LH saltier than 34.6 g kg^{-1} and colder than -1.2°C between the continental slope and 81°N (**Figures 8c-d**). A temperature front over the slope was located at ~ 160-170°E, with colder water to the west compared to the east. The eastward slope current, previously not extending beyond the Lomonosov Ridge, intensified (v > 7 cm s^{-1} along the slope) and followed isobath 1500 m further east until ~ 175°E. In September 2017, cold salty LH were found along the continental slope until 180°W and in the entire studied part of the Makarov Basin, including the location of the IAOOS25 (**Figures 8e-f**). The eastward circulation along the continental slope and the northward circulation branch above Mendeleev Ridge were both intensified compared to 2015 (v > 10 cm s^{-1}, **Figures 8c and 8e**).

We focused on a transect across the continental slope (shown in **Figure 8)** to investigate interannual changes in the slope-basin interaction in the LH (**Figure 9**). From 2007 until winter 2011-2012, the slope and basin water had distinct LH properties: LH was saltier, colder and deeper in the basin (S_A > 33.8 g kg^{-1}, $\Theta_{27.6}$ < -0.4 °C, $z_{27.6}$ ~ 220 m, **Figures 9a-c**), than on the slope. In winter 2011-2012, LH properties strikingly changed on the slope and the abrupt change coincided with the sharp eastward progression of Atlantic-derived LH: LH became saltier (+1 g kg^{-1}), colder (-1°C) and shallower (100 m) (**Figures 9a-c**). LH properties on-slope were progressively found off-shore from 2012 onwards, indicating active slope-basin exchanges in the LH. A large salinity front located in the deep basin after 2012, associated with westward velocity (v_x ~ -7 cm s^{-1}, **Figure 9d**), marked the northern limit of slope water influence, and likely corresponded to the boundary of the Beaufort Gyre (Bertosio, Provost, Athanase, et al., in *revision in JGR*; Regan et al., 2019). From 2012 onwards, large eastward velocities between isobaths 500 and 2000 m marked the intense slope current (v_x > 8 cm s^{-1}, **Figure 9d**). In parallel, the water column stratification weakened along the slope from 2012 onwards, and progressively northward in the Makarov Basin (APE < 10×10^4 J m^{-2}, **Figure 9e).** Note that APE > 30×10^4 J m^{-2} found off-shore from 2012 to 2018 is consistent

with the influence of the BG, inside which APE can be higher than 20×10^4 J m^{-2} (Polyakov et al., 2018).

4.3. Cold-core mesoscale lenses within the lower halocline

Two cold-water lenses were observed in the LH in 2015 and 2017 (respectively in IAOOS15 and IAOOS25 data, **Figure 10**). The first one was sampled from 31 August to 3 September 2015, around 169°E, 80.6°N, between isopycnals 27.4 and 27.7 kg m^{-3} in the Makarov Basin (green part of the IAOOS15 trajectory in **Figures 10a, 10c and 10d**). The second one was found near the continental slope (164°E, 79°N), between isopycnals 27.6 and 27.8 kg m^{-3}, above the 1500m isobath, and sampled from 13 to 16 November 2017 (**Figures 6**, **10e** and **10f**). In 2015 (respectively 2017), the lense, located at 120-170 m depth (100-140 m), had a horizontal scale of 40 km (20 km) and a core temperature at -1.3 °C (-1.5 °C) colder than the surrounding waters ($\Theta \sim$ -0.8 °C, **Figures 10c-f**). Both cold mesoscale lenses were associated with a shoaling of isopycnals (**Figures 6b** and **6d**).

In 2015, the cold lense was located below a cold UH centered on a $\Theta_{min} \sim$ -1.6 °C at 60 m (thick black profile, **Figure 10d**). In contrast, there were no cold lense in the LH in the other profiles sampled by the platform that year in the basin and the UH exhibited a deeper $\Theta_{min} \sim$ -1.5 °C at 140 m (thin grey profiles, **Figure 10d**). This indicated that the water column associated with the cold lense in 2015 was different from the rest of the basin, possibly resulting from different source contributions at this precise location. The UH overlying the cold-water lense in 2017 at the East Siberian slope did not exhibit any Θ_{min} (**Figure 10f**).

Modelled horizontal velocity fields averaged in September 2015 displayed a large salty cyclonic branch detaching from the intensified slope current and crossing the IAOOS15 trajectory in the Makarov Basin, where the cold mesoscale lense was sampled in the LH (**Figure 8c**, **Figure 10** and see **Figure S4a** for the synoptic map). In November 2017, PSY4 suggested that the cold lense sampled by the IAOOS25 was encountered on the continental slope after that Atlantic-derived LH had shifted eastward along the slope (**Figure 8e** and **Figure S4b).** This suggested that the two cold mesoscale lenses were composed of cold Atlantic-derived LH water from the Eurasian Basin that flowed along the slope of the East Siberian shelf. From 2007 onwards, the strengthening of the boundary current along the continental slope likely contributed to shed mesoscale lenses and eddies in the Makarov Basin.

Similar processes have been observed near the Atlantic Water Boundary Current in the Eurasian Basin (e.g., Athanase et al., 2019; 2021; Pérez-Hernández et al., 2017). Our study suggests these cold mesoscale lenses detaching from the slope current likely increased the contribution of Atlantic-derived waters from the slope to the LH in the Makarov Basin (**Figures 8a, 8c, 8e and 9d**).

5. Summary and Conclusion

We examined the evolution of the halocline in the Makarov Basin and along the East Siberian Sea (ESS) slope combining in-situ measurements and modelled fields from the operational physical model PSY4**.** Mercator Ocean simulations were highly complementary to the hydrographic measurements and provided valuable insights on the evolution of the halocline in the Makarov Basin and along the East Siberian continental slope. **Figure 11** summarizes our findings. We identified three distinct periods.

During the 2007-2011 period, the upper halocline (UH) in the western Makarov Basin was influenced by ESS waters (e.g., Alkire et al., 2019; Anderson et al., 2013) and by western Chukchi Sea Pacific waters near Mendeleev Ridge. The underlying lower halocline (LH) was cold and mainly comprised Atlantic-derived LH entering the Makarov Basin near the Lomonosov Ridge (**Figure 11a**). At that time, relatively shallow and cold Atlantic-derived LH were documented west of ~155-160°E, along the East Siberian continental slope.

During 2012-2015, Makarov Basin UH properties (thicker layer, warmer and fresher) were consistent with the presence of Pacific water from Chukchi Plateau, driven by the westward extension of the Beaufort Gyre (e.g. Alkire et al., 2019; Nishino et al., 2013; Proshutinsky et al., 2019; Regan et al., 2019). In winter 2012, cold Atlantic-derived LH abruptly shifted eastward along the East Siberian continental shelf and slope (from 155°E to 170°E, above the 1000 m isobath), causing a reduction in the halocline strength along the slope (**Figure 11b**). Upwelled AW along the slope mixed with bottom shelf waters and formed warmer LH. From 2012 onwards, the velocity along the continental slope increased, and the enhanced boundary current was observed to shed mesoscale structures in the LH, toward the Makarov Basin. Drifting platform data and PSY4 fields suggested that these mesoscale structures observed East of 164°E in 2015 and 2017 comprised cold Atlantic-derived lower halocline waters. The shedding of mesoscale lenses from the slope current likely increased the contribution of

Atlantic-derived lower halocline water to the LH of the Makarov Basin. Atlantic Water, thus, influenced the Makarov Basin LH in two ways: (i) with cold Atlantic-derived LH from the Eurasian Basin and (ii) with warm LH resulting from diapycnal mixing on the slope with shelf waters. Concomitantly, the halocline weakened in the basin.

After 2016, the Beaufort Gyre was located further east (Bertosio, Provost, Athanase et al., in *revision in JGR*) and Makarov Basin UH properties differed from previous years: the cold UH likely resulted from advected fresh East Siberian cold shelf water (Alkire et al., 2019; Wang et al., 2021) or fresh Pacific winter waters (Woodgate & Peralta-Ferriz, 2021). In parallel, cold Atlantic-derived LH reached the western Chukchi Sea, which is consistent with the high-salinity cold waters found south of Mendeleev Ridge in summer 2017 at 120-150 m by Jung et al. (2021) (**Figure 11c**). In the meantime, the halocline strength along the slope of the East Siberian shelf was similar to that from the Eurasian Basin.

Our study suggests that the weakening of the halocline along the East Siberian continental slope and in the Makarov Basin is related to an increased contribution of Atlantic-derived waters into the LH. Polyakov et al. (2017; 2020) showed that the weakening of the halocline resulted from the gradual shoaling of the AW in the Eurasian Basin (a process called "Atlantification"). Here we show that a similar process is now impacting the western Amerasian Basin, reaching the Chukchi Borderland.

Data Availability Statement:

ITP data are available on the *Beaufort Gyre Exploration Project* website (*https://www2.whoi.edu/site/beaufortgyre/data/*) (Krishfield et al., 2008; Proshutinsky et al., 2009). IAOOS data are available on *SEANOE* (Bertosio, Provost, Sennéchael, et al., 2021). NABOS and SWERUS data are available on the Arctic Data Center website (NABOS 2007 and 2008: https://arcticdata.io/catalog/view/dfbf7fa6-6aed-403b-b188-3e308270a779 ; NABOS-II: https://arcticdata.io/catalog/view/doi%3A10.18739%2FA20C4SK4J ; NABOS 2018: https://arcticdata.io/catalog/view/doi%3A10.18739%2FA2X34MS0V ; SWERUS doi:10.18739/A2CZ9N). Data from the Korean campaign are available on the KOPRI data servers (https://kpdc.kopri.re.kr/search/80785502-2cb4-4146-a799-b7c76d65f47c). The data from the Russian campaign in 2016 can be obtained at the following website: https://doi.org/10.5281/ze-nodo.4507584. The model outputs are available at Copernicus Marine Environment Monitoring Service (CMEMS; http://marine.copernicus.eu/).

Acknowledgements:

Cecilia Bertosio acknowledges support from the IAOOS grant S18JROI002 at Sorbonne University, and Marylou Athanase from a postdoc funded by the BMBF research group Seamless Sea Ice Prediction. The IAOOS platforms were developed with funding from Equipex IAOOS (Ice Atmosphere Ocean Observing System) (ANR-10- EQPX-32-01). We thank Matthieu Labaste, Vincent Marriage and Zoé Koenig for their contribution to the preparation and deployment of the IAOOS platforms used in this study. The deployment took place from the Korean Icebreaker R/V Araon and the authors are thankful to Araon crews and scientific team members. This research was a part of the project titled 'Korea-Arctic Ocean Warming and Response of Ecosystem (K-AWARE, KOPRI, 1525011760)', funded by the Ministry of Oceans and Fisheries, Korea. We are deeply grateful to Editor Laurence Padman, the Associate Editor Mar Flexas and the two anonymous reviewers whose detailed comments and suggestions helped improve the manuscript.

FIGURE AND TABLE

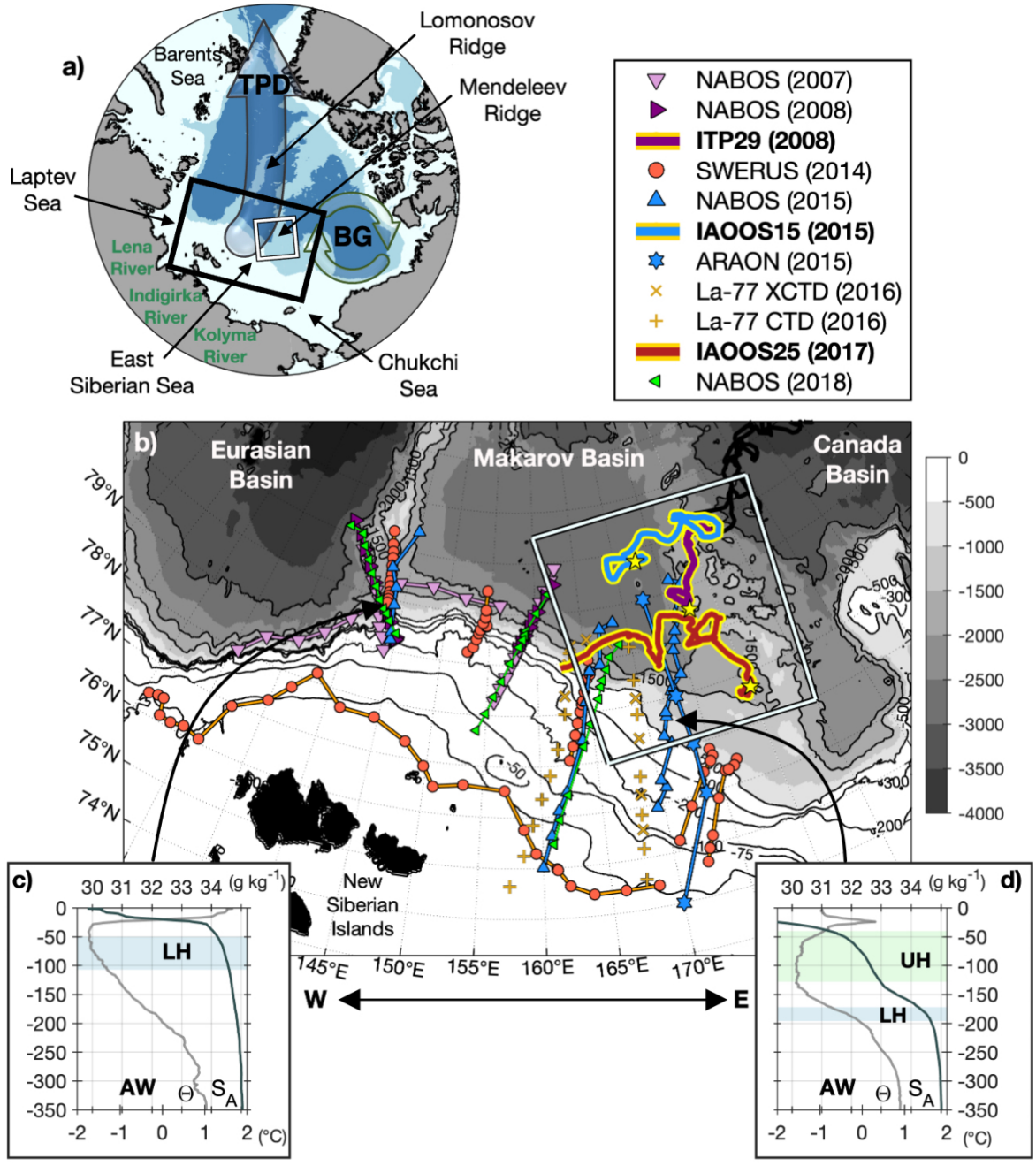

Figure 1: (**a**) Arctic bathymetry, the black rectangle limits the area under study. Ocean floor shallower than 500 m in light blue, between 500 and 2500 m in medium blue, larger than 2500m in dark blue. Transparent arrows indicate the Transpolar Drift (TPD) and the Beaufort Gyre (BG). (**b**) Shipborne CTD and drifting platforms data used in this study. Yellow stars indicate the starting point of the drifting platforms ITP29, IAOOS15 and IAOOS25. The white

box highlights the ITP trajectories. IBCAO bathymetry is in greyscale. An "eastward shift" (resp. "westward shift") refers to a shift toward **E** (**W**) indicated below the lower panel. Two temperature (Θ; light grey) and salinity (S_A; dark grey) profiles are shown in (**c**) and (**d**) respectively (from NABOS 2015). A black arrow points to the location of each profile. *UH: Upper Halocline (green); LH: Lower Halocline (blue); AW: Atlantic Waters*

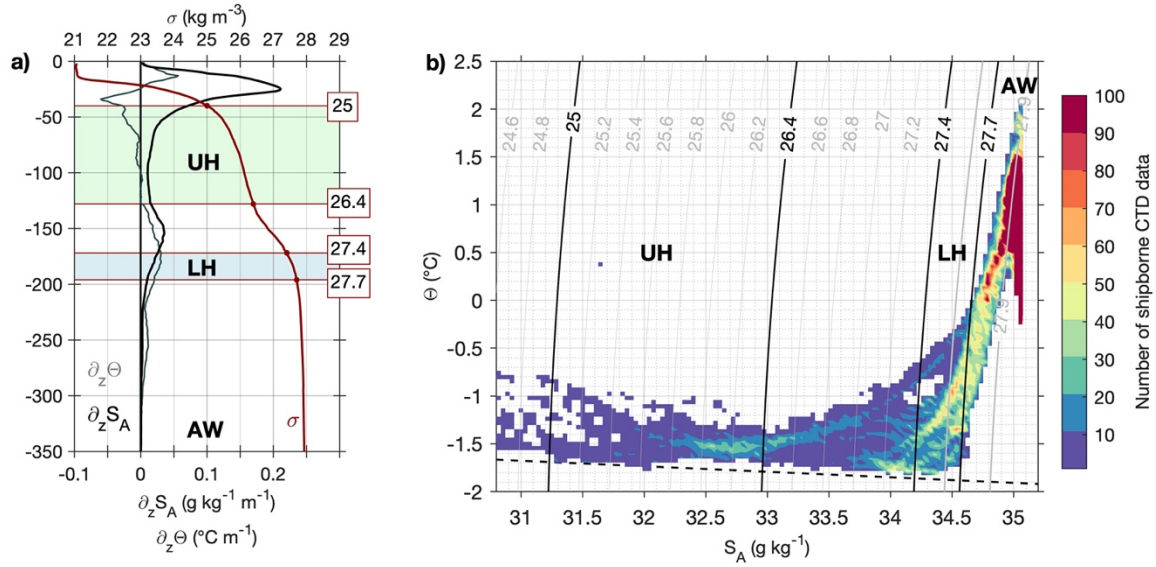

Figure 2: (**a**) Example of profiles of vertical gradients of salinity ($\partial_z S_A$ in black; g kg^{-1} m^{-1}; bottom x-axis), temperature ($\partial_z \Theta$ in grey; °C m^{-1}; bottom x-axis), and profiles of density (σ in red; kg m^{-3}; top x-axis). Data are from NABOS 2015 (same as in *Figure 1d*). Horizontal red lines indicate the density limits of the layers (σ values in the red boxes). (**b**) Θ-S_A diagram from shipborne CTD data shown in Figure 1. Color is the number of data points. *UH: Upper Halocline (green); LH: Lower Halocline (blue); AW: Atlantic Waters.*

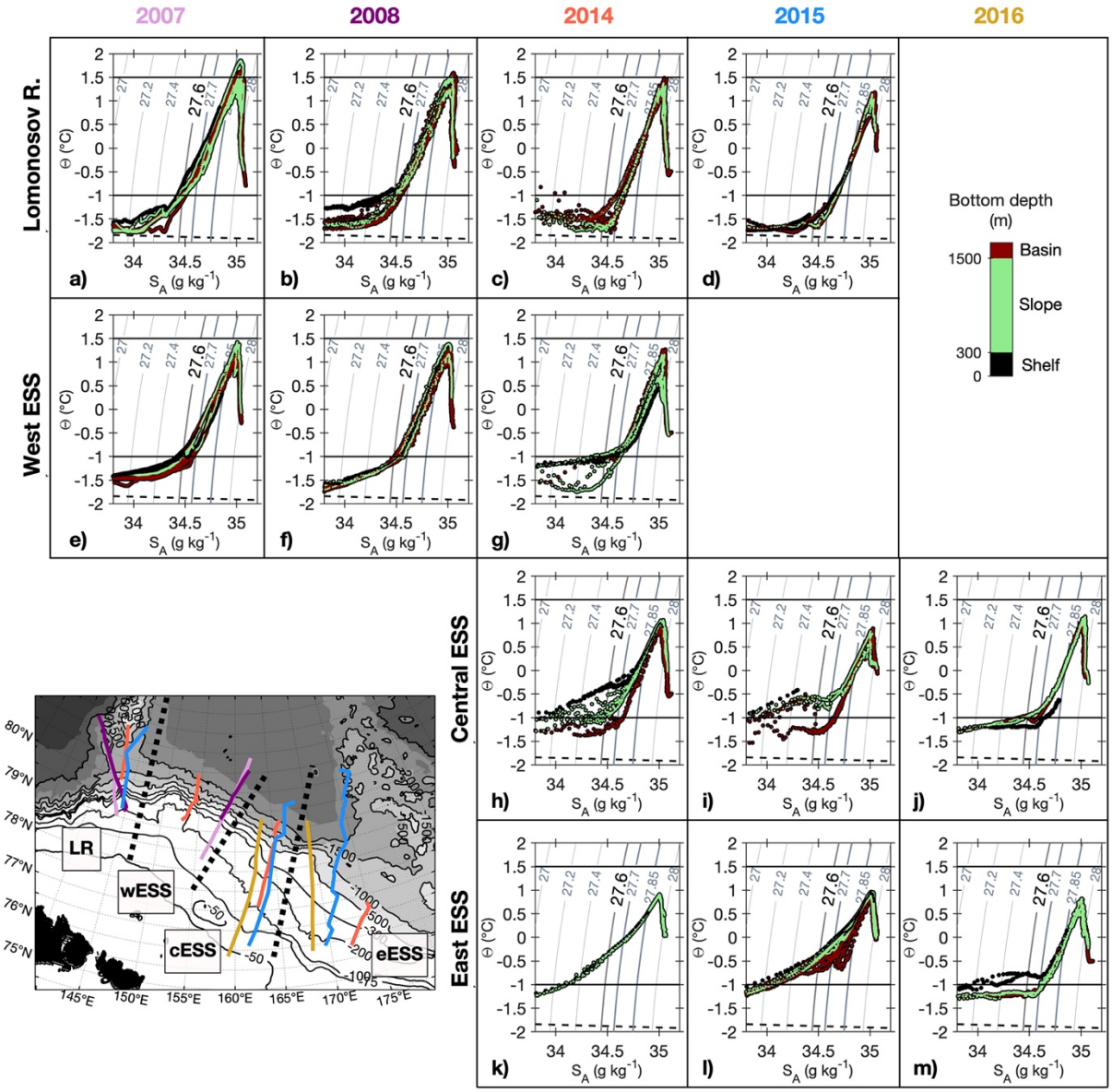

Figure 3: Θ-S_A diagrams from sections along the East Siberian Sea (y-axis in °C and x-axis in g kg^{-1}). Columns indicate years and rows correspond to the four areas delimited with dashed black lines on the map: the Lomonosov Ridge (LR) and the west, central and east East Siberian Sea (wESS, cESS and eESS respectively). Isopycnal 27.6 kg m^{-3} corresponds to a landmark for the LH. Color in Θ-S_A diagrams corresponds to bathymetry (in m) at each point. Color of hydrographic sections on the map indicate the year (same color code as in *Figure 1*; 2007: light purple; 2008: purple; 2014: orange; 2015: blue; and 2016: yellow).

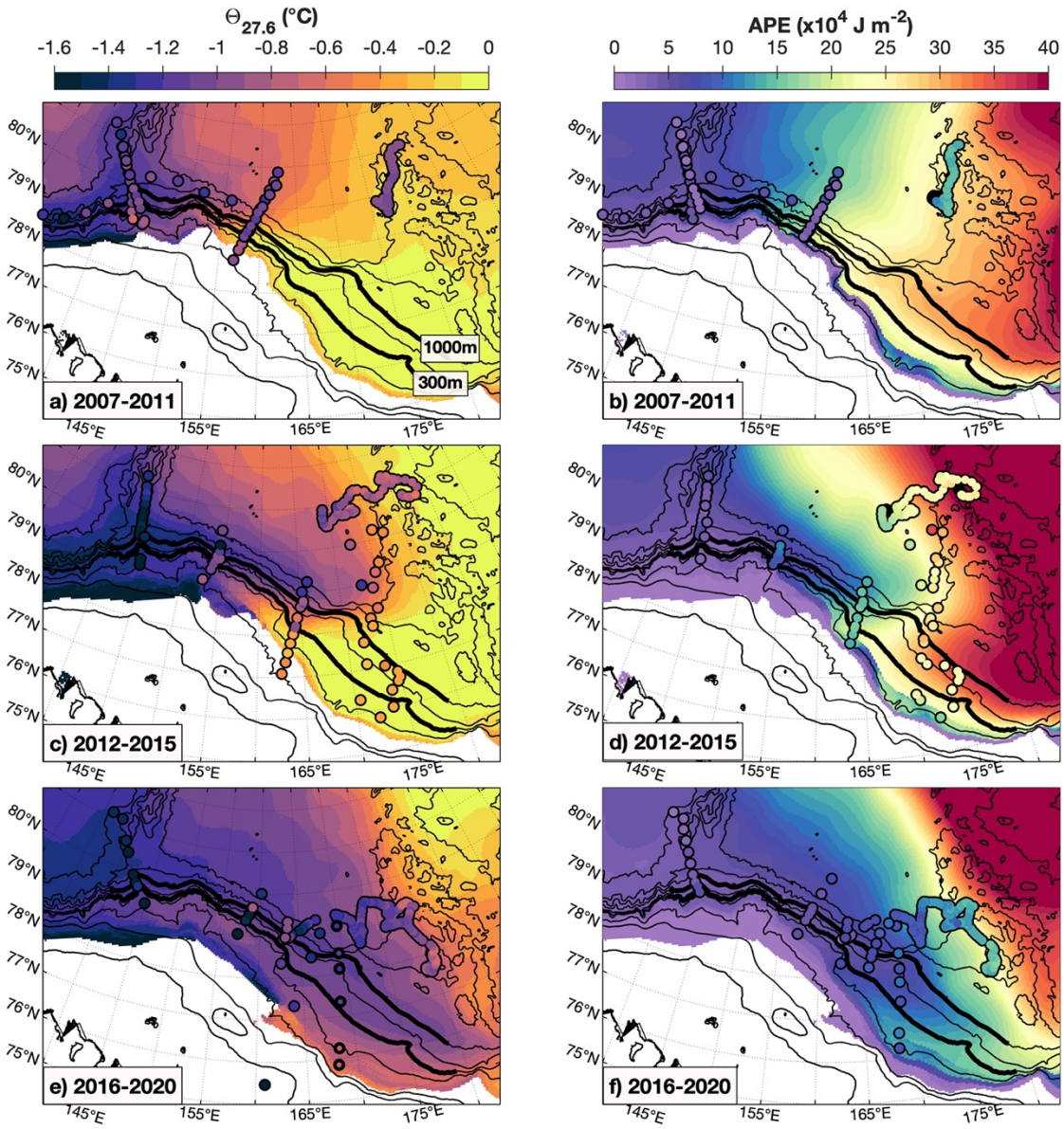

Figure 4: (**a, c**, **e**) PSY4 temperature on the 27.6 kg m^{-3} isopycnal, in the lower halocline ($\Theta_{27.6}$, °C). (**b**, **d**, **f**) Available potential energy (APE; 10^4 J m^{-2}). Model values are averaged over (**a-b**) 2007-2011, (**c-d**) 2012-2015 and (**e-f**) 2016-2020. Colored circles correspond to contemporaneous observed data. Note that PSY4 fields are averaged over several years while observations are synoptic. Black lines are for isobaths and thick black lines indicate isobath 300 m and 1000 m.

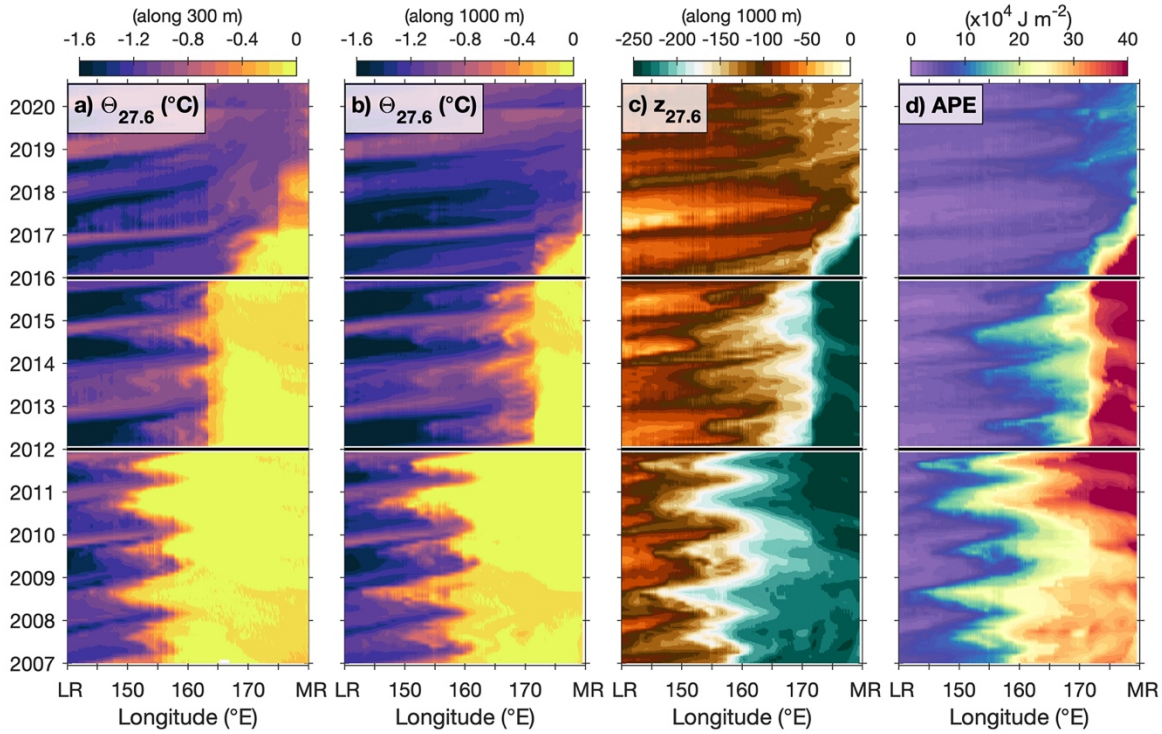

Figure 5: Evolution of 27.6 kg m^{-3} isopycnal temperature $\Theta_{27.6}$ (°C) along isobath (**a**) 300 m and (**b**) 1000 m. (**c**) Evolution of the depth of the 27.6 kg m^{-3} isopycnal above isobath 1000 m. (**d**) Available Potential Energy (APE; 10^4 J m^{-2}) along isobath 1000 m. Thick horizontal lines mark January 2012 and 2016. *LR: Lomonosov Ridge; MR: Mendeleev Ridge*

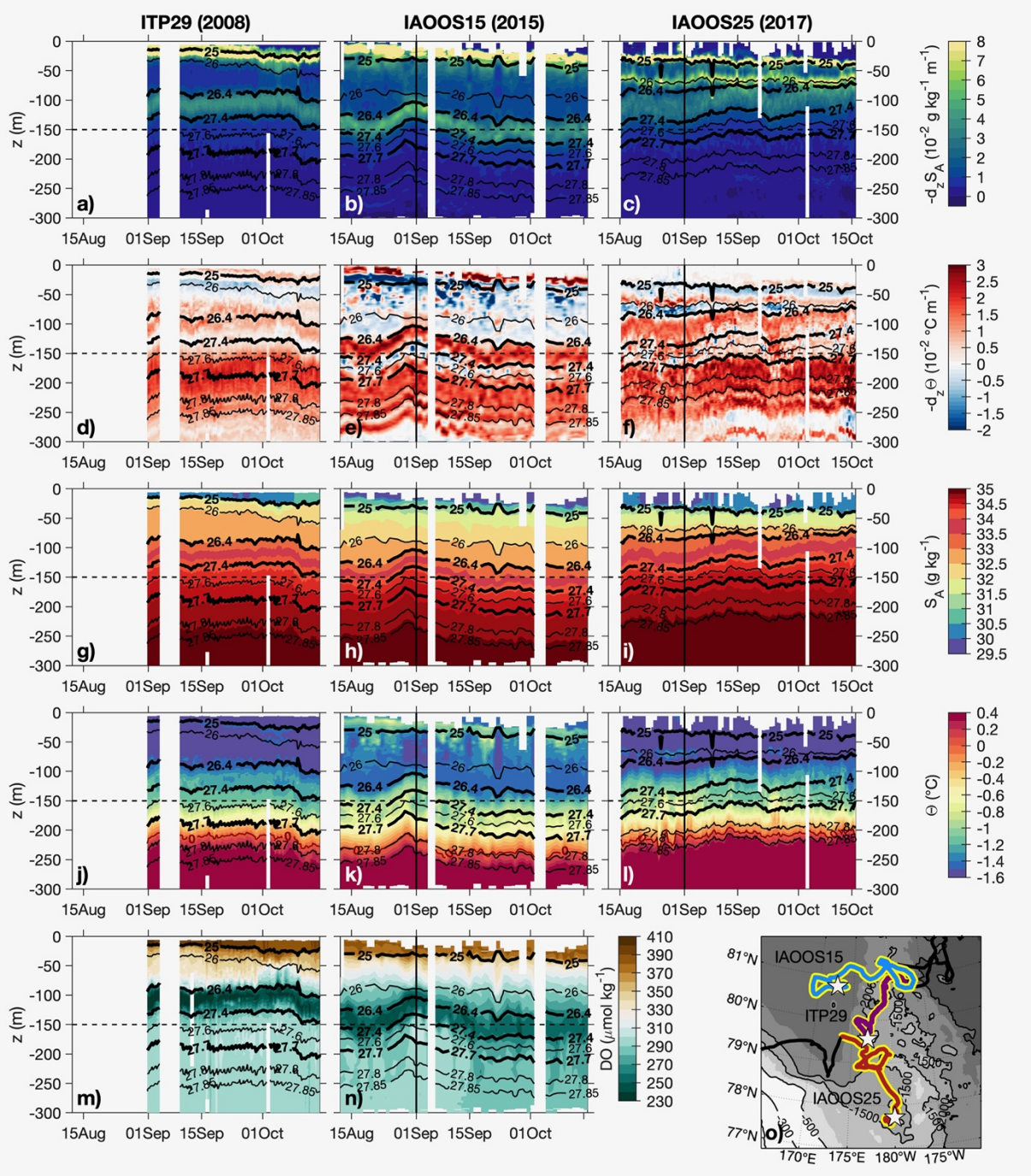

Figure 6: Along-drift profiles from ITP29 (*left*), IAOOS15 (*middle*) and IAOOS25 (*right*): (**a, b, c**) vertical gradient of absolute salinity (10^{-2} g kg^{-1} m^{-1}), (**d, e, f**) vertical gradient of conservative temperature (10^{-2} °C m^{-1}), (**g, h, i**) absolute salinity S_A (g kg^{-1}), (**j, k, l**) conservative temperature Θ (°C) and (**m, n**) dissolved oxygen (μmol kg^{-1}). The horizontal dashed line indicates the depth 150 m. Isopycnals are in black lines. Isopycnal 25 kg m^{-3} roughly marks the base of the mixed layer, 26.4 kg m^{-3} the base of the upper halocline and 27.7 kg m^{-3} the base of the lower halocline and upper boundary of Atlantic Waters. (**o**)

Platforms trajectories (purple: ITP29; blue: IAOOS15; red: IAOOS25).

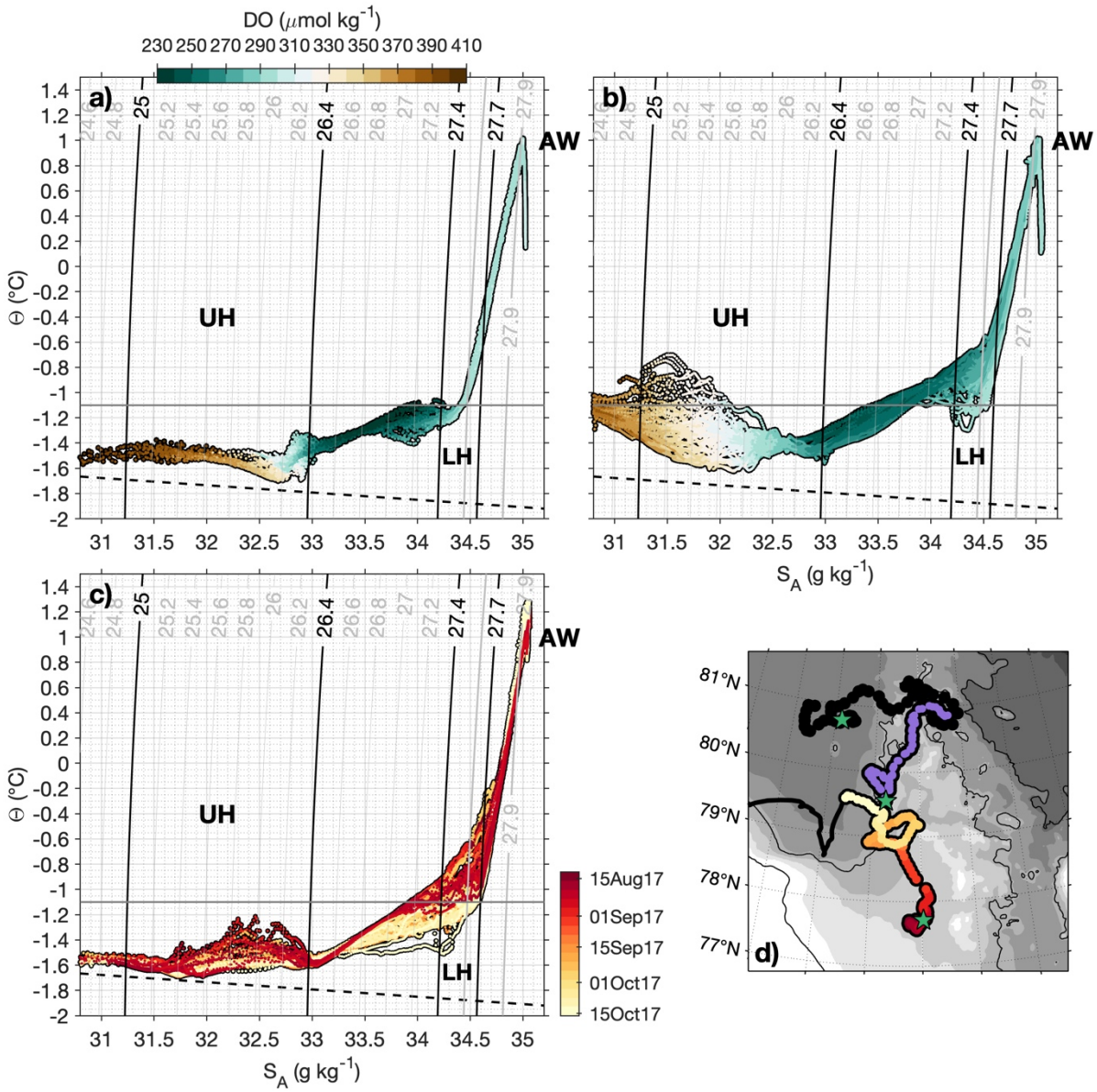

Figure 7: Θ-S_A diagrams from (**a**) ITP29 (2008), (**b**) IAOOS15 (2015) and (**c**) IAOOS25 (2017) data. Color corresponds to dissolved oxygen concentrations (μmol kg^{-1}) in (**a**) and (**b**) and to time in (**c**). Dashed line indicates the freezing line. (**d**) Platforms trajectories of ITP29 (purple), IAOOS15 (black) and IAOOS25 (color is time as in (**c**)). Isopycnal 25 kg m^{-3} roughly marks the base of the mixed layer, 26.4 kg m^{-3} the base of the upper halocline (UH) and 27.7 kg m^{-3} the base of the lower halocline (LH) and upper boundary of Atlantic Waters (AW).

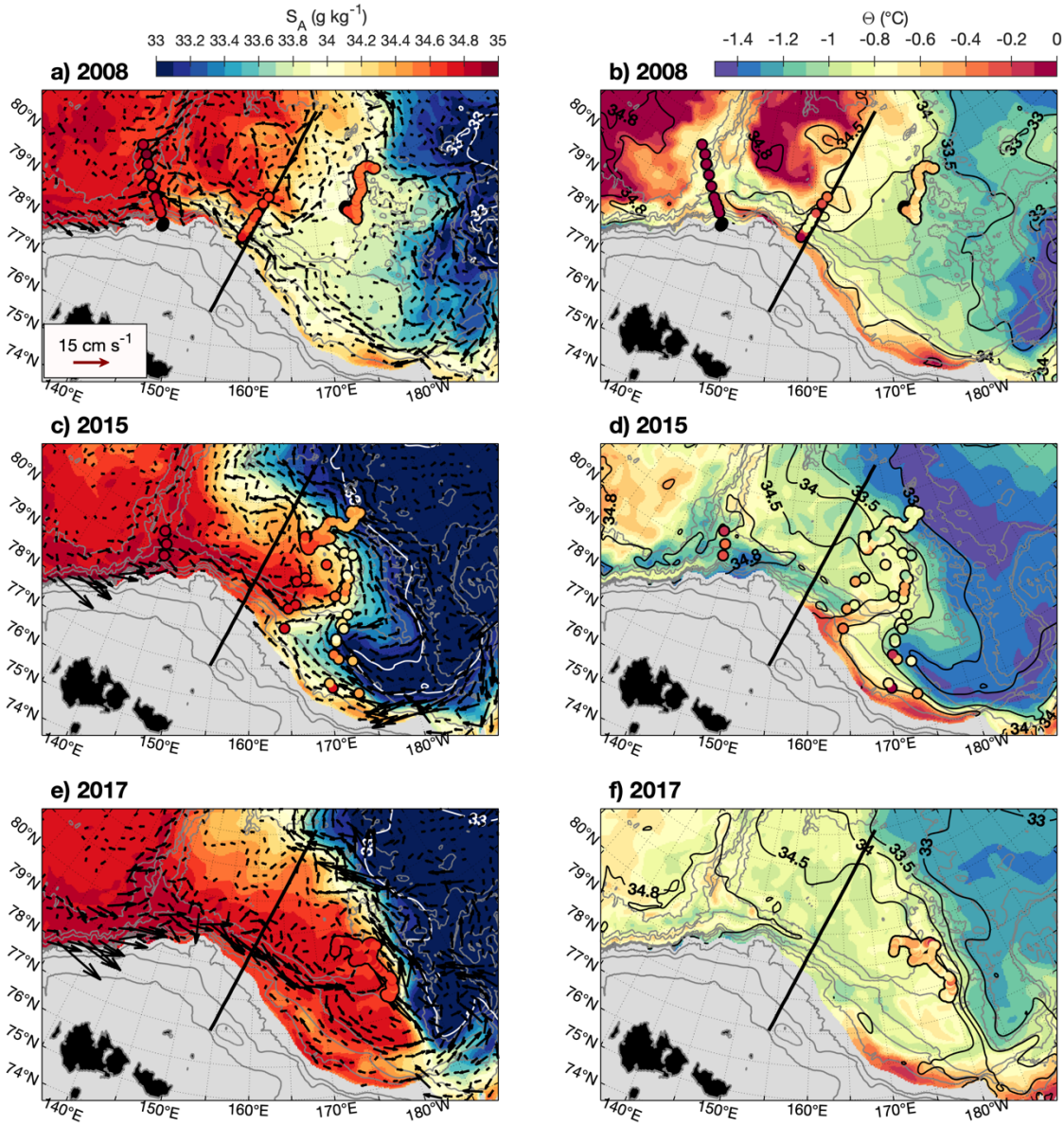

Figure 8: Monthly mean (**left**) absolute salinity and (**right**) conservative temperature in the lower halocline layer (150 m) in September (**a, b**) 2008, (**c, d**) 2015 and (**e, f**) 2017 in PSY4. Round markers correspond to in-situ values. Arrows correspond to monthly mean horizontal velocities larger than 1 cm s^{-1}. Time evolutions of parameters along the black transect are shown in *Figure 9*.

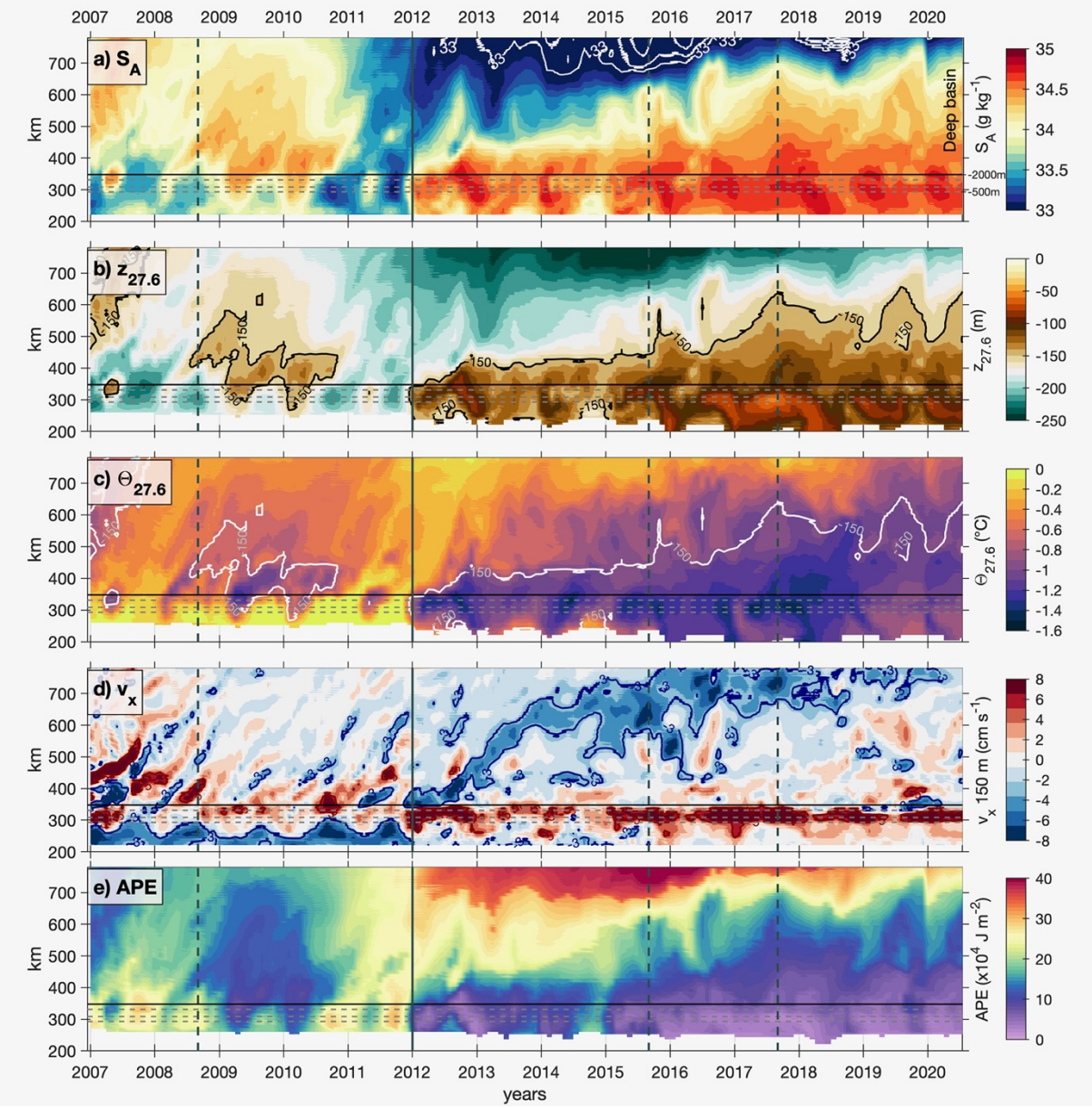

Figure 9: Monthly mean properties along the transect shown in *Figure 8*. (**a**) Absolute salinity at 150 m (S_A, g kg^{-1}). (**b**) Depth of isopycnal 27.6 kg m^{-3} ($z_{27.6}$, m). (**c**) Temperature on the 27.6 kg m^{-3} isopycnal ($\Theta_{27.6}$,°C). (**d**) Cross-section velocity at 150 m (v_x, cm s^{-1}), positive values being oriented south-eastward. (**e**) Available Potential Energy (APE, x10^4 J m^{-2}). Vertical dashed lines mark September 2008, 2015 and 2017 for which horizontal fields are shown *in Figure 9*. Vertical plain line marks January 2012. The horizontal thick black line (around km 350) marks the position of isobath 2000 m which separates the basin from the slope. Horizontal dashed grey lines (around km 300) mark isobaths 500 m, 1000 m and 1500 m.

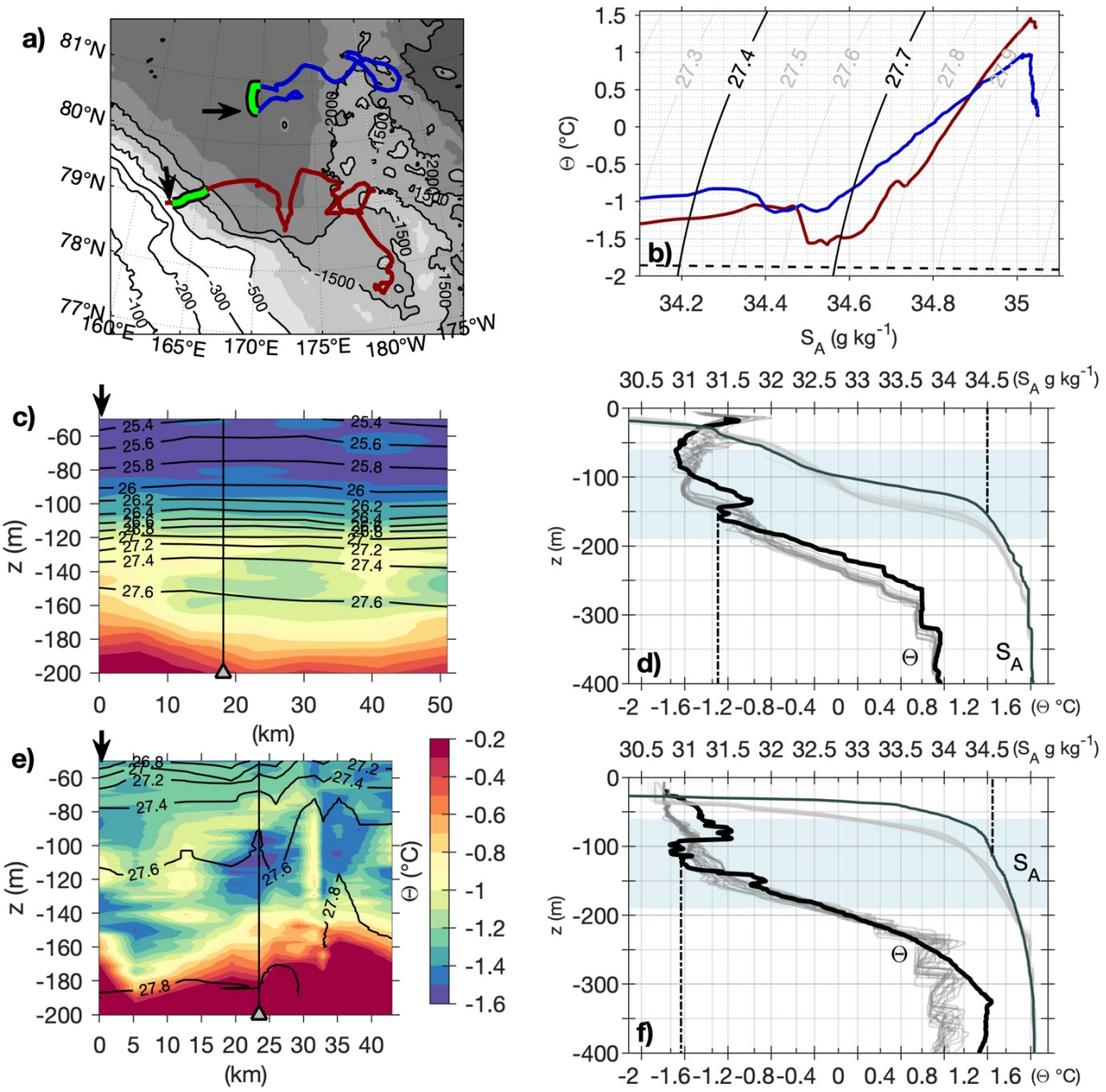

Figure 10: (**a**) Trajectories of IAOOS15 (blue) and IAOOS25 (red). Cold lenses were found in the green sub-sections. (**b**) Temperature-salinity curve in the cold lens for IAOOS15 (blue) and IAOOS25 (dark red). (**c**) IAOOS15 (September 2015) temperature along the green sub-sections, and (**d**) temperature (black thick lines) and salinity (dark grey thick lines) profiles in the cold lens. (**e-f**) Same for IAOOS25 (November 2017). The beginning of the section is indicated by an arrow in (**a**), (**c**) and (**e**) and the position of the cold lens is indicated by thick vertical black lines. Light grey profiles in (**d**) and (**f**) are outside the cold lens area (15 profiles preceding the green sub-section in time) and vertical dotted lines indicate temperature and salinity in the cold lens. The blue shade corresponds to the depths shown in sections (**c**) and (**e**). Corresponding synoptic horizontal PSY4 fields are shown in ***Figure S4***.

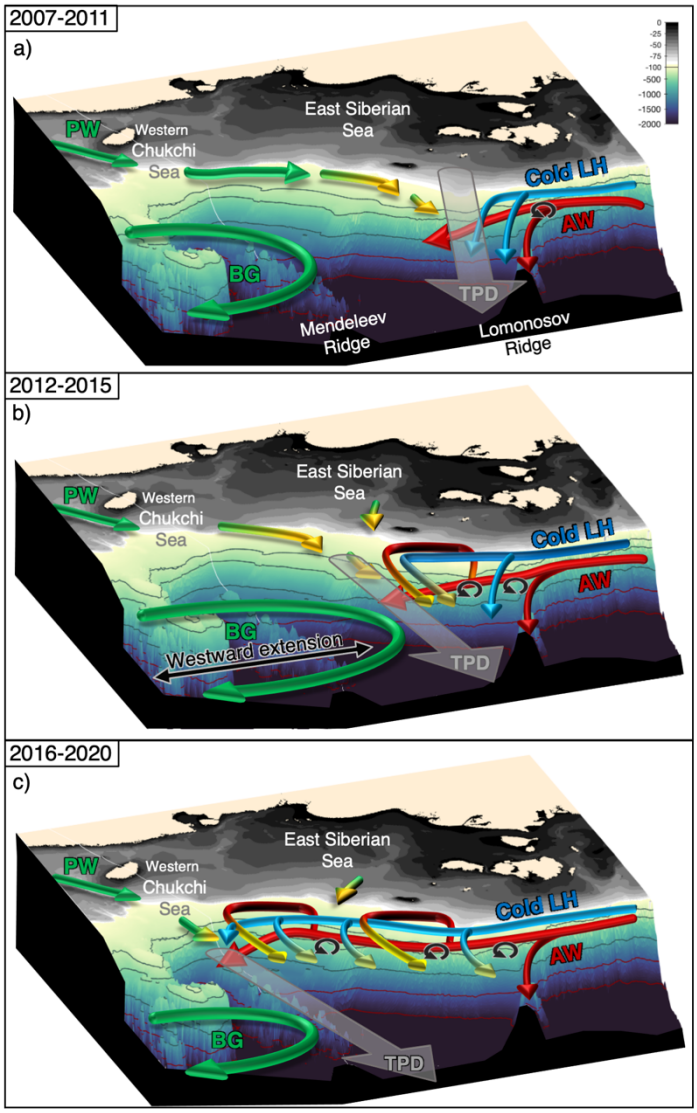

Figure 11: Schematics of halocline water circulation along the East Siberian Sea slope (ESS) and in the Makarov Basin during the periods (**a**) 2007-2011, (**b**) 2012-2015 and (**c**) 2016-2020. Blue arrows show the eastward progression of the relatively cold Atlantic-derived lower halocline (LH) waters, influencing the Makarov Basin lower halocline. The underlying Atlantic Water (AW, red arrows) upwells over the slope and mixes with shelf waters (in yellow), forming warmer LH waters. Black arrows represent mesoscale activity, increasing to the east, and contributing to enhance slope water influence in the Makarov Basin interior. The Beaufort Gyre (BG) extended westward in 2012-2015 and likely brought additional contributions of Pacific Water (PW, green arrows) to the upper halocline in the Makarov Basin. In 2016-2020, the BG retreated to the east, and the Transpolar Drift (TPD, grey arrow) shifted towards Mendeleev Ridge.

Table 1: Lower halocline mean density (σ, kg m^{-3}), absolute salinity (S_A, g kg^{-1}), and conservative temperature (Θ, °C) over the East Siberian shelf (bathymetry < 300 m), slope (300 to 1500 m isobath) and in the Makarov Basin (beyond 2000 m isobath). See *Figure 3* for the locations. *ESS: East Siberian Sea.*

		2007-2008			**2014-2015**			**2016**		
		Shelf	Slope	Basin	Shelf	Slope	Basin	Shelf	Slope	Basin
Lomonosov Ridge	σ	27.4	27.4	27.4	27.6	27.6	27.6			
	S_A	34.2	34.2	34.2	34.4	34.5	34.5			
	Θ	-1.3	-1.6	-1.7	-1.5	-1.5	-1.5			
West ESS	σ	27.5	27.5	27.6	27.7	27.7	27.7			
	S_A	34.3	34.3	34.4	34.6	34.6	34.6			
	Θ	-1.2	-1.2	-1.2	-0.9	-1.1	-1.1			
Central ESS	σ				27.7	27.6	27.7	27.7	27.6	27.7
	S_A				34.6	34.5	34.6	34.6	34.5	34.6
	Θ				-0.4	-0.7	-1.2	-1.2	-0.9	-1
East ESS	σ						~27.7	27.7	27.7	27.7
	S_A						~34.6	34.6	34.6	34.6
	Θ						~-0.6	-0.8	-1.2	-1.2

Table 2: Hydrographic characteristics in the Makarov Basin during summers 2008, 2015 and 2017. Boundaries in density (σ, kg m^{-3}) are given for each layer, together with the mean observed properties: depth (z, m), absolute salinity (S_A, g kg^{-1}), conservative temperature (Θ, °C), and dissolved oxygen (DO, µmol kg^{-1}). Minimum and maximum values are given in square brackets.

Layer	σ (kg m^{-3})		ITP29 (2008)		IAOOS15 (2015)		IAOOS25 (2017)	
Upper halocline	[25; 26.4]	z	55	[20; 90]	80	[20; 130]	60	[20; 80]
		S_A	32.5	[31; 33]	32.3	[31; 33]	32.1	[31; 33]
		Θ	-1.6	[-1.7; 1.3]	-1.4	[-1.6; -0.7]	-1.6	[-1.7; -1.2]
		DO	330	[238; 410]	304	[242; 381]		
Intermediate layer	[26.4; 27.4]	z	110	[90; 140]	145	[130; 180]	100	[80; 130]
		S_A	33.6	[33; 34.2]	33.6	[33; 34.2]	33.6	[33; 34.2]
		Θ	-1.3	[-1.6; -1.1]	-1.4	[-1.6; -0.8]	-1.3	[-1.6; -0.9]
		DO	250	[219; 296]	250	[239; 297]		
Lower halocline	[27.4; 27.7]	z	160	[140; 190]	190	[180; 200]	145	[130; 160]
		S_A	34.5	[34.2; 34.6]	34.5	[34.2; 34.6]	34.5	34.2; 34.6]
		Θ	-1.2	[-1.3; -1.1]	-0.9	[-1.3; -0.7]	-1.1	[-1.5; -0.7]
		DO	290	[250; 300]	270	[240; 300]		
Thermocline	[27.7; 27.85]	z	210	[190; 260]	220	[200; 260]	180	[160; 220]
		S_A	34.8	[34.6; 34.9]	34.8	[34.6; 34.9]	34.8	[34.6; 34.9]
		Θ	-0.1	[-1; 0.7]	-0.3	[-1.1; 0.8]	-0.5	[-1.2; 0.6]
		DO	297	[283; 311]	286	[261; 303]		
Top Atlantic layer	~ 27.85	z	260		260		220	
		S_A	34.9		34.9		34.9	
		Θ	0.6		0.4		0.2	
		DO	295		287			

REFERENCES

Alkire, M. B., Rember, R., & Polyakov, I. (2019). Discrepancy in the Identification of the Atlantic/Pacific Front in the Central Arctic Ocean: NO Versus Nutrient Relationships. Geophysical Research Letters, 46(7), 3843–3852. https://doi.org/10.1029/2018GL081837

Anderson, L. G., Björk, G., Jutterström, S., Pipko, I., Shakhova, N., Semiletov, I., & Wåhlström, I. (2011). East Siberian Sea, an Arctic region of very high biogeochemical activity. Biogeosciences, 8(6), 1745–1754. https://doi.org/10.5194/bg-8-1745-2011

Anderson, L. G., Andersson, P. S., Björk, G., Jones, E. P., Jutterström, S., & Wåhlström, I. (2013). Source and formation of the upper halocline of the Arctic Ocean. Journal of Geophysical Research: Oceans, 118(1), 410–421. https://doi.org/10.1029/2012JC008291

Anderson, L. G., Björk, G., Holby, O., Jutterström, S., Mörth, C. M., O'Regan, M., et al. (2017). Shelf–Basin interaction along the East Siberian Sea. Ocean Science, 13(2), 349–363. https://doi.org/10.5194/os-13-349-2017

Athanase, M., Provost, C., Artana, C., Pérez-Hernández, M. D., Sennéchael, N., Bertosio, C., et al. (2021). Changes in Atlantic Water circulation patterns and volume transports North of Svalbard over the last 12 years (2008–2020). Journal of Geophysical Research: Oceans, 126, e2020JC016825. https:// doi.org/10.1029/2020JC016825

Athanase, M., Provost, C., Pérez-Hernández, M. D., Sennéchael, N., Bertosio, C., Artana, C., et al. (2020). Atlantic Water Modification North of Svalbard in the Mercator Physical System From 2007 to 2020. Journal of Geophysical Research: Oceans, 125(10), e2020JC016463. https://doi.org/10.1029/2020JC016463

Athanase, M., Sennéchael, N., Garric, G., Koenig, Z., Boles, E., & Provost, C. (2019). New Hydrographic Measurements of the Upper Arctic Western Eurasian Basin in 2017 Reveal Fresher Mixed Layer and Shallower Warm Layer Than 2005–2012 Climatology. Journal of Geophysical Research: Oceans, 124(2), 1091–1114. https://doi.org/10.1029/2018JC014701

Bauch, D., & Cherniavskaia, E. (2018). Water Mass Classification on a Highly Variable Arctic Shelf Region: Origin of Laptev Sea Water Masses and Implications for the Nutrient Budget. Journal of Geophysical Research: Oceans, 123(3), 1896–1906. https://doi.org/10.1002/2017JC013524

Bauch, D., Cherniavskaia, E., & Timokhov, L. (2016). Shelf basin exchange along the Siberian continental margin: Modification of Atlantic Water and Lower Halocline Water. Deep Sea Research Part I: Oceanographic Research Papers, 115, 188–198. https://doi.org/10.1016/j.dsr.2016.06.008

Bertosio, C., Provost, C., Sennéchael, N., Artana, C., Athanase, M., Boles, E., et al. (2020). The Western Eurasian Basin Halocline in 2017: Insights From Autonomous NO Measurements and the Mercator Physical System. Journal of Geophysical Research: Oceans, 125(7), e2020JC016204. https://doi.org/10.1029/2020JC016204

Bertosio, C., Provost, C., Sennéchael, N., Koenig, Z., Labaste, M., & Athanase, M. (2021). Arctic Makarov Basin : IAOOS14, IAOOS15 and IAOOS25 ocean CTD-DO profiles in 2015 and 2017. SEANOE. https://doi.org/10.17882/83520

Bertosio, C., Provost, C., Athanase, M., Sennéchael, N., Lellouche, J.-M., Garric, G., et al. (*revision; JGR*). Changes in freshwater distribution and pathways in the Arctic Ocean since 2007 in the Mercator Ocean global operational system. Journal of Geophysical Research: Oceans.

Bourgain, P., & Gascard, J. C. (2011). The Arctic Ocean halocline and its interannual variability from 1997 to 2008. Deep Sea Research Part I: Oceanographic Research Papers, 58(7), 745–756. https://doi.org/10.1016/j.dsr.2011.05.001

Bourgain, P., & Gascard, J. C. (2012). The Atlantic and summer Pacific waters variability in the Arctic Ocean from 1997 to 2008, Geophys. Res. Lett., 39, L05603, doi:10.1029/2012GL051045.

Carmack, E. C., (2007). The alpha/beta ocean distinction: A perspective on freshwater fluxes, convection, nutrients and productivity in high-latitude seas. Deep-Sea Res. II, 54, 2578–2598, doi:10.1016/j.dsr2.2007.08.018.

Carmack, E. C., Yamamoto-Kawai, M., Haine, T. W. N., Bacon, S., Bluhm, B. A., Lique, C., et al. (2016). Freshwater and its role in the Arctic Marine System: Sources, disposition, storage, export, and physical and biogeochemical consequences in the Arctic and global oceans. Journal of Geophysical Research: Biogeosciences, 121(3), 675–717. https://doi.org/10.1002/2015JG003140

Colin de Verdière, A., Huck, T., Pogossian, S., & Ollitrault, M. (2018). Available Potential Energy in Density Coordinates. Journal of Physical Oceanography, 48(8), 1867–1883. https://doi.org/10.1175/JPO-D-17-0272.1

Dmitrenko, I. A., Ivanov, V. V., Kirillov, S. A., Vinogradova, E. L., Torres-Valdes, S., & Bauch, D. (2011). Properties of the Atlantic derived halocline waters over the Laptev Sea continental margin: Evidence from 2002 to 2009. Journal of Geophysical Research: Oceans, 116(C10). https://doi.org/10.1029/2011JC007269

Feistel, R. (2018). Thermodynamic properties of seawater, ice and humid air: TEOS-10, before and beyond. Ocean Science, 14(3), 471–502. https://doi.org/10.5194/os-14-471-2018

Fer, I., Koenig, Z., Kozlov, I. E.,Ostrowski, M., Rippeth, T. P., & Padman, L., et al. (2020). Tidally forced lee waves drive turbulent mixing along the Arctic Ocean margins. Geophysical Research Letters, 47, e2020GL088083. https://doi.org/10.1029/2020GL088083

Fichefet, T. and Maqueda, M. A. (1997). Sensitivity of a global sea ice model to the treatment of ice thermodynamics and dynamics, J. Geophys. Res., 102, 12609-12646. https://doi.org/10.1029/97JC00480

Haine, T. W. N., Curry, B., Gerdes, R., Hansen, E., Karcher, M., Lee, C., et al. (2015). Arctic freshwater export: Status, mechanisms, and prospects. Global and Planetary Change, 125, 13–35. https://doi.org/10.1016/j.gloplacha.2014.11.013

Jung, J., Cho, K.-H., Park, T., Yoshizawa, E., Lee, Y., Yang, E. J., et al. (2021). Atlantic-Origin Cold Saline Water Intrusion and Shoaling of the Nutricline in the Pacific Arctic. Geophysical Research Letters, 48(6), e2020GL090907. https://doi.org/10.1029/2020GL090907

Kikuchi, T., Hatakeyama, K., & Morison, J. H. (2004). Distribution of convective Lower Halocline Water in the eastern Arctic Ocean. Journal of Geophysical Research: Oceans, 109(C12). https://doi.org/10.1029/2003JC002223

Koenig, Z., Provost, C., Villacieros-Robineau, N., Sennéchael, N., Meyer, A., Lellouche, J.-M., & Garric, G. (2017). Atlantic waters inflow north of Svalbard: Insights from IAOOS observations and Mercator Ocean global operational system during N-ICE2015. Journal of Geophysical Research: Oceans, 122(2), 1254–1273. https://doi.org/10.1002/2016JC012424

Koenig, Z., Provost, C., Sennéchael, N., Garric, G., & Gascard, J.-C. (2017). The Yermak Pass Branch: A Major Pathway for the Atlantic Water North of Svalbard? Journal of Geophysical Research: Oceans, 122(12), 9332–9349. https://doi.org/10.1002/2017JC013271

Krishfield, R., Toole, J., Proshutinsky, A., & Timmermans, M.-L. (2008). Automated Ice-Tethered Profilers for Seawater Observations under Pack Ice in All Seasons. Journal of Atmospheric and Oceanic Technology, 25(11), 2091–2105. https://doi.org/10.1175/2008JTECHO587.1

Lellouche, J.-M., Greiner, E., Galloudec, O. L., Garric, G., Regnier, C., Drevillon, M., et al. (2018). Recent updates to the Copernicus Marine Service global ocean monitoring and forecasting real-time 1⁄12° high-resolution system. Ocean Science, 14(5), 1093–1126. https://doi.org/10.5194/os-14-1093-2018

Lenn, Y. D., Wiles, P. J., Torres-Valdes, S., Abrahamsen, E. P., Rippeth, T. P., Simpson, J. H., et al. (2009). Vertical mixing at intermediate depths in the Arctic boundary current. Geophysical Research Letters, 36(5). https://doi.org/10.1029/2008GL036792

Madec, G. and Imbard, M. (1996). A global ocean mesh to overcome the North Pole singularity, Clim. Dynam., 12, 381–388.

Madec, G. and the NEMO team: NEMO ocean engine (2008). Note du Pôle de modélisation, Institut Pierre-Simon Laplace (IPSL), France, No. 27 ISSN, 1288-1619

McDougall, T.J. and Barker, P.M. (2011). Getting started with TEOS-10 and the Gibbs Seawater (GSW) Oceanographic Toolbox, 28pp., SCOR/IAPSO WG127, ISBN 978-0-646-55621-5.

McLaughlin, F. A., Carmack, E. C., Macdonald, R. W., Melling, H., Swift, J. H., Wheeler, P. A., et al. (2004). The joint roles of Pacific and Atlantic-origin waters in the Canada Basin, 1997–1998. Deep Sea Research Part I: Oceanographic Research Papers, 51(1), 107–128. https://doi.org/10.1016/j.dsr.2003.09.010

Morison, J., Steele, M., & Andersen, R. (1998). Hydrography of the upper Arctic Ocean measured from the nuclear submarine U.S.S. Pargo. Deep Sea Research Part I: Oceanographic Research Papers, 45(1), 15–38. https://doi.org/10.1016/S0967-0637(97)00025-3

Morison, J., Kwok, R., Peralta-Ferriz, C., Alkire, M., Rigor, I., Andersen, R., & Steele, M. (2012). Changing Arctic Ocean freshwater pathways. Nature, 481(7379), 66–70. https://doi.org/10.1038/nature10705

Nishino, S., Shimada, K., Itoh, M., Yamamoto-Kawai, M., & Chiba, S. (2008). East–west differences in water mass, nutrient, and chlorophyll a distributions in the sea ice reduction region of the western Arctic Ocean. Journal of Geophysical Research: Oceans, 113(C1). https://doi.org/10.1029/2007JC004666

Nishino, S., Itoh, M., Williams, W. J., & Semiletov, I. (2013). Shoaling of the nutricline with an increase in near-freezing temperature water in the Makarov Basin. Journal of Geophysical Research: Oceans, 118(2), 635–649. https://doi.org/10.1029/2012JC008234

Peralta-Ferriz, C., & Woodgate, R. A. (2017). The Dominant Role of the East Siberian Sea in Driving the Oceanic Flow Through the Bering Strait—Conclusions From GRACE Ocean Mass Satellite Data and In Situ Mooring Observations Between 2002 and 2016. Geophysical Research Letters, 44(22), 11,472-11,481. https://doi.org/10.1002/2017GL075179

Pérez-Hernández, M. D., Pickart, R. S., Pavlov, V., Våge, K., Ingvaldsen, R., Sundfjord, A., et al. (2017). The Atlantic Water boundary current north of Svalbard in late summer. Journal of Geophysical Research: Oceans, 122(3), 2269–2290. https://doi.org/10.1029/2018JC014299

Pisareva, M. N., Pickart, R. S., Spall, M. A., Nobre, C., Torres, D. J., Moore, G. W. K., & Whitledge, T. E. (2015). Flow of pacific water in the western Chukchi Sea: Results from the 2009 RUSALCA expedition. Deep Sea Research Part I: Oceanographic Research Papers, 105, 53–73. https://doi.org/10.1016/j.dsr.2015.08.011

Polyakov, I. V., Pnyushkov, A. V., Alkire, M. B., Ashik, I. M., Baumann, T. M., Carmack, E. C., et al. (2017). Greater role for Atlantic inflows on sea-ice loss in the Eurasian Basin of the Arctic Ocean. Science, 356(6335), 285–291. https://doi.org/10.1126/science.aai8204

Polyakov, I. V., Pnyushkov, A. V., & Carmack, E. C. (2018). Stability of the Arctic halocline:

A new indicator of arctic climate change. Environmental Research Letters, 13(12), 125,008. https://doi.org/10.1088/1748-9326/aaecle

Polyakov, I. V., Rippeth, T. P., Fer, I., Alkire, M. B., Baumann, T. M., Carmack, E. C., et al. (2020). Weakening of Cold Halocline Layer Exposes Sea Ice to Oceanic Heat in the Eastern Arctic Ocean. Journal of Climate, 33(18), 8107–8123. https://doi.org/10.1175/JCLI-D-19-0976.1

Proshutinsky, A., Krishfield, R., Timmermans, M.-L., Toole, J., Carmack, E. C., McLaughlin, F., et al. (2009). Beaufort Gyre freshwater reservoir: State and variability from observations. Journal of Geophysical Research: Oceans, 114(C1). https://doi.org/10.1029/2008JC005104

Proshutinsky, A., Krishfield, R., Toole, J. M., Timmermans, M.-L., Williams, W., Zimmermann, S., et al. (2019). Analysis of the Beaufort Gyre Freshwater Content in 2003–2018. Journal of Geophysical Research: Oceans, 124(12), 9658–9689. https://doi.org/10.1029/2019JC015281

Rainville, L., & Winsor, P. (2008). Mixing across the Arctic Ocean: Microstructure observations during the Beringia 2005 Expedition. Geophysical Research Letters, 35(8). https://doi.org/10.1029/2008GL033532

Regan, H., Lique, C., & Armitage, T. W. K. (2019). The Beaufort Gyre Extent, Shape, and Location Between 2003 and 2014 From Satellite Observations. Journal of Geophysical Research: Oceans, 124(2), 844–862. https://doi.org/10.1029/2018JC014379

Rudels, B., Anderson, L. G., & Jones, E. P. (1996). Formation and evolution of the surface mixed layer and halocline of the Arctic Ocean. Journal of Geophysical Research: Oceans, 101(C4), 8807–8821. https://doi.org/10.1029/96JC00143

Rudels, B., Korhonen, M., Schauer, U., Pisarev, S., Rabe, B., & Wisotzki, A. (2015). Circulation and transformation of Atlantic water in the Eurasian Basin and the contribution of the Fram Strait inflow branch to the Arctic Ocean heat budget. Progress in Oceanography, 132, 128–152. https://doi.org/10.1016/j.pocean.2014.04.003

Rudels, B., Meyer, R., Fahrbach, E., Ivanov, V. V., Østerhus, S., Quadfasel, D., et al. (2000). Water mass distribution in Fram Strait and over the Yermak Plateau in summer 1997. Annales Geophysicae, 18(6), 687–705. https://doi.org/10.1007/s00585-000-0687-5

Schulz, K., Büttner, S., Rogge, A., Janout, M., Hölemann, J., & Rippeth, T. P. (2021). Turbulent mixing and the formation of an intermediate nepheloid layer above the Siberian continental shelf break. Geophysical Research Letters, 48, e2021GL092988. https://doi.org/10.1029/2021GL092988

Schulz, K., Janout, M., Lenn, Y.-D., Ruiz-Castillo, E., Polyakov, I., Mohrholz, V., et al. (2021). On the along-slope heat loss of the Boundary Current in the Eastern Arctic Ocean. Journal of Geophysical Research: Oceans, 126, e2020JC016375. https://doi.org/10.1029/2020JC016375

Serreze, M. C., Barrett, A. P., Crawford, A. D., & Woodgate, R. A. (2019). Monthly Variability in Bering Strait Oceanic Volume and Heat Transports, Links to Atmospheric Circulation and Ocean Temperature, and Implications for Sea Ice Conditions. Journal of Geophysical Research: Oceans, 124(12), 9317–9337. https://doi.org/10.1029/2019JC015422

Shimada, K., Carmack, E. C., Hatakeyama, K., & Takizawa, T. (2001). Varieties of shallow temperature maximum waters in the western Canadian Basin of the Arctic Ocean. Geophysical Research Letters, 28(18), 3441-3444.

Shimada, K., Itoh, M., Nishino, S., McLaughlin, F., Carmack, E. C., & Proshutinsky, A. (2005). Halocline structure in the Canada Basin of the Arctic Ocean. Geophysical Research Letters, 32(3). https://doi.org/10.1029/2004GL021358

Steele, M., & Boyd, T. (1998). Retreat of the cold halocline layer in the Arctic Ocean. Journal

of Geophysical Research: Oceans, 103(C5), 10419–10435. https://doi.org/10.1029/98JC00580

Steele, M., Morison, J., Ermold, W., Rigor, I., Ortmeyer, M., and Shimada, K. (2004). Circulation of summer Pacific halocline water in the Arctic Ocean, J. Geophys. Res., 109, C02027, doi:10.1029/2003JC002009.

Swift, J. H., Jones, E. P., Aagaard, K., Carmack, E. C., Hingston, M., MacDonald, R. W., et al. (1997). Waters of the Makarov and Canada basins. Deep Sea Research Part II: Topical Studies in Oceanography, 44(8), 1503–1529. https://doi.org/10.1016/S0967-0645(97)00055-6

Timmermans, M.-L., Cole, S., Toole, J. (2012). Horizontal density structure and restratification of the Arctic Ocean surface layer. Journal of Physical Oceanography 42 (4), 659–668. http://dx.doi.org/10.1175/JPO-D-11-0125.1.

Timmermans, M. L., & Jayne, S. R. (2016). The Arctic Ocean Spices Up. Journal of Physical Oceanography, 46(4), 1277-1284.

Timmermans, M.-L., Krishfield, R., Laney, S., & Toole, J. (2010). Ice-Tethered Profiler Measurements of Dissolved Oxygen under Permanent Ice Cover in the Arctic Ocean. Journal of Atmospheric and Oceanic Technology, 27(11), 1936–1949. https://doi.org/10.1175/2010JTECHO772.1

Timmermans, M.-L., Proshutinsky, A., Golubeva, E., Jackson, J. M., Krishfield, R., McCall, M., et al. (2014). Mechanisms of Pacific Summer Water variability in the Arctic's Central Canada Basin. Journal of Geophysical Research: Oceans, 119(11), 7523–7548. https://doi.org/10.1002/2014JC010273

Timmermans, M.-L., Marshall, J., Proshutinsky, A., & Scott, J. (2017). Seasonally derived components of the Canada Basin halocline. Geophysical Research Letters, 44(10), 5008–5015. https://doi.org/10.1002/2017GL073042

Wang, X., Zhao, J., Lobanov, V. B., Kaplunenko, D., Rudykh, Y. N., He, Y., & Chen, X. (2021). Distribution and Transport of Water Masses in the East Siberian Sea and Their Impacts on the Arctic Halocline. Journal of Geophysical Research: Oceans, 126(8), e2020JC016523. https://doi.org/10.1029/2020JC016523

Woodgate, R. A. (2018). Increases in the Pacific inflow to the Arctic from 1990 to 2015, and insights into seasonal trends and driving mechanisms from year-round Bering Strait mooring data. Progress in Oceanography, 160, 124–154. https://doi.org/10.1016/j.pocean.2017.12.007

Woodgate, R. A., & Peralta-Ferriz, C. (2021). Warming and Freshening of the Pacific Inflow to the Arctic From 1990-2019 Implying Dramatic Shoaling in Pacific Winter Water Ventilation of the Arctic Water Column. Geophysical Research Letters, 48(9), e2021GL092528. https://doi.org/10.1029/2021GL092528

Woodgate, R. A., Aagaard, K., Swift, J. H., Falkner, K. K., & Smethie, W. M. (2005). Pacific ventilation of the Arctic Ocean's lower halocline by upwelling and diapycnal mixing over the continental margin. Geophysical Research Letters, 32(18). https://doi.org/10.1029/2005GL023999

Journal of Geophysical Research Ocean
Supporting Information for

Changes in Arctic Halocline Waters along the East Siberian Slope and in the Makarov Basin from 2007 to 2020

Cécilia Bertosio[1], Christine Provost[1], Marylou Athanase[2], Nathalie Sennéchael[1], Jean-Michel Lellouche[3], Gilles Garric[3], Joo-Hong Kim[4], Kyoung-Ho Cho[4], Tae-Wook Park[4]

[1]: LOCEAN-IPSL, Sorbonne Université (UPMC, Univ. Paris 6), CNRS, IRD, MNHN, Paris, France.
[2]: Alfred-Wegener-Institut, Bremerhaven, Germany.
[3]: MERCATOR-OCEAN, Toulouse, France.
[4]: Division of Polar Ocean Sciences, Korea Polar Research Institute, Incheon 21990, Republic of Korea

Contents of this file

Figures S1 to S4

Introduction

Figures S1 to S4 provide supporting information for results described in the main text. Observed and modelled profiles were linearly interpolated to the same 2-m vertical resolution. We reproduced the drifting platform section from Figure 2 using PSY4 collocated profiles and the section from SWERUS over the shelf in 2014 (**Figure S1**). Modelled sections were consistent with observation both in the Makarov Basin and over the shelf, showing similar patterns. SWERUS section with PSY4 profiles highlighted bottom shelf water less dense ($\Delta\sigma \sim 1$ kg.m^{-3}) and a thicker warm layer near the surface (~ 10 m). Modelled temperature and salinity fronts between the west and east ESS were properly located compared with observations. The eastern ESS exhibited particularly low model-observation temperature differences ($\Delta\Theta \sim 0$°C). PSY4 temperature and salinity mean profiles were compared with in-situ measurements and a distinction was made with profiles over the shelf (< 300 m) (**Figure S2**). Differences were similar to those described in Bertosio, Provost, Athanase, et al. (2021): modelled Atlantic waters were colder than in-situ measurements ($\Delta\Theta \sim 1$°C) and salinity differences were larger than 2 g.kg^{-1} in the 50

first meters. However, temperature and salinity differences were small respectively in the cold halocline and Atlantic layers. Two daily mapped-snapshots of the salinity with horizontal velocity PSY4 fields (**Figure S3**) and surface conditions (ice and winds) at the transect from Figure 7 (**Figure S4**) are also included in the supporting information.

Reference

Bertosio, C., Provost, C., Athanase, M., Sennéchael, N., Lellouche, J.-M., Garric, G., et al. (2021). Changes in freshwater distribution and pathways in the Arctic Ocean since 2007 in the Mercator Ocean global operational system. Journal of Geophysical Research: Oceans (*Under review in this special issue*)

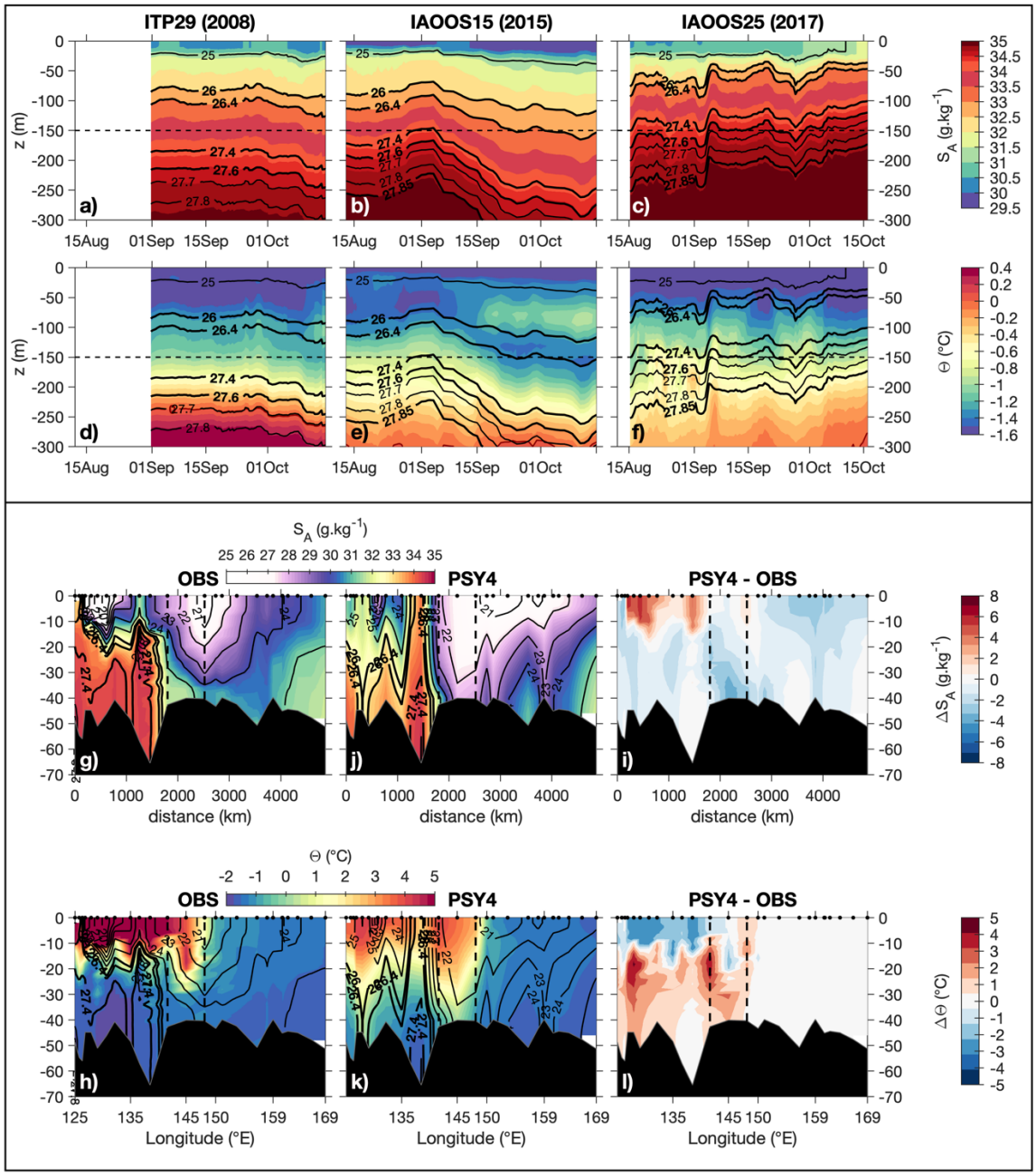

Figure S1: (*Top panels*) Sections as in Figure 2 with collocated PSY4 values to ITP29 (left), IAOOS15 (middle) and IAOOS25 (right) drifts. (**a**, **b**, **c**) Absolute salinity S_A ($g.kg^{-1}$) and (**d**, **e**, **f**) conservative temperature Θ (°C). Horizontal dashed line indicates the depth 150 m.

(*Bottom panels*) Meridional section from SWERUS campaign (2014) over the East Siberian shelf (position in Figure 1) of (**g**, **j**) absolute salinity S_A ($g.kg^{-1}$) and (**h**, **k**) conservative temperature Θ (°C) from (**g**, **h**) in-situ data and (**j**, **k**) collocated PSY4 profiles. Vertical dashed lines indicate major fronts. (**i**, **j**) Salinity and temperature differences OBS-PSY4.

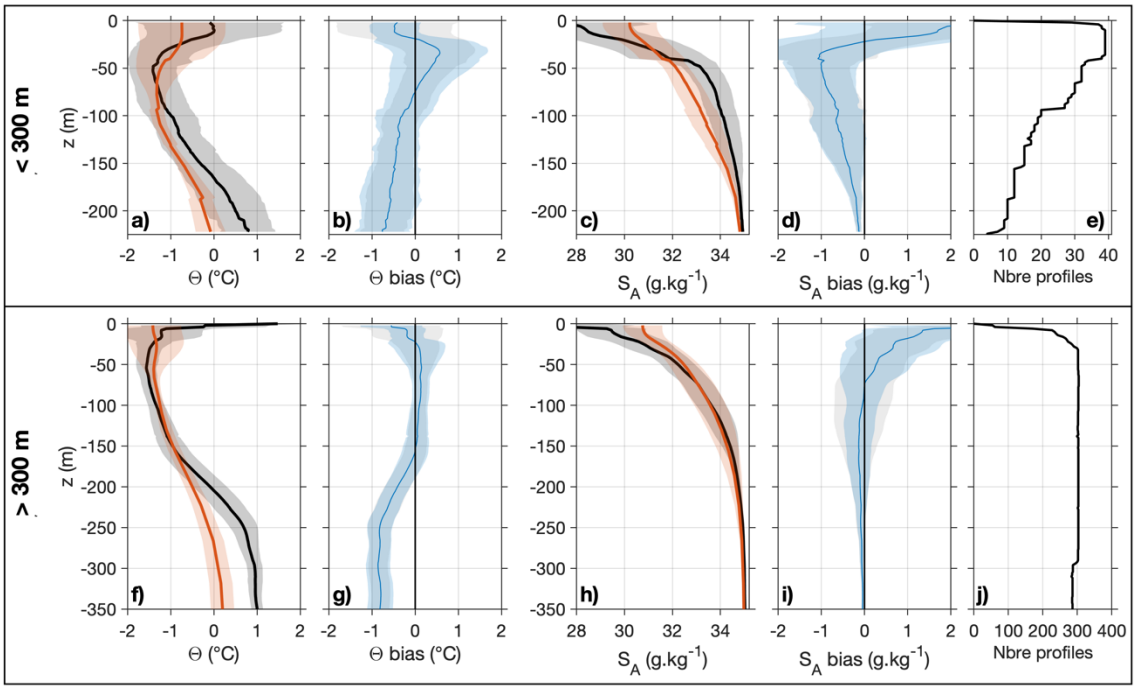

Figure S2: Comparison between in-situ data (black) and PSY4 collocated profiles (orange) in the East Siberian Sea and Makarov Basin over bathymetry shallower (top panels) and deeper (bottom panels) than 300 m depth. (**a**, **f**) Mean conservative temperature Θ (°C) and (**b**, **g**) absolute salinity S_A (g.kg^{-1}) profiles. Shaded envelopes are STD around the mean for observations (grey) and model (orange). (**c**, **h**) Mean bias profiles of Θ and (**e**, **i**) S_A. Shaded envelopes are for bias STD (blue) and sum of model and observations STDs (grey) at each level. (**e**, **j**) Number of data at different depths.

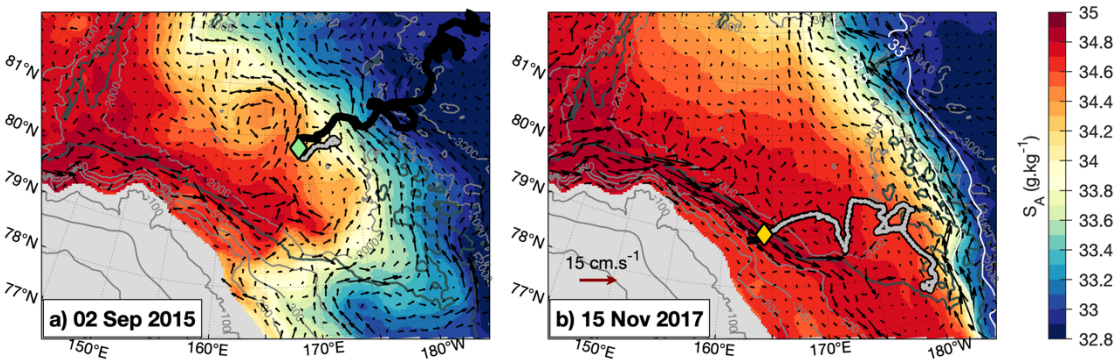

Figure S3: Snapshots of PSY4 absolute salinity (g.kg^{-1}) on (**a**) 2 September 2015 and (**b**) 15 November 2017 at 150 m (in the lower halocline). Black arrows correspond to the modeled velocity field. The thick grey line corresponds to (**a**) the IAOOS15 or (**b**) IAOOS25 trajectory. Diamonds mark the position of the platforms at the selected date when they crossed cold-core mesoscale structures within the lower halocline (*Figure 4*).

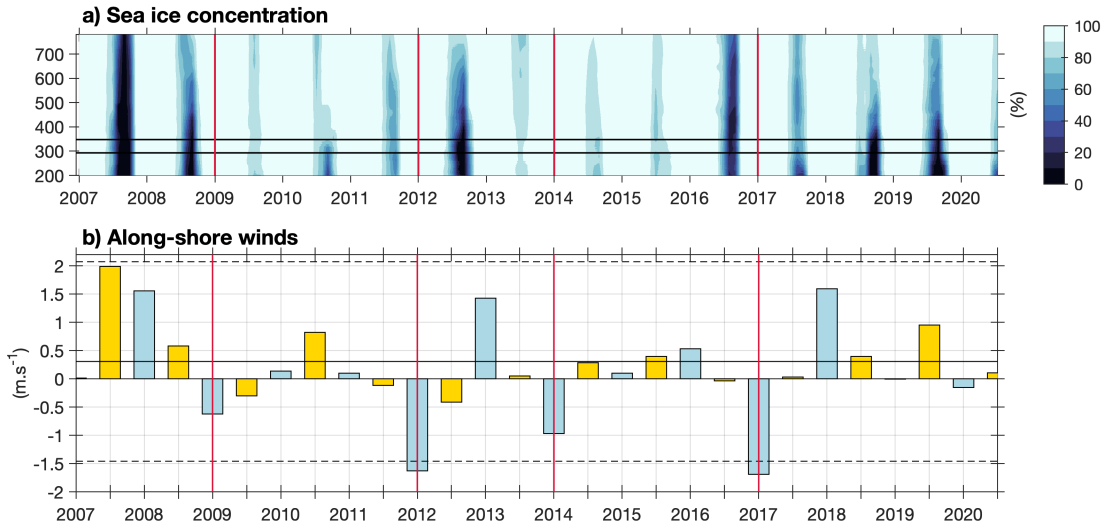

Figure S4: (**a**) PSY4 sea ice concentration (%) and (**b**) ERA-5 winds along the transect shown in *Figure 7*. (**b**) Seasonal along-shore wind velocity ($m.s^{-1}$) on the slope (between isobath 500 and 2000m, indicated in (**a**) by horizontal black lines). Negative values (meaning westward winds) are favorable conditions for upwelling. Winter (from December to March) is in blue and summer (from June to September) in yellow. Horizontal plain and dashed lines mark the mean and the standard deviation respectively. Vertical red lines mark large westward winter winds.

Chapter V
Conclusions and Perspectives

Content

V.1. Conclusions

We examined the evolution of the halocline in the upper Arctic Ocean since 2007 using in-situ measurements and simulations from the high resolution (1/12°) Mercator Ocean global system PSY4V3R1 (hereafter PSY4). Major results are summarized in **Figure 5.1**.

The halocline strength, structure and sources in the western Eurasian Basin were investigated in 2017 combining measurements from the IAOOS 2017 and PSY4 simulations (Bertosio et al., 2020). We combined oxygen and nitrate values to compute the semi-conservative NO parameter which helped in characterizing the halocline. The lower halocline of the western Eurasian Basin was associated with a local NO minimum (NO ~ 390 µM) on 27.8 $kg.m^{-3}$ isopycnal.

In the Nansen Basin, the lower halocline resulted from deep winter convection of dense shelf waters, from Kara or Barents Sea, and recirculating Atlantic Waters. The base of the lower halocline was associated with an absolute salinity of 34.9 $g.kg^{-1}$, a significantly more saline level than the 34.3 psu isohaline documented by Rudels (1996) in data from 1991. This denser and more saline level was in accordance with deeper winter mixed layers observed in the last 10 years on the slope of Nansen Basin and the on-going Atlantification.

In the Amundsen Basin, the halocline was additionally influenced by the Transpolar Drift which advected waters from the Siberian Seas and supplied a cold halocline layer. This cold halocline was associated with a marked NO minimum on 27.4 $kg.m^{-3}$ isopycnal (NO < 380 µM).

The Available Potential Energy computed using PSY4 simulations and IAOOS measurements showed a weaker halocline in Nansen Basin in 2017 (APE ~ 1.5 x 10^4 $J.m^{-2}$). Mercator physical system provided reasonable APE estimates when compared to in-situ data (**Figure 5.2**).

The PSY4 performance was evaluated in the pan-Arctic region using nearly 20,000 independent temperature and salinity profiles over 2007-2020 period (Bertosio et al., 2021a, submitted). Mean spatial distribution of modelled hydrographic properties and water mass were

in good agreement with observations. Major salinity biases were confined in the upper 100 m, in the Canada Basin. At the Fram Strait gateway, AW inflow was found in good agreement with observations (Athanase et al., 2020), and we additionally showed that PSY4 represents realistic Pacific Water inflow and hydrographic properties. The large-scale distribution of sea surface height was consistent with altimetry data, and freshwater content in PSY4 was congruent to the rather scarce observations in the Arctic Ocean or the mooring data in the Canada Basin.

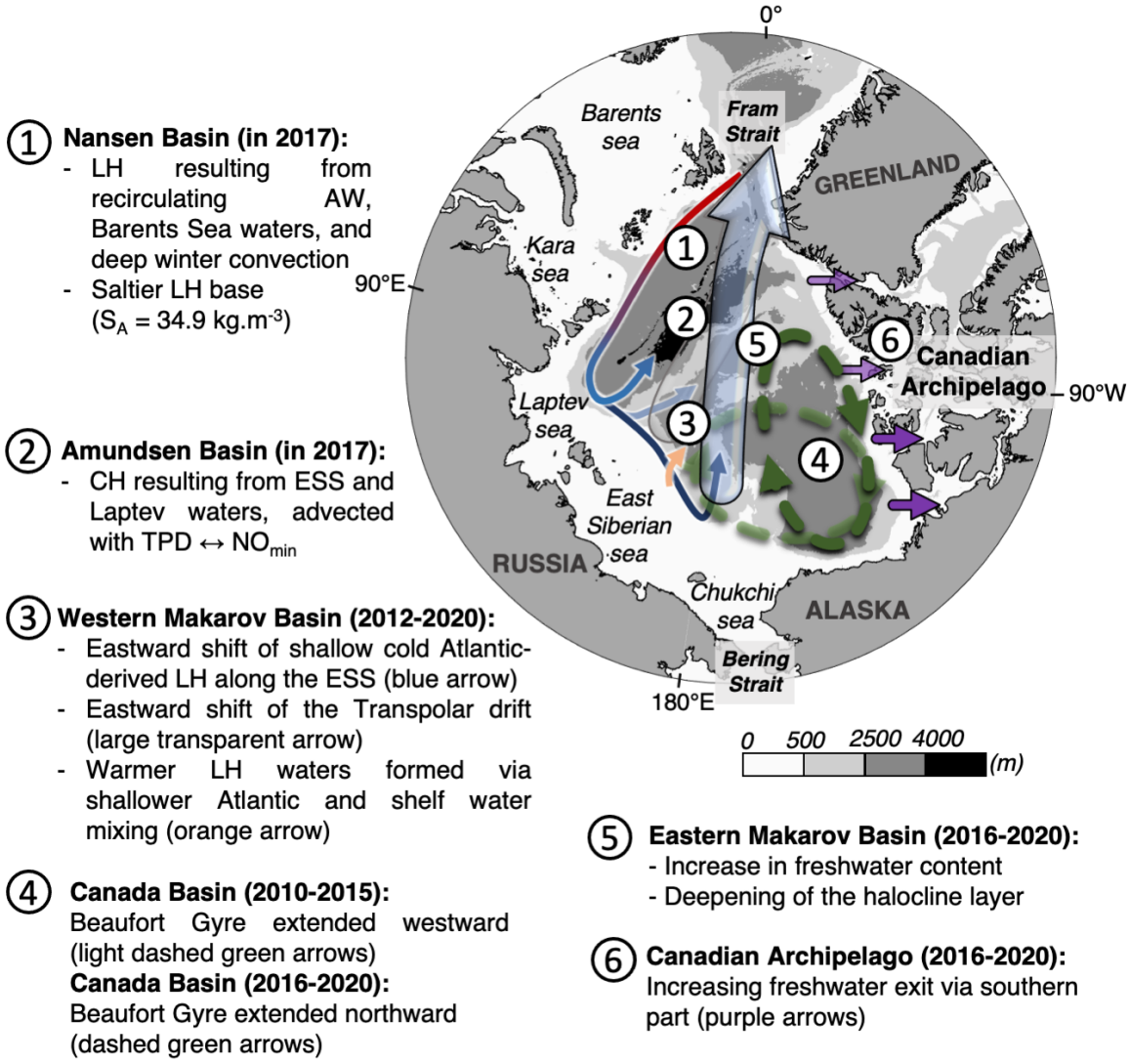

Figure 5.1: Summary of the main results of the PhD-thesis. LH: Lower halocline; CH: Cold halocline; ESS: East Siberian Sea; TPD: Transpolar Drift; BG: Beaufort Gyre.

We took advantage of the PSY4 fields to investigate changes in freshwater distribution and circulation since 2007, as freshwaters contributes to the halocline. In the Amerasian Basin, the largest reservoir of freshwater, the Beaufort Gyre, extended west toward Mendeleev Ridge until 2011, as suggested by Regan et al. (2019). After 2012, the modelled freshwater content increased near the North Pole and the Beaufort Gyre shifted to the northeast. Coincidentally, Atlantic Waters were shallower along the Siberian slope and deeper into the Makarov Basin, and the Transpolar Drift moved from the Lomonosov Ridge to align with the Mendeleev Ridge. The deepening of the isohalines near the North Pole led to the reinforcement of the halocline

stratification in center of the Arctic. In contrast, the halocline weakened all along the continental slope in the Nansen Basin, as well as along the East Siberian Sea slope.

We focused on the changes in halocline waters along the East Siberian Slope and in the Makarov Basin from 2007 to 2020, which appeared to be an area highly impacted by the Atlantification. Autonomous platforms data, shipborne CTD measurements and PSY4 simulations were combined and highlighted three major changes. First, the upper halocline in the Makarov Basin was particularly warm, fresh and thick compared to 2008 and 2017. Following our pan-Arctic analysis of freshwater distribution changes, we concluded that the upper halocline of the Makarov Basin in 2015 was supplied by Beaufort Gyre halocline waters in addition to shelf water influence. Second, after 2012, cold Atlantic-derived lower halocline progressed eastward along the East Siberian slope and supplied the lower halocline of the Makarov Basin. Finally, shallower Atlantic Waters along the slope mixed with dense shelf waters and formed warmer lower halocline water supplying the lower halocline of the Makarov Basin. This contribution of warm waters to the Makarov Basin lower halocline seemed to be a consequence of the Atlantification that now have reached the Amerasian Basin (**Figure 5.2**).

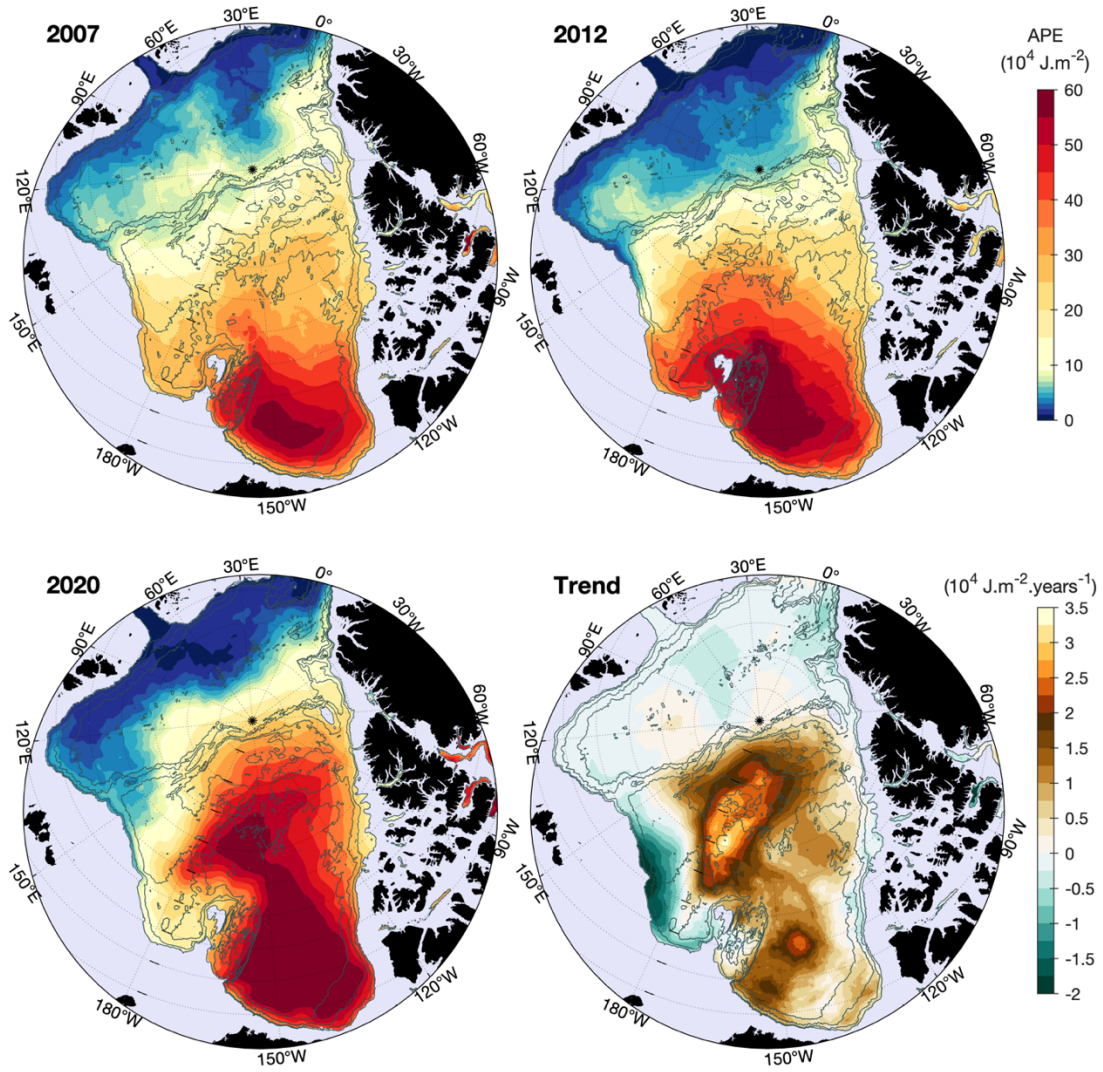

Figure 5.2: Available Potential Energy from PSY4 in the upper water column, above the base of the LH at sigma 27.85 kg.m^{-3}, in 2007, 2012 and 2020. Yearly trends are shown in the last panel.

V.2. Perspectives

We focused on the changes in the structure, strength or sources of the halocline, however our last result suggested changes in the halocline heat content that still need to be investigated, especially in the Makarov Basin. The WHOI drifting platform ITP92, deployed in Makarov Basin one month after the IAOOS15, drifted north across the Makarov Basin with a high temporal resolution (~ 10 profiles a day). Temperatures measured by the ITP92 suggested that dense warm waters of the lower halocline ($27.4 < \sigma < 27.7$ kg.m^{-3}) extended from the East Siberian Slope in the Makarov Basin as far north as 83°N.

Our analyze of the contributions to the halocline was mainly qualitative. The next step could be to quantify the contributions (percentage of pacific Waters for example as in Alkire et al., 2019) and in that perspective, there is an increasing need in biogeochemical measurements (e.g., nutrients, silicates, oxygen, pH, CDOM) as well as isotopes that help in determining the origin of the water masses. Another option, would be to use modelled velocity fields and performed 3D-backtrajectories. During this thesis, only 2D-backtrajectories were computed to investigate the sources in the halocline layer. PSY4 grid is an ORCA12 grid which is non regular in the Arctic domain, complicating the computations. Consequently, we have not been able to compute 3D-backtrajectories using numerical tools, such as OceanParcels (Van Sebille et al., 2018), and further work would be needed.

A key question is to determine whether the on-going Atlantification, now reaching the Amerasian Basin, is resulting from a temporary cyclonic Arctic regime. In case of extended regime in time, will shallower AW reach the Canada Basin and how could they impact the highly stratified water column of the Beaufort Gyre?

Data in the Arctic remain scarce while Arctic Ocean changes are quickly intensifying. Numerical models appeared to be an efficient solution to analyze the evolution of the Arctic in real time, when compared to the time needed for getting proper in-situ measurements. Nevertheless, improvements such as higher horizontal and vertical resolution or modelled shelf-slope processes (e.g., winter ventilation, diapycnal mixing) are still needed to proper catch the changes in the Arctic Ocean.

REFERENCES

Aagaard, K., & Carmack, E. C. (1989). The role of sea ice and other fresh water in the Arctic circulation. Journal of Geophysical Research: Oceans, 94(C10), 14485–14498. https://doi.org/10.1029/JC094iC10p14485

Aagaard, K., Coachman, L. K., & Carmack, E. C. (1981). On the halocline of the Arctic Ocean. Deep Sea Research Part A. Oceanographic Research Papers, 28(6), 529–545. https://doi.org/10.1016/0198-0149(81)90115-1

Alkire, M. B., Falkner, K. K., Morison, J., Collier, R. W., Guay, C. K., Desiderio, R. A., et al. (2010). Sensor-based profiles of the NO parameter in the central Arctic and southern Canada Basin: New insights regarding the cold halocline. Deep Sea Research Part I: Oceanographic Research Papers, 57(11), 1432–1443. https://doi.org/10.1016/j.dsr.2010.07.011

Alkire, M. B., Polyakov, I., Rember, R., Pnyushkov, A., Ivanov, V., & Ashik, I. (2017). Combining physical and geochemical methods to investigate lower halocline water formation and modification along the Siberian continental slope. Ocean Science, 13(6), 983–995. https://doi.org/10.5194/os-13-983-2017

Alkire, M. B., Rember, R., & Polyakov, I. (2019). Discrepancy in the Identification of the Atlantic/Pacific Front in the Central Arctic Ocean: NO Versus Nutrient Relationships. Geophysical Research Letters, 46(7), 3843–3852. https://doi.org/10.1029/2018GL081837

Anderson, L. G., Björk, G., Jutterström, S., Pipko, I., Shakhova, N., Semiletov, I., & Wåhlström, I. (2011). East Siberian Sea, an Arctic region of very high biogeochemical activity. Biogeosciences, 8(6), 1745–1754. https://doi.org/10.5194/bg-8-1745-2011

Anderson, L. G., Björk, G., Holby, O., Jutterström, S., Mörth, C. M., O'Regan, M., et al. (2017). Shelf–Basin interaction along the East Siberian Sea. Ocean Science, 13(2), 349–363. https://doi.org/10.5194/os-13-349-2017

Armitage, T. W. K., Bacon, S., Ridout, A. L., Thomas, S. F., Aksenov, Y., & Wingham, D. J. (2016). Arctic sea surface height variability and change from satellite radar altimetry and GRACE, 2003–2014. Journal of Geophysical Research: Oceans, 121(6), 4303–4322. https://doi.org/10.1002/2015JC011579

Armitage, T. W. K., Bacon, S., Ridout, A. L., Petty, A. A., Wolbach, S., & Tsamados, M. (2017). Arctic Ocean surface geostrophic circulation 2003–2014. The Cryosphere, 11(4), 1767–1780. https://doi.org/10.5194/tc-11-1767-2017

Armitage, T. W. K., Bacon, S., & Kwok, R. (2018). Arctic Sea Level and Surface Circulation Response to the Arctic Oscillation. Geophysical Research Letters, 45(13), 6576–6584. https://doi.org/10.1029/2018GL078386

Athanase, M., Provost, C., Pérez-Hernández, M. D., Sennéchael, N., Bertosio, C., Artana, C., et al. (2020). Atlantic Water Modification North of Svalbard in the Mercator Physical System From 2007 to 2020. Journal of Geophysical Research: Oceans, 125(10), e2020JC016463. https://doi.org/10.1029/2020JC016463

Bertosio, C., Provost, C., Sennéchael, N., Artana, C., Athanase, M., Boles, E., et al. (2020). The Western Eurasian Basin Halocline in 2017: Insights From Autonomous NO Measurements and the Mercator Physical System. Journal of Geophysical Research: Oceans, 125(7), e2020JC016204. https://doi.org/10.1029/2020JC016204

Beszczynska-Möller, A., Woodgate, R.A., H. Melling, C. Lee & Karcher, M. A synthesis of exchanges through the main oceanic gateways to the Arctic Ocean. Oceanography 24(3), 82-99, doi:10.5670/oceanog.2011.59 (2011).

Bintanja, R., & Andry, O. (2017). Towards a rain-dominated Arctic. Nature Climate Change, 7(4), 263–267. https://doi.org/10.1038/nclimate3240

Bintanja, R., & Selten, F. M. (2014). Future increases in Arctic precipitation linked to local evaporation and sea-ice retreat. Nature, 509(7501), 479–482. https://doi.org/10.1038/nature13259

Bourgain, P., & Gascard, J. C. (2011). The Arctic Ocean halocline and its interannual variability from 1997 to 2008. Deep Sea Research Part I: Oceanographic Research Papers, 58(7), 745–756. https://doi.org/10.1016/j.dsr.2011.05.001

Boyd, T. J., Steele, M., Muench, R. D., & Gunn, J. T. (2002). Partial recovery of the Arctic Ocean halocline. Geophysical Research Letters, 29(14), 2-1-2–4. https://doi.org/10.1029/2001GL014047

Carmack, E. C. (2007). The alpha/beta ocean distinction: A perspective on freshwater fluxes, convection, nutrients and productivity in high-latitude seas. Deep Sea Research Part II: Topical Studies in Oceanography, 54(23), 2578–2598. https://doi.org/10.1016/j.dsr2.2007.08.018

Carmack, E. C., Yamamoto-Kawai, M., Haine, T. W. N., Bacon, S., Bluhm, B. A., Lique, C., et al. (2016). Freshwater and its role in the Arctic Marine System: Sources, disposition, storage, export, and physical and biogeochemical consequences in the Arctic and global oceans. Journal of Geophysical Research: Biogeosciences, 121(3), 675–717. https://doi.org/10.1002/2015JG003140

Coachman, L. K. (1969). Physical Oceanography in the Arctic Ocean: 1968. ARCTIC, 22(3), 214–224. https://doi.org/10.14430/arctic3215

Collins, M., Knutti, R., Arblaster, J., Dufresne, J.-L., Fichefet, T., Friedlingstein, P., et al. (2013). Long-term Climate Change: Projections, Commitments and Irreversibility. Climate Change 2013 - The Physical Science Basis: Contribution of Working Group I to the Fifth Assessment Report of the Intergovernmental Panel on Climate Change, 1029–1136. Retrieved from https://research.monash.edu/en/publications/long-term-climate-change-projections-commitments-and-irreversibil

Corlett, W. B., & Pickart, R. S. (2017). The Chukchi slope current. Progress in Oceanography, 153, 50–65. https://doi.org/10.1016/j.pocean.2017.04.005

Davis, P. E. D., Lique, C., & Johnson, H. L. (2014). On the Link between Arctic Sea Ice Decline and the Freshwater Content of the Beaufort Gyre: Insights from a Simple Process Model. Journal of Climate, 27(21), 8170–8184. https://doi.org/10.1175/JCLI-D-14-00090.1

Dickson, R. R., Meincke, J., Malmberg, S.-A., & Lee, A. J. (1988). The “great salinity anomaly” in the Northern North Atlantic 1968-1982. Progress in Oceanography, 20, 103–151. https://doi.org/10.1016/0079-6611(88)90049-3

Dmitrenko, I. A., Ivanov, V. V., Kirillov, S. A., Vinogradova, E. L., Torres-Valdes, S., & Bauch, D. (2011). Properties of the Atlantic derived halocline waters over the Laptev Sea continental margin: Evidence from 2002 to 2009. Journal of Geophysical Research: Oceans, 116(C10). https://doi.org/10.1029/2011JC007269

Doddridge, E. W., Meneghello, G., Marshall, J., Scott, J., & Lique, C. (2019). A Three-Way Balance in the Beaufort Gyre: The Ice-Ocean Governor, Wind Stress, and Eddy Diffusivity. Journal of Geophysical Research: Oceans, 124(5), 3107–3124. https://doi.org/10.1029/2018JC014897

Dukhovskoy, D. S., Johnson, M. A., & Proshutinsky, A. (2004). Arctic decadal variability: An auto-oscillatory system of heat and fresh water exchange. Geophysical Research Letters, 31(3). https://doi.org/10.1029/2003GL019023

Falkner, K. K., Steele, M., Woodgate, R. A., Swift, J. H., Aagaard, K., & Morison, J. (2005). Dissolved oxygen extrema in the Arctic Ocean halocline from the North Pole to the Lincoln Sea. Deep Sea Research Part I: Oceanographic Research Papers, 52(7), 1138–1154. https://doi.org/10.1016/j.dsr.2005.01.007

Haak, H., Jungclaus, J., Mikolajewicz, U., & Latif, M. (2003). Formation and propagation of great salinity anomalies. Geophysical Research Letters, 30(9). https://doi.org/10.1029/2003GL017065

Haine, T. W. N., Curry, B., Gerdes, R., Hansen, E., Karcher, M., Lee, C., et al. (2015). Arctic freshwater export: Status, mechanisms, and prospects. Global and Planetary Change, 125, 13–35. https://doi.org/10.1016/j.gloplacha.2014.11.013

Hunkins, K. L. (1974). Subsurface eddies in the Arctic ocean. Deep Sea Research and Oceanographic Abstracts, 21(12), 1017–1033. https://doi.org/10.1016/0011-7471(74)90064-3

Ingvaldsen, R., Loeng, H., & Asplin, L. (2002). Variability in the Atlantic inflow to the Barents Sea based on a one-year time series from moored current meters. Continental Shelf Research, 22(3), 505–519. https://doi.org/10.1016/S0278-4343(01)00070-X

Itoh, M., Shimada, K., Kamoshida, T., McLaughlin, F., Carmack, E. C., & Nishino, S. (2012). Interannual variability of Pacific Winter Water inflow through Barrow Canyon from 2000 to 2006. Journal of Oceanography, 68(4), 575–592. https://doi.org/10.1007/s10872-012-0120-1

Jakobsson, M. Hypsometry and volume of the Arctic Ocean and its constituent seas. Geochem. Geophys. Geosyst. 3, doi:10.1029/2001GC000302 (2002).

Jung, T., Doblas-Reyes, F., Goessling, H., Guemas, V., Bitz, C., Buontempo, C., et al. (2015). Polar Lower-Latitude Linkages and Their Role in Weather and Climate Prediction. Bulletin of the American Meteorological Society, 96(11), ES197–ES200. https://doi.org/10.1175/BAMS-D-15-00121.1

Kikuchi, T., Hatakeyama, K., & Morison, J. H. (2004). Distribution of convective Lower Halocline Water in the eastern Arctic Ocean. Journal of Geophysical Research: Oceans, 109(C12). https://doi.org/10.1029/2003JC002223

Krishfield, R., Toole, J., Proshutinsky, A., & Timmermans, M.-L. (2008). Automated Ice-Tethered Profilers for Seawater Observations under Pack Ice in All Seasons. Journal of Atmospheric and Oceanic Technology, 25(11), 2091–2105. https://doi.org/10.1175/2008JTECHO587.1

Kwok, R. (2018). Arctic sea ice thickness, volume, and multiyear ice coverage: losses and coupled variability (1958–2018). Environmental Research Letters, 13(10), 105005. https://doi.org/10.1088/1748-9326/aae3ec

Kwok, R., Spreen, G., & Pang, S. (2013). Arctic sea ice circulation and drift speed: Decadal trends and ocean currents. Journal of Geophysical Research: Oceans, 118(5), 2408–2425. https://doi.org/10.1002/jgrc.20191

Lin, P., Pickart, R. S., Moore, G. W. K., Spall, M. A., & Hu, J. (2019). Characteristics and dynamics of wind-driven upwelling in the Alaskan Beaufort Sea based on six years of mooring data. Deep Sea Research Part II: Topical Studies in Oceanography, 162, 79–92. https://doi.org/10.1016/j.dsr2.2018.01.002

Lind, S., Ingvaldsen, R. B., & Furevik, T. (2018). Arctic warming hotspot in the northern Barents Sea linked to declining sea-ice import. Nature Climate Change, 8(7), 634. https://doi.org/10.1038/s41558-018-0205-y

Linders, J., Pickart, Robert. S., Björk, G., & Moore, G. W. K. (2017). On the nature and origin of water masses in Herald Canyon, Chukchi Sea: Synoptic surveys in summer 2004, 2008, and 2009. Progress in Oceanography, 159, 99–114. https://doi.org/10.1016/j.pocean.2017.09.005

Manley, T. O., & Hunkins, K. (1985). Mesoscale eddies of the Arctic Ocean. Journal of Geophysical Research: Oceans, 90(C3), 4911–4930. https://doi.org/10.1029/JC090iC03p04911

Manucharyan, G. E., & Isachsen, P. E. (2019). Critical role of continental slopes in halocline and eddy dynamics of the Ekman-driven Beaufort Gyre. Journal of Geophysical Research: Oceans, 0(ja). https://doi.org/10.1029/2018JC014624

Manucharyan, G. E., & Spall, M. A. (2016). Wind-driven freshwater buildup and release in the Beaufort Gyre constrained by mesoscale eddies. Geophysical Research Letters, 43(1), 273–282. https://doi.org/10.1002/2015GL065957

Manucharyan, G. E., Spall, M. A., & Thompson, A. F. (2016). A Theory of the Wind-Driven Beaufort Gyre Variability. Journal of Physical Oceanography, 46(11), 3263–3278. https://doi.org/10.1175/JPO-D-16-0091.1

Mathis, J. T., Pickart, R. S., Hansell, D. A., Kadko, D., & Bates, N. R. (2007). Eddy transport of organic carbon and nutrients from the Chukchi Shelf: Impact on the upper halocline of the western Arctic Ocean. Journal of Geophysical Research: Oceans, 112(C5). https://doi.org/10.1029/2006JC003899

McLaughlin, F. A., Carmack, E. C., Williams, W. J., Zimmermann, S., Shimada, K., & Itoh, M. (2009). Joint effects of boundary currents and thermohaline intrusions on the warming of Atlantic water in the Canada Basin, 1993–2007. Journal of Geophysical Research: Oceans, 114(C1). https://doi.org/10.1029/2008JC005001

McPhee, M. G. (2012). Intensification of Geostrophic Currents in the Canada Basin, Arctic Ocean. Journal of Climate, 26(10), 3130–3138. https://doi.org/10.1175/JCLI-D-12-00289.1

Meneghello, G., Marshall, J., Cole, S. T., & Timmermans, M.-L. (2017). Observational Inferences of Lateral Eddy Diffusivity in the Halocline of the Beaufort Gyre: eddy diffusivity in the Beaufort Gyre. Geophysical Research Letters, 44(24), 12,331-12,338. https://doi.org/10.1002/2017GL075126

Meneghello, G., Marshall, J., Timmermans, M.-L., & Scott, J. (2018). Observations of Seasonal Upwelling and Downwelling in the Beaufort Sea Mediated by Sea Ice. Journal of Physical Oceanography, 48(4), 795–805. https://doi.org/10.1175/JPO-D-17-0188.1

Meneghello, G., Marshall, J., Campin, J.-M., Doddridge, E., & Timmermans, M.-L. (2018). The Ice-Ocean Governor: Ice-Ocean Stress Feedback Limits Beaufort Gyre Spin-Up. Geophysical Research Letters, 45(20), 11,293-11,299. https://doi.org/10.1029/2018GL080171

Morison, J., Steele, M., & Andersen, R. (1998). Hydrography of the upper Arctic Ocean measured from the nuclear submarine U.S.S. Pargo. Deep Sea Research Part I: Oceanographic Research Papers, 45(1), 15–38. https://doi.org/10.1016/S0967-0637(97)00025-3

Morison, J., Steele, M., Kikuchi, T., Falkner, K., & Smethie, W. (2006). Relaxation of central Arctic Ocean hydrography to pre-1990s climatology. Geophysical Research Letters, 33(17). https://doi.org/10.1029/2006GL026826

Morison, J., Kwok, R., Peralta-Ferriz, C., Alkire, M., Rigor, I., Andersen, R., & Steele, M. (2012). Changing Arctic Ocean freshwater pathways. Nature, 481(7379), 66–70. https://doi.org/10.1038/nature10705

Morison, J., Kwok, R., Dickinson, S., Andersen, R., Peralta-Ferriz, C., Morison, D., et al. (2021). The Cyclonic Mode of Arctic Ocean Circulation. Journal of Physical Oceanography, 51(4), 1053–1075. https://doi.org/10.1175/JPO-D-20-0190.1

Muench, R. D., Schumacher, J. D., & Salo, S. A. (1988). Winter currents and hydrographic conditions on the northern central Bering Sea shelf. Journal of Geophysical Research: Oceans, 93(C1), 516–526. https://doi.org/10.1029/JC093iC01p00516

Nansen, F. (1902). The oceanography of the North Polar Basin. The Norwegian North Polar Expedition 1893-1896. Scient. Results, 3(9). Retrieved from https://ci.nii.ac.jp/naid/10007477148/

Nikolopoulos, A., Pickart, R. S., Fratantoni, P. S., Shimada, K., Torres, D. J., & Jones, E. P. (2009). The western Arctic boundary current at 152°W: Structure, variability, and transport. Deep Sea Research Part II: Topical Studies in Oceanography, 56(17), 1164–1181. https://doi.org/10.1016/j.dsr2.2008.10.014

Nishino, S., Shimada, K., Itoh, M., Yamamoto-Kawai, M., & Chiba, S. (2008). East–west differences in water mass, nutrient, and chlorophyll a distributions in the sea ice reduction region of the western Arctic Ocean. Journal of Geophysical Research: Oceans, 113(C1). https://doi.org/10.1029/2007JC004666

Notz, D., & Stroeve, J. (2016). Observed Arctic sea-ice loss directly follows anthropogenic CO2 emission. Science, 354(6313), 747–750. https://doi.org/doi:10.1126/science.aag2345

Nummelin, A., Ilicak, M., Li, C., & Smedsrud, L. H. (2016). Consequences of future increased Arctic runoff on Arctic Ocean stratification, circulation, and sea ice cover. Journal of Geophysical Research: Oceans, 121, 617– 637. https://doi.org/10.1002/2015JC011156

Overland, J. E., & Wang, M. (2016). Recent Extreme Arctic Temperatures are due to a Split Polar Vortex. Journal of Climate, 29(15), 5609–5616. https://doi.org/10.1175/JCLI-D-16-0320.1

Peralta-Ferriz, C., & Woodgate, R. A. (2015). Seasonal and interannual variability of pan-Arctic surface mixed layer properties from 1979 to 2012 from hydrographic data, and the dominance of stratification for multiyear mixed layer depth shoaling. Progress in Oceanography, 134, 19–53. https://doi.org/10.1016/j.pocean.2014.12.005

Pickart, R. S., Weingartner, T. J., Pratt, L. J., Zimmermann, S., & Torres, D. J. (2005). Flow of winter-transformed Pacific water into the Western Arctic. Deep Sea Research Part II: Topical Studies in Oceanography, 52(24), 3175–3198. https://doi.org/10.1016/j.dsr2.2005.10.009

Pickart, R. S., Moore, G. W. K., Torres, D. J., Fratantoni, P. S., Goldsmith, R. A., & Yang, J. (2009). Upwelling on the continental slope of the Alaskan Beaufort Sea: Storms, ice, and oceanographic response. Journal of Geophysical Research: Oceans, 114(C1). https://doi.org/10.1029/2008JC005009

Pisareva, M. N., Pickart, R. S., Spall, M. A., Nobre, C., Torres, D. J., Moore, G. W. K., & Whitledge, T. E. (2015). Flow of pacific water in the western Chukchi Sea: Results from the 2009 RUSALCA expedition. Deep Sea Research Part I: Oceanographic Research Papers, 105, 53–73. https://doi.org/10.1016/j.dsr.2015.08.011

Polyakov, I. V., Pnyushkov, A. V., Alkire, M. B., Ashik, I. M., Baumann, T. M., Carmack, E. C., et al. (2017). Greater role for Atlantic inflows on sea-ice loss in the Eurasian Basin of the Arctic Ocean. Science, 356(6335), 285–291. https://doi.org/10.1126/science.aai8204

Polyakov, I. V., Pnyushkov, A. V., & Carmack, E. C. (2018). Stability of the arctic halocline: a new indicator of arctic climate change. Environmental Research Letters, 13(12), 125008. https://doi.org/10.1088/1748-9326/aaec1e

Polyakov, I. V., Alkire, M. B., Bluhm, B. A., Brown, K. A., Carmack, E. C., Chierici, M., et al. (2020). Borealization of the Arctic Ocean in Response to Anomalous Advection From Sub-Arctic Seas. Frontiers in Marine Science, 7. https://doi.org/10.3389/fmars.2020.00491

Polyakov, I. V., Rippeth, T. P., Fer, I., Alkire, M. B., Baumann, T. M., Carmack, E. C., et al. (2020). Weakening of Cold Halocline Layer Exposes Sea Ice to Oceanic Heat in the Eastern Arctic Ocean. Journal of Climate, 33(18), 8107–8123. https://doi.org/10.1175/JCLI-D-19-0976.1

Proshutinsky, A., & Johnson, M. A. (1997). Two circulation regimes of the wind-driven Arctic Ocean. Journal of Geophysical Research: Oceans, 102(C6), 12493–12514. https://doi.org/10.1029/97JC00738

Proshutinsky, A., Bourke, R. H., & McLaughlin, F. A. (2002). The role of the Beaufort Gyre in Arctic climate variability: Seasonal to decadal climate scales. Geophysical Research Letters, 29(23), 15-1-15–4. https://doi.org/10.1029/2002GL015847

Proshutinsky, A., Krishfield, R., Timmermans, M.-L., Toole, J., Carmack, E. C., McLaughlin, F., et al. (2009). Beaufort Gyre freshwater reservoir: State and variability from observations. Journal of Geophysical Research: Oceans, 114(C1). https://doi.org/10.1029/2008JC005104

Proshutinsky, A., Dukhovskoy, D., Timmermans, M.-L., Krishfield, R., & Bamber Jonathan L. (2015). Arctic circulation regimes. Philosophical Transactions of the Royal Society A: Mathematical, Physical and Engineering Sciences, 373(2052), 20140160. https://doi.org/10.1098/rsta.2014.0160

Proshutinsky, A., Krishfield, R., Toole, J. M., Timmermans, M.-L., Williams, W., Zimmermann, S., et al. (2019). Analysis of the Beaufort Gyre Freshwater Content in 2003–2018. Journal of Geophysical Research: Oceans, 124(12), 9658–9689. https://doi.org/10.1029/2019JC015281

Proshutinsky, A., Krishfield, R., & Timmermans, M.-L. (2020). Introduction to Special Collection on Arctic Ocean Modeling and Observational Synthesis (FAMOS) 2: Beaufort Gyre Phenomenon. Journal of Geophysical Research: Oceans, 125(2), e2019JC015400. https://doi.org/10.1029/2019JC015400

Provost, C., Pelon, J., Sennéchael, N., Calzas, M., Blouzon, F., Desautez, A., et al. (2015). IAOOS (Ice - Atmosphere - Arctic Ocean Observing System, 2011-2019). Mercator Ocean Quarterly Newsletter, (51), 13–15. Retrieved from https://hal.archives-ouvertes.fr/hal-01138872

Regan, H., Lique, C., & Armitage, T. W. K. (2019). The Beaufort Gyre Extent, Shape, and Location Between 2003 and 2014 From Satellite Observations. Journal of Geophysical Research: Oceans, 124(2), 844–862. https://doi.org/10.1029/2018JC014379

Rigor, I. G., Wallace, J. M., & Colony, R. L. (2002). Response of Sea Ice to the Arctic Oscillation. Journal of Climate, 15(18), 2648–2663. https://doi.org/10.1175/1520-0442(2002)015<2648:ROSITT>2.0.CO;2

Rudels, B. (2012). Arctic Ocean circulation and variability-advection and external forcing encounter constraints and local processes. Ocean Science, 8(2), 261–286. https://doi.org/10.5194/os-8-261-2012

Rudels, B., Anderson, L. G., & Jones, E. P. (1996). Formation and evolution of the surface mixed layer and halocline of the Arctic Ocean. Journal of Geophysical Research: Oceans, 101(C4), 8807–8821. https://doi.org/10.1029/96JC00143

Rudels, B., Jones, E. P., Schauer, U., & Eriksson, P. (2004). Atlantic sources of the Arctic Ocean surface and halocline waters. Polar Research, 23(2), 181–208. https://doi.org/10.1111/j.1751-8369.2004.tb00007.x

Rudels, B., Jones, E. P., Anderson, L. G., & Kattner, G. (2013). On the Intermediate Depth Waters of the Arctic Ocean. In O. M. Johannessen, R. D. Muench, & J. E. Overland (Eds.), Geophysical Monograph Series (pp. 33–46). Washington, D. C.: American Geophysical Union. https://doi.org/10.1029/GM085p0033

Rudels, B., Korhonen, M., Schauer, U., Pisarev, S., Rabe, B., & Wisotzki, A. (2015). Circulation and transformation of Atlantic water in the Eurasian Basin and the contribution of the Fram Strait inflow branch to the Arctic Ocean heat budget. Progress in Oceanography, 132, 128–152. https://doi.org/10.1016/j.pocean.2014.04.003

Schauer, U., Rudels, B., Jones, E. P., Anderson, L. G., Muench, R. D., Björk, G., et al. (2002). Confluence and redistribution of Atlantic water in the Nansen, Amundsen and Makarov basins. Annales Geophysicae, 20(2), 257–273. https://doi.org/10.5194/angeo-20-257-2002

Semiletov, I., Dudarev, O., Luchin, V., Charkin, A., Shin, K.-H., & Tanaka, N. (2005). The East Siberian Sea as a transition zone between Pacific-derived waters and Arctic shelf waters. Geophysical Research Letters, 32(10). https://doi.org/10.1029/2005GL022490

Serreze, M. C., Barrett, A. P., Slater, A. G., Woodgate, R. A., Aagaard, K., Lammers, R. B., et al. (2006). The large-scale freshwater cycle of the Arctic. Journal of Geophysical Research: Oceans, 111(C11). https://doi.org/10.1029/2005JC003424

Serreze, M. C., & Barrett, A. P. (2011). Characteristics of the Beaufort Sea High. Journal of Climate, 24(1), 159–182. https://doi.org/10.1175/2010JCLI3636.1

Serreze, M. C., Barrett, A. P., & Cassano, J. J. (2011). Circulation and surface controls on the lower tropospheric air temperature field of the Arctic. Journal of Geophysical Research: Atmospheres, 116(D7). https://doi.org/10.1029/2010JD015127

Sévellec, F., Fedorov, A. V., & Liu, W. (2017). Arctic sea-ice decline weakens the Atlantic Meridional Overturning Circulation. Nature Climate Change, 7(8), 604– 610. https://doi.org/10.1038/nclimate3353

Shimada, K., Itoh, M., Nishino, S., McLaughlin, F., Carmack, E. C., & Proshutinsky, A. (2005). Halocline structure in the Canada Basin of the Arctic Ocean. Geophysical Research Letters, 32(3). https://doi.org/10.1029/2004GL021358

Spall, M. A., Pickart, R. S., Fratantoni, P. S., & Plueddemann, A. J. (2008). Western Arctic Shelfbreak Eddies: Formation and Transport. Journal of Physical Oceanography, 38(8), 1644–1668. https://doi.org/10.1175/2007JPO3829.1

Steele, M., & Boyd, T. (1998). Retreat of the cold halocline layer in the Arctic Ocean. Journal of Geophysical Research: Oceans, 103(C5), 10419–10435. https://doi.org/10.1029/98JC00580

Steele, M., Morison, J. H., & Curtin, T. B. (1995). Halocline water formation in the Barents Sea. Journal of Geophysical Research: Oceans, 100(C1), 881–894. https://doi.org/10.1029/94JC02310

Steele, M., Morison, J., Ermold, W., Rigor, I., Ortmeyer, M., & Shimada, K. (2004). Circulation of summer Pacific halocline water in the Arctic Ocean. Journal of Geophysical Research: Oceans, 109(C2). https://doi.org/10.1029/2003JC002009

Thompson, D. W. J., & Wallace, J. M. (1998). The Arctic oscillation signature in the wintertime geopotential height and temperature fields. Geophysical Research Letters, 25(9), 1297–1300. https://doi.org/10.1029/98GL00950

Thornalley, D. J., Oppo, D. W., Ortega, P., Robson, J. I., Brierley, C. M., Davis, R., Hall, I., Moffa-Sanchez, P., Rose, N. L., Spooner, P. T., Yashayaev, I., & Keigwin, L. D. (2018). Anomalously weak Labrador Sea convection and Atlantic overturning during the past 150 years. Nature, 556(7700), 227– 230. https://doi.org/10.1038/s41586-018-0007-4

Thorndike, A. S., & Colony, R. (1982). Sea ice motion in response to geostrophic winds. Journal of Geophysical Research: Oceans, 87(C8), 5845–5852. https://doi.org/10.1029/JC087iC08p05845

Timmermans, M.-L., & Marshall, J. (2020). Understanding Arctic Ocean circulation: a review of ocean dynamics in a changing climate. Journal of Geophysical Research: Oceans, n/a(n/a), e2018JC014378. https://doi.org/10.1029/2018JC014378

Timmermans, M.-L., Toole, J., Proshutinsky, A., Krishfield, R., & Plueddemann, A. (2008). Eddies in the Canada Basin, Arctic Ocean, Observed from Ice-Tethered Profilers. Journal of Physical Oceanography, 38(1), 133–145. https://doi.org/10.1175/2007JPO3782.1

Timmermans, M.-L., Proshutinsky, A., Krishfield, R. A., Perovich, D. K., Richter-Menge, J. A., Stanton, T. P., & Toole, J. M. (2011). Surface freshening in the Arctic Ocean's Eurasian Basin: An apparent consequence of recent change in the wind-driven circulation. Journal of Geophysical Research: Oceans, 116(C8). https://doi.org/10.1029/2011JC006975

Timmermans, M.-L., Proshutinsky, A., Golubeva, E., Jackson, J. M., Krishfield, R., McCall, M., et al. (2014). Mechanisms of Pacific Summer Water variability in the Arctic's Central Canada Basin. Journal of Geophysical Research: Oceans, 119(11), 7523–7548. https://doi.org/10.1002/2014JC010273

Timmermans, M.-L., Marshall, J., Proshutinsky, A., & Scott, J. (2017). Seasonally derived components of the Canada Basin halocline. Geophysical Research Letters, 44(10), 5008–5015. https://doi.org/10.1002/2017GL073042

Timmermans, M.-L., Toole, J., & Krishfield, R. (2018). Warming of the interior Arctic Ocean linked to sea ice losses at the basin margins. Science Advances, 4(8), eaat6773. https://doi.org/10.1126/sciadv.aat6773

Van Sebille, E., Griffies, S. M., Abernathey, R., Adams, T. P., Berloff, P., Biastoch, A., et al. (2018). Lagrangian ocean analysis: Fundamentals and practices. Ocean Modelling, 121, 49–75. https://doi.org/10.1016/j.ocemod.2017.11.008

Vihma, T. (2014). Effects of Arctic Sea Ice Decline on Weather and Climate: A Review. Surveys in Geophysics, 35(5), 1175–1214. https://doi.org/10.1007/s10712-014-9284-0

Wang, Q. (2021). Stronger Variability in the Arctic Ocean Induced by Sea Ice Decline in a Warming Climate: Freshwater Storage, Dynamic Sea Level and Surface Circulation. Journal of Geophysical Research: Oceans, 126(3), e2020JC016886. https://doi.org/10.1029/2020JC016886

Wang, X., Zhao, J., Lobanov, V. B., Kaplunenko, D., Rudykh, Y. N., He, Y., & Chen, X. (2021). Distribution and Transport of Water Masses in the East Siberian Sea and Their Impacts on the Arctic Halocline. Journal of Geophysical Research: Oceans, 126(8), e2020JC016523. https://doi.org/10.1029/2020JC016523

Weingartner, T. J., Cavalieri, D. J., Aagaard, K., & Sasaki, Y. (1998). Circulation, dense water formation, and outflow on the northeast Chukchi Shelf. Journal of Geophysical Research: Oceans, 103(C4), 7647–7661. https://doi.org/10.1029/98JC00374

Williams, W. J., & Carmack, E. C. (2015). The 'interior' shelves of the Arctic Ocean: Physical oceanographic setting, climatology and effects of sea-ice retreat on cross-shelf exchange. Progress in Oceanography, 139, 24–41. https://doi.org/10.1016/j.pocean.2015.07.008

Woodgate, R. A. (2012). Arctic Ocean Circulation : Going around at the top of the world, 15.

Woodgate, R. A., & Peralta-Ferriz, C. (2021). Warming and Freshening of the Pacific Inflow to the Arctic From 1990-2019 Implying Dramatic Shoaling in Pacific Winter Water Ventilation of the Arctic Water Column. Geophysical Research Letters, 48(9), e2021GL092528. https://doi.org/10.1029/2021GL092528

Woodgate, R. A., Aagaard, K., Swift, J. H., Falkner, K. K., & Smethie, W. M. (2005). Pacific ventilation of the Arctic Ocean's lower halocline by upwelling and diapycnal mixing over the continental margin. Geophysical Research Letters, 32(18). https://doi.org/10.1029/2005GL023999

Woodgate, R. A., Aagaard, K., Swift, J. H., Smethie, W. M., & Falkner, K. K. (2007). Atlantic water circulation over the Mendeleev Ridge and Chukchi Borderland from thermohaline intrusions and water mass properties. Journal of Geophysical Research, 112(C2), C02005. https://doi.org/10.1029/2005JC003416

Woods, C., & Caballero, R. (2016). The Role of Moist Intrusions in Winter Arctic Warming and Sea Ice Decline. Journal of Climate, 29, 4473–4485. https://doi.org/10.1175/JCLI-D-15-0773.1

Zhang, J., Weijer, W., Steele, M., Cheng, W., Verma, T., & Veneziani, M. (2021). Labrador Sea freshening linked to Beaufort Gyre freshwater release. Nature Communications, 12(1), 1229. https://doi.org/10.1038/s41467-021-21470-3

Zhao, M., Timmermans, M.-L., Cole, S., Krishfield, R., Proshutinsky, A., & Toole, J. (2014). Characterizing the eddy field in the Arctic Ocean halocline. Journal of Geophysical Research: Oceans, 119(12), 8800–8817. https://doi.org/10.1002/2014JC010488

Zhao, M., Timmermans, M.-L., Cole, S., Krishfield, R., & Toole, J. (2016). Evolution of the eddy field in the Arctic Ocean's Canada Basin, 2005–2015. Geophysical Research Letters, 43(15), 8106–8114. https://doi.org/10.1002/2016GL069671